Structured Photonic Materials for Multi-Spectral Imaging Applications

Iain James Hugh McCrindle

A Thesis submitted to

School of Engineering

University of Glasgow

in fulfilment of the requirements for the degree of

Doctor of Philosophy

March 2015

Abstract

Structured photonic materials are typically composed of periodic subwavelength elements where the unit cell geometries can impact the overall optical characteristics of the bulk material. By using micro and nanofabrication technologies it is possible to engineer the electromagnetic properties of structured photonic materials for a given application and create a variety of optical components such as band pass filters and absorbers. Two structured photonic materials that have gained substantial interest in recent years are plasmonic filters and metamaterials which are well suited for optical and terahertz imaging applications, respectively. In addition to imaging applications within individual wavebands, structured photonic materials, such as plasmonic filters and metamaterials, could be hybridised and combined with suitable sensors to create a multi-spectral imaging system capable of imaging at optical and terahertz wavebands simultaneously. These new hybrid structured photonic materials are known as synthetic multi-spectral materials, and their development will be presented in this work.

To design synthetic multi-spectral materials it was necessary to optimise the plasmonic filter and metamaterial components independently. This involved electromagnetic simulation studies using finite-difference time-domain techniques, fabrication of the structured materials and characterisation using suitable techniques for the relevant spectral band. It was also necessary to ensure that all structures used the same materials and similar fabrication processing techniques as a means of simplifying hybridisation of the two structures.

Plasmonic filters exhibit extraordinary optical transmission due to coupling of light with surface plasmons at a metal-dielectric interface. A 16 colour plasmonic filter set, consisting of triangular hole arrays etched into an aluminium film, was optimised for imaging applications in the visible and near infrared spectral range. Initial work on the integration of synthetic multi-spectral materials with CMOS image sensors was undertaken by developing fabrication processes to integrate plasmonic colour filters with two different CMOS chips. Preliminary results from the characterisation of the optical filters fabricated on to the chips have been presented. The resonant wavelengths of the plasmonic colour filters were then scaled up to infrared wavelengths where it was necessary to consider the role of spoof surface plasmons on the extraordinary optical transmission phenomenon. This led to the fabrication of 8 short wave infrared plasmonic filters.

Metamaterial band pass filters consist of a single metal film etched with a periodic complementary electric ring resonator unit cell structure. Metamaterial absorbers consist of

an electric ring resonator, separated by a metallic ground layer by a dielectric spacer. In the course of this work, two metamaterial filters and four metamaterial absorbers were designed. The metamaterial structures exhibit resonant characteristics at terahertz frequencies.

Three synthetic multi-spectral materials, each consisting of hybrid plasmonic filter and terahertz metamaterial structures, have been simulated, fabricated and characterised. The first synthetic multi-spectral material combines 16 plasmonic filters with a terahertz metamaterial filter and is capable of filtering 15 optical wavelengths and a single near infrared wavelength, whilst simultaneously filtering a single terahertz frequency. The multi-spectral filter demonstrates that it is possible to engineer the optical passband characteristics of a thin metal film over several decades of wavelength using a single electron beam lithography step. The second synthetic multi-spectral material consists of 16 plasmonic filters hybridised with a terahertz metamaterial absorber and can filter 15 optical wavelengths and a single near infrared wavelength whilst simultaneously absorbing a single terahertz frequency. Plasmonic filters and metamaterial absorbers are promising components for use in the development of new optical and terahertz imaging systems, respectively, and therefore the second synthetic multi-spectral material represents a significant step forward in the development of a visible and terahertz multi-spectral camera. The third synthetic multi-spectral material combines 7 plasmonic filters with a low metal fill factor metamaterial absorber, to increase the measured transmission of the plasmonic filter components. The third synthetic multi-spectral material is capable of filtering three optical wavelengths, a single near infrared wavelength, a single short wave infrared wavelength and two mid infrared wavelengths, whilst simultaneously absorbing a single terahertz frequency. Such a synthetic multi-spectral material could aid in the development of a visible, infrared and terahertz multi-spectral camera.

Declaration

Unless otherwise acknowledged, the content of this Thesis is the result of my own work. None of this material has been submitted for any other degree at the University of Glasgow or any other institution.

Iain James Hugh McCrindle

Acknowledgements

None of this would have been possible without the support of a large of number of friends and family members. I want to thank all of the people without whom my life, and these pages, would be far emptier.

To begin with I would like to thank my supervisor, David Cumming, for giving me the opportunity to work on such a challenging, rewarding and exciting PhD project. I'd also like to thank him for all the time that he has invested in me over the past 4 years. His support, patience and guidance kept me on the right track and ensured that my PhD research was a success. Special thanks also go to my second supervisor, Tim Drysdale, for his assistance and advice, specifically with regards to scientific writing and running challenging optical simulations. I am particularly indebted to my third supervisor, James Grant, whose support and guidance has been invaluable throughout the course of this project. I'd like to thank him for always being available to answer silly questions, for devoting a substantial amount of time to my training, and for every discussion that I left with a renewed optimism and excitement for whatever we were working on. I'd also like to thank James for taking the time to review this Thesis.

I want to extend my thanks to all members of the Microsystem Technology Group. I cannot imagine a more talented and exceptional group of individuals and it has been a pleasure working with you all. I'd like to thank Qin Chen for introducing me to plasmonic filters and for assisting with my initial clean room training. I am grateful to Kirsty Walls for all of our discussions on plasmonics, which have been invaluable in aiding my understanding of the field. Special thanks go to Luiz Gouveia for designing the chips used in this project and for assisting with the characterisation of processed chips. Thanks also to my office buddies: Mohammed Al-Rawhani, Vasileios Papageorgiou (V-Man) and Boon Chong Cheah.

I am particularly grateful to the staff of the James Watt Nanofabrication Centre. None of the devices presented in this Thesis would have been possible without their assistance, and their dedication in running and maintaining the facility.

I would also like to thank Harry Atwater and the Atwater Group for hosting my research placement at the California Institute of Technology and for making me feel welcome during my visit.

In addition to the above, I would like to thank all of my friends who have no idea or interest in what I've spent the last 4 years doing, but have made sure that I've spent many nights at gigs and many weekends in the pub.

I'd like to thank all of my family for their support. Thank you to my wife, Emma, for her constant encouragement throughout the course of my PhD and for putting up with all of my science facts and awesome jokes. Thank you for cheering me up whenever I've had a hard day, always making me laugh and for just being an all-round tremendous wife. I also have to give a special mention to Glen, our first budgie, and Dennis, our latest budgie friend. Finally, thank you to my Mum and Dad who have always been there whenever I've needed them over the past 26 years. I wouldn't have got this far without your support and I hope that I have done you both proud.

Publications

Journal Papers

I. J. H. McCrindle, J. Grant, L. C. Gouveia, and D. R. S. Cumming, "Infrared plasmonic filters integrated with an optical and terahertz multi-spectral material," Physica Status Solidi A: Applications and Materials Science, *accepted for publication*, March 2015.

J. Grant, I. J. H. McCrindle, C. Li, and D. R. S. Cumming, "Multispectral metamaterial absorber," Optics Letters, Vol. 39, No. 5, 1227-1230, 2014.

I. J. H. McCrindle, J. Grant, T. D. Drysdale, and D. R. S. Cumming, "Multi-Spectral Materials: Hybridisation of Optical Plasmonic Filters and a Terahertz Metamaterial Absorber," Advanced Optical Materials, 2, 149-153, 2014.

J. Grant, I. Escorcia-Carranza, C. Li, I. J. H. McCrindle, J. Gough, and D. R. S. Cumming, "A monolithic resonant terahertz sensor element comprising a metamaterial absorber and micro-bolometer," Laser and Photonics Reviews, 7, 1043-1048, 2013.

I. J. H. McCrindle, J. Grant, T. D. Drysdale, and D. R. S. Cumming, "Hybridization of optical plasmonics with terahertz metamaterials to create multi-spectral filters," Optics Express, Vol. 21, No. 16, 19142-19152, 2013. Also selected to feature in The Virtual Journal for Biomedical Optics, Vol. 8, Iss. 9, 2013.

J. P. Grant, I. J. H. McCrindle, and D. R. S. Cumming, "Simulation, Fabrication and Characterization of THz Metamaterial Absorbers," Journal of Visualized Experiments, 70, e50114, 2012.

Conference Papers

D. R. S. Cumming, J. Grant, and I. J. H. McCrindle, "Plasmonic and metamaterial technologies for imaging," SPIE Security + Defence, 2014.

D. R. S. Cumming, I. J. H. McCrindle, J. Grant, and T. D. Drysdale, "Design and Implementation of Synthetic Multi-spectral Materials," Progress in Electromagnetics Research Symposium (PIERS), 2014.

I. J. H McCrindle, J. Grant, T. D. Drysdale, and D. R. S. Cumming, "Optical and near infrared plasmonic filters integrated with terahertz metamaterials," Conference on Lasers and Electro-Optics (CLEO), 2014.

I. J. H. McCrindle, J. Grant, T. D. Drysdale, and D. R. S. Cumming, "Multi-Spectral Materials Using Metamaterial and Surface Plasmon Resonance Technologies," The 11th International Symposium on Photonic and Electromagnetic Crystal Structures (PECS-XI), 2014.

J. Grant, I. Escorcia-Carranza, C. Li, I. J. H. McCrindle, and D. R. S. Cumming, "Terahertz Image Sensor Comprising a Metamaterial Absorber and Micro-bolometer," The 11th International Symposium on Photonic and Electromagnetic Crystal Structures (PECS-XI), 2014.

D. R. S. Cumming, I. J. H. McCrindle, C. Martin, and Q. Chen, "Direct write and nanoprinting for plasmon resonance color filters," The 57th International Conference on Electron, Ion, and Photon Beam Technology and Nanofabrication (EIPBN), 2013.

D. R. S. Cumming, T. D. Drysdale, J. Grant, I. J. H. McCrindle, K. Walls, "Planar Photonics for CMOS integration," Photonics Global Conference (PGC), 2012.

Posters

I. J. H. McCrindle, J. Grant, T. D. Drysdale, and D. R. S. Cumming, "Nanoplasmonic structures and metamaterials: engineered optical materials and their applications," Multicorder IAB meeting, 2014.

I. J. H. McCrindle, J. Grant, T. D. Drysdale, and D. R. S. Cumming, "Multi-spectral materials: hybridisation of optical plasmonics and terahertz metamaterials," The long arm of microelectronics – satellite meeting, The Royal Society, 2013.

Q. Chen, I. J. H. McCrindle, and D. R. S. Cumming, "Nanophotonics for digital imaging," James Watt Nanofabrication Centre (JWNC) Open Day, 2012. Prize winning poster.

Oral Presentations

I. J. H. McCrindle, "Structured Photonic Materials for Multispectral Imaging Applications," Atwater Group, California Institute of Technology, 2014. Presentation given to the Atwater Group during my Mobility Scholarship funded research placement.

I. J. H. McCrindle, "Multi-spectral materials and my experiences as a PhD Student," Centre for Doctoral Training in Sensing and Measurement Induction Day, 2014.

I. J. H McCrindle, "Plasmonic filters and metamaterials for imaging," James Watt Nanofabrication Centre (JWNC) user meeting, 2014.

I. J. H. McCrindle, "My experiences as a PhD student," Prospective PhD student information day, 2013.

I. J. H McCrindle, "Plasmonic devices for visible light imaging," SU2P Integrated Photonics Theme Workshop, 2012.

Other Publications

D. R. S. Cumming, J. P. Grant, I. J. H. McCrindle, "Terahertz radiation detector, focal plane array incorporating terahertz detector, multispectral metamaterial absorber, and combined optical filter and terahertz absorber," Patent Application, 2014.

I. J. H. McCrindle, D. R. S. Cumming, "Integrierte plasmonische Farbfilter für CMOS-Bildsensoren," or "Plasmonic Filters integrated with CMOS Image Sensors," Photonik, 6, 38-40, 2013.

Contributors

Two complementary metal-oxide semiconductor (CMOS) image sensors, consisting of arrays of photodiodes, were used in this project. My role was to fabricate plasmonic filters on the surface of these chips, as is described in Section 5.3 and Section 5.4. I also contributed to the characterisation of Chip 1 after processing.

Chip 1, presented in Section 5.3, was originally designed for another project and therefore acknowledgements must be given to the head of the project: Bhaskar Choubey, and the chip designer: Luiz Gouveia. The chip was manufactured using a 0.35 µm AMS process. Luiz Gouveia also constructed the measurement set up, wrote the LabVIEW control software and assisted with characterising the processed chips. The results are presented in Section 5.3.2.

Chip 2, presented in Section 5.4 and Section 7.5, was designed specifically for this project. The chip was designed by Luiz Gouveia following discussions between myself, James Grant, Chong Li, Luiz Gouveia, Ivonne Escorcia-Carranza and David Cumming. The chip was manufactured using a 0.18 µm Texas Instruments (TI) process. Luiz Gouveia constructed the measurement set up, wrote the LabVIEW control software and provided the spectral characterisation results that are presented in Section 5.4.2.

Contents

List of Figures

List of Tables

List of Acronyms

ADC	analogue to digital convertor
AFM	atomic force microscope/microscopy
APS	active pixel sensor
BCB	benzocyclobutene
BEOL	back-end-of-line
BSI	back side illumination/illuminated
BWO	backward-wave oscillator
CAD	computer aided design
CCD	charge-coupled device
cERR	complementary electric ring resonator
CFA	colour filter array
CIE	Commission International de l'Eclairage
CMF	colour matching functions
CMOS	complementary metal-oxide semiconductor
CSV	comma separated values
DF	dark field
DLaTGS	deuterated, L-alanine-doped triglycine sulfate
EBL	electron beam lithography
EMT	effective medium theory
EOT	extraordinary optical transmission
ERR	electric ring resonator
FD	finite-difference
FDTD	finite-difference time-domain

FEL	free electron laser
FET	field effect transistor
FIR	far infrared
FPA	focal plane array
FSI	front side illumination/illuminated
FSS	frequency selective surface
FT	Fourier transform
FTIR	Fourier transform infrared spectroscopy/spectrometer
FWHM	full width at half maximum
hCG	human chorionic gonadotropin hormone
HSI	hyper-spectral imaging
ICP-CVD	inductively coupled plasma chemical vapour deposition
IPA	isopropyl alcohol
IPA:MIBK	isopropyl alcohol:methyl isobutyl ketone
IR	infrared
ITRS	International Technology Roadmap for Semiconductors
JWNC	James Watt Nanofabrication Centre
L, M, S	long, medium and short cone cells
LSP	localised surface plasmon
LSPR	localised surface plasmon resonance
MA6	Suss Microtec Mask Aligner 6
MIM	metal-insulator-metal
MIR	mid infrared
MM	metamaterial

MMF	metal mesh filter
MMW	millimetre wave
MOS	metal oxide semiconductor
MSI	multi-spectral imaging
NIR	near infrared
PEC	perfect electric conductor
PECVD	plasma enhanced chemical vapour deposition
PML	perfectly matched layer
PMMA	poly(methyl methacrylate)
PVD	physical vapour deposition
QCL	quantum cascade laser
RF	radio frequency
RIE	reactive ion etching
RO	reverse osmosis
ROIC	read out integrated circuit
RTD	resonant tunnelling diodes
S	scattering (parameters)
SEM	scanning electron microscope/microscopy/micrograph
SERS	surface-enhanced Raman spectroscopy
SMM	synthetic multi-spectral material
SP	surface plasmon
SPP	surface plasmon polariton
SPR	surface plasmon resonance
SRR	split ring resonator

SWIR	short wave infrared
TDS	time domain spectroscopy
TE	transverse electric
THz	terahertz
TI	Texas Instruments
TM	transverse magnetic
UV	ultraviolet
VOx	vanadium oxide
VRU	variable resolution unit

1. Introduction

1.1 Motivation

Multi-spectral imaging (MSI) systems, operating over large spectral ranges, typically combine several spectrally specific imagers into a single imaging system. Image fusion techniques can then be applied to the spectrally different images to extract more information from the scene than is available from each of the individual images [1,2]. The requirement to use several different cameras to create a wide-band MSI system is a result of the necessity for different imaging optics and detector materials to image distinct spectral bands. For example, a common digital camera for use at visible wavelengths uses silicon photodiodes within a complementary metal-oxide semiconductor (CMOS) chip to image, whereas infrared (IR) detection requires a different semiconductor material such as indium antimonide [3]. An alternative method of IR imaging uses bolometric detection methods [4,5] and such techniques have also been applied to terahertz (THz) imaging applications [6]. Further spectral selectivity can be acquired by using filters, for example dye doped colour filters to enable colour imaging in the visible band. Existing work has demonstrated the potential for integrating visible, IR and THz detectors into a single chip, however the visible/IR detectors and the THz detectors are positioned over different regions of the chip [7,8].

In this Thesis an alternative method to create a wide-band MSI system that uses structured photonic materials is proposed and investigated. Structured photonic materials typically consist of periodic subwavelength unit cells, where altering the unit cell geometry can impact the electromagnetic properties of the bulk material. The scalability of the materials means that it is possible to use micro and nanofabrication techniques to engineer desirable spectral characteristics for a given application. Two such structured photonic materials that were investigated in the course of this project were plasmonic filters, which are well suited for optical wavelengths, and metamaterials (MM), which are well suited for THz frequencies. Plasmonic filters have been shown to be a good alternative to conventional colour filters in CMOS image sensors [9–11] and MM absorbers are promising components for use in THz imaging systems [12–14].

In this Thesis it will be demonstrated that by ensuring both components share common materials and fabrication processing techniques it is possible to create hybrid plasmonic and MM structures to create synthetic multi-spectral materials (SMM). SMMs can exploit

both plasmonic and MM phenomena simultaneously in a single structured material, which exhibits engineered electromagnetic characteristics over several decades of wavelength. SMMs could be integrated with suitable detectors to create a coaxial MSI system, where the different spectrally specific pixels share a common axis, thereby maximising the spectral information density of the imaging system. Such a MSI system could combine visible, IR and THz imagers into a single high resolution, multipurpose camera that operates in a similar manner to a standard digital camera.

1.2 Aims and Objectives

The main aim of this project was to hybridise plasmonic filters and MMs to create SMMs with engineered electromagnetic properties over different wavebands. SMMs were developed with a view to creating a MSI system through integration with CMOS technology. The aims of this project can be described as follows:

- Simulation, fabrication and characterisation of optical and IR plasmonic filters, designed to be integrated with THz MMs.
- Simulation, fabrication and characterisation of THz MM filters and MM absorbers, designed to be integrated with plasmonic filters.
- Hybridisation of plasmonic filters with THz MMs to create the SMMs with engineered optical properties over several decades of wavelength.
- Integration of plasmonic filters with CMOS image sensors as the first step in developing a MSI system through integration of SMMs with CMOS technology.

1.3 Thesis Outline

This Section provides a description of the Chapters that compose this Thesis.

Chapter 2 provides a literature study on the current state of technology with regards to structured photonic materials and imaging systems. The Chapter begins with an introduction to plasmonics and plasmonic colour filters, followed by some discussion on digital colour imaging systems and how plasmonic colour filters can offer several advantages over current filtering technology. The Chapter continues with an introduction to MMs and the development of MM filters and absorbers, specifically with regards to the benefits that they present at THz frequencies. THz imaging systems are then presented, followed by some discussion on how THz MM absorbers are well suited for the development of a THz camera. The Chapter concludes with a discussion on MSI and

hyper-spectral imaging (HSI) systems and how structured photonic materials exhibit properties that are beneficial for spectral imaging applications.

The background theory of the structured photonic materials that are presented in this Thesis is outlined in **Chapter 3**. Initial discussion is concerned with Maxwell's equations and the dielectric properties of metals which underlie the operation of all structures that have been designed in the course of this work. This is followed by an in depth description of the phenomenon underlying extraordinary optical transmission (EOT). The final Section outlines effective medium theory (EMT) as applied to MMs and also presents the theory underlying the operation of MM filter and MM absorber structures.

The methods used to simulate, fabricate and characterise the structured photonic materials presented in this work are described in **Chapter 4**. The first Section provides an overview of the finite-difference time-domain (FDTD) method, followed by a description of Lumerical FDTD Solutions which has been used to simulate all of the optical structures that have been designed during the course of this project. The next section provides some discussion on micro and nanofabrication processes carried out in the James Watt Nanofabrication Centre to create the structure photonic materials and the Chapter concludes with a description of the characterisation methods, namely: spectrophotometry and Fourier transform infrared spectroscopy (FTIR).

The next three Chapters present the overall results of this project, beginning with **Chapter 5** which describes the development of plasmonic filters and their integration with CMOS technology. The first Section of the Chapter presents 15 optical plasmonic filters, targeted for different colours throughout the visible band, and a single near infrared (NIR) filter that operates just outside optical wavelengths. This is followed by the presentation of 8 IR plasmonic filters which were designed by scaling the features of the optical filters. The final half of the Chapter describes the process of integrating plasmonic filters with two different CMOS chips and also shows some early results from characterisation of the plasmonic filters on the chip surfaces.

Chapter 6 presents results from the fabrication of MM components, and begins with the design of a metal mesh filter (MMF) for IR wavelengths. This is followed by an in depth investigation into two MM filters that have been optimised for use at THz frequencies. The Chapter concludes with an investigation into four different MM absorber structures which have also been optimised for THz applications. All MMs were designed to allow integration with the plasmonic filters that were presented in the previous Chapter. As a consequence, both components use the same materials and similar fabrication processes.

The SMMs designed through hybridisation of plasmonic and MM structures are presented in **Chapter 7**. The first SMM combines a THz MM filter with 15 optical plasmonic filters and a NIR plasmonic filter, and demonstrates that it is possible for a single metal film to be engineered to act as multiple band pass filters over a large wavelength range. The second SMM combines a THz MM absorber with 15 optical plasmonic filters and NIR plasmonic filter and this is followed by a third SMM that combines an alternative MM absorber structure with optical and IR plasmonic filters. The Chapter ends with some discussion on how SMMs could be integrated with a CMOS chip to create a MSI system.

Chapter 8 summarises the work that has been presented in this Thesis and also offers some discussion on future work that could be undertaken as a continuation of this project.

2. Literature Review

This Chapter presents an overview of structured photonic materials, from their inception to modern advancements in plasmonics and metamaterials, with a focus on imaging applications. This Chapter will also describe common imaging methods at visible and far infrared wavelengths, and present some of the benefits of structured photonic components over conventional optical materials and technologies. The Chapter will conclude with an overview of multi and hyper-spectral imaging systems, which could greatly benefit from the implementation of hybrid plasmonic and metamaterial structures with multiple independently engineered resonances.

2.1 Plasmonics

The free electron model considers a metal as consisting of negatively charged plasma with a positively charged background of ionic cores. Displacement of the electron density from the positive core results in an oscillation at a material-dependent resonant frequency, known as the plasma frequency. The quasiparticles associated with this type of oscillation are known as plasmons and are essential in understanding the optical properties of metals [15,16]. Surface plasmons (SP) are electron density oscillations at the interface between a dielectric and conductor, which can interact with incident light to form either localised surface plasmons (LSP) on nanoparticles or surface plasmon polaritons (SPP) on metal surfaces [16–22]. Both LSP and SPP represent interaction of light with matter on a subwavelength scale and exhibit high confinement of the incident light field, which can be exploited for a variety of applications [16,22,23]. This area of research is known as plasmonics.

2.1.1 Localised Surface Plasmons

The field of plasmonics is centuries old and actually predates many of the discoveries that underpin our understanding of modern optics - as a reference point Isaac Newton's *"Opticks"* was first published in the early 1700s [24]. The Lycurgus Cup is a Roman cup dating from the 4th century that depicts the story of King Lycurgus [25,26]. The glass that makes up the body of the cup displays unusual optical properties in that it reflects and transmits different colours due to plasmonic resonances [22]. When the cup is illuminated by white light and the light is reflected by the cup surface it appears green, however when light is transmitted through the cup it appears red. The stained glass of the Sainte Chappelle in Paris also exhibits interesting optical properties because of plasmonic resonances; in addition to the brilliant colours, the transmitted light exhibits a strong

angular dependence, which creates unique effects depending on the time of day the window is being observed [22].

The unique optical properties associated with the Lycurgus Cup are attributed to localised surface plasmon resonances (LSPR) occurring due to metallic nanoparticles of a gold-silver alloy embedded in the glass, however several centuries passed before the phenomenon could be explained; the necessary physics, mainly Maxwell's equations and the Drude free electron model, were not described until over a millennium after the creation of the Lycurgus Cup. In the early 1900s there were several investigations into the interaction of light with spherical particles [27,28] and in 1970 the colours associated with glasses embedded with metallic nanoparticles were attributed to the interaction of light with SPs [29].

A schematic illustrating the interaction of light with a metallic nanoparticle and the resultant LSPR interaction is illustrated in Figure 2.1(a). When a metallic nanoparticle of sub-skin depth thickness, in this case a sphere, is illuminated by a plane wave source, the electric field acts to displace the free electrons. This results in surplus negative charges at one side of the particle, and surplus positive ionic cores at the other. The electrostatic attraction between charge densities, results in a restoring force resulting in an oscillation of charge, which is known as LSPR. Close to the plasma frequency, this leads to resonantly enhanced scattering and absorption of the incident light, resulting in the unique optical properties of the metal colloid [16,20,22,30]. Scanning electron microscope (SEM) images and dark field (DF) images of a range of differently shaped metallic nanoparticles demonstrating how shape affects colour is shown in Figure 2.1(b) [20].

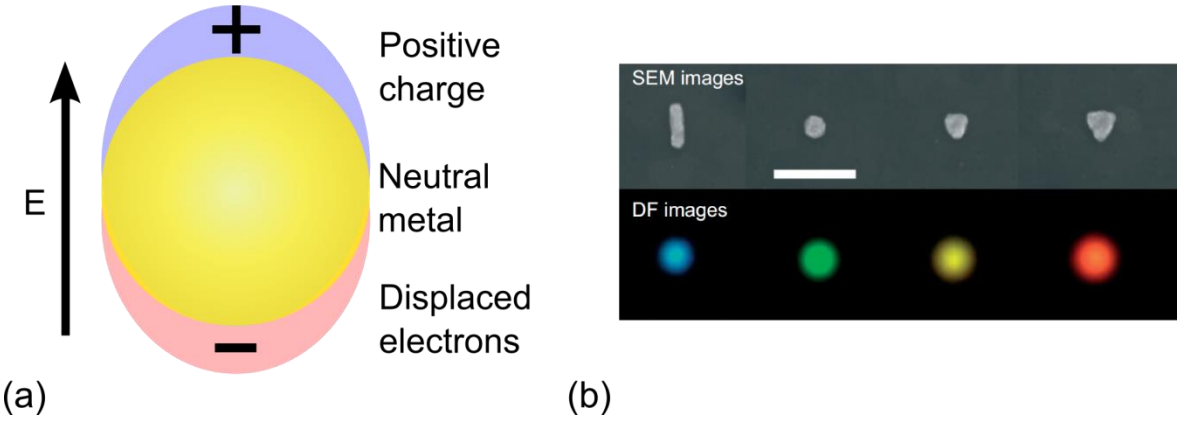

Figure 2.1 Illustration of localised surface plasmon resonance (LSPR) and the optical properties of metallic nanoparticles due to LSPR. (a) Illustration of LSPR in a nanoparticle exposed to a light field showing the accumulated charge and resultant imbalance [22]. (b) Scanning electron micrographs (SEM) with accompanying dark field (DF) microscope images of plasmonic nanoparticles where the scale bar corresponds to 300 nm. (b) has been reproduced with permission: [W. A. Murray and W. L. Barnes, "Plasmonic Materials," Adv. Mater. **19**, 3771–3782 (2007) [20]], ©2007 WILEY-VCH Verlag GmbH & Co. KGaA, Weinheim.

In addition to glassware and stained glass windows, LSPR has been exploited for other applications such as biosensing [31], and can even be found in the home pregnancy test. In the pregnancy test, the human chorionic gonadotropin hormone (hCG) associated with pregnancy binds to antibodies on a sensing strip; gold nanoparticles linked to a secondary antibody then bind to the hCG, resulting in accumulation of gold nanoparticles and the appearance of a bright red colour, thereby indicating pregnancy [22]. LSPR is also used to enhance Raman scattering in a technique known as Surface-enhanced Raman spectroscopy (SERS), which has been shown to be capable of detecting single molecules [32].

2.1.2 Surface Plasmon Polaritons

In 1902, Wood observed unusually large drops in intensity in the reflection spectrum of light diffracted by a metallic grating; this phenomenon was later termed "Wood's anomaly" [33–35]. Wood observed that the anomaly was polarisation dependent, and required the electric field vector of the incident light to be perpendicular to the grating slits. In 1941, Fano introduced the concept of surface waves into the explanation of Wood's anomaly [36] and in 1968 Ritchie *et. al.* described the phenomenon in terms of light resonantly interacting with SPs on the grating surface [37].

Under certain resonant conditions, it is possible for light that is incident on a metal surface to couple with the SPs at the metal-dielectric interface in a process known as surface plasmon resonance (SPR). This results in the formation of SPPs which are hybrid light-SP waves that propagate across the interface. SPPs are tightly confined to the metal surface, and their bound nature is demonstrated by the evanescent decay of fields perpendicular to the surface [16,17,19]. A schematic of the propagating SPP at a metal-dielectric interface is shown in Figure 2.2 [19]. The field components are illustrated in Figure 2.2(a), where it can be observed that the electric field is normal to the interface and the magnetic field is perpendicular to the direction of propagation. The evanescent decay of the fields that are perpendicular to the interface are illustrated in Figure 2.2(b), where δ_d and δ_m denote the decay length into the dielectric and metal, respectively. This shows how the SPPs are bound to the surface of the metal-dielectric interface. The high confinement, which is typically subwavelength in scale, leads to a large field enhancement close to the surface. The SPP is therefore very sensitive to changes in the local dielectric environment close to the metal surface, making it well suited for biosensing applications [23].

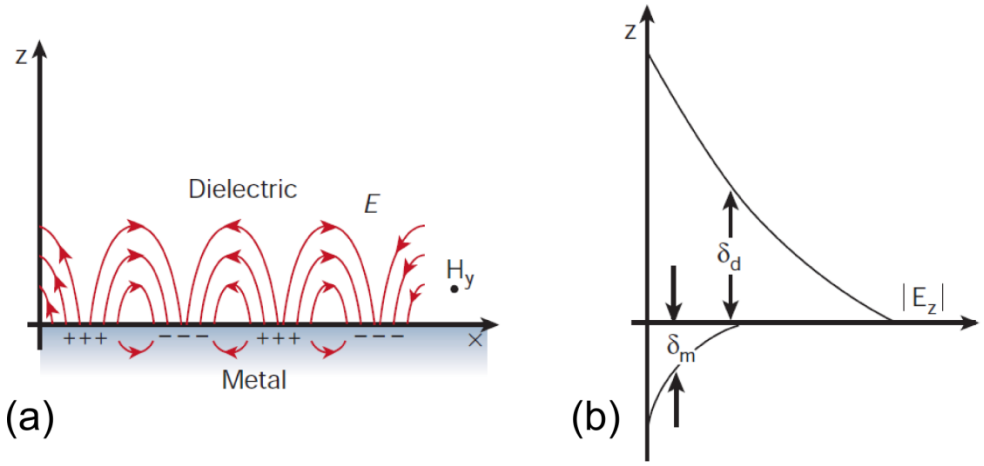

Figure 2.2 Illustration of a surface plasmon polariton (SPP) propagating at a metal-dielectric interface. (a) A schematic of a SPP propagating in the *x* direction with electric and magnetic field components shown. (b) Evanescent decay of the field component that is perpendicular to the interface into both the metal and the dielectric. Reprinted by permission from Macmillan Publishers Ltd: Nature [W. L. Barnes, A. Dereux, and T. W. Ebbesen, "Surface plasmon subwavelength optics," Nature **424**, 824–830 (2003) [19]], copyright 2003.

There is a momentum mismatch between the incident light and SPs that must be overcome before SPPs can form [19]. The first method to provide the incident light photons with additional momentum has already been described in the discussion of Wood's anomaly; a periodic corrugation in a metal surface can diffract incident light into the plane of the metal-dielectric interface, resulting in resonant coupling of light with SPs. A schematic illustrating the excitation of SPPs with grating coupling is shown in Figure 2.3(a). An alternative method is known as prism coupling. There are two prism coupling methods for the formation of SPPs: the Kretschmann configuration [38], shown in Figure 2.3(b) and the Otto configuration [39], shown in Figure 2.3(c). Both methods use attenuated total internal reflection [16]. In the Kretschmann configuration, the prism is in contact with a metal film, whereas there is an air gap between prism and metal in the Otto configuration.

Prism coupling is commonly used in SPR biosensors. The sensitivity of the SPPs to changes in the dielectric environment of the metal film results in detectable changes in the reflection light for a given angle as biomolecular interactions occur, which result in a shift in the effective refractive index of the surface [22,40]. The highly confined nature of SPPs means that they can also be used for a range of applications overcoming the diffraction limit, such as subwavelength focussing through plasmonic lenses [41,42] and subwavelength photolithography [43,44].

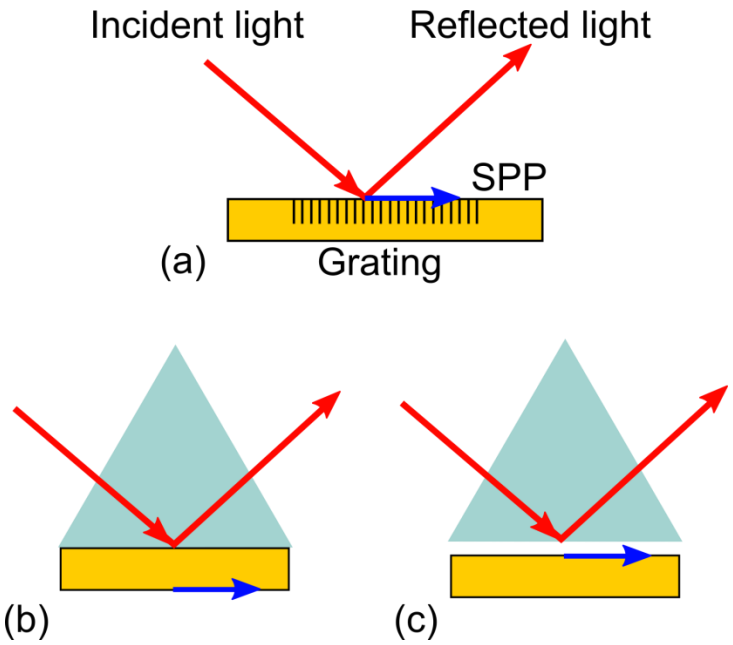

Figure 2.3 Illustrations of the different methods by which incident light can couple with surface plasmons (SP) to form surface plasmon polaritons (SPP) [16]. (a) Grating coupling. (b) Prism coupling – Kretschmann configuration. (c) Prism coupling – Otto configuration.

2.1.3 Extraordinary Optical Transmission

In 1998, Ebbesen *et. al.* reported on extraordinary optical transmission (EOT) through arrays of subwavelength holes etched into metal films [45], followed by a more in depth study on phenomenon reported by Ghaemi *et. al.* [46]. Initial investigations looked at a square array of holes, of diameter 150 nm and period 900 nm, etched into a 200 nm silver film on a quartz substrate. The transmission spectrum exhibited two large transmission peaks at wavelengths greater than the period, a_o. The first peak was positioned just after the minimum that is positioned at a wavelength equal to a_o and corresponds to the silver-air interface. The second peak was positioned just after the next minimum, which is at a wavelength equal to $a_o n$, where n is the refractive index of the quartz and corresponds to the silver-quartz interface.

A surprising outcome of this experiment was the observation that the transmitted light was of a wavelength that was significantly longer than the diameter of the holes in the structure. Bethe describes the efficiency of light transmission through a hole of radius, r, as being proportional to $(r/\lambda)^4$, where λ is the wavelength of the incident radiation [47]. From Bethe's description, it can be found that there should be an exponential decrease in efficiency for hole sizes much smaller than the wavelength of the incident light and that the light should evanescently decay through the subwavelength holes, such that transmission in the far field is expected to be negligible [48].

Not only is the transmission much higher than expected with regards to Bethe's aperture theory, but there is also a transmission enhancement when considering the ratio of the hole area to the metal surface area; light transmitted through the hole array is larger than would be expected from the hole area divided by the metal surface area. This can be quantified in terms of the fill factor, which is approximately 2 % for the hole array presented in [45]. The transmission peak at 1370 nm exceeds 4 % which corresponds to an observed transmission efficiency greater than 2. The transmission efficiency from the hole array presented in [45] is expected to be on the order of 10^{-3} from the Bethe theory. Ghaemi *et. al.* [46] reported a transmission enhancement factor of about 1000, however subsequent studies have suggested a much more modest enhancement factor due to uncertainty in the diameter of the fabricated holes [49,50].

In the work carried out by Ebbesen *et. al.* EOT was attributed to coupling of incident light with SPs to form SPPs. The evidence presented for this conclusion was the lack of enhanced transmission in germanium films etched with holes, and also a distinct angular dependence associated with the transmission spectrum. Hole arrays in gold and chromium were also investigated in addition to silver. The three metals exhibited transmission peaks in similar locations for the same array periods, thereby suggesting that the peak positions are dependent on the hole period [45].

Since the seminal work by Ebbesen *et. al.* there has been significant interest in explaining exactly how SPPs act to enhance transmission [51,52]. Ghaemi *et. al.* [46] acknowledged the significance of resonant coupling between SP modes on both surfaces of the metal through the holes and observed that the results were independent of whether or not the metal was illuminated on the quartz-silver side, or the silver-air side. It was also suggested that the transmission minima were associated with occurrences of Wood's anomaly. Investigations into various aspects such as hole depth [53], metal type [54–56] and the properties of the surrounding dielectric layers [57–59] have been undertaken.

The process underlying EOT can be described as follows: incident light couples with SPs on the metal-dielectric interface to form SPPs via grating coupling; the tightly confined SPPs result in a field enhancement on top of the aperture, which acts to increase transmission; the light evanescently tunnels through the holes; the light is then scattered and re-transmitted [19,48,52]. This process is optimised when the index of the dielectric is matched on both sides of the film, and the metal is sufficiently thin for SPPs on both surfaces to become coupled [19,53,57].

Many experimental and simulation studies have been carried out to further elucidate on the intricacies of the phenomenon of EOT. Krishnan *et. al.* describes the holes as acting like resonant cavities for evanescent waves, with SPPs acting as mirrors at either side, where constructive interference and the high electric fields lead to enhanced transmission at resonance. In this case the SPPs are analogous to mirrors in a Fabry-Perot resonator [57]. Fan *et. al.* describes how the hole arrays aid the transfer of energy between the SPPs on either side of the metal film via overlapping evanescent modes [60]. Gao *et. al.* presents near-field optical images of SPPs on metallic hole arrays that exhibit EOT [61].

2.1.3.1 Spoof Surface Plasmons

Towards far infrared (FIR) wavelengths, or terahertz (THz) frequencies, there is a diminished plasmonic response and the metal can typically be considered as a perfect electric conductor (PEC), where real SPs do not exist [62,63]. In this region, at wavelengths far longer than the plasma frequency, losses in the material result in poorly confined light waves with properties more akin to surface grazing Sommerfeld-Zenneck waves than SPP [16]. However, a PEC perforated with subwavelength holes can still exhibit properties that are typically associated with the formation of SPPs, and metal films etched with hole arrays have been shown to demonstrate enhanced transmission and wavelength filtering at FIR wavelengths [64–66]. These unusual characteristics were resolved by the introduction of spoof, or designer SPs, which are a result of an engineered effective plasma frequency due to the perforations in the metal surface; this is characteristics of a type of metamaterial (MM) [62,63]. It should also be acknowledged that any subwavelength hole array in a metal film will result in the formation of a MM such that both real and spoof SPs will be present [62].

EOT has also been observed just out-with the optical range, at IR wavelengths [67,68], where common metals exhibit high dielectric loss and are therefore generally considered poor plasmonic materials [48,69]. To account for the observed optical properties it is necessary to consider spoof SPs, and this will be explored further in Chapter 3.

2.1.4 Plasmonic Colour Filters

Plasmonic filters exploit the wavelength dependent EOT associated with the formation of SPPs to create colour filters, which have many promising applications and offer a desirable alternative to conventional optical filters in colour imaging. By scaling array period and the diameter of the holes, it is possible to engineer the filtered wavelength through the visible waveband. Despite silver and gold generally being considered the best materials for optical plasmonics due to low dielectric loss [69], aluminium is more desirable for practical applications due its low cost, ease of fabrication and compatibility with complementary metal oxide semiconductor (CMOS) technology.

Lee *et. al.* demonstrated that it was possible to create red and green plasmonic filters by etching square hole arrays into a 50 nm aluminium film sputtered on to a quartz substrate [70]. An index matching oil was used on the surface with a refractive index equal to that of the quartz substrate, thereby optimising the transmission characteristics of the filters. The green and red filters exhibited transmission peaks of 50% and 57%, respectively, however the large bandwidth and unwanted transmission at longer wavelengths resulted in poor colour discrimination, such that the green filter appeared yellow.

Subsequent work by Chen *et. al.* [59], Inoue *et. al.* [71] and Yokogawa *et. al.* [72] represented a significant advancement in plasmonic colour filters made on aluminium films, where the three studies have converged on a similar optimised design. The plasmonic filter structure presented by Chen *et. al.* consists of a 150 nm aluminium film, etched with subwavelength holes and sandwiched between a silicon dioxide substrate and 200 nm silicon dioxide cap layer. A triangular hole array was used as an alternative to the conventional square array design because it exhibits a larger gap between adjacent peaks in the transmission spectrum [48,59,73]. Three colour filters were designed, with transmission spectra corresponding to blue, green and red transmission filters. The array period was 250 nm, 330 nm and 430 nm for the blue, green and red filters, respectively. When a 200 nm silicon dioxide cap layer is used, the transmission of the three primary colour filters was found to be greater than 30% with a full width at half maximum (FWHM) of approximately 100 nm. As expected, the transmission characteristics were optimised when a silicon dioxide over layer was used to index match the top and bottom surfaces of the aluminium film. Chen *et. al.* also found that larger holes relative to the period, or thinner metal resulted in an increase in transmission and slight redshift, but with the trade-off that the FWHM was larger. Results presented by Chen *et. al.* are shown in

Figure 2.4: a scanning electron micrograph of a hole array etched into aluminium is shown in Figure 2.4(a), and the transmission spectra from red, green and blue colour filters with different silicon dioxide cap layer thickness are shown in Figure 2.4(b-d) [59].

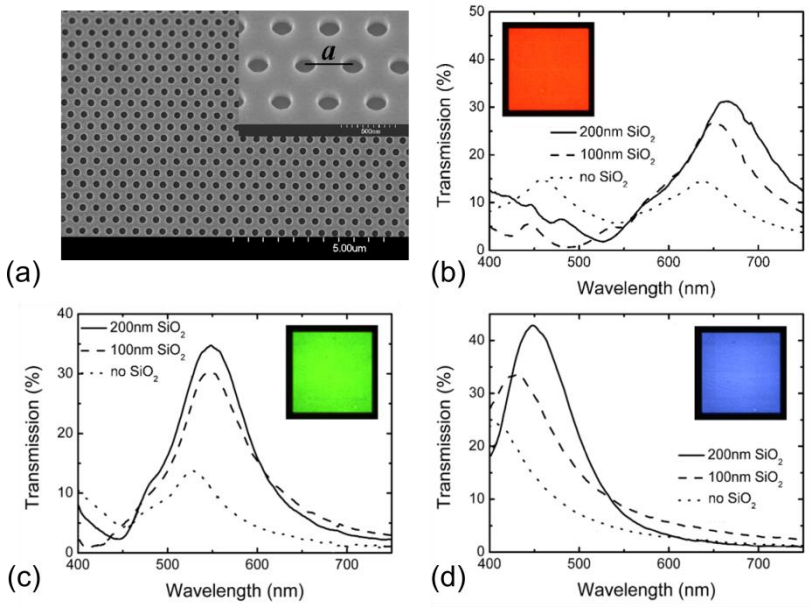

Figure 2.4 Plasmonic colour filters. (a) Scanning electron micrograph (SEM) of a triangular hole array etched into aluminium, with period, a = 430 nm. Transmission spectra of (b) red, a = 430 nm, (c) green, a = 330 nm and (d) blue, a = 250 nm, plasmonic colour filters for varying cap layer thicknesses. The image in the inset is the transmission microscope image showing the filter under white light illumination. Reproduced with permission: [Q. Chen and D. R. S. Cumming, "High transmission and low color cross-talk plasmonic color filters using triangular-lattice hole arrays in aluminum films," Opt. Express **18**(13), 14056–14062 (2010) [59]].

2.2 Digital Imaging

Digital imaging systems consist of an array of electronic photosensitive elements that can be used to detect light that is focussed on to the array using imaging optics [74–76]. Each photosensitive element, or pixel, is used to record the energy incident on each detector from discrete wave packets of light, known as photons, which can be transmitted reflected, or emitted from objects in the scene to be imaged. The photon energy is dependent on the wavelength of the light. The intensity of the light corresponds to the observed brightness and is dependent on the number of photons incident on an area of the detector for a given exposure time [77,78]. After detection, the analogue signals from the photodetectors are converted into a digital signal using an analogue to digital convertor (ADC). Image processing is then carried out to reconstruct the image such that it matches the scene witnessed by an observer [74,76,77]. A simple illustration of the imaging process is shown in Figure 2.5.

The light sensitive component of the camera is typically made of a semiconductor material suitable for the waveband that is being imaged. The bandgap energy of a semiconductor

material is the minimum photon energy required to move electrons from the valence band to the conduction band, therefore, the semiconductor material is sensitive to light of a wavelength corresponding to an energy greater than the bandgap energy. Silicon is well suited to visible imaging, whereas indium antimonide is well suited to infrared imaging [3,77].

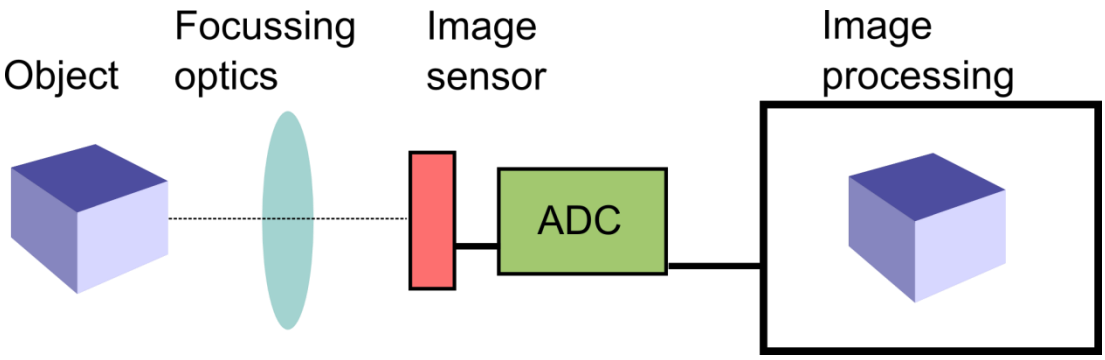

Figure 2.5 Light from the object or scene is focussed on to the image sensor which converts the electromagnetic radiation into an electrical signal. This is then converted to a digital signal using the analogue to digital convertor (ADC) and then image processing steps are carried out to reproduce the initial object or scene.

The two types of image sensors present in digital cameras today are charge-coupled devices (CCD) and CMOS active pixel sensors (APS). Both fulfil the role of the image sensor in detecting light as described previously, however they are distinct technologies with unique advantages and disadvantages when compared to the other [74,76]. A CCD sensor consists of an array of closely spaced metal oxide semiconductor (MOS) capacitors, which convert photons into stored charge that is proportional to the incident light intensity. The charge is held in a potential well until the end of the exposure period then sequentially passed to the neighbouring well until it reaches the end of the row where it is converted into an electrical signal. Using this method the information from the entire image can be extracted and sampled using an ADC prior to further processing [74,77]. A CMOS image sensor typically consists of an array of pixels, which each contain a photodiode and additional circuitry. The charge is converted to a voltage at the pixel level and the signal can then be passed to an on-chip ADC to be converted to a suitable format for subsequent image processing [74,77,79,80].

Since their development in the 1970s, CCD imagers were the dominant technology over CMOS image sensors. However, advancements in CMOS image sensor technology in the 1990s, leading to the development of the CMOS APS, allowed CMOS image sensors to compete with CCD imagers [76,78,80,81]. CCDs offer higher quality images in addition to lower noise and dark current when compared with CMOS image sensors. CMOS image

sensors also exhibit high fixed pattern noise due to each pixel having its own amplifier [77]. The main advantage of CMOS image sensors is that they can incorporate much of the relevant electronics of an imaging system, such as: exposure control, signal processing electronics and ADC, on a single chip, thereby creating single chip camera [77,80]. This ultimately creates a low cost, low power imaging system when compared to CCD technology [77,80,81] and is therefore suitable for a range of applications, including optical mice, mobile phone and tablet cameras, computer cameras, security cameras and machine vision where increased noise is a reasonable compromise for decreased cost and lower power requirements [76,81]. CCD imagers are common in applications where higher quality images are desirable such as: digital photography and astronomy [81].

2.2.1 Colour Theory

The perception of colour is a feature of the human visual system and therefore to store and reproduce colour images as seen by an observer, it is necessary to measure and numerically represent colour [74,82–85]. As the purpose of many colour imaging systems is to reconstruct the image of a scene as observed by a human observer, quantification of the observed colour is necessary. Other imaging systems, such as multispectral and hyperspectral imagers, do not always aim to reconstruct the image seen by a human observer, and will be explored in more detail in Section 2.5.

The human eye is sensitive to electromagnetic radiation ranging from 380 nm to 780 nm [74,84]. The retina at the back of the eye consists of two types of photoreceptors that are responsible for detecting light: rod cells and cone cells. The rods are more sensitive than the cones, however the cones are responsible for colour vision. The cone cells occur in three different types: long (L), medium (M) and short (S) wavelength cones, where the name describes the wavelengths that they are sensitive to. This constitutes three-colour, or trichromatic vision, where all observable colours correspond to a combination of the response of the three cones [74,84,85].

The human visual system is trichromatic, and therefore it should be possible to reproduce or record any colour using different levels of three primary colours. This can be represented in terms of three integrals, known as tristimulus values which are dependent on the spectral power distribution associated with the object or source being observed and the colour matching functions (CMF), which represent the spectral responses of the cones [74,75,83–85]. In 1931, The Commission International de l'Eclairage (CIE) presented a set of CMF, which were based on the results of experiments that involved

human participants varying the light levels of three primaries to match the colour of a reference light of known wavelength. If two objects have the same tristimulus values, then they can be said to be the same colour [74,83]. The CIE 1931 standard observer CMF are shown in Figure 2.6 [86].

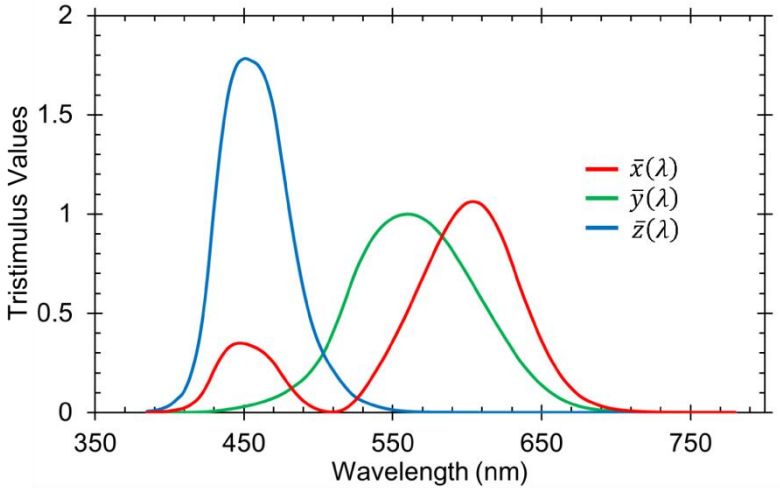

Figure 2.6 The CIE 1931 standard observer colour matching functions: $\bar{x}(\lambda)$, $\bar{y}(\lambda)$ and $\bar{z}(\lambda)$ [86].

2.2.2 CMOS Colour Imaging

A standard colour imaging system requires three spectrally selective sensors to record an image as observed by a human observer. Silicon photodiodes that are used in CMOS image sensors are sensitive over the whole visible band and therefore a spatially varying mosaic of colour filters, known as a colour filter array (CFA) is required to selectively transmit light from different wavebands to different photodiodes [74,75]. The most common CFA is the Bayer pattern, which consists of a 2 x 2 pixel unit cell, containing one blue filter, one red filter and two green filters [87]. The unit cell is periodically repeated to compose the Bayer CFA. The green filter is often used in the Bayer pattern to acquire the luminance signal as it is the closest match of the three filters to the response of the human eye. Honda *et. al.* presented an alternative array that replaced the green filter of the Bayer pattern with an unfiltered region [88]. The inclusion of "white" pixels ensures that incident light is not lost during filtering, resulting in an improved method of measuring the luminance. The Bayer CFA and the CFA presented by Honda *et. al.* are illustrated in Figure 2.7(a) and Figure 2.7(b), respectively [87,88].

The image recorded by a CMOS colour imager is a composite that contains all the colour information of the scene. The image can be separated into the constituent colour channels with reference to the CFA layout, however each colour channel image would have "dead" pixels associated with the other two colours. It would be possible to reconstruct the images

at this stage by simply removing the blank pixels, however it would be at the expense of the spatial resolution of the image. As an alternative, it is common to use CFA interpolation techniques to approximate the colour information held in the blank pixels, by referencing adjacent pixels, thereby maintaining spatial resolution of the sensor [74,75]. It is also possible to forgo the array structure in favour of using three separate sensors with separate colour filters. A series of beam splitters can be employed to focus the image on to each of the sensors simultaneously, therefore eliminating the requirement for interpolation, as is illustrated in Figure 2.8. However, the alignment requirements and the need for multiple sensors mean that this method is costly and only occurs in high-end camera equipment [74,75].

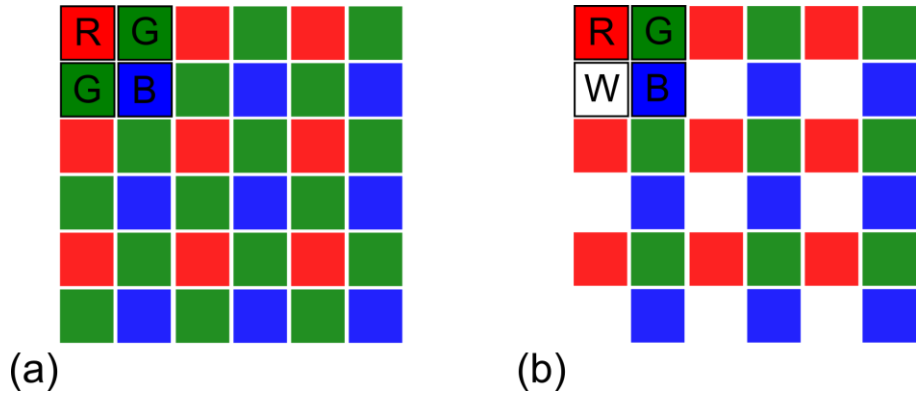

Figure 2.7 Colour filter arrays (CFA) with 2 x 2 pixel unit cell highlighted. (a) Bayer array [87]. (b) Honda *et. al.* array [88].

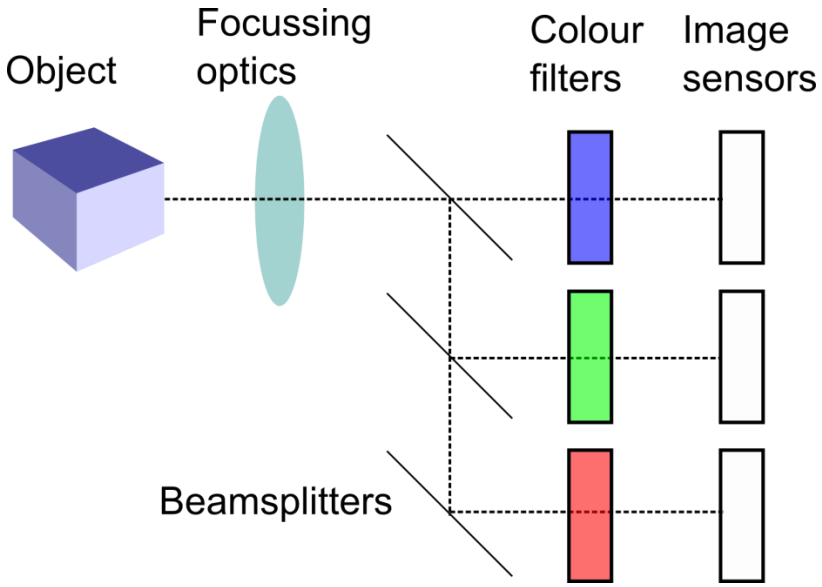

Figure 2.8 Illustration of colour imaging method using three separate image sensors [75].

The layer structure of the conventional front side illuminated (FSI) CMOS image sensor pixel is shown in Figure 2.9(a). Microlenses are used to focus light on to the individual pixels, thereby improving optical efficiency [76,89,90]. An alternative design uses back

side illumination (BSI) that can be used to improve efficiency, by decreasing the height from filter to detector and eliminating light lost to scattering by the interconnects. In a BSI sensor, the reverse side of the sensor is thinned, such that it can be illuminated from the back, however this results in more expensive processing than the FSI imager [79,91]. The layer structure of a BSI CMOS image sensor pixel is shown in Figure 2.9(b).

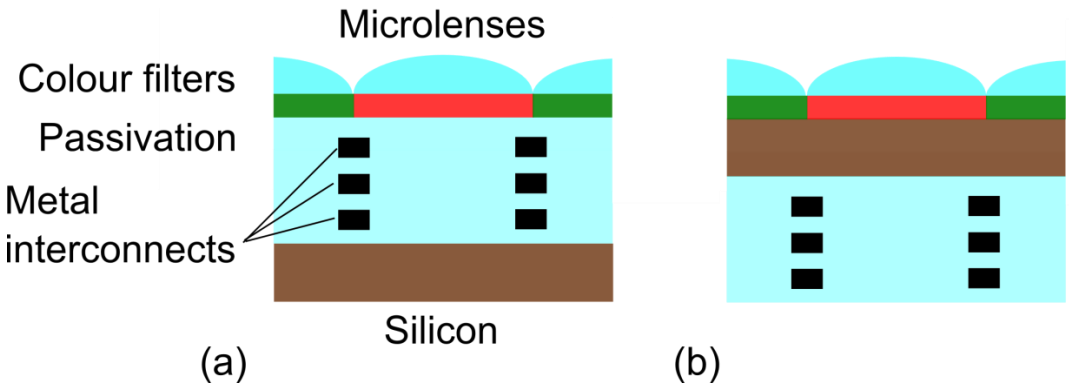

Figure 2.9 CMOS image sensor cross section illustrations for (a) front side illuminated (FSI) sensor and (b) back side illuminated (BSI) sensor [91].

The scalability of CMOS technology means that the pixel size of CMOS image sensors periodically decreases, resulting in higher pixel density imagers which can therefore exhibit higher pixel resolution over the same surface area. Smaller pixel size can also lead to decreased cost and decreased energy requirements [92]. The International Technology Roadmap for Semiconductors (ITRS) describes the technology nodes, or the half pitch between two adjacent features on a semiconductor device achievable by the current technology, as they decrease with time [93]. The technology node associated with CMOS image sensors is slightly larger than that of the ITRS technology nodes, as there are additional considerations for optimising CMOS chips for imaging applications. Pixel size also scales with these trends, as is shown in Figure 2.10 [92]. Within the last decade pixel size has scaled to sub 2 µm levels [94,95].

Back-end-of-line (BEOL) describes the formation of interconnects, vias and passivation on the silicon surface in CMOS processing. Standard semiconductor fabrication methods such as photolithography, dielectric deposition, metallisation and etching are used to fabricate the relevant features on the semiconductor surface. Common materials used in the CMOS process include aluminium and copper, silicon dioxide and silicon nitride [3,96].

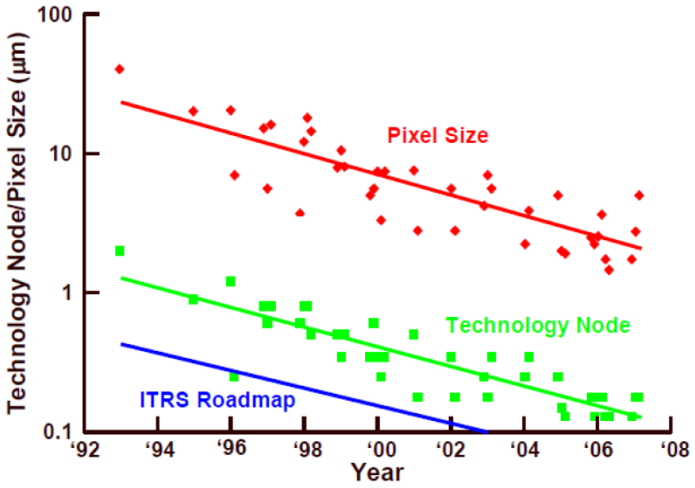

Figure 2.10 ITRS Roadmap denotes the scaling of feature sizes in CMOS technology with time. The technology node refers to the technology node used for the fabrication of CMOS imagers and pixel size refers to the corresponding pixel size associated with the imagers using this technology node. Reprinted from [92], © 2007 IEEE.

The CFA on a CMOS image sensor is typically composed of dye doped or pigmented polymers that are optimised for the required colour [75,97,98]. Ensuring the CFA exhibits the desired spectral characteristics is a challenging process, which is limited by the availability of certain dyes that exhibit both desirable mechanical and spectral properties for the application [75]. As the colour filter array is partially-transparent at NIR wavelengths, a NIR cutoff filter is also used in the imaging system [74,75,97].

2.2.3 Plasmonic Filters for Colour Imaging

Common pixel sizes of imagers in production are as small as 1.75 µm [95] and 1.4 µm [94] with 1.12 µm technology appearing in some mobile phone cameras [79]. Huo *et. al.* [90] reported that as CMOS image sensor pixels scale to sub 2 µm levels, diffraction effects can have a significant impact on the performance of the imager; at pixel sizes below 1.4 µm the microlens is no longer suitable for light focussing on to the photodetector for a 3 metal layer CMOS sensor. The large stack height results in decreased optical efficiency and increased colour cross talk for smaller pixel sizes. Reducing the stack height, could improve the performance of the imager, as would be the case for two or one metal layer CMOS sensors [90]. Catrysse *et. al.* reported on the patterning of CMOS metal layers with structured optical filters, which could further decrease the stack height and result in improved optical efficiency and decreased crosstalk for a given pixel size [96,99,100]. This would also eliminate the additional processing required to make the conventional CFA.

Structured optical filters can offer alternative to conventional dye-doped filters, where desired spectral characteristics can often be engineered simply by altering geometric or material parameters. Arrays of silicon nanowires, with spectral properties that are

dependent on the nanowire radius, have been integrated with photodetectors to create a multispectral imager by Park *et. al*. [101]. Frey *et. al.* integrated Fabry-Perot filters with a CMOS image sensor, which eliminated the requirement for an IR cut-off filter, and was capable of colour imaging [97]. Nanostructured Fabry-Perot filters have been presented by Walls *et. al.* and have been shown as being particularly adept at producing narrowband transmission spectra [102]. Structured optical filters, such as the plasmonic colour filters that were presented in Section 2.1.4, can be fabricated using materials that are native to the CMOS process and can therefore be fabricated into the lowest metal layer as part of the CMOS chip fabrication.

In recent years there have been significant advancements in introducing plasmonic filters to CMOS technology. Junger *et. al.* presented plasmonic filters fabricated into the metal layers of a CMOS sensor using a modified CMOS process [103]. Chen *et. al.* has fabricated plasmonic filters on the surface of single pixel [9] and multipixel [10] CMOS image sensors and demonstrated that it is possible to produce a suitable spectral response for colour imaging using this method. Recently, colour imaging has been demonstrated by integration of a plasmonic CFA with a CMOS image sensor by Burgos *et. al.* [11]. A genetic algorithm has also been created to automate the design of plasmonic filters for imaging; it has been used to design three filters that match the spectral characteristics of the CIE 1931 CMF [104].

2.3 Metamaterials

A MM consists of periodic subwavelength resonant elements, such as split ring resonators (SRR) [105,106] or electric ring resonators (ERR) [107,108], where the geometry of the microscopic structures dictates the macroscopic characteristics of the metamaterial [105,109,110]. The electromagnetic properties of the composite material can be characterised by effective complex electromagnetic parameters using effective medium theory (EMT). A metamaterial can be described in terms of its effective refractive index, effective wave impendence, effective permittivity and effective permeability which can be controlled by the unit cell geometry, and is analogous to the electromagnetic parameters of real materials due to their constituent atoms [111,112]. Using metamaterials it is possible to engineer electromagnetic characteristics that are not found in naturally occurring materials.

Initial work on MMs considered the possibility of a negative refractive index [113] and the implications of realising such a material: primarily the possibility of creating a perfect lens [114]. Later work on MMs led to the invention of a range of devices including

invisibility cloaks [115] and perfect absorbers [116]. The scalability of metamaterials also means that they have been demonstrated in many spectral regions, however metamaterials are of particular interest at terahertz frequencies where there is a lack of naturally occurring frequency selective materials [117].

2.3.1 Negative Refractive Index

In 1968 Vesalago presented a theoretical study on the optical properties of a material with simultaneously negative values of permittivity and permeability, which would result in the material having a negative refractive index [118]. Negative refractive index materials are also known as left handed materials as the wave vector is anti-parallel to the Poynting vector, in contrast with conventional materials known as right handed materials, where this is not the case. The negative refractive index leads to a range of unusual phenomena including the reversal of the Doppler shift and anomalous refraction when considering Snell's Law [106,118]. Snell's law applied to materials with positive and negative refractive indices is shown in Figure 2.11(a) and Figure 2.11(b), respectively. Despite the promise of negative index materials, the required negative permeability is not found in ordinary materials and in the rare cases it does occur, losses are high or it does not coincide with a negative permittivity [106].

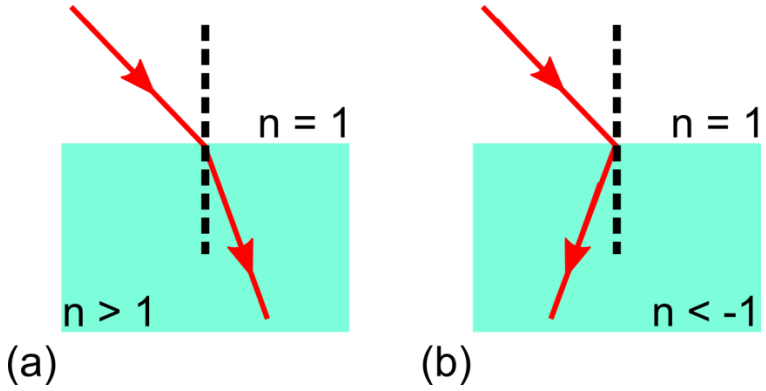

Figure 2.11 Snell's Law applied to a material with (a) positive refractive index and (b) a negative refractive index. The red line is the light ray and the dashed black line is the normal to the surface of the material.

A classification of materials, with regards to the sign of the permittivity and the permeability is illustrated in Figure 2.12. As Maxwell's equations and therefore the electromagnetic response of materials are determined by these quantities, the permittivity and permeability determine the optical characteristics of a material. The upper left quadrant contains materials with a negative permittivity and positive permeability, which can be classified as electric plasma. As will be outlined in the Chapter 3, common metals that can be used in plasmonic applications are modelled in this way. The upper right quadrant contains materials with both positive permittivity and permeability,

corresponding to dielectric materials, or right handed media. The lower right quadrant contains materials with positive permittivity and negative permeability, which can be classified as magnetic plasma, and are realised by some gyrotropic magnetic materials at certain frequencies. Finally, the lower left quadrant corresponds to negative refractive index materials, or left handed media, which are not found in nature [119,120].

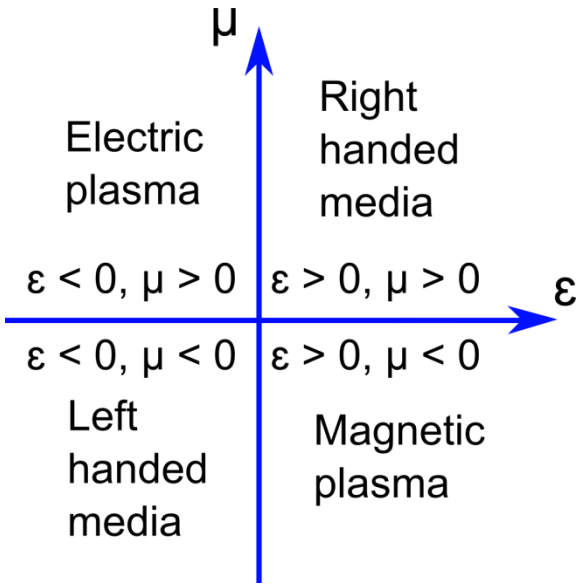

Figure 2.12 Classification of materials based on their electromagnetic properties [119].

In 1996 Pendry *et. al.* demonstrated that wire media could be used to create an artificial material with an effective plasma frequency and therefore effective permittivity [105]. Following this discovery Pendry *et. al.* used an array of SRRs to present a design for artificial magnetism, corresponding to an engineered effective permeability due to inductive and capacitive effects [109]. In 2000 Smith *et. al.* combined an array of wires and SRRs to create a metamaterial with simultaneously negative permittivity and permeability [106]. This was followed by the realisation of a negative refractive index at microwave frequencies by Shelby *et. al.* in 2001 [113].

Conventional optical lenses, consisting of a curved dielectric material encounter a fundamental limit, known as the diffraction limit, which determines the theoretical maximum resolution of an imaging system using a given lens for a given wavelength [121,122]. In 2000, Pendry presented an application for negative index materials in the idea of the perfect lens which can theoretically overcome the diffraction limit. Pendry's perfect lens consists of a planar material with a refractive index of n = -1, in a vacuum with refractive index, n = 1. In this case, light from a point source is focussed to a point inside the material and then diverges before converging to a point again outside the material, as illustrated in Figure 2.13 [114].

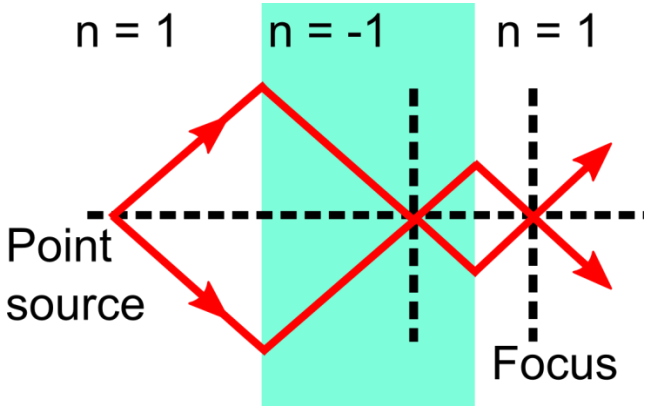

Figure 2.13 Illustration of Pendry's perfect lens [114].

2.3.2 Metamaterial Filters

MM filters can be engineered on a subwavelength scale using structures known as ERRs [107,108] and their inverse structures known as complementary electric ring resonators (cERR) [123]. ERRs are forms of SRRs engineered to have a resonant response to the electric field component of incident electromagnetic radiation while supressing or eliminating the magnetic response [107,108].

Filtering can also be achieved by using metal mesh filters (MMF), which are a type of frequency selective surface (FSS) and bear many similarities to the ERR and cERR structures. For example, both can be modelled using their capacitive and inductive characteristics [124,125]. Traditionally MMF unit cells are larger than ERR and cERR unit cells, such that they may not be considered sufficiently subwavelength to constitute a MM; MMFs typically have unit cells and features on the order of half a wavelength [125] whereas MM unit cells require dimensions significantly smaller than the wavelength in order to be characterised as an effective material [112]. Despite the larger unit cells when compared with MMs, MMFs are still attractive structured optical components for the purposes of this research; the large unit cell geometries simplifies fabrication, specifically at shorter wavelengths where the fabrication of small MM unit cells can be challenging.

2.3.2.1 Metal Mesh Filters

The geometry of the unit cell of the MMF leads to the filtering characteristics of the material. The two simplest MMFs are the inductive MMF and the capacitive MMF as shown in Figure 2.14(a) and Figure 2.14(b), respectively [124,126]. The inductive grid acts as a high pass filter, whereas the capacitive grid acts as a low pass filter [124]. The superposition of these structures yields a inductive cross shape filter, as shown in Figure 2.14(c) which can act as a band pass filter, and its complementary structure yields a capacitive cross filter, as shown in Figure 2.14(d) which can act as a band reject filter, in

accordance with Babinet's principle [126]. There has been substantial interest in MMFs at THz frequencies [125,127–129], however MMFs can also be engineered to operate at shorter wavelengths [130,131].

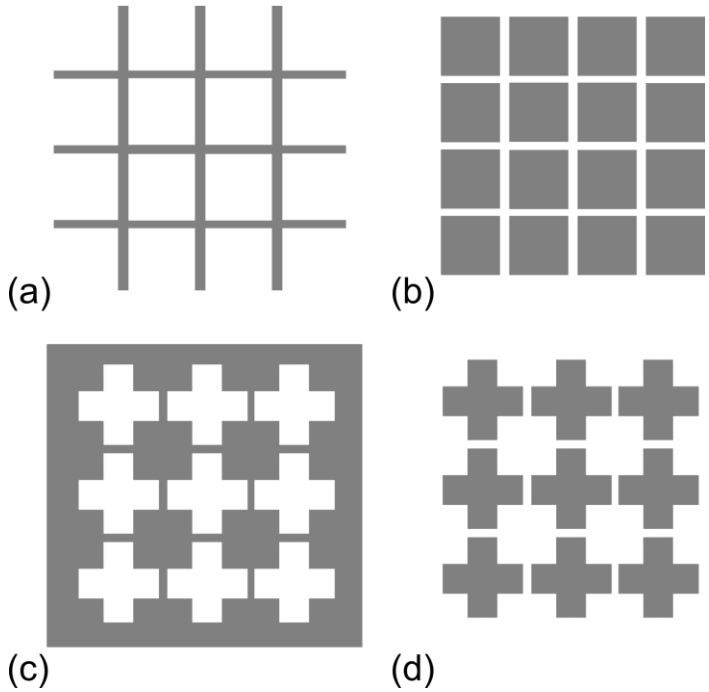

Figure 2.14 Illustrations of metal mesh filters (MMF) [126]. The grey areas denote metal regions. (a) Inductive grid MMF. (b) Capacitive grid MMF. (c) Inductive cross MMF. (d) Capacitive cross MMF.

2.3.2.2 Electric Ring Resonators and their Complementary Structures

In 2006 Schurig *et. al.* presented a new type of SRR that could be used to engineer the effective permittivity of a MM [107]. The following year, Padilla *et. al.* presented the design, simulation and experimental results of a set of resonant artificial materials with an engineered permittivity at terahertz frequencies [108]. As mentioned previously, Pendry *et. al.* had presented wire media with engineered dielectric properties [105], however such structures offer drawbacks, such as the requirement for connected wires as opposed to standalone localised unit cells [107]. SRR designs can also exhibit resonant effective permittivity, but this is coupled to the magnetic response [132]. However it is possible to alter the SRR geometry, specifically with respect to the symmetry, such that a magnetic response is suppressed and the material only exhibits an electric response. These metamaterial unit cells are often referred to as ERRs [107,108].

Two polarisation insensitive MM unit cells, as presented by Padilla *et. al.* [108] and Chen *et. al.* [123], are shown in Figure 2.15(a-b) [123]. The MMs exhibit polarisation independence because of the fourfold rotational symmetry of the ERRs. The MMs were fabricated on a semi-insulating gallium arsenide substrate using 200 nm of gold with a 10

nm titanium adhesion layer, and had a unit cell period of 50 µm. At the resonant frequency, between 0.5 THz and 1 THz, the MMs exhibit a transmission minimum and therefore behave like band reject filters. Simulation results from [123], as shown in Figure 2.15(c-d), show the current density and the electric field profile of the ERRs at resonance. The surface currents illustrate the absence of a magnetic response. This is a result of the circulating currents on the metal surfaces effectively cancelling each other out because of their opposite rotational directions.

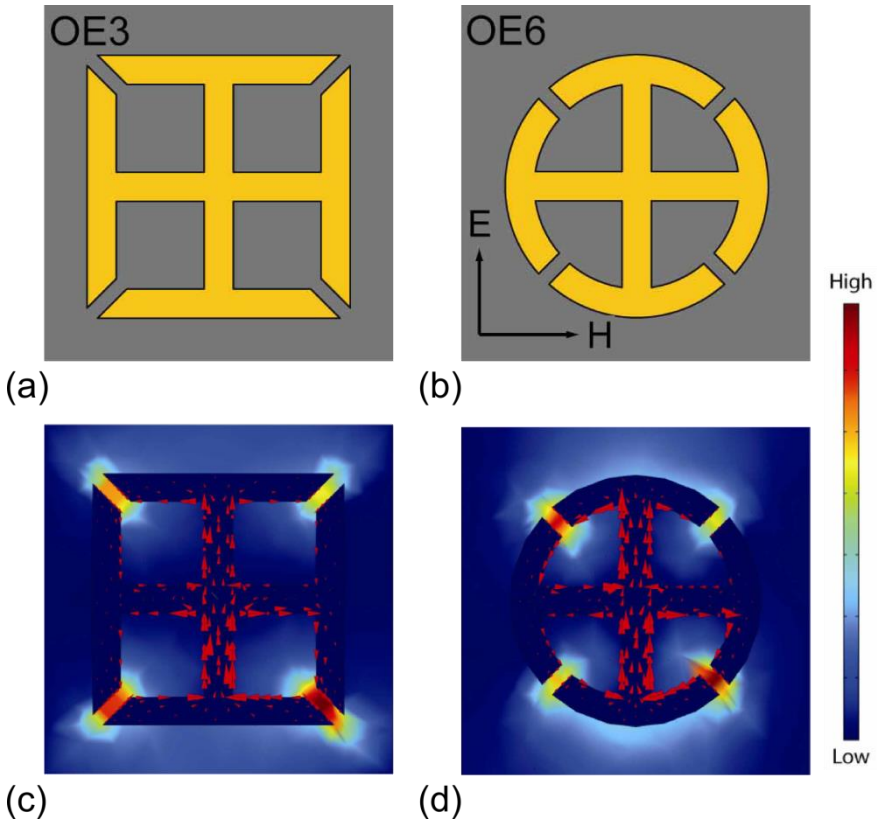

Figure 2.15 Electric ring resonator (ERR) images and simulation results. (a-b) Images of electric ring resonators consisting of a 200 nm gold layer and 10 nm titanium adhesion layer on a semi-insulating gallium arsenide substrate. (c-d) Simulation results showing the surface currents and high local electric fields associated with the ERRs at resonance. Field orientations added to (b). Reproduced with permission: [H.-T. Chen, J. F. O'Hara, A. J. Taylor, R. D. Averitt, C. Highstrete, M. Lee, and W. J. Padilla, "Complementary planar terahertz metamaterials," Opt. Express **15**(3), 1084–1095 (2007) [123]].

In a continuation of the initial work presented by Padilla *et. al.* [108], Chen *et. al.* further explored the resonant behaviour of the previously presented ERR structures, and investigated their inverse, or complementary, structures, which are known as cERRs [123]. Like the MMFs presented previously, the original MM structures and their complements adhere to Babinet's principle, such that at the resonant frequency, the original structure acts as a band reject filter and the complementary structure acts as a band pass filter. The transmission spectra from the original and complementary MM structure presented in Figure 2.15(a) are shown in Figure 2.16(a) [123]. The effective permittivity for the original

structure and complementary structure is shown in Figure 2.16(b) and Figure 2.16(c), respectively [123].

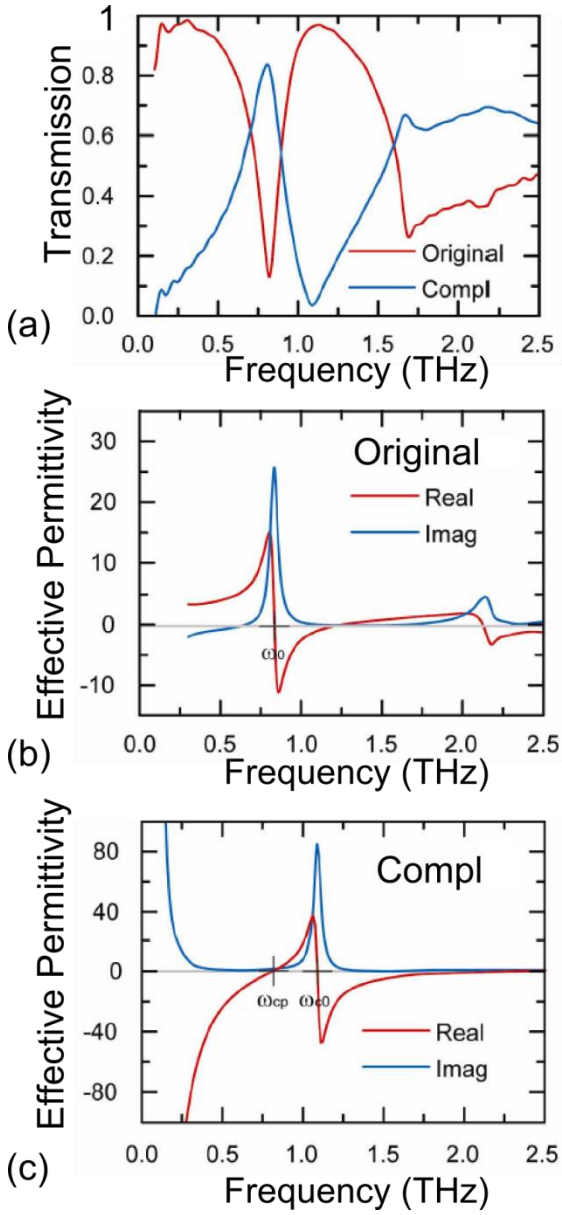

Figure 2.16 Original and complementary metamaterial (MM) (as shown in Figure 2.15(a)) (a) transmission spectra and effective permittivity for the (b) original and (c) complementary structure. Axis titles added to (a-c) and "Original" and "Compl" labels added to (b) and (c), respectively. Reproduced with permission: [H.-T. Chen, J. F. O'Hara, A. J. Taylor, R. D. Averitt, C. Highstrete, M. Lee, and W. J. Padilla, "Complementary planar terahertz metamaterials," Opt. Express **15**(3), 1084–1095 (2007) [123]].

It can be observed that the original MM structures show a Lorentz style resonance corresponding to the dip in the transmission spectra of the MM. The complementary MMs display Drude-like characteristics with corresponding effective plasma frequency close to the peak transmission frequency of the MM. The Drude-like response of the complementary MMs occurs at the same frequency as the Lorentz-like resonance observed in the ERR MMs. The complementary MMs also display a Lorentz-like resonance at a

higher frequency. In these materials the effective permeability is equal to one, thereby reflecting the eliminated magnetic field response [123].

In 2009, Paul *et. al.* presented the transmission characteristics, the surface currents and effective permittivity of an etched cross-slot type MM filter consisting of cERR style unit cells. In this case the MM filter was composed of copper on benzocyclobutene (BCB). The unit cell period was 68 µm and exhibited a transmission peak at 1.3 THz. By using a second MM filter layer, the pass band of the filter was significantly narrowed. Due to anti-parallel currents in the structure resulting in a reduced dipole moment, the resonant transmission for cross-slot structures has been attributed to excitation of trapped modes, which weakly couple to the incident field, resulting in high transmission [133,134]. The structure is effectively a composite of the two cross style MMFs presented in Section 2.3.2.1, where the inner cross is slightly smaller than the complementary surface [117,134,135]. A microscope image of the fabricated cross-slot structure by Paul *et. al.* is shown in Figure 2.17 [133].

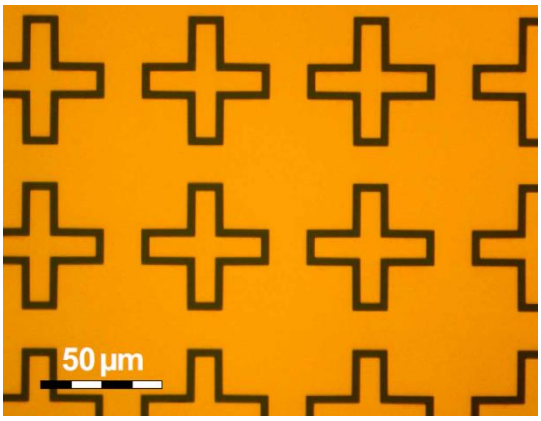

Figure 2.17 Microscope image of the cross-slot style metamaterial (MM) filter from. Reproduced with permission: [O. Paul, R. Beigang, and M. Rahm, "Highly Selective Terahertz Bandpass Filters Based on Trapped Mode Excitation," Opt. Express **17**(21), 18590–18595 (2009) [133]].

2.3.3 Metamaterial Absorbers

In contrast to MM band pass filters, which rely on engineered optical properties to transmit at a single wavelength, MM perfect absorbers are engineered to exhibit low reflection and high loss at a single resonant frequency. This corresponds to matching the effective permittivity and effective permeability, such that the material is impedance matched to free space, thereby minimising reflectivity, and also by engineering high loss, as demonstrated by an effective refractive index with a large imaginary component [12,116,136]. MM absorbers have been presented in many spectral bands including optical [137], IR [138], THz [12] and microwave [116].

In 2008 Landy *et. al.* introduced a design for a perfect MM absorber, with near unity absorbance, at microwave frequencies [116]. The MM absorber consisted of an ERR separated from a wire by a dielectric spacer. The ERR was used to couple to the electric field component of the incident radiation, as has been described in Section 2.3.2.2. Magnetic coupling was provided through antiparallel current generation in the central strip of the ERR, and the wire surface. The independent coupling of the electric and magnetic field components of the incident light to the different MM absorber components allowed independent control of the effective permittivity and effective permeability. The main component of loss in the structure was in the dielectric regions, characterised by high electric fields in the simulated structure. Ohmic losses in the ERR were comparatively small [116].

Following the work by Landy *et. al.* [116], MM absorbers have been scaled to operate at THz frequencies [12,13]. In 2011 Grant *et. al.* presented a polarisation insensitive MM absorber optimised for THz frequencies and investigated the effect of dielectric type and thickness [14]. The MM absorber consisted of a hollow cross ERR, which is the complementary structured of the cross-slot MM filter described in Section 2.3.2.2, separated from a continuous metallic ground plane by a dielectric spacer. The ERR and ground plane were consisted of a 300 nm gold film with a 20 nm titanium adhesion layer on a silicon substrate. The dielectric spacer material and thickness were varied, however the optimised design used a 3.1 μm thick layer of HD Microsystems PI2545 polyimide. The ERR array had a unit cell period of 27 μm. A schematic of the ERR is shown in Figure 2.18(a); a cross section of the MM absorber is shown in Figure 2.18(b); the absorption spectra for different spacer types and thicknesses are shown in Figure 2.18(c); and the extracted effective electromagnetic parameters for the MM absorber with the 3.1 μm polyimide dielectric spacer are shown in Figure 2.18(d) [14]. The effective permittivity exhibits a Drude-like behaviour at resonance, and a Lorentz-like resonance at higher frequencies, similar to what was observed in the cERR style MM filters as described in Section 2.3.2.2. The effective permeability exhibits a Lorentz style response at the resonant frequency [136]. The flexibility of engineering the resonant wavelength of MMs is such that, in addition to single band absorbers, structures such as broadband [139], and multiband absorbers [140–142] have also been presented.

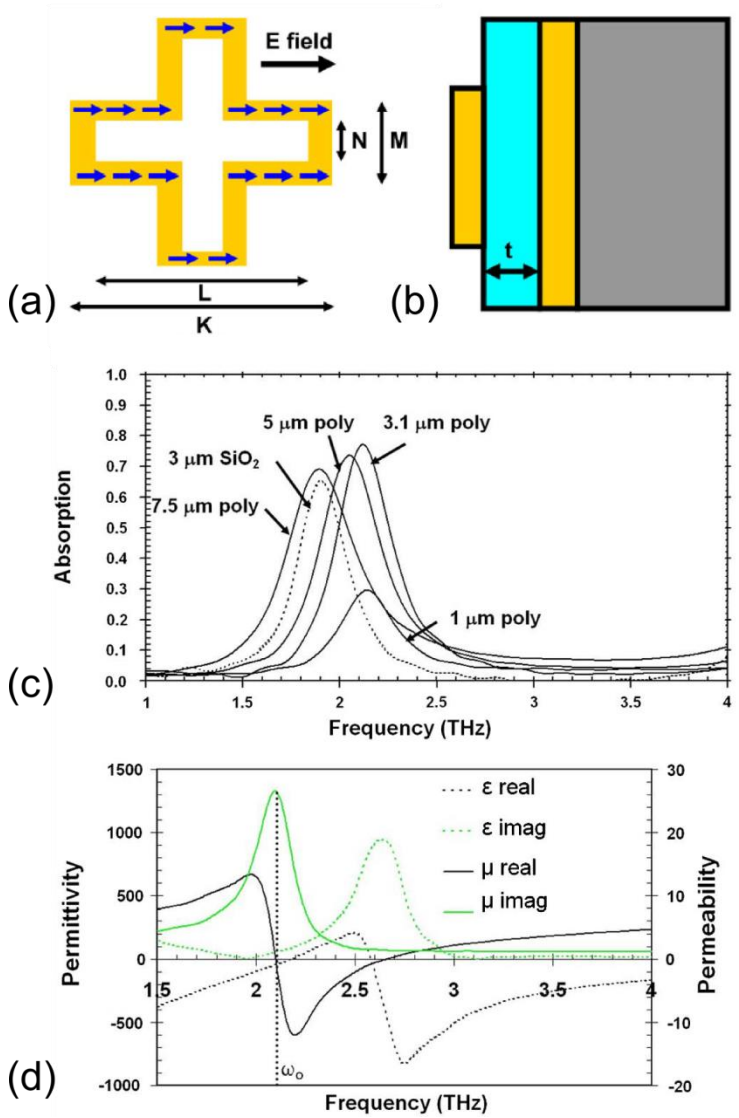

Figure 2.18 Terahertz (THz) metamaterial (MM) absorber. (a) Schematic of the electric ring resonator (ERR) with electric field direction and current flow shown. (b) Cross section of MM absorber illustrating the top ERR layer, the dielectric spacer, the metallic ground plane and the substrate. (c) Absorption spectra for MM absorber using different dielectric materials and thicknesses. (d) Extracted effective permittivity and permeability of the MM absorber. Reproduced with permission: [J. Grant, Y. Ma, S. Saha, L. B. Lok, A. Khalid, and D. R. S. Cumming, "Polarization insensitive terahertz metamaterial absorber," Opt. Lett. **36**(8), 1524–1526 (2011) [14]].

2.4 Terahertz Imaging

The FIR, or THz spectral band, roughly considered to range from 0.1 THz to 10 THz (or 3 mm to 30 μm), lies between IR and microwave radiation. This region is commonly known as the THz gap to reflect the lack of natural materials with desirable electromagnetic responses to create efficient sources and detector technologies when compared with the well-developed optical technologies and microwave technologies in the neighbouring spectral bands. However, there has been recent interest in THz technology due to the rich variety of applications for THz imaging, or T-ray, systems and because of advancements in areas such as nanotechnology and photonics, which can lead to the development of powerful sources and sensitive detectors in this spectral region [143–145]. THz imaging and spectroscopy have applications in areas such as: medical imaging [146–148], security screening of concealed weapons [149–152], explosive detection [149,150], and detection of illegal drugs [150,153].

Terahertz radiation exhibits several beneficial properties which make it of particular interest for the previously listed applications [150,154].

- THz radiation is non-ionising and therefore does not damage biological tissue.
- THz radiation can penetrate several common non-metallic materials, including forms of clothing and packing materials
- Millimetre wave scanners use wavelengths longer than that of THz radiation, therefore a THz scanner could have a higher spatial resolution.
- Many illicit chemicals and explosives display a unique THz spectral signature therefore allowing a non-destructive method of classification even when concealed in a package or clothing that is transparent to THz radiation [153].

THz imaging has been presented as a method for diagnosis of a range of cancers [148], including skin [147] and breast cancer [155], where cancerous tissue displays different optical properties at THz frequencies when compared with the surrounding tissue. In another healthcare application, a THz imaging system has been shown to be capable of three dimensional imaging of dental tissue, which can be used to extract information on enamel thickness [156]. The fact that THz radiation is non-ionising also makes it desirable for medical applications.

Due to the high reflectivity of metals and the transparency of common clothing at THz frequencies, THz imaging is a valuable tool for the detection of concealed weapons such as

guns and knives [149,151,154]. Millimetre wave (MMW) scanners are already employed for the detection of concealed weapons in airport security, however THz imaging systems offer approximately a factor of ten improvement in spatial resolution due to the shorter wavelength of operation. This means that the features of weapons may be completely resolved, leading to improved classification of objects, reduced number of false alarms and increased throughput. THz imaging can also offer spectral classification of certain chemicals, thereby further improving the ability of the imaging system in determining a potential threat [150,154].

THz spectroscopy can be used as a non-destructive identification method for illicit chemicals, including drugs and explosives, concealed in packages [150,153,154]. It has been shown that it is possible to differentiate between materials and detect concealed explosives based on their spectral signature at a one metre standoff distance in air using a THz spectroscopy system [157]. Spectroscopic techniques could be included in complete imaging systems, such that illegal substances could be classified in THz images by their spectral signature; identification of common drugs in mail envelopes through THz imaging and spectral analysis was presented by Kawase *et. al.* in [153]. THz spectroscopy can be performed using Fourier transform infrared (FTIR) spectroscopy or THz time domain spectroscopy (TDS), which also yields phase information [144,145]. FTIR spectroscopy was used to characterise a number of materials presented in this Thesis and will be further described in Chapter 4.

Imaging of a scene can be performed using two methods: active imaging, where a scene or object is illuminated by a source and the transmitted or reflected light is collected by the detector; or passive imaging, where the radiation is provided by the emissivity of the object or provided by reflection due to background, non-specific illumination. Consequently, the active imaging method offers higher dynamic range than the passive method [149,158]. The lack of compact THz sources presents a challenge in the development of compact, low cost, and low power, THz imaging systems, such that the development of THz sources is an active research area in addition to the development of detectors [143,144,159]. THz radiation sources include: optically pumped FIR lasers [160], free electron lasers (FEL) [161], quantum cascade lasers (QCL) [159], backward-wave oscillators (BWO) [162], resonant tunnelling diodes (RTD) [163] and ultrafast lasers used in conjunction with a THz emitter such as a photoconductive antenna, as is used in THz TDS [145].

A THz imaging system should ideally consist of an array of detectors in a focal plane array (FPA) format, which can retain high sensitivity without a requirement for cooling, and is capable of video rate imaging. Most current THz imaging systems use raster scanning with single pixel detectors, and are consequently slow and can be bulky [153,158]. There are a range of available THz detectors including: Schottky barrier diodes [164], bow-tie diodes [165], field effect transistors (FET) [166], Golay cells [167] and pyroelectric sensors [162]. An alternative detection method involves using microbolometers. Bolometric detection methods lend themselves well to scaling to a FPA format, and are commonplace in uncooled IR imagers [4,5]. An IR camera using microbolometer arrays has also been used in a THz imaging experiment, however as the system was not designed for the THz spectral band, the detection efficiency was low [6]. By coupling the microbolometer sensors with antenna structures it has been shown that the detectors can be optimised for imaging at THz frequencies [168–170]. Antenna coupled microbolometers for THz imaging can also be integrated with CMOS technology [171–173]. Quarter wavelength Fabry-Perot resonant cavities, consisting of the antenna and a reflective layer, are commonly employed to improve optical absorption within the structure [4,170].

A cross section of a typical single antenna coupled microbolometer pixel is shown in Figure 2.19. The antenna coupled microbolometer is on a thin membrane to minimise thermal conduction between adjacent pixels, and is connected to the CMOS read out integrated circuit (ROIC) by metallic legs and studs. The ROIC can be used to detect changes in the resistance of the microbolometer which are a consequence of variations in temperature due to absorption induced heating by incident radiation [4,170,171]. Microbolometer materials include vanadium oxide (VOx) [6] and amorphous silicon [170].

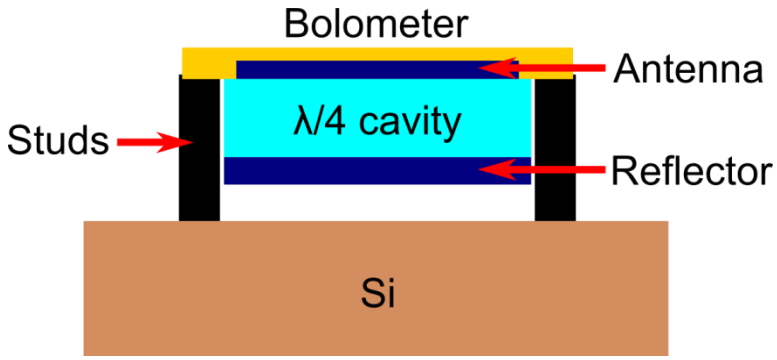

Figure 2.19 Cross section of an antenna coupled microbolometer pixel.

2.4.1 Metamaterial Absorbers for Terahertz Imaging

MM absorbers offer an alternative to traditional antenna structures for THz imaging applications when integrated with a bolometric sensing element. In addition to offering

several advantages over the conventional antenna technology, MM absorber coupled microbolometers could also be integrated with CMOS technology.

Due to their subwavelength unit cells, MM absorbers could theoretically image at a subwavelength scale, assuming the associated imaging optics were not diffraction limited [116]. MM absorbers can also have device thicknesses significantly smaller than the wavelength of radiation (the original MM absorber presented by Landy *et. al*. had a thickness of $\lambda/35$ [116]) which is also significantly smaller than the common quarter wavelength antenna structures. The decrease in thermal mass when compared to traditional structures, can be exploited to either create faster detectors, or to increase the responsivity of the detector [4,13,174]. The detection method is also not restricted to a single narrowband THz frequency; MM absorbers are scalable and have been shown in multiband [140–142] and broadband [139] formats.

2.5 Multi-Spectral and Hyper-Spectral Imaging Systems

Multi-spectral imaging (MSI) can be defined as imaging over a range of colours, or spectral bands, as a means of extracting application specific spectral information from a scene. In contrast with trichromatic imaging, which strives to reproduce an image as observed by a human observer using three colour bands, MSI systems typically image over more than three spectral bands which are determined by the application and are not restricted to visible wavelengths. However, it is still possible that a MSI system will include the red, green and blue colour bands so that the normal trichromatic image can be produced [1,175–177].

By increasing the number of imaged spectral bands and ensuring the spectral bands are sufficiently narrow, it is possible to move into the region of hyper-spectral imaging (HSI). HSI combines imaging and spectroscopy such that the resultant image contains high density spectral information of the scene over a continuous wavelength range. This contrasts with MSI, where the spectral information may be collected over wide spectral bands and may not be continuous [1,175,176].

The data collected by MSI and HSI systems can be represented by a data cube, corresponding to the two dimensional grey scale images that have been collected for each spectral band. A schematic illustrating typical data cubes associated with MSI and HSI systems are shown in Figure 2.20. The HSI data cube consists of many more images than the MSI data cube and consequently for each pixel of the HSI system a high resolution spectrum can be extracted [1,176].

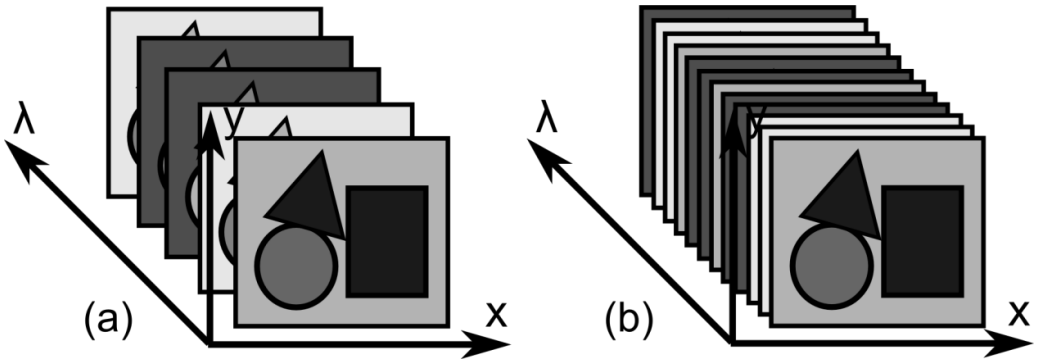

Figure 2.20 Illustration of three dimensional data cubes associated with a (a) multi-spectral imaging (MSI) system and a (b) hyper-spectral imaging (HSI) system.

2.5.1 Spectral Imaging from Visible to Terahertz

Depending on the requirements of the spectral imaging systems, there are a range of different methods for construction of the data cube. Spectral imagers in the visible to NIR bands can use a CFA combined with a single sensor [178–181], as was described previously in Section 2.2.2, however for a large number of filters there will be a greater distance between the same colours which could lead to less successful interpolation or a large decrease in spatial resolution. Nonetheless, this technique ensures fast image acquisition as all spectral scenes in the data cube can be acquired simultaneously, and can therefore be referred to as snapshot mode [179,182].

It is also possible to perform spectral imaging sequentially, for example by using off-chip filters in a rotating filter holder, known as a filter wheel, with a monochromatic camera [183]; a range of images can be acquired with each corresponding to a different spectral band. The filter wheel relies on mechanical rotation of the filters for spectral image acquisition, such that acquisition is longer than the single shot approach, and errors can arise from the misalignment of the optical system [175,182,184].

The CFA and filter wheel techniques are well suited for MSI imaging however it is necessary to consider alternative techniques for HSI, where a high spectral resolution is required. Dispersive optics, such as a grating can be used to acquire data with a high spectral resolution however acquisition time can be long. This technique records spectral data for a single spatial dimension at any given time, and consequently a line scan, or “push broom”, technique is required to construct the three dimensional data cube [182,185].

MSI and HSI systems may also be used for applications outside the visible band, however different detection materials and methods are often required to image different spectral regions. Methods for imaging visible, IR and THz wavebands have already been

introduced in this Chapter, and within these wavebands there a range of applications where the spectral information of an image is of value, for example carbon dioxide detection at IR wavelengths [186], and drug detection at THz frequencies [153].

Each of these individual detection methods could also be combined to create a MSI system operating at visible, IR and THz wavelengths, thereby creating an imaging system that can operate over several decades of wavelength. A key disadvantage in a MSI systems operating over large spectral ranges is the requirement for multiple spectrally specific cameras due to the differences in materials and detection methods necessary for each waveband [187–189]. This can lead to difficulty in optical alignment, and result in expensive and bulky imagers which do not lend themselves well to co-integration in a compact and portable system.

Perenzoni *et. al.* have integrated visible, IR and THz detectors on a single CMOS chip [7,8]. The chip consists of photodiodes for visible detection, in addition to the relevant readout and processing electronics for IR and THz detectors, which were fabricated during post processing of the chip. The IR and THz detectors used amorphous silicon bolometers, and in the case of the THz pixels, they are coupled with antennas. The MSI camera can operate at 50 frames per second, and therefore constitutes video rate MSI. The imager consists of 160 x 160 combined visible and IR pixels with a central area of 32 x 32 THz pixels.

2.5.2 Structured Photonic Materials for Spectral Imaging

Structured photonic materials, such as plasmonic filters and MM absorbers, are of particular interest for spectral imaging applications because their optical properties can often be engineered simply by scaling features of the unit cell structure, such as period or geometry. This could overcome many of the problems associated with the requirement for different optics and detection methods at different wavebands in conventional MSI systems.

As presented in Section 2.1.4, it is possible to engineer the pass band of hole array plasmonic filters by scaling the hole period and diameter [59]. This offers a simple method to create a multi-spectral colour filter set, which could be integrated with CMOS technology to create a MSI camera. Xu *et. al.* presented an alternative plasmonic filter design, composed of metal-insulator-metal (MIM) stacks for spectral imaging. The MIM structures exhibited continuous dispersion over the whole visible spectrum by gradual scaling of the slit period over the filter surface [190]. Other structured materials that have

been presented previously, namely silicon nanowires [101] and Fabry Perot filters [102], have also been shown to be suitable for MSI applications.

The properties of MMs, specifically filters and absorbers, could prove particularly useful for the development of MSI systems. In addition to being inherently scalable, MM absorbers have been presented over many spectral bands [12,116,137,138] and exploitation of multiple resonances has led to multiband designs [140–142], which could be used to create a MSI system.

2.5.3 Applications and Image Processing

Spectral imaging systems typically operate within the spectral range from the ultraviolet (UV) to the IR, to highlight features that are invisible to the human observer, however MSI and HSI systems focussing solely on the visible band can also be useful. Applications within the UV-visible-IR spectral region include: ancient document analysis [183], art inspection and conservation [182,191,192], measurement of food quality [185,193], healthcare [181,194], target detection and tracking [195,196], facial recognition [197] and remote sensing [180,198–201]. As THz imaging systems have been developed there has been an interest in developing MSI systems operating at visible, IR and THz wavelengths [7,8,187–189]. These systems include three very valuable spectral bands for applications in security screening, where a visible image can be acquired in addition to a thermal IR image and a THz image, showing any concealed weapons.

Depending on the spectral range and application of a spectral imaging system, there are a variety of different image processing methods and ways to represent the spectral information. In the case of colour imaging, increased spectral resolution can improve the colour reproduction of the imager. Metamerism occurs when two different colours correspond to the same tristimulus values, and consequently, the colours can be considered to be a metameric match. This can be observed when objects imaged using a trichromatic imager appear to be the same colour under certain illumination conditions despite being spectrally different. Under different illumination conditions, the colours may be observed to be different, and no longer constitute a metameric match, thereby introducing a problem in colour sensing and reproduction. This is due to the limitations of using only three colours to represent the visible spectrum. The higher spectral resolution of a MSI or HSI system in the visible band can eliminate problems associated with metamerism and therefore lead to higher accuracy colour reproduction [83,175,184,202,203].

In other spectral imaging applications, where specific spectral bands hold useful information on a scene, different methods can be used to represent and display the data. Monochrome images of each spectral band can be displayed individually, to extract relevant information associated with each band. It is also possible to generate a false colour image, where different spectral bands detected by the imager are associated with the blue, green and red colour channels. In remote sensing applications mapping vegetation it is common to associate the green colour band with the blue channel, the red colour band with the green channel and the NIR band with the red channel, as healthy vegetation is highly reflective at NIR wavelengths [198,204]. Image fusion is a method of combining multiple images into a single composite image that displays more information than each of the individual input images [1,205]. In remote sensing, this can be used to combine a high resolution panchromatic image, with a low resolution spectrally rich image to result in a final image which is both multi-spectral and high resolution [1,198,205,206].

Fusing visible and IR imaging has found uses in areas such as facial recognition [197] and target tracking [196], by exploiting the benefits of each spectral band. For example, visible light imaging can be affected by unfavourable conditions, such as poor illumination or smoke, which can be alleviated by using the IR thermal imager. The IR system however, operates at a lower resolution and optically transparent features, such as glass, can appear opaque at IR wavelengths. Therefore combining the visible and IR images using image fusion the disadvantages of each can potentially be eliminated. Image fusion using visible and IR images has also been shown to be beneficial in concealed weapon detection [207].

Visible, IR and THz images can be combined using image fusion algorithms, to overcome the low resolution of the THz image when compared to the other spectral bands [187–189,208,209]. This can be used to improve the overall quality of the image, thereby making it easier to detect any concealed weapons. IR imaging can also show thermal information and can be used to maintain high resolution in low lighting conditions.

2.6 Summary

This Chapter has introduced the structured photonic materials used in this project: plasmonic filters, for filtering visible and IR radiation; MMFs and MM filters, for filtering IR and THz radiation, respectively; and MM absorbers, optimised for THz frequencies. Visible and THz imaging systems have also been introduced, demonstrating the state of current technology and how structured photonic materials have been implemented in these systems, and could continue to advance them in future work. Finally, MSI systems and HSI systems have been introduced, where applications have ranged from visible to THz wavelengths. Structured photonic materials are attractive components for spectral imaging systems due to their flexibility and scalability. The prior work presented in this Chapter represents the foundation for the further development and advancement of structured photonic material technology for MSI systems as will be presented in this Thesis.

3. Background Theory

This Chapter outlines the background theory underlying the operation of the plasmonic structures and metamaterials presented in this Thesis. The first section introduces Maxwell's equations followed by a description of the optical properties of metals as described by the free electron model. This is followed by a theoretical description of surface plasmon polaritons, and the coupling mechanism of light and surface plasmons that underlies the extraordinary optical transmission process. The significance of spoof surface plasmons in describing extraordinary optical transmission at longer wavelengths is also discussed. The Chapter also describes effective medium theory and how it can be applied in optical simulations to classify metamaterials. This Chapter concludes with some discussion on how the geometry of the metamaterial structures leads to resonant behaviour, and how the effective electromagnetic parameters of a metamaterial can be engineered to create metamaterial filters and metamaterial absorbers.

3.1 The Dielectric Properties of Metals

Maxwell's equations represent the foundation of classical electromagnetism and are necessary to understand the physics behind the operation of the structured photonic materials that are presented in this Thesis. Maxwell's equations in matter are presented in terms of free charges and free currents and are given by:

$$\nabla . \mathbf{D} = \rho_f \tag{3.1}$$

$$\nabla . \mathbf{B} = 0 \tag{3.2}$$

$$\nabla \times \mathbf{E} = -\frac{\partial \mathbf{B}}{\partial t} \tag{3.3}$$

$$\nabla \times \mathbf{H} = \mathbf{J}_f + \frac{\partial \mathbf{D}}{\partial t} \tag{3.4}$$

where **D** is the electric displacement, **E** is the electric field, **B** is the magnetic induction, **H** is the magnetic field, ρ_f is the free charge density and $\mathbf{J}_f$ is the free current density [210]. The electric displacement and magnetic field can also be linked to the electric field and magnetic induction by the following equations for linear media:

$$\mathbf{D} = \varepsilon_0 \mathbf{E} + \mathbf{P} = \varepsilon_0 \varepsilon_r \mathbf{E} \tag{3.5}$$

$$\mathbf{H} = \frac{\mathbf{B}}{\mu_0} - \mathbf{M} = \frac{\mathbf{B}}{\mu_0 \mu_r} \tag{3.6}$$

where **P** is the polarisation, **M** is the magnetisation, ε_0 and μ_0 are the permittivity and permeability of free space, respectively, and ε_r and μ_r are the relative permittivity and relative permeability of the material, respectively. The material permittivity is given by: $\varepsilon = \varepsilon_0\varepsilon_r$, and the material permeability is given by: $\mu = \mu_0\mu_r$ [16,210]. The electromagnetic wave equation is shown in terms of both the electric and magnetic fields for the case of linear and homogenous media in Equations (3.7) and (3.8):

$$\nabla^2\mathbf{E} - \frac{\varepsilon_r\mu_r}{c^2}\frac{\partial^2\mathbf{E}}{\partial t^2} = 0 \tag{3.7}$$

$$\nabla^2\mathbf{B} - \frac{\varepsilon_r\mu_r}{c^2}\frac{\partial^2\mathbf{B}}{\partial t^2} = 0 \tag{3.8}$$

where c is the speed of light in a vacuum [210].

All materials used in this project are non-magnetic with relative permeability, $\mu_r = 1$, and therefore can be described in terms of their relative permittivities, which are complex quantities, given by equation (3.9) or their complex refractive indices, given by equation (3.10):

$$\varepsilon_r = \varepsilon_1 + i\varepsilon_2 \tag{3.9}$$

$$n = n_1 + in_2 \tag{3.10}$$

where ε_1 and ε_2 are the real and imaginary components of the permittivity, respectively, and n_1 and n_2 are the real and imaginary components of the refractive index, respectively [16]. For a non-magnetic material, the permittivity and refractive index are related by equation (3.11) and therefore the complex quantities can be related as shown in equations (3.12) and (3.13):

$$n = \sqrt{\varepsilon_r} \tag{3.11}$$

$$\varepsilon_1 = n_1^2 - n_2^2 \tag{3.12}$$

$$\varepsilon_2 = 2n_1n_2 \tag{3.13}$$

The Drude free electron model considers electrons in a metal as a negatively charged gas, or plasma, with a positively charged fixed background due to the positive atomic nuclei. Using this model it is possible to describe the optical properties of a metal. If a volume of plasma is displaced by a distance, **x**, it results in a polarisation, **P**, that leads to the formation of an electric field, **E**, given by:

$$\mathbf{E} = \frac{-\mathbf{P}}{\varepsilon_0} = \frac{ne\mathbf{x}}{\varepsilon_0} \tag{3.14}$$

where n is the number density of electrons and e is the electronic charge. The plasma will experience a restoring force given by the equation of motion:

$$m\frac{d^2\mathbf{x}}{dt^2} = -e\mathbf{E} = -\frac{ne^2\mathbf{x}}{\varepsilon_0} \tag{3.15}$$

where m is the electron mass, and the other symbols have their usual meaning. The natural frequency of oscillation associated with the plasma is known as the plasma frequency and is given by:

$$\omega_p = \sqrt{\frac{ne^2}{\varepsilon_0 m}} \tag{3.16}$$

This leads to the defining of plasmons, which are the quanta of plasma oscillations [15,16].

For an electron exposed to a driving electric field of $\mathbf{E}(t) = \mathbf{E_0}e^{-i\omega t}$ the displacement of the electron can be described by, $\mathbf{x}(t) = \mathbf{x_0}e^{-i\omega t}$. Substitution into the equation of motion, given by equation (3.15), yields:

$$\mathbf{x} = \frac{e\mathbf{E}}{m\omega^2} \tag{3.17}$$

Substituting equation (3.17) into equation (3.14) yields the polarisation:

$$\mathbf{P} = \frac{-ne^2}{m\omega^2}\mathbf{E} \tag{3.18}$$

Substituting equation (3.18) into equation (3.5), and substituting in the plasma frequency from equation (3.16) yields the electric displacement:

$$\mathbf{D} = \varepsilon_0\left(1 - \frac{\omega_p^2}{\omega^2}\right)\mathbf{E} \tag{3.19}$$

From comparison between equation (3.5) and equation (3.19) it follows that the relative permittivity of a metal can be written in terms of its plasma frequency as follows:

$$\varepsilon_r = 1 - \frac{\omega_p^2}{\omega^2} \tag{3.20}$$

It can be seen that below the plasma frequency, the permittivity is negative, and above the plasma frequency it is positive. The plasma frequency marks the transition region between

a metal being reflective, when the permittivity is negative, and absorbing, when the permittivity is positive [15,16,50].

It should be acknowledged that equation (3.15) corresponds to the case of an undamped oscillator however in a real metal the electron motion is damped due to collisions, represented by the relaxation time of the free electron gas, τ. Following the previous derivation with the additional damping term, yields the following equations corresponding to the real and imaginary components of the permittivity:

$$\varepsilon_1 = 1 - \frac{\omega_p^2 \tau^2}{1 + \omega^2 \tau^2} \tag{3.21}$$

$$\varepsilon_2 = \frac{\omega_p^2 \tau}{\omega(1 + \omega^2 \tau^2)} \tag{3.22}$$

These equations correspond to the characteristic Drude response exhibited by metals [15,16]. With regards to equation (3.21) and equation (3.22), it can be observed that close to the plasma frequency of the metal, where $\omega\tau >> 1$, the permittivity will tend to the form presented in equation (3.20).

Loss in the material can be described in terms of the imaginary component of the refractive index, n_2, and can be used to define the absorption coefficient or skin depth of a material [16,211]. Typically the absorption coefficient is used to describe loss in a dielectric material where the incident light will pass through to the other side and skin depth is usually used to describe the finite penetration depth of electromagnetic radiation into a metal at low frequencies. The intensity of an electromagnetic wave propagating into a material will decay exponentially and is given by as a function of the penetration distance, z, by:

$$I(z) = I(0)e^{-\alpha z} \tag{3.23}$$

where $I(z)$ and $I(0)$ are the intensities of the incident wave at z, and the initial intensity, respectively. α is the absorption coefficient. The skin depth can also be determined by considering exponential decay into the material, however the skin depth is concerned with the decay of the field amplitude, which is proportional to the square root of the intensity. The absorption coefficient, α, is given by equation (3.24) and also related to the skin depth, δ, as follows:

$$\alpha = \frac{2n_2\omega}{c} = \frac{2}{\delta} \tag{3.24}$$

3.2 Nanoplasmonics

The branch of nanophotonics focussed on the interaction of light with surface plasmons (SP) is known as nanoplasmonics, or plasmonics. In the previous Chapter it was described how light-SP interactions can lead to a range of unique physical properties on a subwavelength scale, which results in a variety of interesting optical phenomena, including extraordinary optical transmission (EOT). In the previous Section the bulk, or volume plasmon, was introduced. Simply put, a SP is a plasmon that is confined to the interface between a dielectric and a conductor. The SP frequency is related to the plasma frequency, given by equation (3.16), by the following relation:

$$\omega_{sp} = \frac{\omega_p}{\sqrt{1+\varepsilon_d}} \tag{3.25}$$

where ε_d is the dielectric constant of the dielectric layer at the interface [16,50]. In terms of the physical parameters outlined in the previous section, a SP exists at the interface between materials where the real components of their permittivities have opposite signs. Complex metal permittivity can be written as:

$$\varepsilon_m = \varepsilon'_m + i\varepsilon''_m \tag{3.26}$$

At optical wavelengths, the dielectrics considered in this work are predominantly real, such that the dielectric permittivity will be given by ε_d in the following derivations. Therefore SPs exist at an interface where $\varepsilon'_m < 0$ and $\varepsilon_d > 0$. Low loss metals are desirable for plasmonic applications, therefore a good plasmonic material is typically characterised as having: $|\varepsilon''_m| \ll |\varepsilon'_m|$ [16,23,48].

3.2.1 Surface Plasmon Polaritons

As outlined in the previous Chapter, surface plasmon polaritons (SPP) form when light couples with SPs at a metal-dielectric interface in a process known as surface plasmon resonance (SPR). To investigate the propagation of SPPs, the electromagnetic wave equation is used to describe waves propagating at the metal-dielectric interface.

The interface is positioned at $z = 0$ with the metal region at $z < 0$ and the dielectric region at $z > 0$. As outlined in [16], the time independent form of the wave equation for wave propagation in the x direction and transverse magnetic (TM) polarisation can be written as:

$$\frac{\partial^2 H_y}{\partial z^2} + (k_0^2 \varepsilon_r - k_x^2) H_y = 0 \tag{3.27}$$

where H_y is the y component of the magnetic field, k_0 is the wave vector in a vacuum, given by $k_0 = \omega/c$, and k_x is the wave vector in the x direction. The corresponding field components for harmonic time dependence and TM polarisation can be derived using equation (3.4) and are given by:

$$E_x = -\frac{i}{\omega \varepsilon_0 \varepsilon_r} \frac{\partial H_y}{\partial z} \tag{3.28}$$

$$D_z = -\frac{k_x}{\omega} H_y \tag{3.29}$$

Using equations (3.27), (3.28) and (3.29) it is possible to describe the propagation of SPPs at a metal-dielectric interface. The dielectric region is positioned above the x axis such that $\varepsilon_d > 0$ when $z > 0$, and the metal region is positioned below the x axis such that $\varepsilon_m < 0$ when $z > 0$. At the interface confinement is marked by an evanescent decay of the form $e^{-k_z z}$ when $\neq 0$, and propagation in the x direction is represented by an exponential of the form $e^{ik_x x}$. In the dielectric region where $z > 0$, solutions to the TM equations can be written as:

$$H_y = C e^{ik_x x} e^{-k_{z,d} z} \tag{3.30}$$

$$E_x = iC \frac{k_{z,d}}{\omega \varepsilon_0 \varepsilon_d} e^{ik_x x} e^{-k_{z,d} z} \tag{3.31}$$

$$D_z = -C \frac{k_x}{\omega} e^{ik_x x} e^{-k_{z,d} z} \tag{3.32}$$

In the metal region, where z < 0, solutions to the TM equations are:

$$H_y = C e^{ik_x x} e^{k_{z,m} z} \tag{3.33}$$

$$E_x = -iC \frac{k_{z,m}}{\omega \varepsilon_0 \varepsilon_m} e^{ik_x x} e^{k_{z,m} z} \tag{3.34}$$

$$D_z = -C \frac{k_x}{\omega} e^{ik_x x} e^{k_{z,m} z} \tag{3.35}$$

where $k_{z,d}$ and $k_{z,m}$ are the z components of the wave vectors in the dielectric and in the metal, respectively [16]. C denotes the field amplitudes which are equal in all solutions due to continuity of H_y and D_z at the interface. Continuity of E_x at $z = 0$ leads to:

$$\frac{k_{z,d}}{k_{z,m}} = -\frac{\varepsilon_d}{\varepsilon_m} \tag{3.36}$$

Substituting the equations (3.30) and (3.33) into the time independent wave equation, given by equation (3.27), yields the following relations:

$$k_{z,d}^2 = k_x^2 - k_0^2 \varepsilon_d \tag{3.37}$$

$$k_{z,m}^2 = k_x^2 - k_0^2 \varepsilon_m \tag{3.38}$$

Combining equations (3.36), (3.37) and (3.38) yields the dispersion relation for SPPs propagating at an interface [16] and is given by:

$$k_{SPP} = k_x = k_0 \sqrt{\frac{\varepsilon_m \varepsilon_d}{\varepsilon_m + \varepsilon_d}} \tag{3.39}$$

Two key parameters when considering propagation of SPPs at an interface are the propagation length and the confinement [16,23]. Losses in the metal result in a complex permittivity, which leads to a complex SPP wave vector, given by $k_{SPP} = k'_{SPP} + ik''_{SPP}$. The propagation length defines how far an SPP can propagate before it decays by e^{-1} of its initial intensity due to losses in the metal and therefore places a limit on the size of plasmonic components. The propagation length is given by:

$$\delta_{SPP} = \frac{1}{2k''_{SPP}} = \frac{(\varepsilon'_m)^2}{k_0 \varepsilon''_m} \left(\frac{\varepsilon'_m + \varepsilon_d}{\varepsilon'_m \varepsilon_d} \right)^{\frac{3}{2}} \tag{3.40}$$

The confinement can be quantified in terms of the decay length into the dielectric which is the inverse of the wave vector in the z direction, and therefore with reference to equation (3.37) and equation (3.39) can be written as:

$$\delta_d = \frac{1}{k_{z,d}} = \frac{1}{\sqrt{k_{SPP}^2 - k_0^2 \varepsilon_d}} = \frac{1}{k_0} \left| \frac{\varepsilon'_m + \varepsilon_d}{\varepsilon_d^2} \right|^{\frac{1}{2}} \tag{3.41}$$

Decay length into the metal, from equations (3.38) and (3.39) is given by:

$$\delta_m = \frac{1}{k_{z,m}} = \frac{1}{\sqrt{k_{SPP}^2 - k_0^2 \varepsilon_m}} = \frac{1}{k_0} \left| \frac{\varepsilon'_m + \varepsilon_d}{{\varepsilon'_m}^2} \right|^{\frac{1}{2}} \tag{3.42}$$

The decay lengths are illustrated in Figure 2.2(b) in Chapter 2. The decay length into the metal can be approximated by the skin depth at low frequencies as is typically of the order

of 20 nm at visible and infrared (IR) wavelengths. SPPs that are tightly bound to the metal-dielectric interface, typically with decay lengths on the order of half the wavelength of the incident light, correspond to a field enhancement which is necessary for plasmonic applications [16,19,23]. At longer wavelengths the decay length into the dielectric can extend over several wavelengths into the dielectric, such that the SPP are no longer confined to the surface and resemble Sommerfeld-Zenneck surface grazing light waves, which results in a diminished plasmonic response [16,17].

3.2.2 Extraordinary Optical Transmission

A typical SPP dispersion curve associated with equation (3.39), compared with the wave vector of light is shown in Figure 3.1 [16,19]. At large wave vectors, the frequency of the SPP tends to the surface plasma frequency, given by equation (3.25).

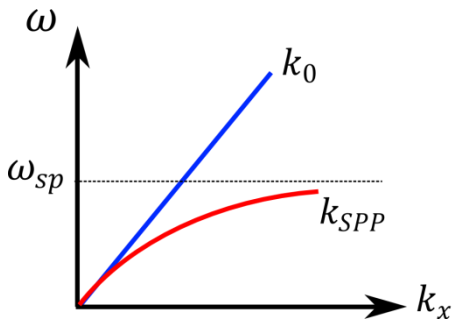

Figure 3.1 Surface plasmon polariton (SPP) dispersion relation showing the SPP wave vector k_{SPP} and the incident light wave vector k_0.

As can be seen by equation (3.39) the SPP wave vector, k_{SPP} is larger than that of the light wave vector, k_0. This is illustrated in Figure 3.1 by the SPP dispersion curve lying to the right of the light line. This highlights the bound nature of SPPs and the momentum mismatch that must be bridged for coupling of the incident light and SPs to occur [19]. Close to the light line, at low frequencies, the confinement is poor and the SPPs act as Sommerfeld-Zenneck surface waves [16].

It is possible to overcome the momentum mismatch using grating coupling of light to the SPs as described in Chapter 2. The resonance condition is given by:

$$\boldsymbol{k}_{SPP} = \boldsymbol{k}_{\parallel} + \boldsymbol{G} \tag{3.43}$$

where $\boldsymbol{k}_{\parallel}$ is the component of the incident light wave vector parallel to the metal-dielectric interface and $\boldsymbol{G}$ corresponds to the reciprocal lattice vector of the grating. The parallel component of the incident wave vector can be expressed as:

$$\boldsymbol{k}_{\parallel} = k_0 \sin\theta \cos\varphi\, \hat{\boldsymbol{x}} + k_0 \sin\theta \sin\varphi\, \hat{\boldsymbol{y}} \tag{3.44}$$

where θ is the incident angle to the normal of the surface and φ is the azimuthal angle, which is the angle of the wave vector from the x axis [45,46,73,212].

Equation (3.44) demonstrates the intrinsic angular dependence of plasmonic filters. For the case of normal incidence, the parallel component of the incident light wave vector is equal to zero and the only contribution to coupling comes from the grating [46,73]. For normal incidence (3.43) can be rewritten as:

$$\boldsymbol{k}_{SPP} = \boldsymbol{G} \tag{3.45}$$

The magnitude of the SPP wave vector and grating momentum wave vector for a square array is given by:

$$|\boldsymbol{k}_{SPP}| = |\boldsymbol{G}| = \frac{2\pi}{a}\sqrt{i^2 + j^2} \tag{3.46}$$

where a is the array period, and i and j are the scattering orders of the array. For a triangular hole array, the magnitude of the SPP wave vector and grating momentum wave vector is given by:

$$|\boldsymbol{k}_{SPP}| = |\boldsymbol{G}| = \frac{4\pi}{\sqrt{3}a}\sqrt{i^2 + ij + j^2} \tag{3.47}$$

Relating equation (3.39) and equation (3.46) yields the resonant wavelength for a square array:

$$\lambda_{square} = \frac{a}{\sqrt{i^2 + j^2}}\sqrt{\frac{\varepsilon_m \varepsilon_d}{\varepsilon_m + \varepsilon_d}} \tag{3.48}$$

and relating equation (3.39) and (3.47) yields the resonant wavelength for a triangular array:

$$\lambda_{triangle} = \frac{a}{\sqrt{\frac{4}{3}(i^2 + ij + j^2)}}\sqrt{\frac{\varepsilon_m \varepsilon_d}{\varepsilon_m + \varepsilon_d}} \tag{3.49}$$

where all symbols have their usual meaning [46,48,73,213]. As $\varepsilon_m \gg \varepsilon_d$, at longer wavelengths it is possible to approximate equation (3.49) as:

$$\lambda_{(1,0)} = \frac{\sqrt{3}an}{2} \tag{3.50}$$

for $i = 1$ and $j = 0$, and where n is the refractive index given by equation (3.11).

The resonant wavelengths given by equations (3.48) and (3.49) have commonly been associated with transmission maxima for hole array structures, however the transmission peaks are often redshifted when compared with the calculated wavelengths [46,48]. The redshift has previously been attributed to the fact that the equation does not account for the impact of the holes on the dielectric properties of the metal [48]. Recent work has shown that equations (3.47) and (3.48) actually predict the transmission minima that occur just before the maxima, and this has been attributed to destructive interference of incident light with SPP modes [56,73].

EOT has also been demonstrated in quasiperiodic arrays, where the formation of SPPs has been associated with the grating momentum attributed to the long range periodicity of the structures that have been used [214,215]. Pacifici *et. al.* commented on shortcomings of the current theory by demonstrating the occurrence of EOT in array structures with only short range order and no distinct grating momentum wave vector. It was suggested that scattering from individual holes are responsible for the generation of the SPPs that are involved in EOT [73]. Nonetheless, equations (3.48) and (3.49) are valuable tools in optimising plasmonic filters based on periodic hole arrays.

3.2.3 Spoof Surface Plasmons

As described previously, a good plasmonic material has $|\varepsilon_m''| \ll |\varepsilon_m'|$ [16,23,48]. The ratio of these two quantities is shown in Figure 3.2(a) as a function of wavelength for aluminium, using the complex refractive index parameters presented by Rakić [216]. The decay length into the dielectric as a fraction of the wavelength for aluminium, from equation (3.41), is shown in Figure 3.2(b). The decay length calculation uses a lossless dielectric layer with a refractive index equal to 1.46.

It can be observed in Figure 3.2(a) that aluminium satisfies the condition for $|\varepsilon_m''| < |\varepsilon_m'|$ out-with the optical band, however as a trade-off, confinement is substantially reduced at IR wavelengths, as is shown in Figure 3.2(b). In the optical region the decay length into the dielectric remains below half a wavelength, up to approximately 580 nm. Another notable feature is the occurrence of high loss close to 800 nm, which is shown by a sudden decrease in the permittivity ratio. Gold and silver are considered better plasmonic materials than aluminium due to lower losses and increased SPP confinement at optical

wavelengths [48,69], however, aluminium is easy to fabricate, is low cost and is compatible with complementary metal-oxide semiconductor (CMOS) technology.

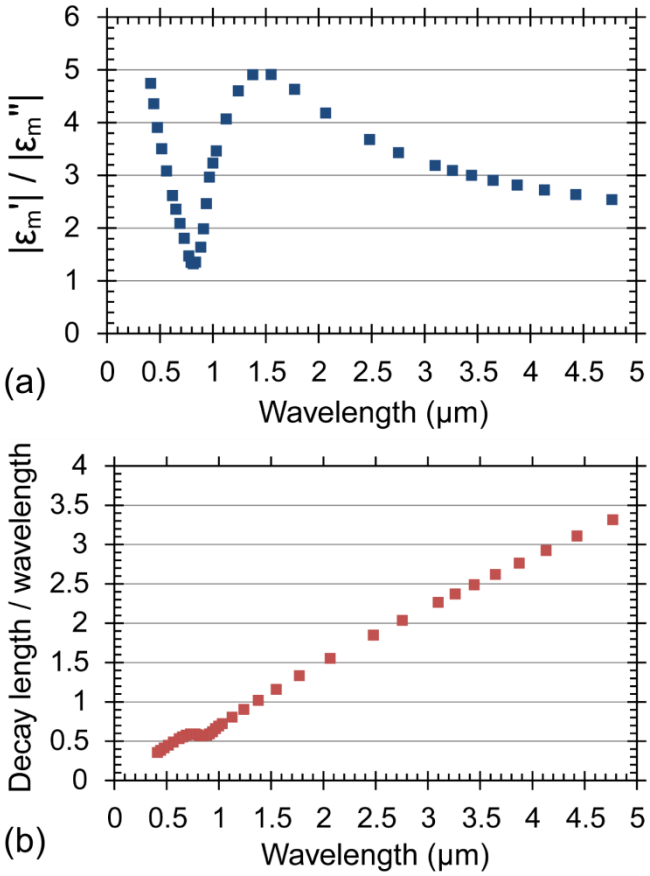

Figure 3.2 Calculation of key quantities underlying the performance of a plasmonic material, applied to aluminium, defined by complex refractive index parameters [216]. (a) Ratio of the real and imaginary components of the metal permittivity. (b) Decay length of the evanescent electric field into the dielectric as a fraction of the incident light wavelength. Refractive index of the dielectric layer is given by: $n = 1.46$.

High loss and poor confinement of the SPPs to the metal surface implies that aluminium, in addition to other common metals used in optical plasmonics, should not exhibit plasmonic phenomena such as EOT at IR wavelengths. Nonetheless, plasmonic filters have been designed for use outside of the optical and NIR regimes [64–68] and EOT has been shown to be possible for hole arrays in perfect electric conductor (PEC) surfaces [62,63], as was reported in Chapter 2. The inconsistency between the understanding of optical plasmonics and the observed enhanced transmission at longer wavelengths was resolved by the introduction of designer, or spoof, SPs [62,63].

A metal film patterned with subwavelength hole arrays can be considered as an effective medium, or a metamaterial (MM), which can be described in terms of its effective electromagnetic parameters. The effective plasma frequency associated with the MM corresponds to the waveguide cut-off associated with the geometry of the individual holes [62,63,217]. The effective plasma frequency for an array of square holes is given by

equation (3.51), and the effective plasma frequency for an array of circular holes is given by equation (3.52).

$$\omega_{square} = \frac{\pi c}{d} \tag{3.51}$$

$$\omega_{circle} = \frac{3.6824c}{d} \tag{3.52}$$

where c is the speed of light in vacuum and d is the square side length and hole diameter for the square and circle equations, respectively [218,219]. The hole arrays allow the electric field of surface waves to penetrate the metal surface, as is illustrated in Figure 3.3 [217]. This aids confinement and produces a bound state analogous to that of SPPs in planar metal surfaces, as described previously. These SPP-like waves arising from the structured surface are referred to as spoof SPs, to reflect their similarities to real SPs [62,63,217]. Spoof SPs can be engineered at wavelengths where metal conductivity is high and real SPs do not exist, thereby opening plasmonics up to a range of new applications. It should be noted that at optical wavelengths subwavelength hole arrays will still lead to the formation of a MM with an associated effective plasma frequency, such that both real and spoof SPs will be generated [62].

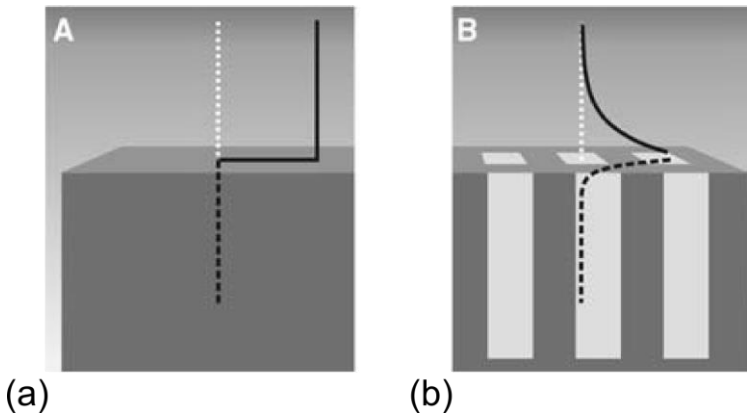

Figure 3.3 Illustration of the electric fields associated with a surface mode in perfect electric conductor (PEC) surface. (a) When no holes are present, the field cannot penetrate the metal and the light grazes the surface. (b) The inclusion of subwavelength holes allows the fields to evanescently decay into the metal, resulting in the formation of bound SPP-like waves, known as spoof SPs. From [A. P. Hibbins, B. R. Evans, and J. R. Sambles, "Experimental Verification of Designer Surface Plasmons," Science **308**, 670–672 (2005) [217]]. Reprinted with permission from AAAS.

3.3 Metamaterials

As described in Chapter 2, MMs are composite structures that are composed of subwavelength resonant elements. Due to the subwavelength nature of the unit cells a MM can be classified by its effective electromagnetic parameters using effective medium theory (EMT) [111,112]. The macroscopic electromagnetic properties of the MMs are dependent on the resonant properties of the microscopic unit cell and therefore, by carefully selecting the resonant elements, can be engineered for a wide range of applications.

MM filters use electrically resonant unit cells to couple to the electric field of incident radiation, resulting in band reject or band pass characteristics at resonance [108,123,133]. MM perfect absorbers use electric ring resonators (ERR) in conjunction with a ground layer, to allow coupling with both electric and magnetic fields of the incident radiation, resulting in high loss at resonance [12,116,136]. Both materials can be described in terms of effective electromagnetic parameters, which are characteristic of their optical properties.

3.3.1 Effective Medium Theory

EMT can be used to describe a MM as an effective medium, where the subwavelength unit cell geometries are ignored and the MM is classified as a bulk material with effective electromagnetic parameters. This is the foundation for MMs, where composite structures are used to create effective electromagnetic characteristics, often with unusual properties not found in nature [111,112].

The effective electromagnetic parameters can be determined by simulating a MM structure and analysing the complex transmission coefficient and complex reflection coefficient, also known as scattering (S) parameters [112]. An illustration of the S parameters from a MM of thickness, d, are shown in Figure 3.4. The transmission spectrum,$T(\omega)$ and the reflection spectrum $R(\omega)$ are related to the scattering parameters as follows: $T(\omega) = |S_{21}^2|$ and $R(\omega) = |S_{11}^2|$.

The S parameters for a MM are given by:

$$S_{21} = S_{12} = \frac{1}{\cos(n_{eff}k_0 d) - \frac{i}{2}\left(z_{eff} + \frac{1}{z_{eff}}\right)\sin(n_{eff}k_0 d)} \tag{3.53}$$

$$S_{11} = S_{22} = \frac{i}{2}\left(\frac{1}{z_{eff}} - z_{eff}\right)\sin(n_{eff}k_0 d) \tag{3.54}$$

where n_{eff} is the effective refractive index of the MM and z_{eff} is the effective wave impedance of the MM [112]. From equations (3.53) and (3.54) it follows that the effective refractive index and the effective wave impendence of the MM can be expressed by:

$$n_{eff} = \frac{1}{k_0 d}\cos^{-1}\left(\frac{1}{2S_{21}}(1 - S_{11}^2 + S_{21}^2)\right) \tag{3.55}$$

$$z_{eff} = \sqrt{\frac{(1 + S_{11})^2 - S_{21}^2}{(1 - S_{11})^2 - S_{21}^2}} \tag{3.56}$$

From equations (3.55) and (3.56) it is possible to determine the effective permittivity and effective permeability, which are given by:

$$\varepsilon_{eff} = \frac{n_{eff}}{z_{eff}} \tag{3.57}$$

$$\mu_{eff} = n_{eff} z_{eff} \tag{3.58}$$

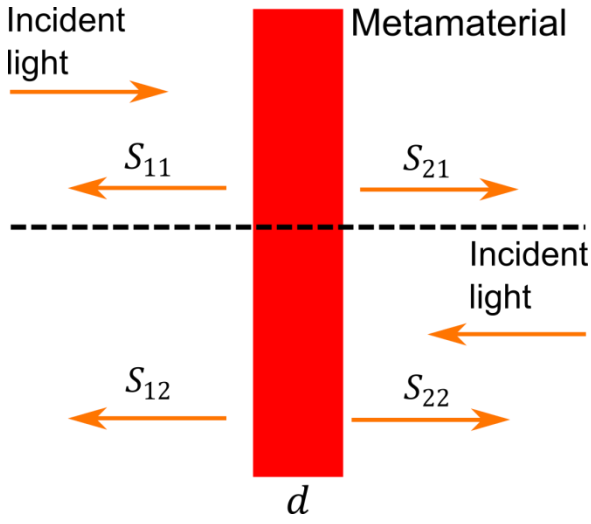

Figure 3.4 S parameters from a metamaterial (MM) of thickness, d, illuminated from the front (above the broken line) and illuminated from behind (below the broken line) [112].

The effective parameter extraction method that has been outlined here approximates a MM as a homogenous and a symmetric structure; however, conventional MMs consist of inhomogeneous structures and may be asymmetric. The approximation of the MM as a homogenous medium requires that the unit cell geometries are sufficiently subwavelength such that their contribution to the electromagnetic characteristics of the devices can be averaged. Inaccuracies in the extracted effective electromagnetic parameters can arise as the scale of the inhomogeneity approaches the wavelength. These include: ambiguity in determining the effective wave impedance, as it will vary throughout the structure; and

differing signs in the imaginary component of the effective permittivity and permeability. An asymmetric structure can also result in two unique definitions for the effective wave impedance, which correspond to illumination of the MM from different sides [112]. The MM structures in this work are asymmetric, however consideration is only given to one propagation direction, such that only one solution for the effective wave impedance is considered. Additional issues can also arise in the calculation of the effective electromagnetic parameters when the S parameters are very small, for example when considering transmission through an optically thick metal film [220].

Effective parameter extraction is an ongoing area of research, and can be a challenging process where approximations and numerical errors can lead inaccuracies in the simulation results, such that care must be taken when interpreting results [112,220,221]. Nonetheless, effective electromagnetic parameters can be used to describe MMs simply and in terms of quantities that appear in Maxwell's equations which can lead to a deeper understanding of the physical processes underlying the operation of a MM, at least qualitatively, if not quantitatively.

3.3.2 Metamaterial Filters

The characteristics of MMs are governed by capacitive and inductive effects due to different features of the MM unit cell geometry. In effect, the unit cells act as resonant circuit elements with an engineered electromagnetic response [107,109]. An illustration of a common ERR-style MM unit cell [107,108,123], which can act as a band reject filter, is shown in Figure 3.5(a) [123]. The direction of current flow and the electric field profile are shown in Figure 3.5(b) [123]. The loops correspond to inductors and the gaps correspond to a capacitor, which are wired in parallel such that the resonant frequency of the ERR MM can be defined as:

$$\omega_0 = \sqrt{\frac{2}{CL}} \tag{3.59}$$

where C and L denote the capacitance and inductance, respectively. The central gap acts as a capacitor, which couples to the incident electric field. This leads to circulating currents in the inductors. The current flow in the inductive loops is counter circulating due to the symmetry of the MM, therefore the generated magnetic dipoles cancel, resulting in no magnetoelectric response. As the structure is planar there are no loops which allow incident magnetic field to induce a current and therefore the ERR cannot couple with the incident magnetic field [107].

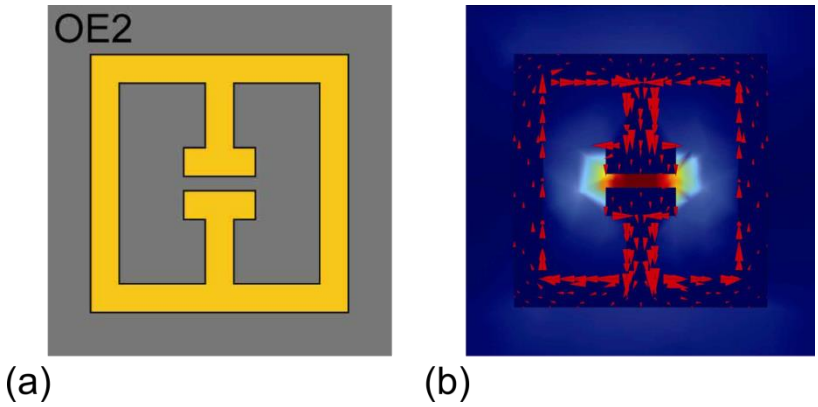

Figure 3.5 Common electric ring resonator (ERR) and simulation results. (a) Image of a common ERR structure. (b) Simulation results showing the surface current and high local electric field at resonance. Reproduced with permission: [H.-T. Chen, J. F. O'Hara, A. J. Taylor, R. D. Averitt, C. Highstrete, M. Lee, and W. J. Padilla, "Complementary planar terahertz metamaterials," Opt. Express **15**(3), 1084–1095 (2007) [123]].

The ERR structure presented in Figure 3.5 acts as a band reject filter. A complementary ring resonator (cERR), where metal regions are replaced by dielectric and dielectric regions are replaced by metal, can be used to act as a band pass filter in accordance with the complementary characteristics expected from Babinet's principle [123]. For polarisation insensitive structures, as will be presented in this Thesis, Babinet's principle states that the transmission spectrum from light passing through an aperture in a conducting screen, added to the transmission spectrum from light passing through the inverse structure, results in the same transmission spectrum as would be observed if no obstruction was present [123,222]. This is illustrated by equation (3.60).

$$T_O(\omega) + T_c(\omega) = 1 \tag{3.60}$$

where $T_O(\omega)$ is the transmission spectrum from the original structure and $T_c(\omega)$ is the transmission spectrum from the complementary structure. From equation (3.60) it follows that the transmitted light from a complementary MM structure would have a transmission spectrum that is the complement of the transmission spectrum of the original MM structure. This can be observed in Figure 2.16 in Chapter 2 [123].

3.3.3 Metamaterial Absorbers

A MM absorber consists of an ERR separated by a lower metal layer, or wire, by a dielectric spacer. As described in Chapter 2, The ERR component is used to couple to the incident electric field, where the mechanism previously described for MM filters applies, and magnetic field coupling is provided by interaction between the ERR and the ground layer [116,136]. The MM absorber offers independent control of the electric response and the magnetic response; the effective permittivity can be controlled by altering the ERR

structure and the effective permeability is sensitive to the spacing between the ERR and the ground layer. A MM absorber requires engineered effective electromagnetic parameters that yield high loss and low reflectivity for a given frequency [12,13,116,136].

The absorption,$A(\omega)$, can be found with reference to the transmission $T(\omega)$ and reflection $R(\omega)$ using equation (3.61):

$$A(\omega) = 1 - T(\omega) - R(\omega) \tag{3.61}$$

From equation (3.61) it can be seen that for unity absorption it is necessary that $T(\omega) = 0$ and $R(\omega) = 0$. The effective wave impedance of a MM can be rewritten using equations (3.57) and (3.58) as:

$$z_{eff} = \sqrt{\frac{\mu_{eff}}{\varepsilon_{eff}}} \tag{3.62}$$

From equation (3.54) it can be seen that when $z_{eff} = 1$, there will be no reflection from the MM surface, given by $R(\omega) = 0$. This corresponds to the condition where the MM wave impedance is matched to that of free space. Therefore, reflections from the MM absorber at resonance can be eliminated by ensuring that $\mu_{eff} = \varepsilon_{eff}$. From equation (3.53) it can be observed that transmission through the structure is dependent on both n_{eff} and z_{eff}, however when $z_{eff} = 1$ the transmission can be represented solely in terms of the effective refractive index, and is given by:

$$T(\omega) = e^{-2n''_{eff}k_o d} \tag{3.63}$$

where n''_{eff} is the imaginary component of the effective refractive index. As the free space wave vector and the MM thickness are fixed, it is necessary to engineer a large imaginary refractive index component to ensure that $T(\omega) = 0$, and $A(\omega) = 1$ at resonance [12,136].

3.4 Summary

In this Chapter, the physical theory behind the operation of nanoplasmonic devices and MMs has been presented. The free electron model can be used to describe the optical properties of a metal by its frequency dependent permittivity, which can be defined in terms of the plasma frequency of the material. The quantum of plasma oscillation is known as the plasmon, and SPs, which are confined to a metal-dielectric interface, are exploited for a range of applications including EOT. The dispersion relation for SPPs has been derived and applied to the case of grating coupling via periodic hole arrays that exhibit EOT. Some discussion has also been presented on how the metal parameters vary at longer wavelengths, such that the theory of spoof SPs must be invoked to describe observed EOT phenomena. This Chapter also includes a description of EMT applied to MMs and some discussion is presented on the validity of the procedure. EMT can be used to approximate a composite material as a bulk material which is described in terms of effective electromagnetic parameters. This Chapter concludes with some discussion on the theory underlying MM filters, consisting of ERRs, and MM absorbers, consisting of ERRs coupled with a metallic ground layer.

An understanding of the physical processes underlying the electromagnetic characteristics of bulk metals and structured photonic materials at wavelengths ranging from optical to far IR (FIR) has been essential in developing the new photonic materials that are presented in this Thesis. This has been particularly true when designing hybrid plasmonic and MM components, as care had to be given to ensure that each structured component did not adversely impact the resonant characteristics of the other.

4. Methods

This Chapter briefly describes the simulation, fabrication and characterisation methods used to design and engineer the structured photonic materials that are presented in this Thesis. An overview of the finite-difference time-domain (FDTD) method is provided in the first section, followed by further discussion on Lumerical FDTD Solutions simulation software, which was used to design and optimise the plasmonic and metamaterial structures prior to fabrication. The optical components were fabricated in the University of Glasgow's James Watt Nanofabrication Centre using the micro and nanofabrication techniques described in the second section. The final section outlines the spectroscopic measurement techniques that were used to characterise the fabricated materials.

4.1 Finite-Difference Time-Domain (FDTD)

Finite-difference time-domain (FDTD) is a method of numerically solving the Maxwell curl equations, given by equations (3.3) and (3.4), by using finite-difference (FD) approximations and proceeding to calculate the fields in incremental time steps through a spatially discretised mesh, or grid [223–225]. FDTD is a fast and reliable technique for determining the optical properties of resonant structured photonic materials, such as plasmonic filters and metamaterials (MM), and is therefore an invaluable tool in designing and optimising structures prior to fabrication.

The foundations of the FDTD method can be attributed to a paper by Yee in 1966 [223]. The Yee cell, illustrating the position of the electric and magnetic field components on a discretised spatial grid, is shown in Figure 4.1. The cell dimensions in x, y and z are given by Δx, Δy and Δz, respectively, and correspond to the spatial increments. The electric field components are in the centre of the cell edges, and the magnetic field components are centred in the cube faces. This corresponds to half integer separation between the different components. The time increment is given by Δt.

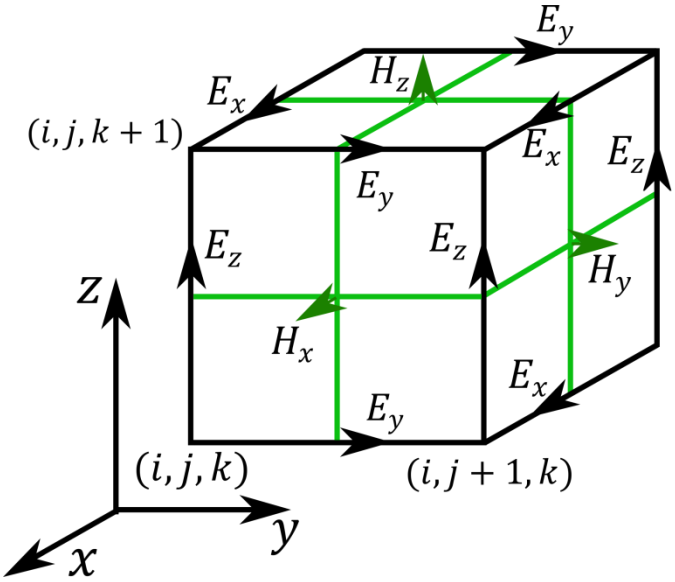

Figure 4.1 Illustration of the Yee cell used in the finite-difference time-domain method (FDTD) [223].

Maxwell's curl equations, shown in Chapter 3 as equations (3.3) and (3.4), can be rewritten as six coupled partial differential equations for a three dimensional coordinate system. These equations relate the different electric and magnetic field components to each other. The x component of the magnetic field, H_x, is related to the y and z components of the electric field by:

$$\frac{\partial H_x}{\partial t} = -\frac{1}{\mu}\left(\frac{\partial E_z}{\partial y} - \frac{\partial E_y}{\partial z}\right) \tag{4.1}$$

where all symbols have their usual meaning. The FD equation from equation (4.1) is given by:

$$\frac{H_x^{n+\frac{1}{2}}(i,j,k) - H_x^{n-\frac{1}{2}}(i,j,k)}{\Delta t} = -\frac{1}{\mu(i,j,k)}\left(\frac{E_z^n\left(i,j+\frac{1}{2},k\right) - E_z^n\left(i,j-\frac{1}{2},k\right)}{\Delta y} - \frac{E_y^n\left(i,j,k+\frac{1}{2}\right) - E_y^n\left(i,j,k-\frac{1}{2}\right)}{\Delta z}\right) \tag{4.2}$$

where, i, j and k denote the integers associated with x, y and z, respectively, and n is the integer associated with the time dimension. Equation (4.2) can be rearranged to give:

$$H_x^{n+\frac{1}{2}}(i,j,k) = H_x^{n-\frac{1}{2}}(i,j,k) - \frac{\Delta t}{\mu(i,j,k)}\left(\frac{E_z^n\left(i,j+\frac{1}{2},k\right) - E_z^n\left(i,j-\frac{1}{2},k\right)}{\Delta y} - \frac{E_y^n\left(i,j,k+\frac{1}{2}\right) - E_y^n\left(i,j,k-\frac{1}{2}\right)}{\Delta z}\right) \quad (4.3)$$

From equation (4.3) it can be seen that it is possible to calculate H_x at time step $n + 1/2$ by using H_x at time step $n - 1/2$, and the electric field components of the neighbouring cells at time step *n*. Applying the FD approximation to the five other partial differentials derived from Maxwell's curl equations yields equations of similar form for determining the five other field components. Consequently, this technique is the foundation for the FDTD method. The fields are calculated in a leapfrog manner, where the magnetic field components are determined for a point in time, followed by the calculation of the electric field at the next point in time, and then repeated [223–225].

4.1.1 Lumerical FDTD Solutions

All electromagnetic simulations presented in this Thesis were performed using Lumerical FDTD Solutions [226,227]. Simulations were prepared using a graphical computer aided design (CAD) environment where 3D structures can be built, simulated, and the results analysed. It should be noted that the features described here are not all exclusive to Lumerical FDTD Solutions, however in this case they benefit from being described in the context of the simulation software.

The optical structure to be simulated is built within the simulation region and can consist of a range of different materials. The materials can be defined using complex refractive index or complex permittivity data over a wavelength range, thereby incorporating dispersive media into the simulation. Lumerical FDTD Solutions contains a database of materials from a range of different sources, however it is also possible to import user-defined material parameters. Unique materials such as "etch", corresponding to a material with parameters matching the vacuum, and a perfect electric conductor (PEC), are also available.

The simulation is performed within the FDTD region. It is bounded by different boundary conditions that will depend on the features of the structure to be simulated and the type of simulation being performed. Perfectly matched layer (PML) boundaries are designed to be

perfectly absorbing to incident light. This ensures no light is reflected back into the simulation region, which could lead to erroneous simulation results. Periodic boundary conditions extend the structure infinitely out with the boundary and can be used to limit simulation time for large structures consisting of a repeated unit cells. Simulation time can be further reduced by using symmetric and anti-symmetric boundary conditions when the structure exhibits symmetry. Beyond the symmetric regions the structure is repeated periodically. Bloch boundary conditions act like periodic boundary conditions and can be used when a phase shift arises between unit cells, such as in angled simulations. The simulation mesh splits the simulation region into a grid consisting of cells of finite volume. This is necessary for the FDTD simulation as described in Section 4.1. It is important to ensure that the mesh size is sufficiently small to define any geometric structures in the simulation, and also large enough to ensure that the simulation time is sufficiently short. The mesh accuracy can be set within the simulation region on a scale ranging from 1 to 8, where 1 is the lowest accuracy and 8 is the highest accuracy. It is also possible to define a mesh override region where the maximum mesh cell sizes can be defined by the user.

In all simulations presented in this Thesis, a broadband plane wave source has been used to investigate the characteristics of structured photonic materials over a range of wavelengths. It is also possible to alter the polarisation and incident angle of the plane wave source. The outputs of the simulation are controlled by using monitors to extract the desired information. As the FDTD method is used to calculate field data in the time domain it is necessary to perform a Fourier transform (FT) to convert the field data to the frequency domain. A frequency-domain field monitor is used to collect the field data and to perform the FT that is required to determine the reflection and transmission spectra for a simulated structure.

Lumerical FDTD Solutions offers a simple interface for visualising the data that is collected by the monitors. It is also possible to use the in-built scripting language to undertake more complex analysis, or to extract the data and use an alternative software package such as Matlab or Microsoft Office Excel for analysis and further processing. To simplify and automate the simulation procedure a script was written to sequentially run simulations stored in a folder and then export the results. The simulation results were plotted and saved as JPEG images, and the exported data was saved in a comma separated values (CSV) format, which could easily be imported into other software packages. A schematic outlining the automated simulation procedure is shown in Figure 4.2.

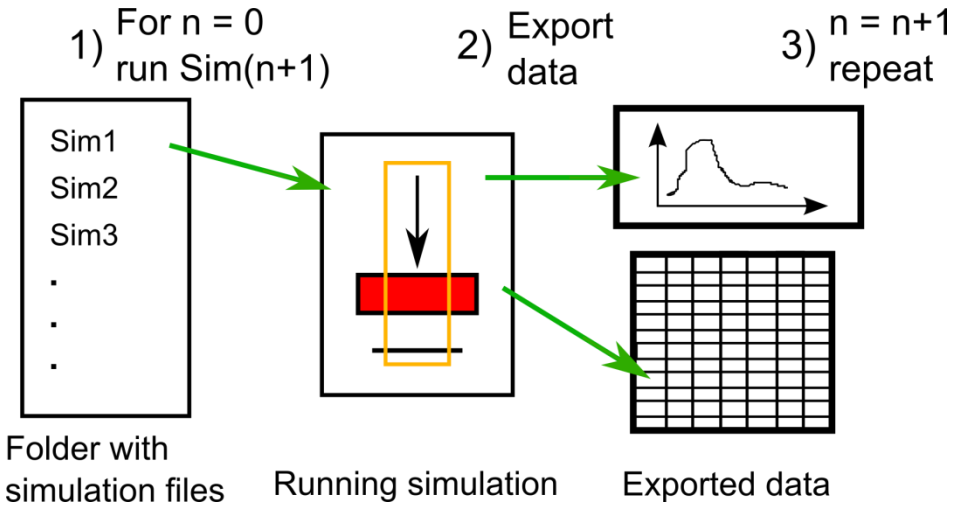

Figure 4.2 Process flow describing the automated simulation script written for Lumerical FDTD Solutions. 1) Select simulation file in folder to open and run. 2) Export simulation results from completed simulation. 3) Restart process for next simulation file on the list and repeat until all simulations have been completed.

4.1.1.1 S Parameter Extraction

The effective electromagnetic parameters of MMs can be extracted using the S Parameter Analysis tool [227], which follows the method outlined in Chapter 3. The S Parameter tool includes the relevant source and monitors in addition to a script for calculating and exporting the effective parameters. The simulation region is required to be sufficiently large to avoid evanescent fields being detected at the monitors. Consequently, it is necessary to account for variation in phase as the fields propagate from the MM surface to the monitors. This correction is included in the S parameter script, such that the complex transmission and reflection coefficients are altered to be as they were measured at the MM interfaces.

Equations (3.55) and (3.56), corresponding to the effective refractive index and effective wave impedance, respectively, each contain two solutions and therefore certain conditions must be imposed to determine which set of roots is correct for a given MM. In the case of the refractive index the root is chosen that results in an imaginary component greater than zero, and in the case of the wave impedance, a root is chosen that results in a real component that is greater than zero [111]. These conditions are imposed by the script prior to calculation of the effective permittivity and effective permeability.

4.1.1.2 Angled Simulations

Simulating a structure at different angles of incidence requires the use of Bloch boundary conditions, as opposed to the conventional periodic boundary conditions. Bloch boundary conditions account for the phase variation between different unit cells of a periodic structure that arise when light is incident at an angle. For broadband plane wave sources at

an angle, the angle of incidence varies as a function of wavelength. Consequently, angled simulations are often only performed for a single frequency point, however a script is available that can perform broadband angled simulations by running a series of simulations at different angles, and interpolating the data such that the spectrum for each angle can be extracted [227].

4.2 Micro/Nanofabrication

All structures presented in this Thesis were fabricated using the equipment that was available in the James Watt Nanofabrication Centre (JWNC). Detailed fabrication process flows will be outlined in the subsequent Chapters, however here an overview will be given of some of the key techniques used to fabricate the structured photonic materials presented in this work. Fabrication was carried out using typical semiconductor fabrication processes and therefore commercial integration of structured photonic materials with complementary metal-oxide semiconductor (CMOS) technology could be possible.

4.2.1 Metallisation

Thin film metallisation was performed using physical-vapour deposition (PVD) methods to construct the devices presented in this Thesis [3]. Electron beam evaporation was used solely for device fabrication, prior to dry etch or lift off processing, and sputtering was occasionally used to coat structures to improve contrast for scanning electron microscopy (SEM) by eliminating charging of dielectric layers.

Metal evaporation was mainly undertaken using a Plassys MEB 550S Electron Beam Evaporator, however a Plassys MEB 400S Electron Beam Evaporator was used when the former machine was unavailable [228]. Electron beam evaporation operates under vacuum, where an electron beam is used to heat metal to the point where it melts and evaporation occurs. The evaporated metal can then pass unimpeded through the vacuum chamber until it reaches the substrate where it condenses and gradually builds up a film to the required thickness. The devices that are presented in this Thesis are typically composed of patterned aluminium films, which were evaporated on to the sample surface prior to lift off or dry etching. Gold was used to fabricate electron beam lithography (EBL) alignment markers. Due to poor adhesion of gold to substrate surfaces, a thin layer of titanium was required as an intermediate layer to improve adhesion.

An ion beam sputtering tool was occasionally used to sputter coat samples prior to imaging in the SEM. Argon gas is used to fill the chamber, and then ionised plasma is formed between two electrodes. Argon ions then strike a palladium/gold target, and the palladium

and gold atoms are ejected and coat the sample. As this technique for improving contrast in imaging is destructive with regards to the optical devices developed in this work, it was used infrequently and only for diagnostic purposes when necessary.

4.2.2 Dielectric Deposition

The dielectric layers of the structured photonic materials presented in this Thesis were deposited using chemical vapour deposition techniques, namely: plasma enhanced chemical vapour deposition (PECVD), for the deposition of silicon dioxide layers, and inductively coupled plasma chemical vapour deposition (ICP-CVD), for the deposition of silicon nitride layers. Silicon dioxide deposition was carried out using an Oxford Instruments PECVD 80+ and silicon nitride deposition was carried out using an Oxford Instruments System 100 ICP 180 PECVD [228].

A PECVD system is composed of two parallel plate electrodes placed horizontally within a vacuum chamber. The bottom electrode is grounded and holds the sample to be coated with the dielectric material. It is also heated to a temperature of 300 ºC for deposition of silicon dioxide during fabrication of the devices presented in this Thesis. Gases are flown into the reaction chamber and a radio frequency (RF) voltage is applied to the top electrode, resulting in the formation of a plasma between the electrodes, which is used to grow the dielectric film [3]. ICP-CVD uses electromagnetic induction to form a high density plasma that allows deposition of dielectric materials at lower temperatures than PECVD and with improved material quality [229,230].

4.2.3 Lithography

Lithography describes the method used to draw patterns or shapes into a radiation sensitive material that can be used to mask certain regions of a substrate or surface to allow selective processing of the underlying material. The mask material is known as resist and can be removed after processing, typically by solvent cleaning. The lithographic method employed to fabricate the structured photonic materials outlined in this Thesis has predominantly been EBL, however photolithography has also been employed for the fabrication of a number of devices. Each technique offers its own set of advantages and disadvantages, which will be explored further in this Section. When determining the most appropriate lithographic method for a given task, consideration must be given to a range of parameters such as: the required resolution of lithographic features; alignment accuracy between different layers, also known as registration; and throughput, which refers to the processing rate of devices patterned using the lithographic technique [3]. Upon completion

of lithographic patterning, further processing is typically carried out on the sample including dry and wet etching to selectively remove material, and metallisation followed by lift off to selectively place material on the substrate or lower surface material. These processes will be further explored in the subsequent Sections.

4.2.3.1 Photolithography

Photolithography uses light at ultraviolet (UV) wavelengths to expose a light sensitive resist, known as photoresist. Photolithographic exposure for processing of the devices presented in this Thesis was performed using a Suss Microtec Mask Aligner 6 (MA6) photolithography tool with a 350 W mercury lamp source [228]. The mercury lamp exhibits well-defined spectral peaks at UV wavelengths. The photolithography process using the MA6 tool uses a shadow printing technique and is described as follows [3].

A sample is spin coated with photoresist; in the case of the structured materials fabricated in this Thesis, AZ4562 photoresist was used. The photomask with the pattern to be transferred is loaded in to the MA6 along with the sample. The photomask pattern is composed of transparent and opaque regions such that UV light can pass through the transparent regions and expose the photoresist on the sample. The sample and photomask are placed into contact and the photoresist is exposed using the mercury source, thereby transferring the pattern on the photomask into the resist.

For positive resists, such as AZ4562, the exposed regions change chemical structure and become soluble to a solution known as a developer. The unexposed regions remain insoluble such that after development the left-over resist forms the pattern. For negative resists, the inverse is true and the exposed region becomes less soluble, and the unexposed region is removed during development. The resist profiles for both positive and negative resists after exposure and development are illustrated in Figure 4.3. It is also possible to have a gap between the mask and the resist, which known as proximity printing as opposed to contact printing. This method can avoid issues of dust damaging the mask when brought into contact with the photoresist at the expense of a decreased resolution due to diffraction effects.

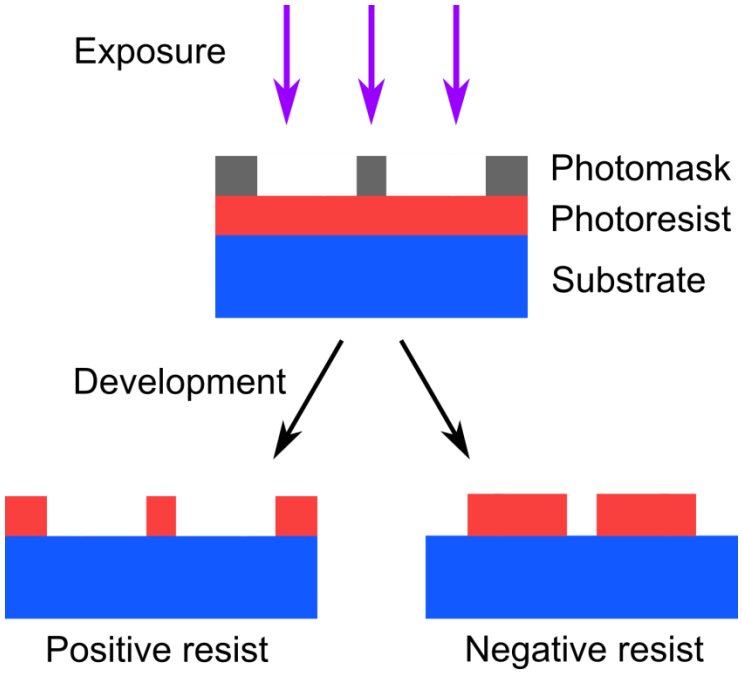

Figure 4.3 Illustration of the positive and negative photoresist profiles after exposure and development.

Photomasks are fabricated using EBL and subsequent processing, to define pattern features in a chromium film on a fused silica substrate. The photomask can be reused, therefore making photolithography a low cost and high throughput technology which is dominant in the mass production of semiconductor technology. The resolution of a photolithography system is limited by the wavelength of light and therefore it is challenging to create features on a scale that is less than 1 μm without using resolution enhancement methods or considering different lithographic techniques [3]. The requirement to fabricate new photomasks for any new patterns also means that it is not simple to frequently change patterns between samples, as was required for the development of the optical devices presented in this Thesis.

4.2.3.2 Electron Beam Lithography

The JWNC is equipped with a Vistec VB6 EBL tool [228]. EBL uses a direct write method, where a beam of electrons are focussed on to electron sensitive resist and used to draw the required shapes and patterns. This process eliminates the requirement for a photomask and results in increased flexibility in changing pattern designs between samples. Electron beam resists are polymers and exhibit similar properties to the photoresists described previously, however in this case, the resist is sensitive to electrons as opposed to optical radiation [3]. The electron beam resists used to fabricate the devices presented in this Thesis are poly(methyl methacrylate) (PMMA) and ZEP520A. A schematic of the EBL system is shown in Figure 4.4 [3,231].

In the VB6, the electron beam is generated in the electron gun using thermal field emission of electrons from a heated zirconium oxide coated tungsten cathode. The suppressor electrode is used to ensure that only electrons generated at the cathode tip are emitted. A large electric field is formed between the extractor and the tip, and electrons are accelerated from the cathode surface. The focussing electrode is used to control beam focussing. The alignment of the beam is then controlled using magnetic fields generated by deflection coils. Apertures are used to limit the divergence of the electron beam throughout the column and a series of lenses are used to focus the beam on the substrate. The electrostatic lens and the first magnetic condenser lens are used to maintain a constant current density and beam focus at the sample surface whilst the diameter of the beam can be controlled. The second magnetic condenser lens focusses the electron beam on to the sample at the bottom of the column. Blanking plates are used to turn the beam off by deflecting it away from the optical axis.

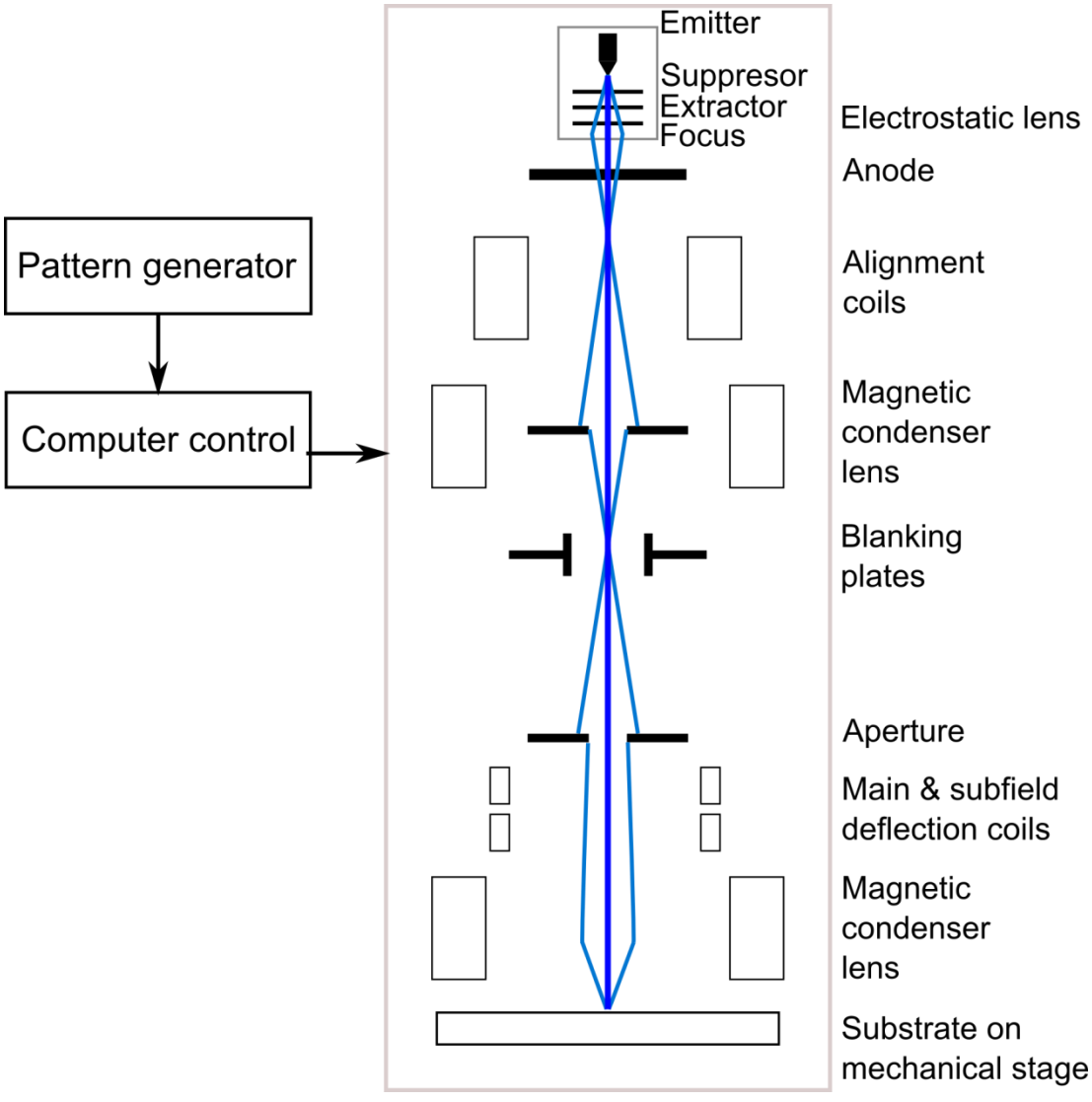

Figure 4.4 Schematic of the electron beam lithography (EBL) tool [3,231].

It is possible to pattern the resist with the electron beam using either raster or vector scanning methods. Raster scanning is the process of scanning the beam over the whole sample surface and turning the beam off or on depending on whether or not a given region is to be patterned. Vector scanning methods only scan the beam over regions where the resist is to be exposed and therefore can save a significant amount of processing time [3]. The Vistec VB6 uses the vector scanning method.

Tanner L-Edit CAD software is used to draw the structures and patterns to be drawn on to the resist using the EBL tool. Upon completion of the design, the file is then exported in the GDSII file format and fractured using Beamer before being transferred to the EBL tool [232]. Fracturing separates the patterns into rectangles and trapezoids, which are necessary for patterning with the EBL tool. Fracturing also separates the pattern into main fields and sub fields. The sample surface is divided into main fields which are accessed by mechanical movement of the sample stage. The main fields are divided into smaller subfields which are accessed using the main deflection coils and the beam is controlled within each subfield using the subfield deflection coils to expose the resist and write the rectangle and trapezoid shapes that compose the pattern. The layout of the fractured patterns on the substrate are set using Belle software [233], prior to patterning of the resist.

In addition to the shapes to be patterned, it is necessary to set other parameters in the software to control the EBL process [232]. These include beam spot size, resolution and variable resolution unit (VRU). To write the pattern, the electron beam exposes a point on a grid, then moves on to the next point, until the shape is completed. The beam step size, associated with the previously mentioned parameters, is illustrated in Figure 4.5 and is given by equation (4.4).

$$\text{Beam step size} = \text{VRU} \times \text{resolution} \tag{4.4}$$

It is also possible to control the dose of the electron beam incident on the resist surface. Dose is given in terms of micro Coulombs per square centimetre ($\mu C/cm^2$). It is often necessary to perform a dose test by creating small test samples over a range of different doses when fabricating new structures, as various aspects such as feature size and resist type can impact the required exposure dose.

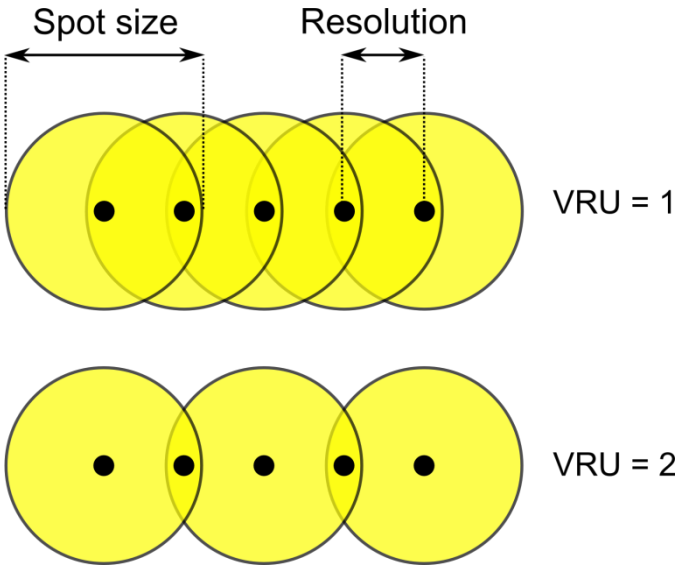

Figure 4.5 Illustration of beam step size for variable resolution unit, VRU = 1 and VRU = 2 [232].

EBL offers a substantial improvement in attainable resolution when compared with photolithography, which is essential for the fabrication of most of the structured photonic materials presented in this Thesis. The lack of a photomask in EBL means that it is simple to redesign structures between different samples without having a requirement to fabricate new photomasks for each new design. However, EBL can be significantly slower and more expensive than photolithography. It is therefore often necessary to compromise on certain features, such as total surface area to be patterned, in order to ensure writing can be completed in a reasonable time.

4.2.4 Dry Etch

In the work presented in this Thesis, materials were etched using reactive ion etching (RIE) methods. Aluminium was etched using silicon tetrachloride ($SiCl_4$) in an Oxford Instruments RIE100 tool. Silicon nitride and silicon dioxide were etched in an Oxford Instruments RIE80+ tool using trifluoromethane/oxygen (CHF_3/O_2) and trifluoromethane/argon (CHF_3/Ar), respectively. Silicon nitride etching was occasionally carried out in a BP80 RIE when the RIE80+ tool was unavailable. Silicon etching was performed using octafluorocyclobutane/sulphur hexafluoride/oxygen ($C_4F_8/SF_6/O_2$) in a STS ICP RIE tool. Oxygen (O_2) plasma was used to ash samples after development of resist and also used at a higher power to remove resists at the end of processing. This was carried out in either the Oxford Instruments RIE80+, the BP80 RIE or, more commonly, a Gala Instruments Plasmaprep 5 Barrel Asher [228].

RIE uses ionised plasma to selectively remove material from a sample surface. The regions to be etched can controlled by using a dry etch resistant resist which has been patterned

using photolithography or EBL. A typical RIE system consists of parallel-plate electrodes within a vacuum chamber, where the lower electrode holds the sample to be etched. Gas is flown into the chamber, the top electrode is grounded and the lower capacitively coupled electrode is used to apply a RF signal and ionise the gas. This is illustrated in Figure 4.6. The greater mobility of electrons, compared with ions, results in the lower electrode becoming negatively charged which leads to physical sputtering of the sample surface by positive ions. Selectivity of etching is improved by choosing the correct gases to form the plasma with respect to the material to be etched, thereby exploiting appropriate etch chemistries. In chemical etching, a reaction occurs between the ions and the material surface allowing it to be removed and diffused into the surrounding gas [3,234]. A typical process flow for dry etching is illustrated in Figure 4.7. It is desirable to use a resist with high dry etch resistance and consideration must be given to resist thickness with regards to the thickness of material that is to be etched. Unlike wet etching, which is typically isotropic resulting in undercut of the etched material, dry etch methods can yield anisotropic etch profiles [3].

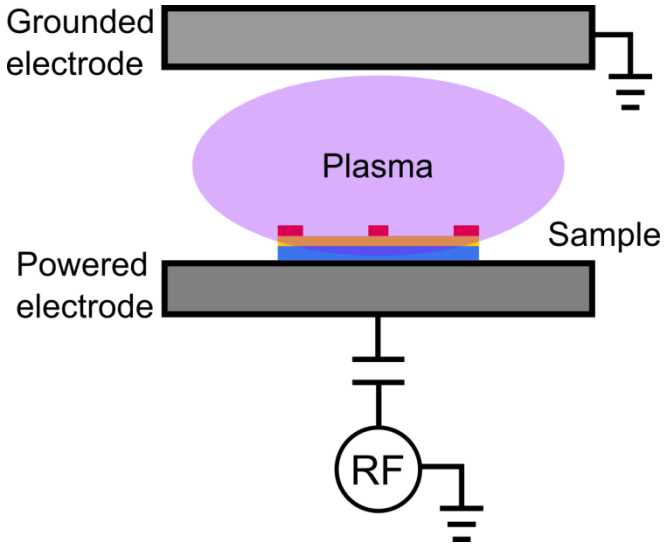

Figure 4.6 Schematic of a reactive ion etching (RIE) tool [234].

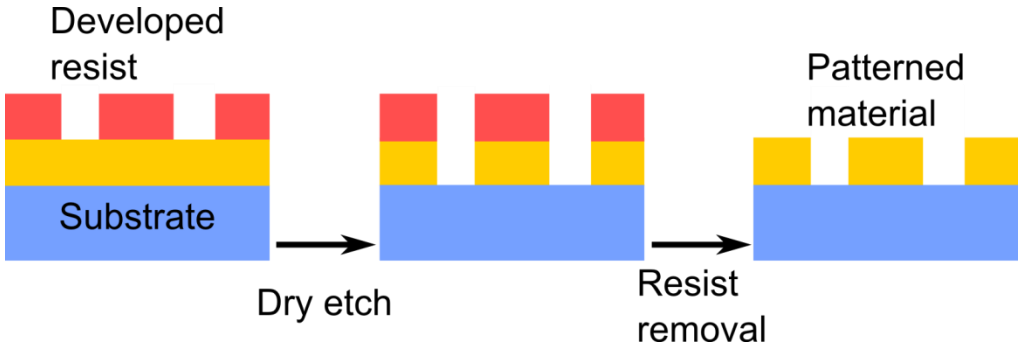

Figure 4.7 Dry etch process flow. After resist development, the sample undergoes reactive ion etching (RIE). The resist can then be removed, leaving the patterned material on the substrate.

4.2.5 Lift Off

Lift off is an alternative method of pattern transfer. In this case, the material is deposited over the surface of developed resist, and then the surplus resist is removed to leave the desired pattern on the substrate [3]. It is also possible to use a bilayer of resist, where the top layer is less sensitive to the incident electron beam dose than the bottom layer. After development, there would be an overhang, which would ensure discontinuity between the material deposited on the resist and on the substrate. This can overcome problems associated with a non-vertical resist profile, or material being deposited on the resist sidewalls. It is possible to create an overhanging resist profile by using different concentrations of PMMA for each layer. The lift off process using a bilayer of resist is illustrated in Figure 4.8.

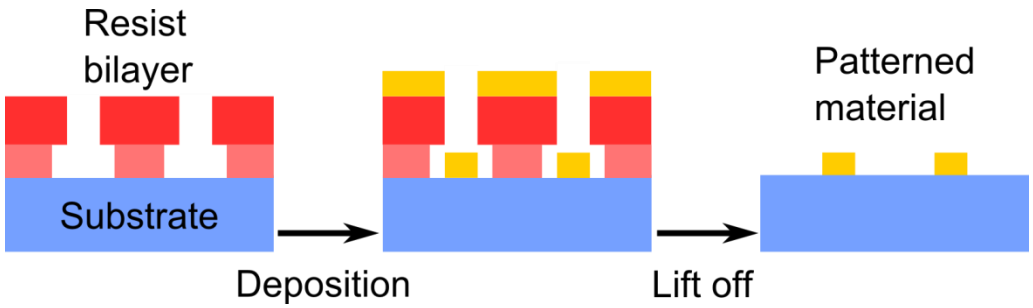

Figure 4.8 Lift off process flow. After development of the resist bilayer, material is deposited on the sample surface. The resist and surplus material is then removed to leave the patterned material on the substrate.

4.3 Spectral Characterisation

Optical characterisation of the structured photonic materials presented in this Thesis was undertaken using two different techniques: microspectrophotometry and Fourier Transform Infrared Spectroscopy (FTIR). The requirement for multiple measurement methods is due to the large spectral range of operation covered by the plasmonic, MM and hybrid structures. Optical and near infrared (NIR) plasmonic filters were characterised using a microspectrophotometer whereas the longer wavelength plasmonic filters and MM structures were characterised using two FTIRs. The hybrid structures required the use of both techniques to fully characterise the materials.

4.3.1 Microspectrophotometry

An Angstrom Sun Technologies TFProbe MSP300 microspectrophotometer [235] was used to measure the transmission spectra of the optical and NIR plasmonic filters in the spectral region from 400 nm to 1 µm. It consists of a microscope, capable of operation in transmission or reflection mode, combined with dispersive optics and a CCD detector for

spectral measurement. In transmission mode, the plasmonic filters are illuminated from below using an unpolarised white light halogen lamp source. The light is collected through a 4x magnification objective lens with a spot size of 100 µm. A dispersive element is then used to separate the light into its constituent colours which are detected by the sensor.

Transmission measurements are performed by first acquiring a measurement of the spectrum from the white light source. The spectrum is then measured when no light is incident on the sensor, to acquire a measure of the dark current. After these initial calibration steps are complete, the filter is placed on the microscope stage and aligned using the camera. The transmission spectrum from the filter can then be acquired, and the dark background elimination and white light normalisation steps are carried out in software. The normalised transmission spectrum is displayed after acquisition and can be exported for further analysis.

4.3.2 Fourier Transform Infrared Spectroscopy

A FTIR spectrometer contains a Michelson interferometer, consisting of a source, a beamsplitter, mirrors and a detector [236,237]. A schematic of a FTIR is shown in Figure 4.9. The beamsplitter reflects half of the light to Mirror 1 and transmits the other half to Mirror 2. Initially the distance between the beamsplitter surface and each of the mirrors is given by *d*, such that the light reflected from each mirror has the same optical path length. This results in constructive interference, and peak intensity is measured at the detector. The position of Mirror 2 is varied by a distance, *x*, resulting in a change in path length of the light that is transmitted to Mirror 2. The optical path difference results in a difference in phase between the two light beams, which results in a decrease in the intensity of the recombined beam. The resulting interference pattern at the detector can be represented by the measured intensity as a function of mirror position. This is known as the interferogram. A FT is then performed on the interferogram to yield the intensity as a function of the wavenumber, which can simply be converted to frequency or wavelength, depending on the preferred units for a given application. A sample placed in the optical path will result in an interferogram that is dependent on the optical properties of the sample. In the case of a transmission measurement, normalisation of the measured sample spectrum to the measured spectrum when no obstruction is present would yield the transmission spectrum of the sample.

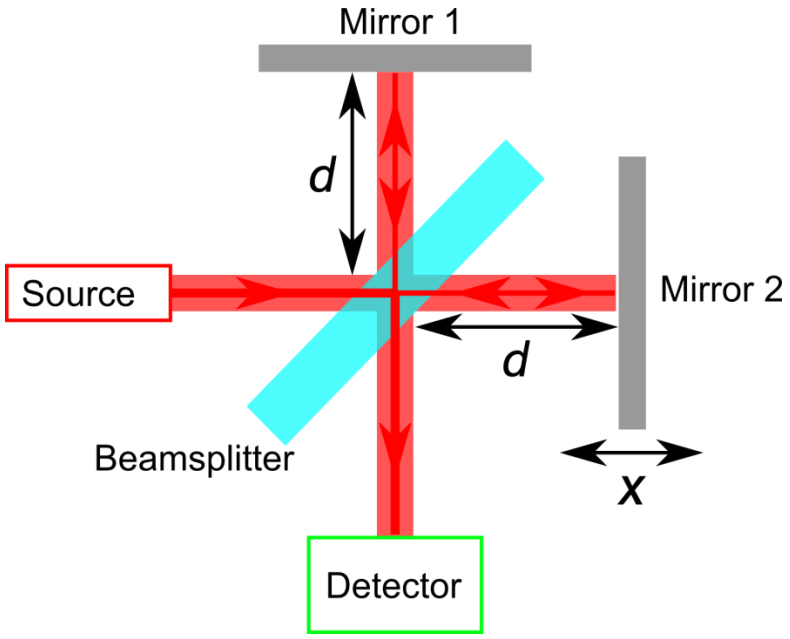

Figure 4.9 Illustration of a Michelson interferometer, which is used in a Fourier Transform Infrared (FTIR) Spectrometer [237].

Infrared (IR) plasmonic filter transmission spectra were measured using a Bruker Vertex 70 FTIR with a tungsten source, calcium fluoride beamsplitter and liquid nitrogen cooled indium antimonide detector in the range from 1 µm to 5 µm. The transmission measurements were normalised to a 2 mm diameter circular window aperture in an opaque mask material illuminated using the IR source. The source aperture had a 0.25 mm diameter. Characterisation of the terahertz (THz) MM components were performed using a Bruker IFS 66v/S FTIR with a mercury source, Mylar beamsplitter and a deuterated, L-alanine-doped triglycine sulfate (DLaTGS) detector. THz measurements were within the range of 1 THz to 9 THz. Transmission measurements were normalised to a mask with a 7 mm diameter circular window that was illuminated using the mercury source. The source aperture in this case was 12 mm. Reflection measurements were carried out at 30º incidence with a 10 mm diameter circular aperture and 4 mm source aperture. The reflection spectrum of the MM was normalised to that of a gold mirror.

4.4 Summary

This Chapter has provided an overview of the techniques underlying the design, fabrication and characterisation of the structured photonic materials that are presented in this Thesis. A brief description of the FDTD technique has been outlined with a focus on the simulation software: Lumerical FDTD Solutions. All devices presented in this Thesis have been simulated using Lumerical FDTD Solutions and it has been an essential tool in the design and optimisation of the optical materials. The fabrication techniques employed to make the devices presented in this work have also been outlined in this Chapter. Similar processing steps were used for plasmonic and MM structures, as a means of ensuring both devices shared common materials to simplify the fabrication of hybrid, multi-spectral structures. However there are some variations in processing, which is mainly due to the relative size scales of the plasmonic materials compared with the MM components. Further detail on the specifics of the fabrication processes for individual devices will be explored in subsequent Chapters. Both microspectrophotometry and FTIR spectroscopy have been described. Two unique measurement methods were necessary to fully characterise the structured photonic materials that are presented in this work. The remainder of this Thesis will demonstrate how these tools have been used to produce and characterise structured photonic materials and also how they have been employed to engineer new synthetic multi-spectral materials (SMM) operating from optical to far infrared (FIR) wavelengths.

5. Plasmonic Filters

In previous Chapters, the history of plasmonics, the discovery of extraordinary optical transmission and the physical theory underlying plasmonic devices has been described. The advantages of plasmonic filters for colour imaging and some of the recent advances in this area have also been discussed. In this Chapter the design, simulation, fabrication and characterisation of a 16 colour plasmonic filter set optimised for high narrowband transmission within the 400 nm to 1 μm range is presented. A simulation study has also been undertaken to investigate the impact of incident angle and hole size on the performance of plasmonic colour filters.

By scaling the hole size and the array period it is possible to create plasmonic filters that operate at infrared wavelengths, which is outside the spectral range where common metals such as aluminium are considered to be good plasmonic materials. The observed enhanced transmission at longer wavelengths is assisted by spoof surface plasmons, as has been discussed previously. The simulation, fabrication and characterisation of 8 infrared plasmonic filters, which are an extension of the earlier colour filter designs, are also presented in this Chapter. The optical and infrared plasmonic filters have been designed with hybridisation with terahertz metamaterials and integration with CMOS technology in mind, and consequently an attempt has been made to ensure the use of common processing and materials between different structures.

CMOS image sensors consist of an array of photodiodes that are sensitive to light across the visible band. Fabrication of different plasmonic colour filters above the photodiode array can make individual photodiodes sensitive to specific colour bands. By fabricating a suitable plasmonic colour filter array on the surface of a CMOS image sensor it should be possible to create a colour imager. Plasmonic colour filters offer advantages over conventional filtering materials for imaging applications, however there are challenges in integrating new materials with CMOS technology. In this Chapter, the fabrication processes for integrating plasmonic filters with two different CMOS chips, in addition to some early experimental results, are presented.

5.1 Optical and Near Infrared Plasmonic Filters

The plasmonic filters presented in this work were simulated using Lumerical FDTD Solutions, prior to fabrication. The optimised plasmonic filters consist of triangular hole arrays etched into an aluminium film that has been evaporated on to a glass substrate. A silicon dioxide cap layer was used to index match the top and bottom surfaces. 15 colour filters and a single near infrared (NIR) filter have been designed and fabricated by scaling the hole period and hole size linearly in accordance with equation (3.49). Some of the filters correspond approximately to the CIE 1931 standard observer colour matching functions (CMF), as presented in Chapter 2, and were used for complementary metal-oxide semiconductor (CMOS) integration in Section 5.3 and Section 5.4. The filter designs presented here also act as the basis for the design of the plasmonic filter component of synthetic multi-spectral materials (SMM) described in Chapter 7.

5.1.1 Design and Simulation

The electromagnetic simulations were prepared as follows: a broadband plane wave source in the range 400 nm to 1 μm was incident on a 150 nm aluminium surface that was sandwiched between a 200 nm silicon dioxide cap layer and semi-infinite silicon dioxide substrate. A transmission monitor was placed on the opposite side of the film. The aluminium film was perforated with two silicon dioxide cylindrical holes and the silicon dioxide cap layer was perforated with two corresponding etch holes to account for the non-uniform cap layer after deposition. A mesh override region was used in the vicinity of the metal film to set a maximum cell size of 5 nm in the x, y and z directions. Suitable mesh parameters were determined using convergence analysis. Anti-symmetric and symmetric boundary conditions were used in x and y, respectively, to form the periodic triangular array. Perfectly matched layers (PML) were used in the z direction. The aluminium and silicon dioxide "Palik" models were used to define the materials [238]. Other aluminium models are available, however the Palik model contains a large number of data points at optical and NIR wavelengths, which ensures accurate representation of the metal film in this wavelength range. Aluminium and silicon dioxide Palik models have also been employed previously in plasmonic filter simulations [11].

Schematics of the top-down view and cross section of a simulated plasmonic filter are shown in Figure 5.1(a) and Figure 5.1(b), respectively. The hole period is given by P and the hole diameter is given by d. The hole period and diameter of the 16 simulated filters are listed in Table 5.1. The transmission spectra from the 16 simulated filters are shown in Figure 5.2(a-c).

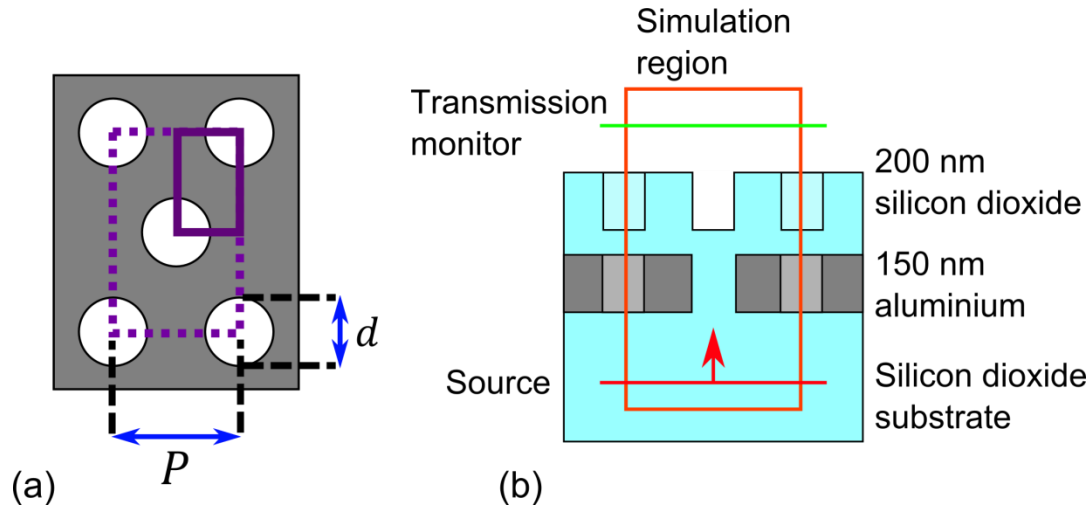

Figure 5.1 Schematic of the simulated plasmonic filter structure. (a) Top-down view of the plasmonic filter. The simulated region is enclosed by the solid purple box and the broken line encloses the unit cell of the triangular hole array structure. *P* denotes the array period and *d* denotes the hole diameter. (b) Cross section of the simulated plasmonic filter. The orange box encloses the simulated unit cell.

Period, *P* (nm)	Diameter, *d* (nm)	Period, *P* (nm)	Diameter, *d* (nm)
230	130	340	185
250	140	350	190
260	145	370	200
270	150	380	205
290	160	390	210
300	165	410	220
310	170	430	230
330	180	550	290

Table 5.1 Array period and hole diameter for the 16 colour plasmonic filter set.

It can be observed from the simulation results presented in Figure 5.2 that scaling the array period from 230 nm to 550 nm yields a filter set operating throughout the visible band and up to NIR wavelengths. As the peak wavelength of the filter rises, it can be seen that there is a decrease in transmission and broadening of the peak. It is possible that this can be attributed to increased losses within the aluminium, as illustrated by the ratio of the real and imaginary components of the permittivity shown in Figure 3.2(a) in Chapter 3.

The simulations were modified by replacing either the symmetric or anti-symmetric boundary conditions, depending on the orientation of the source, with Bloch boundary conditions to allow angled simulations to be performed. The broadband angled simulation method, as described in Chapter 4, was used to simulate the plasmonic filter structure in the incident angle range from 0º to 30º from 400 nm to 1 µm. A total of 30 simulations

were performed over this range. The mesh override was altered to have a maximum cell size of 10 nm in x and y to reduce simulation time due to the number of required simulations in each sweep. Two plane wave orientations were simulated: the first corresponded to the electric field vector parallel (0º) to the array period, P, shown in Figure 5.1, and the second corresponded to the electric field vector perpendicular (90º) to the array period, P. The simulated transmission spectra for plasmonic filters corresponding to different angles of incidence are shown in Figure 5.3. Transverse electric (TE) and transverse magnetic (TM) polarisations for two plane wave orientations, for blue, green and red filters, corresponding to hole periods of 250 nm, 330 nm and 430 nm, respectively, were simulated.

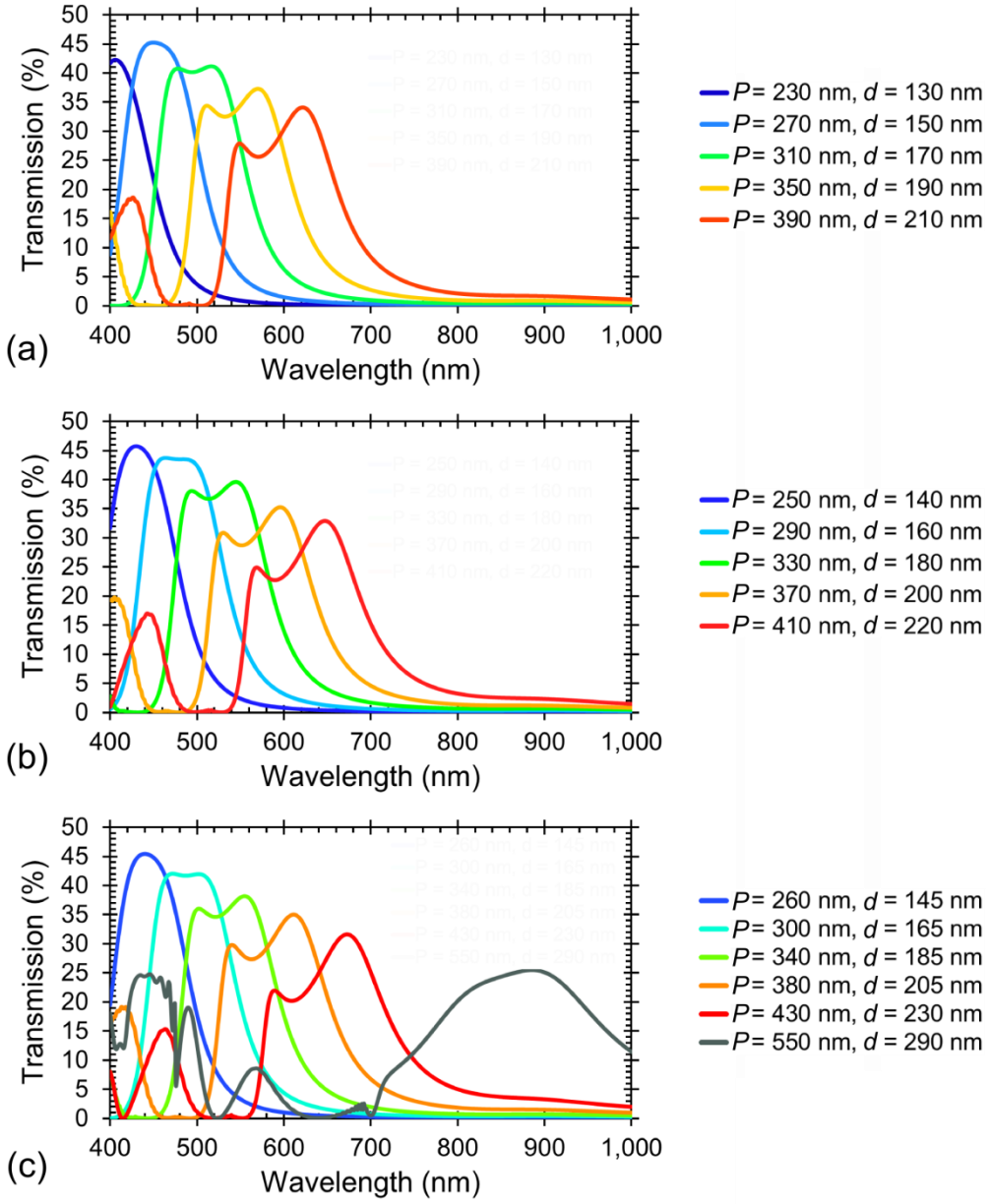

Figure 5.2 Simulation results for the 16 colour plasmonic filter set. The individual filter transmission spectra are shown in (a-c). The legend denotes the hole period, P, and the hole diameter, d.

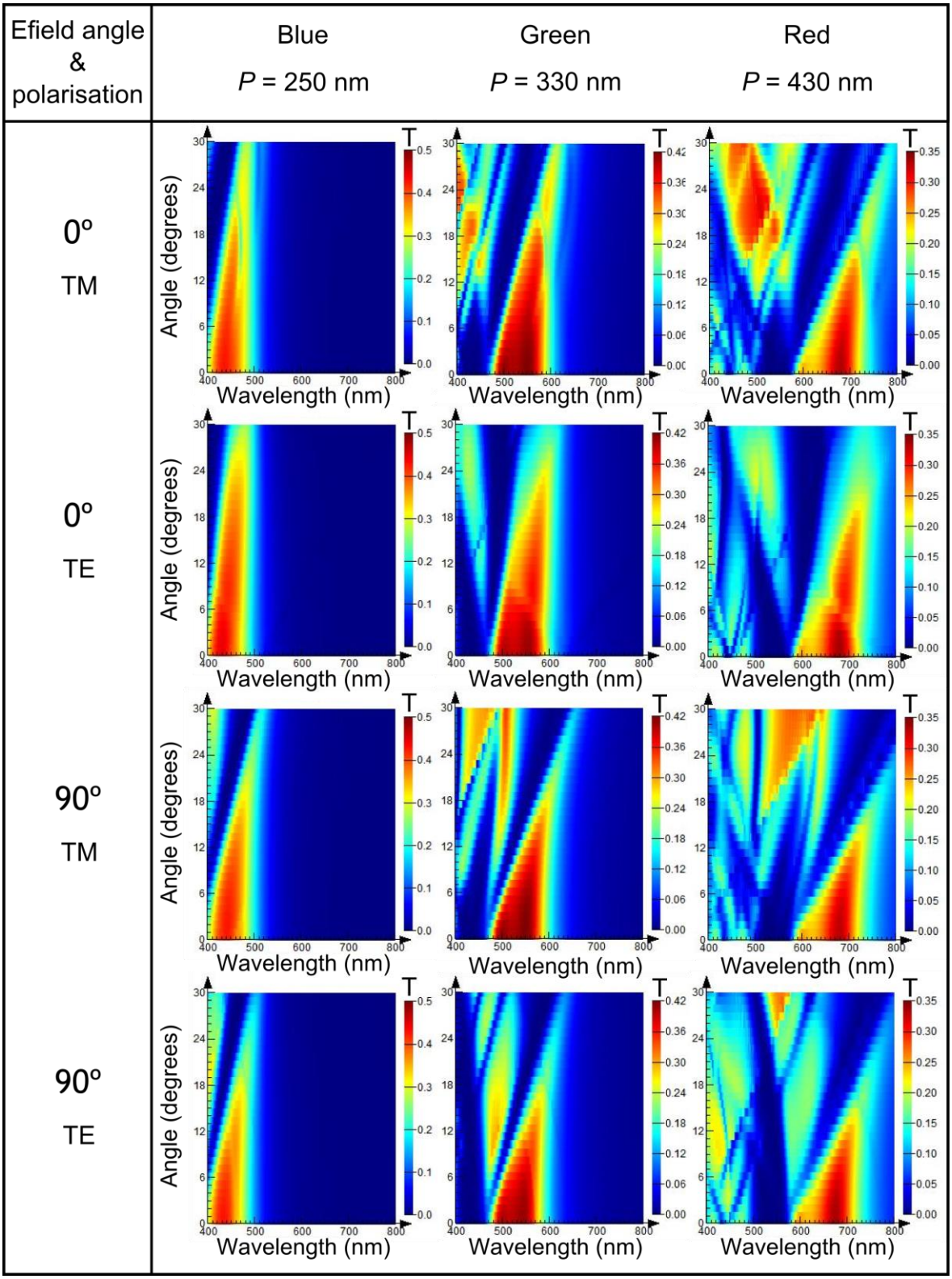

Figure 5.3 Transmission spectra for plasmonic filters as a function of incident angle for different electric field orientations and transverse magnetic (TM) and transverse electric (TE) polarisations. Results are shown for blue, green and red filters, corresponding to hole periods of 250 nm, 330 nm and 430 nm, respectively.

It can be observed from Figure 5.3 that the plasmonic filters exhibit an angular dependence in their transmission characteristics, as expected from equation (3.44). At steeper incident angles the transmission decreases and the peak wavelength becomes redshifted. Additional shorter wavelength peaks also appear. Consideration must be given to the angular dependence of plasmonic filters if they are to be integrated with an imaging system, as focussing optics would lead to light detection at non-normal incidence. The range of incident angles, and therefore the impact on colour reproduction, can be determined by considering the f-number of the lens, as was investigated by Burgos *et. al.* [11]. For sufficiently high f-numbers, the incident light is approximately collimated and therefore the plasmonic filters can be considered to be operating close to normal incidence. As the f-number decreases, the maximum angle of incidence at the filter increases. This has an impact on the plasmonic filter transmission spectra in accordance with what is shown in Figure 5.3, and consequently will lead to variations in colour reproduction for different f-numbers. For a given f-number, light is collected from normal incidence up to the maximum angle associated with the lens, and therefore consideration must be given to the entire range of incident angles and not just the maximum angle. Burgos *et. al.* demonstrated that the transmission spectrum of a plasmonic filter used in an imaging system can be estimated by averaging the transmission spectra over the different polarisations and over the range of incident angles associated with the f-number of the lens [11]. It was shown that the averaged transmission spectrum for a green plasmonic filter used with a lens with an f-number of 1.8, which corresponds to a maximum angle of incidence of 15.5°, exhibited similar spectral characteristics to that of the normal incidence filter. Burgos *et. al.* also acquired colour images using a CMOS image sensor integrated with plasmonic filters for f-numbers ranging from 1.8 to 11. Other than marginally duller colours appearing in the images associated with low f-numbers, all images exhibited fairly consistent colour reproduction.

For f-numbers below 1.8, the maximum angle of incidence could increase to a point where the plasmonic filters no longer exhibit average spectral characteristics that are similar to that of the filters at normal incidence. In Figure 5.3 it can be seen that the green and red filters also filter a significant amount of shorter wavelength light at incident angles beyond approximately 12°. This becomes more prominent at larger incident angles and in some cases the transmission of the shorter wavelength light exceeds that of the main resonant peak. It may be possible to design a filter set that is suitable for use with a low f-number by altering the array period and hole size from the normal incidence design, such that the

averaged transmission spectra exhibits the desired characteristics for imaging. Otherwise it may be necessary to limit the minimum usable f-number in the optical system.

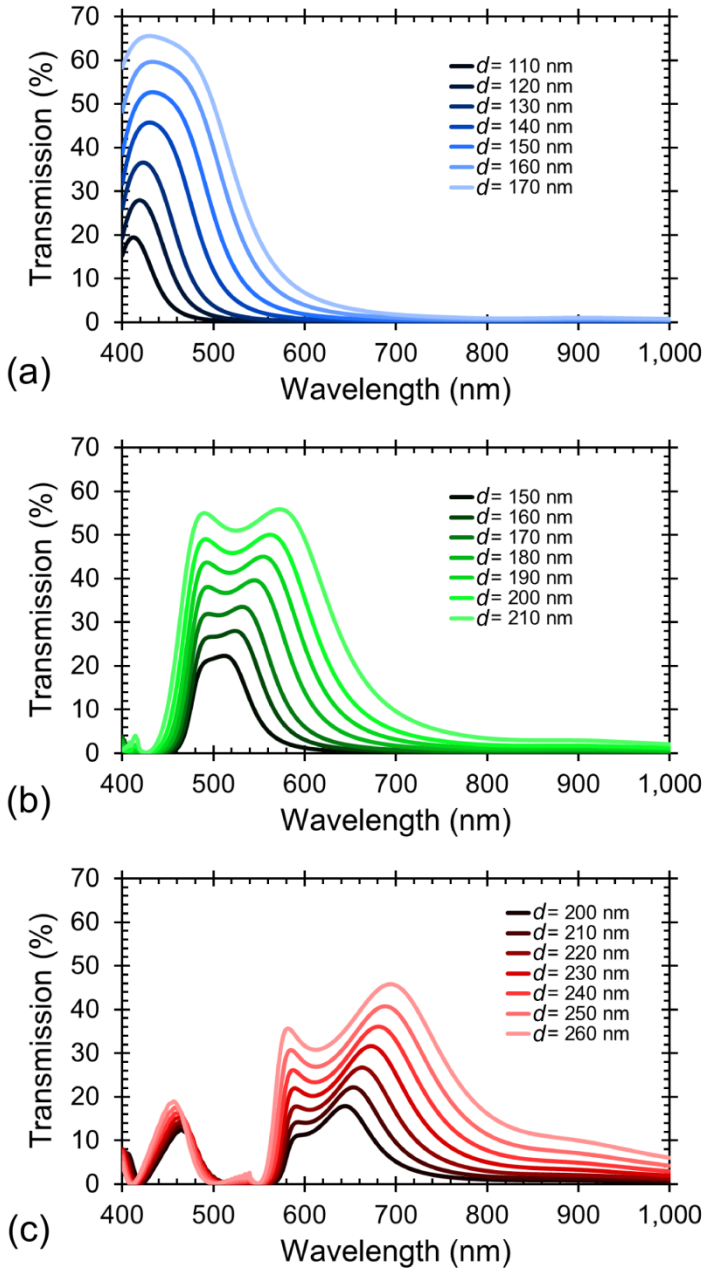

Figure 5.4 Simulation results for blue green and red plasmonic filters with varying hole diameters, d. (a) Blue filter, period, P = 250 nm. (b) Green filter, period, P = 330 nm. (c) Red filter, period, P = 430 nm.

Additional simulations were performed to investigate the impact of hole size on the blue, green and red filters with the array periods, structure and simulation parameters as listed previously. There is often a slight variation in the fabricated hole sizes when compared to those designed using the computer aided design (CAD) software for electron beam lithography (EBL). This can result from a number of factors such as variations in development temperature or time, electron beam dose and certain aspects of dry etch processing. It is therefore useful to quantify the variation in the transmission spectra as the

hole diameter deviates from the intended size. The transmission spectra of the plasmonic filters with varying hole sizes are shown in Figure 5.4.

Generally speaking larger holes result in higher transmission but at the expense of larger filtered wavebands, as has been reported previously [59]. There is also a slight redshift in the transmission peak. It can be observed that the transmission minimum remains constant as the hole size varies, which is in agreement with equation (3.49), as the calculated wavelength is independent of the hole diameter.

5.1.2 Fabrication

Plasmonic filters were fabricated on the surface of a 500 µm thick square glass slide with a side length of 2 cm. The first step of the fabrication process was solvent cleaning of the substrate, in which the substrate was sequentially placed in beakers of OptiClear, acetone and isopropyl alcohol (IPA), where it underwent 5 minutes of ultrasonic agitation with each solvent. The substrate was then rinsed thoroughly with reverse osmosis (RO) water and dried using a nitrogen gun.

Following the solvent cleaning stage, a 150 nm aluminium layer was evaporated on to the sample surface using a Plassys MEB 550S Electron Beam Evaporator. A 50 nm layer of silicon nitride was then deposited on to the aluminium surface using inductively coupled plasma chemical vapour deposition (ICP-CVD) in an Oxford Instruments System 100 ICP 180 PECVD. The silicon nitride layer was necessary to improve adhesion of the ZEP520A electron beam resist to the sample surface. Neglecting this step resulted in a non-uniform etch mask, which led to the appearance of unwanted etched “patches” in masked regions across the metal surface.

The ZEP520A was diluted using anisole with a ratio of ZEP520A to anisole of 2:1. To determine the appropriate spin speed of the spin coater for the diluted ZEP520A a spin curve was plotted. The ZEP520A was spin coated on a sample surface at different speeds, then baked in a 180 ºC oven for 40 minutes. A scratch was then made on the sample surface and the resist thickness was measured using a Veeco Dektak 6M Height Profiler [228]. A spin curve for 2:1 ZEP520A to anisole dilution is shown in Figure 5.5.

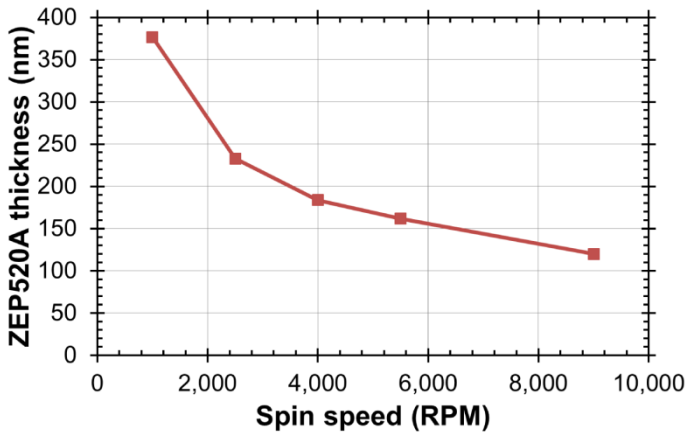

Figure 5.5 2:1 ZEP520A to anisole dilution, spin curve.

The optimum ZEP520A thickness for fabrication of the plasmonic filters was found to be in the region between 200 nm and 300 nm. This thickness provided sufficient dry etch resistance, in addition to sufficiently low scattering of the electron beam within a reasonable dose range. The ZEP520A was spin coated on to the sample surface at a speed of 2,250 rpm with an acceleration ramp of 20,000 $rpms^{-1}$ for 60 seconds and then decelerated at 3,000 $rpms^{-1}$ to yield a resist thickness of approximately 250 nm. The sample was then baked in a 180 ºC oven for 40 minutes prior to patterning of the resist using the Vistec VB6 EBL tool. The spot size of the electron beam was set as 4 nm, the variable resolution unit (VRU) was 5 and the resolution was 1 nm.

Each plasmonic filter was fabricated over a square area with a 1 mm side length to allow accurate alignment using the microspectrophotometer for measurement. For the 16 colour plasmonic filter set, this corresponded to a lengthy EBL patterning process, therefore the filter fabrication was optimised prior to fabrication of the final sample for measurement. This was carried out by performing dose tests, to determine the optimum dose for the final fabricated plasmonic filters. The dose test consisted of a smaller hole array pattern within a square region, typically of side length 100 µm, repeated 9 times for a range of electron beam doses. A transmission microscope image of dose tests for blue and green plasmonic filters, with doses from 200 $\mu C/cm^2$ to 500 $\mu C/cm^2$ are shown in Figure 5.6(a) and Figure 5.6(b), respectively. The best dose could be determined by acquiring scanning electron microscope (SEM) images after etching, and by observing the transmitted colour from the different filters using a transmission microscope. It can be observed in Figure 5.6 that the lower doses in this case correspond to insufficient exposure of the resist to form the hole arrays necessary for filtering.

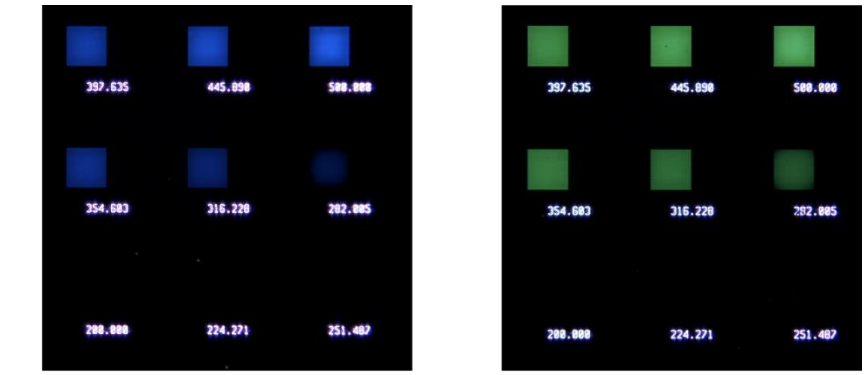

(a) (b)

Figure 5.6 Transmission microscope images of dose tests for (a) blue plasmonic filters and (b) green plasmonic filters. The numbers below each filter corresponds to the associated dose in units of $\mu C/cm^2$.

After the resist was patterned the sample was developed in o-xylene at 23 ºC for 35 seconds and then placed in a beaker of IPA for 30 seconds before being dried using a nitrogen gun. Residual resist left in the developed holes was then removed by using oxygen (O_2) plasma in a Gala Instruments Plasmaprep 5 Barrel Asher at 40 W for 30 seconds. At this stage the resist thickness was measured using the Veeco Dektak 6M Height Profiler. This is a useful method of monitoring the resist thickness over time, as it typically gets thicker for the same spin speed as the solvent in the ZEP520A dilution evaporates. The silicon nitride within the holes was then etched using trifluoromethane/oxygen (CHF_3/O_2) in an Oxford Instruments RIE80+. A laser interferometer spot was used to measure the reflectivity from an exposed square region in the resist, as a means of monitoring the etch rate. After the square region was fully etched, the sample underwent an over-etch period corresponding to approximately 70% of the initial etch time. This was required to ensure that the holes were fully etched, as the etch rate is lower inside the smaller structures. An illustration of the interferometer trace is shown in Figure 5.7. The typical etch time was found to range between approximately 40 and 60 seconds with an over-etch time of approximately 30 and 40 seconds, respectively. This corresponded to total etch times typically ranging from 70 seconds to 100 seconds.

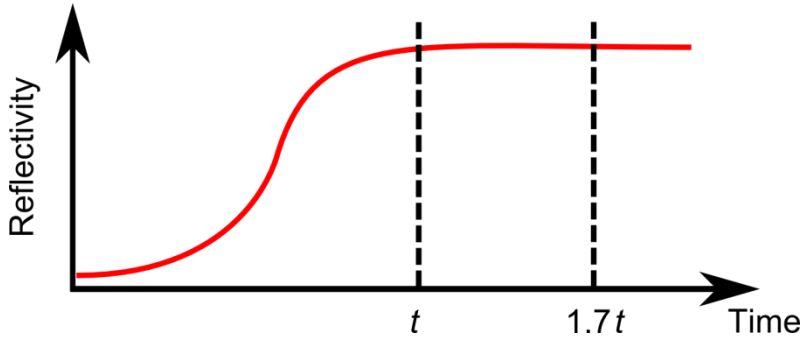

Figure 5.7 Illustration of the interferometer trace. When the trace levels out at time *t*, etching of the material in the large square etch marker region is completed. At time 1.7*t*, corresponding to a 70% over-etch, the material within the holes can be assumed to have been etched.

The aluminium etching was performed using silicon tetrachloride ($SiCl_4$) in an Oxford Instruments RIE System 100 tool. Once again the laser interferometer was used to monitor the etch time using the same method as described previously. The typical etch time was approximately 3 minutes 30 seconds with an over-etch time of approximately 2 minutes 30 seconds. The resist was then removed using the Gala Instruments Plasmaprep 5 Barrel Asher at 200 W for 5 minutes, before returning the sample to the Oxford Instruments RIE80+ for the removal of the silicon nitride layer. The etch parameters for the silicon nitride and aluminium etching are shown in Table 5.2.

Etch Parameter	RIE 80+ (Si_3N_4 etch)	System 100 (Al etch)
Gas	CHF_3/O_2	$SiCl_4$
RF Power	150 W	250 W
Flow Rate	50/5 sccm	18 sccm
Pressure	55 mT	9 mT

Table 5.2 Etch parameters for silicon nitride etching in the Oxford Instruments RIE80+ and aluminium etching in the Oxford Instruments RIE System 100.

Following removal of the resist and silicon nitride layer, it is possible to image the hole arrays using a SEM. SEM images can yield valuable information about the hole quality and also provide a means of measuring the fabricated hole size. SEM images of fabricated hole arrays are shown in Figure 5.8. Figure 5.8(a) and Figure 5.8(b) show a red plasmonic filter at different magnifications. Figure 5.8(c) and Figure 5.8(d) show green and NIR plasmonic filters, respectively, tilted by 30º.

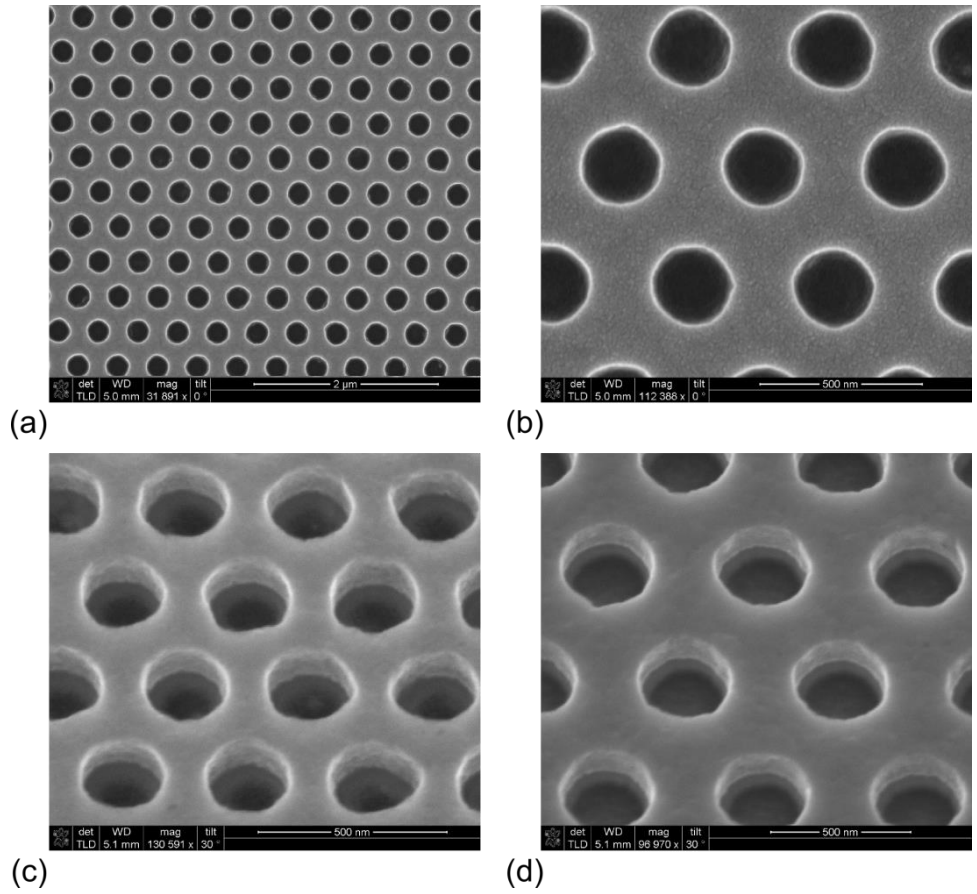

Figure 5.8 Scanning electron micrographs of hole arrays etched into 150 nm aluminium films. (a-b) Red plasmonic filter, with hole period, P = 430 nm, at different magnifications. (c) Green plasmonic filter, P = 330 nm, tilted by 30º. (d) Near infrared (NIR) plasmonic filter, P = 550 nm, tilted by 30º.

The sample was then solvent cleaned using acetone and IPA sequentially, with 5 minutes of ultrasonic cleaning at each stage. The sample was then rinsed with RO water and dried, before the Oxford Instruments PECVD 80+ was used to deposit a 200 nm silicon dioxide cap layer on the aluminium surface. A tessellated transmission microscope image of the 16 colour plasmonic filter set is shown in Figure 5.9. A schematic illustrating the complete fabrication procedure is shown in Figure 5.10.

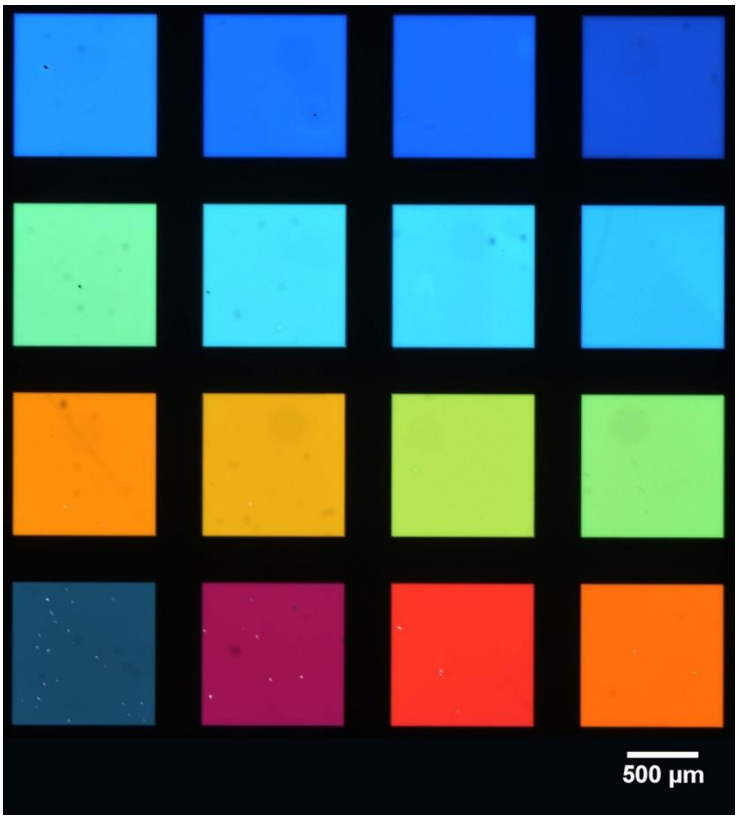

Figure 5.9 Tessellated transmission microscope image of the 16 plasmonic filter colour swatch.

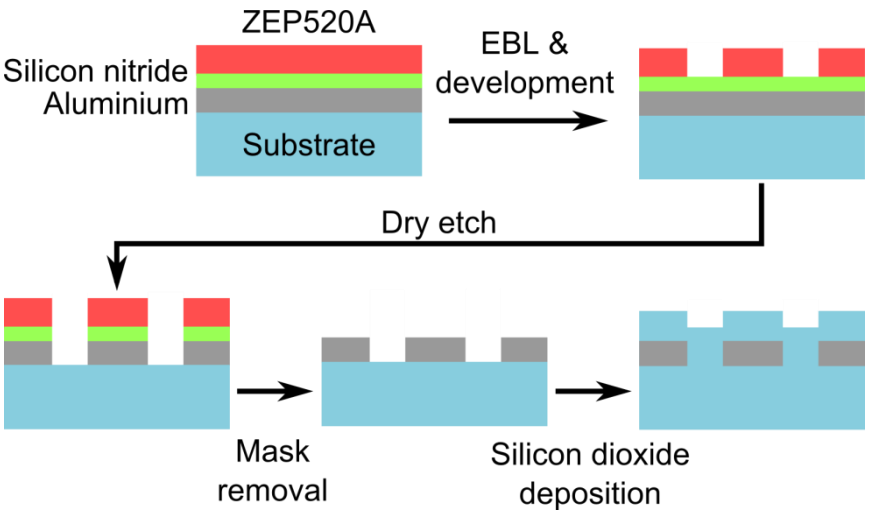

Figure 5.10 Illustration of plasmonic filter fabrication process flow. After evaporation of aluminium, deposition of silicon nitride and spin coating with ZEP520A, the sample is submitted for electron beam lithography (EBL). After development, dry etch is used to define the hole array before the remaining resist and silicon nitride is removed. The final step is the deposition of the silicon dioxide cap layer.

5.1.3 Characterisation and Results

Optical characterisation was performed using the TFProbe MSP300 microspectrophotometer and the spectral measurement method described in Chapter 4. The measured transmission spectra from the 16 filter colour swatch are shown in Figure 5.11. As the fabricated holes varied slightly from the hole sizes designed using L-Edit, the SEM was used to measure the hole diameter of the fabricated filters. The measured hole sizes are listed next to the period on the legend of Figure 5.11.

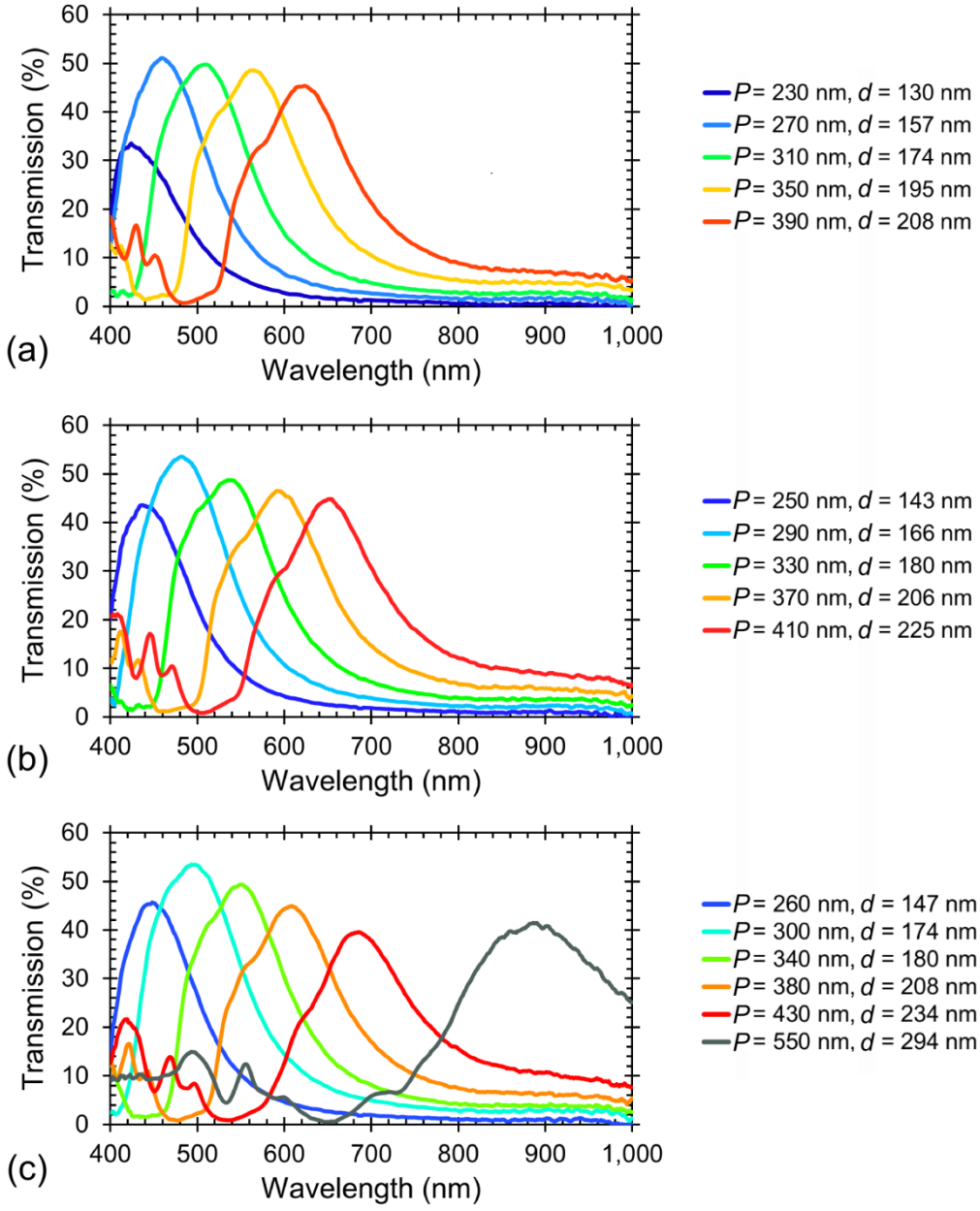

Figure 5.11 Experimental results for the 16 colour plasmonic filter set. The individual filter transmission spectra are shown in (a-c). The legend denotes the hole period, *P*, and the hole diameter, *d*. The hole diameters correspond to the hole sizes that were measured using a scanning electron microscope (SEM).

The peak transmission for the 16 colour filters ranges from 34 % to 54 % with full width at half maximum (FWHM) values ranging from approximately 100 nm, at short wavelengths to approximately 150 nm, at longer wavelengths, with a FWHM approaching 200 nm for the NIR filter. Simulation results for the measured hole sizes, compared with the experimental results for the blue, green and red plasmonic filters with hole periods of 250 nm, 330 nm and 430 nm, respectively, are shown in Figure 5.12(a), where it can be observed that there is good agreement between both experimental and simulation results for the plasmonic filters.

Generally speaking, the peak transmission can be seen to decrease for filters operating at longer wavelengths. This is most pronounced in the simulation results and it can be observed in Figure 5.12(a) that the peak transmission of the simulated blue filter is higher than that of the fabricated filter, however for the green and red filters the experimentally measured peak transmission exceeds that of the simulated filters. As shown in Figure 3.2(a), aluminium exhibits increasing loss as wavelength increases through the visible band. This is illustrated by a decrease in the ratio of the real and imaginary components of the aluminium permittivity at longer wavelengths. As described in Chapter 3, high loss should result in a poor plasmonic filter, and this is reflected in the decrease in transmission and wider bandwidth of the filters operating at longer wavelengths. It should be noted that in Figure 3.2(a), the aluminium parameters correspond to the Rakić model [216], however the Palik model [238], as used in the plasmonic filter simulations, follows a similar trend. The discrepancy in the simulated and experimental transmission spectra can possibly be attributed to variations between the fabricated aluminium and the aluminium model used in the simulations; the fabricated plasmonic filters display characteristics that suggest that the fabricated aluminium exhibits less variation in the real to imaginary permittivity ratio than the simulated aluminium in the visible band.

In Figure 5.12(a) the simulated green and red filters exhibit two peaks in the main transmission band. The occurrence of short and long wavelength peaks for a given resonance can be attributed to odd and even modes of coupled SPPs at either side of the metal film [16,59]. Although not as prominent in the experimental results, a “shoulder” can still be observed at a wavelength below that of the peak transmission. It is likely that both peaks have merged into a single peak due to variations between the fabricated plasmonic filter and the idealised simulated filter.

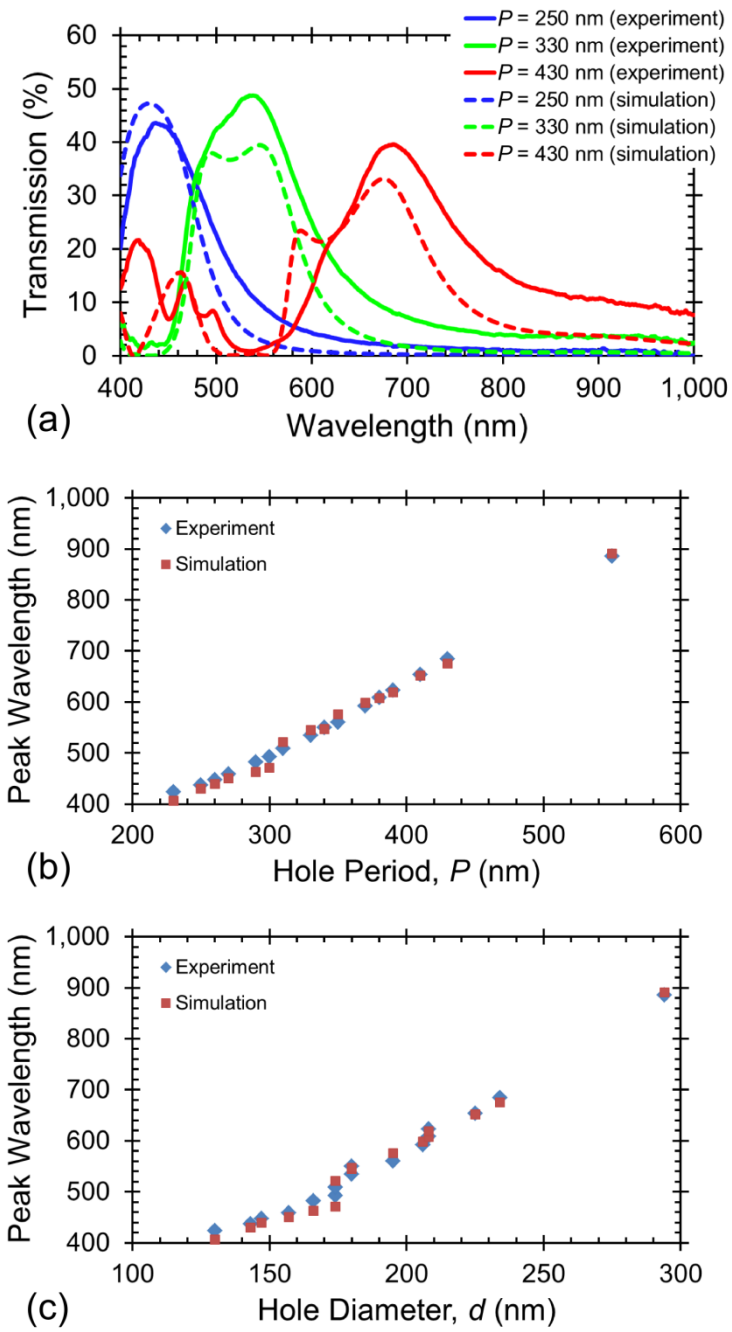

Figure 5.12 Comparison of the experimental and simulation results from the 16 colour plasmonic filter set. (a) Simulated plasmonic filters corresponding to blue, green and red filters, compared with the experimental results. The array periods are listed in the legend. The simulated filters have hole diameters as measured on the fabricated filters, and listed in the legend of Figure 5.11. (b) Peak wavelength versus array period for the fabricated and simulated plasmonic filters. (c) Peak wavelength versus hole diameter for the fabricated and simulated plasmonic filters.

The experimental and simulation results showing the peak wavelength of the plasmonic filters varying with hole period and hole diameter are shown in Figure 5.12(b) and Figure 5.12(c), respectively. It can be observed that the peak wavelength varies linearly with both the array period and the hole diameter. This is to be expected because the hole diameter is loosely scaled with the array period. In the simulation results presented in Figure 5.12(b) there is a sudden increase in peak wavelength between the filter with an array period of

300 nm, and the filter with an array period of 310 nm. As discussed previously, two peaks can be observed in the simulated filter transmission band. The sudden increase in peak wavelength arises because the peak transmission switches from the short wavelength peak to the long wavelength peak as the filter period changes from 300 nm to 310 nm. This can also be observed in Figure 5.12(c), where the two points with hole diameters equal to 174 nm correspond to the plasmonic filters with 300 nm and 310 nm array periods. The sudden change in peak wavelength is not observed in the experimental results because they typically exhibit a single peak with a shorter wavelength "shoulder", as described previously.

5.2 Infrared Plasmonic Filters

Further scaling of the period and hole size of the optical plasmonic filters, yielded a filter set with high narrowband transmission at short wave infrared (SWIR) wavelengths. The layer structure and hole array type is the same as described for the optical filters in Section 5.1, which ensured that both optical and infrared (IR) plasmonic filters could easily be fabricated on the same metal film using a single lithographic process. 8 plasmonic filters for operation in the 1 µm to 3 µm spectral range have been designed and fabricated. The high and consistent transmission in the IR range, where aluminium is generally considered to be a poor plasmonic metal and SPP confinement is poor, suggests that spoof SPs play a role in the observed extraordinary optical transmission (EOT), as discussed in Chapter 3, Section 3.2.3. IR filters based on the designs described here were extended to mid infrared (MIR) wavelengths and used as a component in a SMM which will be presented in Chapter 7.

5.2.1 Design and Simulation

Simulations were performed in Lumerical FDTD Solutions by following the procedure outlined in Section 5.1.1 for the optical filters, but with parameters scaled to account for the longer wavelength filters. The simulation region was extended in the z direction as the larger operating wavelength required a larger distance between the simulation PML and the surface of the filter structure. The mesh override in the z direction was fixed as 5 nm, however it varied in x and y between 10 nm for the shortest wavelength filter and 30 nm for the longest, to maintain short simulation times as the filter period and hole size were scaled. The aluminium was characterised by the electromagnetic parameters defined by Rakić [216] and the silicon dioxide was modelled using the Palik parameters [238]. The layer structure and triangular array were as illustrated in Figure 5.1. The hole diameters for

the different hole periods, determined by linearly scaling the optical filter features, are shown in Table 5.3. The simulation results for the 8 IR filters are shown in Figure 5.13.

Array period, *P* (nm)	Hole diameter, *d* (nm)
648	339
853	442
1059	544
1264	647
1470	750
1675	853
1881	955
2086	1058

Table 5.3 Array period and hole diameter for the 8 infrared (IR) plasmonic filters.

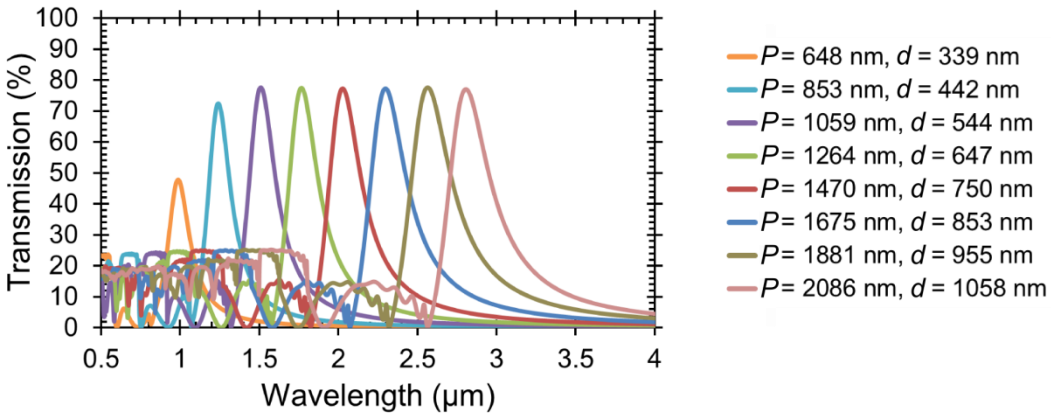

Figure 5.13 Simulation results for the 8 infrared (IR) plasmonic filters. The legend denotes the hole period, *P*, and the hole diameter, *d*.

From Figure 5.13 it can be observed that scaling the hole period and the hole diameter of the optical filters presented previously yields high transmission and narrowband IR plasmonic filters. It can also be seen that beyond the first two IR filters with array periods, P = 648 nm and P = 853 nm, the transmission magnitude remains at approximately 77 % throughout the IR range.

5.2.2 Fabrication

The fabrication procedure followed the same process as described in Section 5.1.2, however in this case the electron beam spot size varied between 12 nm and 33 nm for exposure of the smallest diameter circle to the largest. The VRU in all cases was equal to the spot size. The larger hole sizes of the IR filters compared to the optical filters generally

resulted in faster EBL and better quality hole profiles. SEM images of an IR filter with array period, P = 1059 nm, are shown in Figure 5.14.

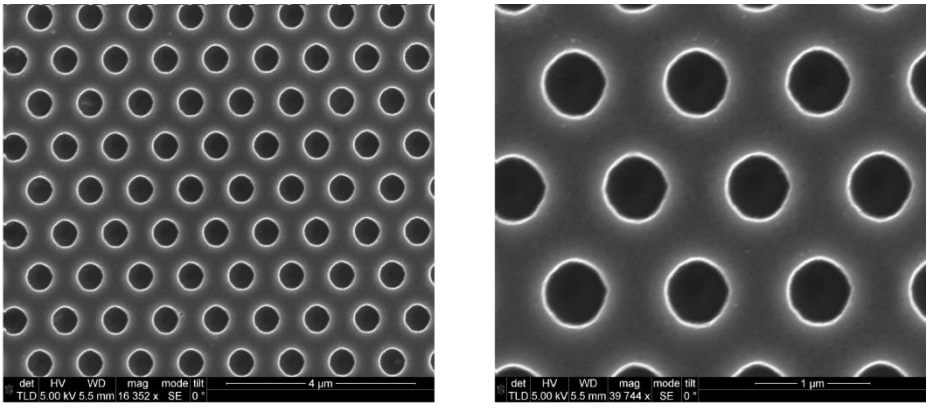

(a) (b)

Figure 5.14 Scanning electron micrographs of hole arrays etched into 150 nm aluminium films to make an infrared (IR) plasmonic filter. (a-b) IR plasmonic filter, with hole period, P = 1059 nm, at different magnifications.

5.2.3 Characterisation and Results

The transmission spectra from the IR plasmonic filters were measured using the Bruker Vertex 70 Fourier Transform Infrared (FTIR) spectrometer as described in Chapter 4. The 8 IR plasmonic filter transmission spectra are shown in Figure 5.15. The SEM measured hole diameter is listed next to the hole period in the legend. Losses in the glass substrate were seen to have an impact on the transmission at longer wavelengths and therefore transmission through an unprocessed glass substrate is also shown in Figure 5.15. The (1,0) transmission minimum wavelength versus the hole period for the fabricated and simulated filters is shown in Figure 5.16. The simulated filters used the hole diameters listed in the legend of Figure 5.15. The calculated wavelengths from equation (3.50), and assuming a refractive index of 1.46, are also shown. The experimental and simulation results for the 8 IR plasmonic filters are shown in Figure 5.17.

It can be seen in Figure 5.15 that the transmission maxima associated with the IR plasmonic filters exceed 60 % until the final filter with array period, P = 2086 nm, where transmission is reduced to 37 % due to the glass substrate. Transmission through the substrate continues to decrease at longer wavelengths, and approaches zero at 5 µm (not shown). It is possible to extend the operation of the filters to longer wavelengths, and MIR plasmonic filters will be presented in Chapter 7, however beyond 5 µm a different substrate material would be required.

From Figure 5.16 and Figure 5.17 it can be observed that there is good agreement between both the experimental and simulation results. The calculated wavelengths of the

transmission minima, determined using equation (3.50), also align well with the experimental and simulation results, as can be seen in Figure 5.16. The experimental FWHM ranges from approximately 230 nm to approximately 330 nm for the IR filters shown in Figure 5.17(b-g), however a larger FWHM of approximately 490 nm is observed in Figure 5.17(h). The simulated FWHM ranges from approximately 210 nm to approximately 350 nm.

The simulated filters exhibit higher transmission than the fabricated filters in all cases except for the plasmonic filter with an array period of 648 nm, as is shown in Figure 5.17(a). This was also observed for green and red plasmonic filters and can possibly be attributed to variations between the aluminium model used in the simulations and the fabricated aluminium, as was discussed in Section 5.1.3. In Figure 5.17(b-g), with array periods ranging from 853 nm to 1881 nm, the simulated transmission exceeds that of the fabricated filters by between 11 % and 14 % which can possibly be associated with differences between fabricated and simulated materials or uncertainties arising during fabrication.

In Figure 5.17(h), where the array period is 2086 nm, the simulated filter exhibits significantly higher transmission than the fabricated filter. As mentioned previously, the poor experimental transmission is due to loss in the glass substrate. The simulated silicon dioxide, corresponding to the Palik model [238], does not exhibit significant loss at the peak wavelength of the IR filter, however the glass substrate used to fabricate the filters can be seen to transmit less light beyond approximately 2.7 μm, as shown in Figure 5.15. Therefore it can be concluded that the silicon dioxide Palik model [238] does not accurately represent the glass substrate at the resonant wavelength of the IR filter. It should also be noted that the simulation region, and consequently the simulated glass layer, is significantly smaller than the thickness of the glass substrate used to fabricate the filters. Therefore the inclusion of loss in the silicon dioxide model would be unlikely to have a substantial impact on the simulated transmission unless it was suitably large to compensate for the small simulation region. In addition to variations in transmission, a slight redshift in the experimental results compared with the simulation results can be observed in Figure 5.17(a-h). This is most likely a result of minor differences between the refractive index of the simulated and fabricated silicon dioxide.

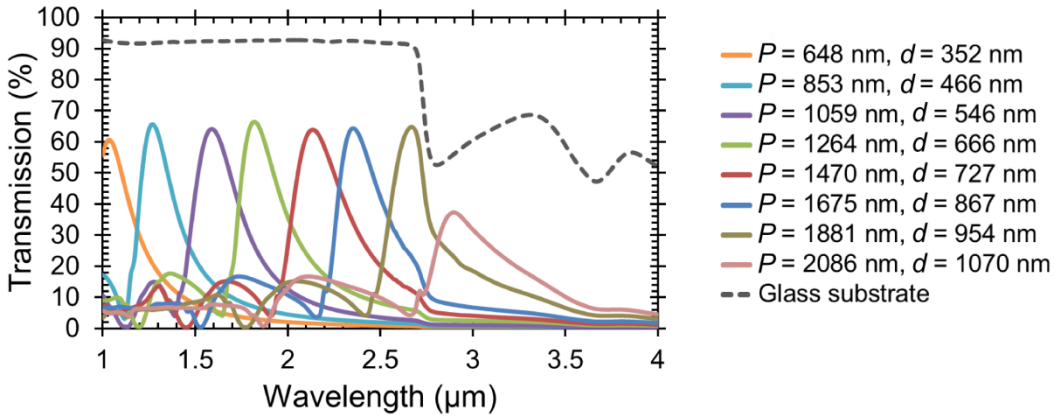

Figure 5.15 Experimental results for the 8 infrared (IR) plasmonic filters. The legend denotes the hole period, *P*, and the hole diameter, *d*.

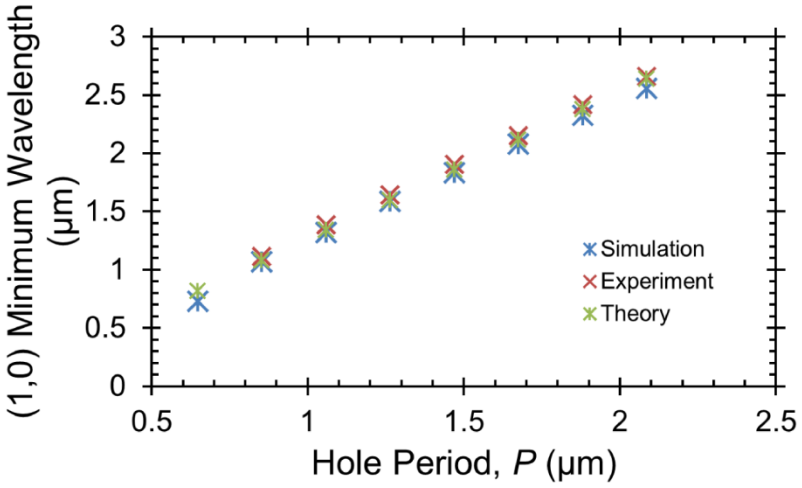

Figure 5.16 Minimum wavelength versus array period, P for $i = 1$ and $j = 0$ showing simulation, experimental and theoretical results calculated using equation (3.50) with refractive index, $n = 1.46$.

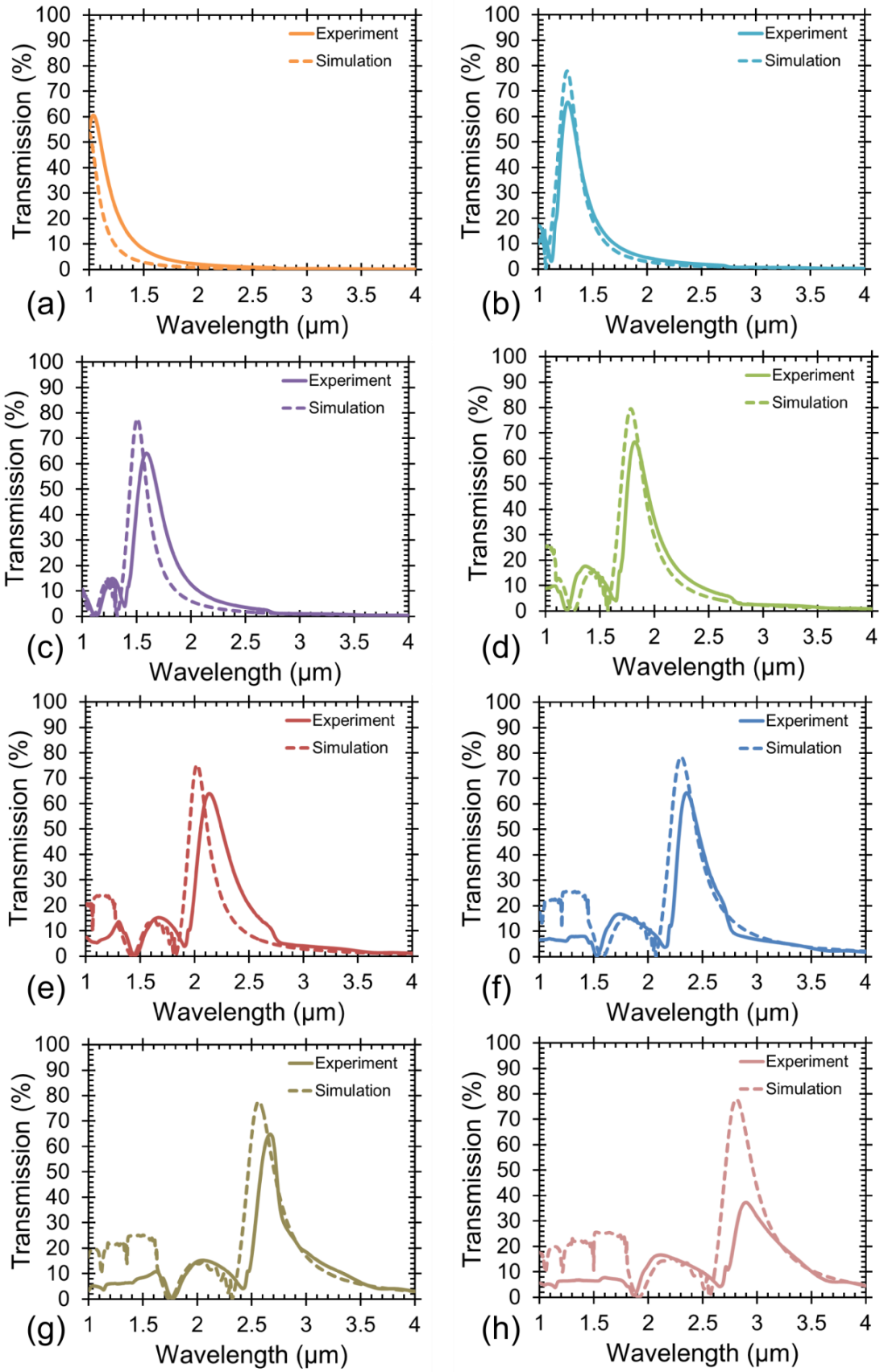

Figure 5.17 Comparison of the experimental and simulation results from the infrared (IR) plasmonic filter set. The experimental and simulation results correspond to filters with array periods of (a) 648 nm, (b) 853 nm, (c) 1059 nm, (d) 1264 nm, (e) 1470 nm, (f) 1675 nm, (g) 1881 nm and (h) 2086 nm. The simulated filters have hole diameters as measured on the fabricated filters, and listed in the legend of Figure 5.15.

5.3 Integration of Colour Filters with CMOS Image Sensors – Chip 1

The process of integrating plasmonic colour filters with CMOS image sensors is described in the remainder of this Chapter. Integration with the first CMOS chip is described in this section. A method of aligning to the features of the chip was devised and plasmonic filters on the chip surface were characterised. It was determined that due to the surface topography of the chip, it presented an unsuitable surface for fabrication of plasmonic filters. The shortcomings of the first chip, with regards to plasmonic filter integration, influenced the design of the second chip, which will be described in Section 5.4.

The chip was manufactured using a 0.35 µm AMS process. It consisted of a 480 x 640 pixel array and the chip size was approximately 5.8 mm x 4.9 mm. For colour imaging, the initial intention was to use the array structure presented by Honda *et. al.* [88] as shown in Chapter 2, Section 2.2.2. Using the alignment method described in the next section, the accuracy of positioning the plasmonic filters to the photodiode array meant that it was required that each filter covered four photodiodes. This would correspond to a colour image resolution of 240 x 320, assuming interpolation was used. Issues with fabrication of the hole arrays meant that it was necessary to perform dose tests to optimise the processing. The fabrication limitations and the fabrication processing are explored in the next section.

5.3.1 Fabrication

Alignment markers can be found using the VB6 EBL tool and set as a reference point when aligning successive layers. Markers are therefore necessary to accurately align each of the individual plasmonic colour filters, constituting the colour filter array (CFA), to the photodiodes on the chip. However EBL alignment markers were not included in the CMOS chip design such that the filters could not be fabricated above the photodiodes without significant error in position. It was therefore necessary to fabricate alignment markers on the chip surface by performing a simple EBL job followed by optical quantification of the misalignment before correcting for the misalignment in the L-Edit CAD software.

The alignment procedure uses a single cross shape and several smaller square markers; the cross is used for rough alignment, and then the square markers are used for finer and accurate alignment. The markers are required to be a sufficient size and also a sufficient distance from any neighbouring features to ensure that they can be found by the VB6 EBL tool. A tessellated image of the CMOS chip, built of multiple images acquired using the

VB6 EBL tool, is shown in Figure 5.18. This image represents what the VB6 tool can "see" during the alignment procedure and therefore any markers must be positioned sufficiently far away from any features with sufficient contrast to be observed in this image. Optical microscope images of alignment markers and the photodiode array are also shown in Figure 5.18 and related to their positions on the image of the entire chip. The cross has an arm width and length of 20 µm and 100 µm, respectively. The square markers have side lengths of 20 µm and the misalignment bars are 65 µm x 95 µm. Three square markers were placed in the same section as the cross, fourteen square markers were placed at the top and bottom of the chip on blank silicon regions, respectively, and nine misalignment bars were positioned between bond pads at different positions on the chip. The nine misalignment markers were designed to be centred between two non-essential bond pads and were positioned 4.95 µm away from the inner chip. Each bond pad is 95 µm x 95 µm and there is a gap of 105 µm between adjacent bond pads, which corresponds to a distance of 20 µm from each side of the misalignment markers to the adjacent bond pads.

Fabrication of structures using a simple EBL job, without alignment, typically results in misalignment on the order of several microns. However, it is possible to use the known position of features on the chip to place a value on the misalignment between fabricated structures and chip features. The bond pads are used as a reference point on the chip to quantify the misalignment of the fabricated misalignment markers compared to the L-Edit designed positioning. The shift in the misalignment markers can be measured optically and then averaged to yield an approximate value for the misalignment. The cross and square markers can then be repositioned in L-Edit to their approximate fabricated position and can subsequently be used for EBL registration of the plasmonic filters on the chip surface to the photodiodes.

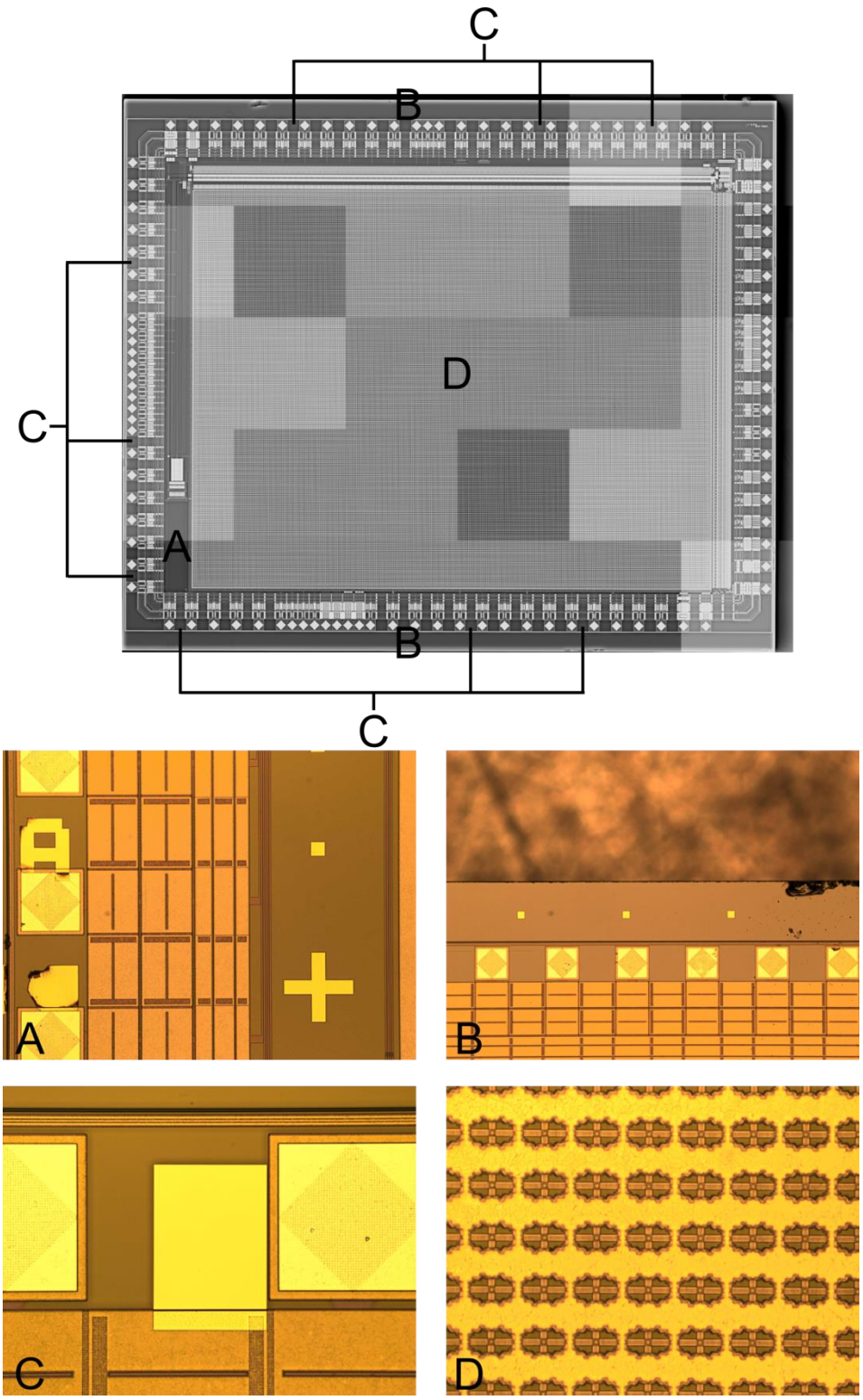

Figure 5.18 Image of the complementary metal-oxide semiconductor (CMOS) chip acquired using the VB6 electron beam lithography (EBL) tool. The labelled regions correspond to areas patterned with alignment markers and the photodiode array. A is the region corresponding to the cross and three alignment markers. B denotes the regions where 14 alignment markers are fabricated. C shows the positions of the misalignment quantification markers and D is the photodiode array.

The fabrication procedure for the alignment markers is as follows. The chip was solvent cleaned by placing it sequentially in acetone and IPA, and exposing the sample to ultrasonic agitation for five minutes at each stage before rinsing the chip in RO water. The CMOS chip was then attached to a small silicon carrier piece by spin coating the carrier at 2,000 rpm with 15% 2010 PMMA for 1 minute, placing the chip on the carrier piece and then baking on a hot plate at 154 ºC for 2 minutes. The chip was then coated with a bilayer of PMMA consisting of 12% 2010 PMMA and 4% 2041 PMMA, both spun at 5,000 rpm for 1 minute and baked on the hot plate at 154 ºC for 2 minutes at each stage. The VB6 EBL tool was then used to pattern the cross, square markers and misalignment markers on to the resist. The dose was 700 μC/cm^2, the resolution was 1 nm, the VRU was 50 and the beam spot size was 50 nm. Following the patterning of the chip, it was developed using 2.5:1 isopropyl alcohol:methyl isobutyl ketone (IPA:MIBK) at 23 ºC for 45 seconds, then rinsed in IPA for 30 seconds. The position of the markers was then verified using an optical microscope. As no formal registration procedure is used at this stage, the marker pattern is positioned by the VB6 EBL tool operator and significant misalignment can occasionally occur which may make the markers unusable if they are rotated or translated over features of the chip. When this occurred, the resist was removed using the previously described solvent cleaning process and the marker fabrication procedure was restarted.

Assuming adequate positioning of the markers, the sample was ashed using O_2 plasma in the Barrel Asher at 50 W for 1 minute. A 10 nm adhesion layer of titanium followed by a 100 nm gold layer was then evaporated on to the chip surface and a lift off procedure was carried out where the resist and surplus metal was removed by placing the sample in hot acetone, prior to rinsing in IPA. The fabricated markers were shown previously, in Figure 5.18. The position of the misalignment markers with respect to their neighbouring bond pads could then be quantified optically using a microscope and ImageJ image analysis software [239]. Using this information, the marker positioning was adjusted in L-Edit, thereby allowing an alignment step to be performed during fabrication of the plasmonic filter array.

However, due to the limitations of the optical microscope in accurately determining the position of the misalignment markers, there was some uncertainty in the measurement. This translates to an uncertainty in how accurately the plasmonic filters can be positioned above the photodiodes and consequently limits the resolution of the imager. Using this method, the attainable alignment accuracy was estimated as being between 1 μm and 2 μm. Due to the spacing between adjacent photodiodes, having one filter corresponding to a

single photodiode was considered to be beyond the capabilities of the alignment technique, and as an alternative it was proposed that each filter would be positioned over four photodiodes, therefore maintaining the checkerboard colour filter array pattern, but with a decreased resolution.

Following the correction to the marker misalignment, the chip was solvent cleaned again and then 500 nm of silicon dioxide was deposited on to the sample surface using PECVD. Following deposition of the passivation layer, the chip was reattached to the silicon carrier and a 150 nm aluminium window was fabricated over the photodiode array using the same EBL and lift off procedure as described previously for the gold markers. After evaporation of the aluminium layer a 50 nm silicon nitride layer was deposited on to the chip surface using ICP-CVD. The plasmonic filter fabrication was then carried out by aligning to the gold markers and using the procedure described in Section 5.1.2. A parallel plasmonic filter sample was also fabricated on a glass slide, as a means to monitor the etch rate as described previously.

After deposition of the 200 nm silicon dioxide cap layer, the passivation over the bond pads was etched to allow wire bonding from the bond pads to the chip carrier. The chip was reattached to the silicon carrier and the surface was coated with a bilayer of PMMA using 15 % 2010 PMMA and 12 % 2010 PMMA spin coated at a speed of 5,000 rpm for 1 minute. The first layer was baked in the 180 ºC oven for 2 hours and the second layer was baked in the oven overnight. The bond pad regions were exposed using EBL with a dose of 1000 μC/cm^2, a VRU of 50, resolution of 1 nm and a spot size of 50 nm. The pattern was aligned using the fabricated markers. Following EBL patterning, the exposed resist was developed using 1:1 IPA:MIBK at 23 ºC for 3 minutes and rinsed in IPA for 30 seconds. Prior to etching, the chip was subjected to O_2 plasma in the Barrel Asher at 50 W for 1 minute. The silicon dioxide over the bond pads was etched using the RIE80+ for 40 minutes using the etch parameters presented in Table 5.4.

Etch Parameter	RIE 80+ (SiO_2 etch)
Gas	CHF_3/Ar
RF Power	200 W
Flow Rate	25/18 sccm
Pressure	30 mT

Table 5.4 Etch parameters for silicon dioxide etching in the Oxford Instruments RIE80+.

To determine if the bond pads were exposed and that all of the dielectric material had been removed, a Probe Station was used to ensure that probing each bond pad yielded a short circuit, as would be expected from an exposed metal surface. If the bond pads had not been completely exposed the chip was subjected to further etching prior to removal of the resist. The CMOS chip was then solvent cleaned and glued to the chip carrier prior to wire bonding.

Initial processing attempted to pattern the chip surface with the necessary plasmonic filter CFA array to acquire a colour image, however the colour discrimination between different colour filter regions was found to be poor and the etched hole arrays were of poor quality and varied significantly over the chip surface. This was most likely due to surface topography as a result of the upper passivation layer on the chip surface conforming to the top metal layer in the chip. A schematic of the surface profile of the chip across two photodiodes is shown in Figure 5.19. The passivation above the photodiodes is lower than the passivation on the surrounding regions of the chip. This would result in non-uniform spinning of the electron beam resist which would translate to variable quality over the chip surface. The topography was also seen to impact the etch rates over different chip regions. A SEM image of a plasmonic filter with an array period of 430 nm on the surface of a CMOS chip is shown in Figure 5.20. It can be seen in Figure 5.20 that the holes are not fully etched, especially towards the edges of the photodiode regions, and that the resist and silicon nitride layer has not been completely removed above the photodiodes. Using a Veeco Dimension 3100 Atomic Force Microscope (AFM), the step height between the passivation region over the photodiode and out with the photodiode region was determined to be approximately 1 µm.

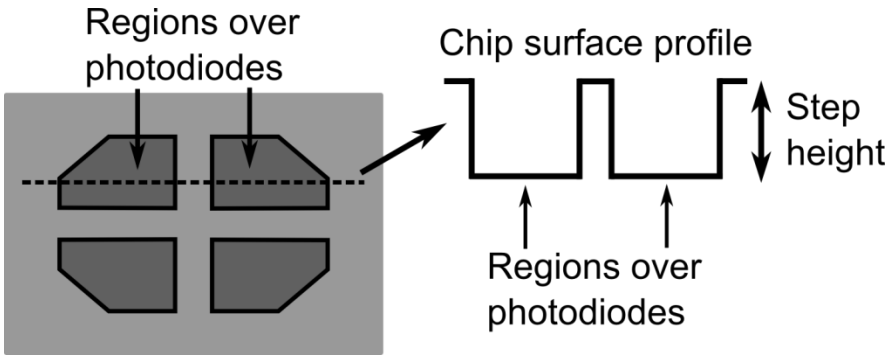

Figure 5.19 Schematic illustration of a top down view of the complementary metal-oxide semiconductor (CMOS) chip and an illustration of the surface profile of the chip along the dashed line.

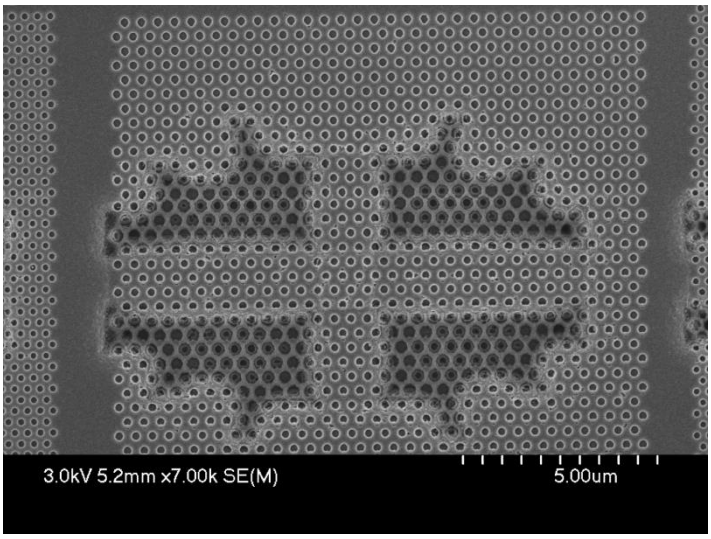

Figure 5.20 Scanning electron micrograph of a plasmonic filter hole array with a period of 430 nm on the surface of a complementary metal-oxide semiconductor (CMOS) chip. The four darker regions are over the photodiodes which are lower than the surrounding areas. It can be observed that the hole size over the different regions varies, and also that within the photodiode regions the holes are not fully etched.

In an attempt to improve the plasmonic filter patterning on the chip surface, dose tests of blue, green and red plasmonic filters were performed on the chip surface for different dry etch times and designed hole sizes. For each colour, 3 different hole sizes were designed, and 9 doses were used, resulting in 81 colour filter patterns. Each of the 81 patterns extended over an area of 16 x 16 photodiodes and open windows, where the aluminium had been completely etched, were positioned close to each filter for normalisation. The hole quality was investigated using the SEM. The excess resist and silicon nitride was removed simply by performing longer cleaning steps than described previously for the plasmonic filters. This consisted of O_2 plasma cleaning in the Barrel Asher for up to 12 minutes at 200 W, followed by silicon nitride etching using CHF_3/O_2 for up to 10 minutes in the RIE80+.

An attempt to ensure that the holes were fully etched was made by increasing the length of the dry etch processing which was monitored with consideration given to the over-etch times as described in Section 5.1.2. The initial O_2 ashing stage, prior to dry etch processing, and the first RIE80+ silicon nitride etch were varied, however it was found that the most significant factor on the quality of the fabricated holes was a result of increasing the aluminium etch timing in the System 100. The test chips used aluminium over-etch times of 300 % or 500 %. It was found that in all cases the hole profiles of the red plasmonic filter dose tests were generally better than the green and blue filters, which is to be expected from the larger hole diameters associated with the red plasmonic filters. However, in all cases the hole quality generally remained poor and as the over etch time approached 500 %, the mask layer began to fail and some of the surrounding aluminium

was etched, as is shown in Figure 5.21(a). This suggests that for longer aluminium etch times, as would most likely be required to ensure the smaller green and blue plasmonic filter holes were fully etched, an alternative etch mask would be required. SEM images over red plasmonic filter regions, with array periods of 430 nm, on CMOS chips having undergone 300 % and 500 % over-etches are shown in Figure 5.21(b) and (c), respectively. Surface cleanliness issues also arose between different samples which were not be fixed by the longer cleaning steps, and were not present in the plasmonic filters fabricated on glass slides. The fabrication issues that arose when working with this chip directly fed into the design of the second chip as is presented in Section 5.4.

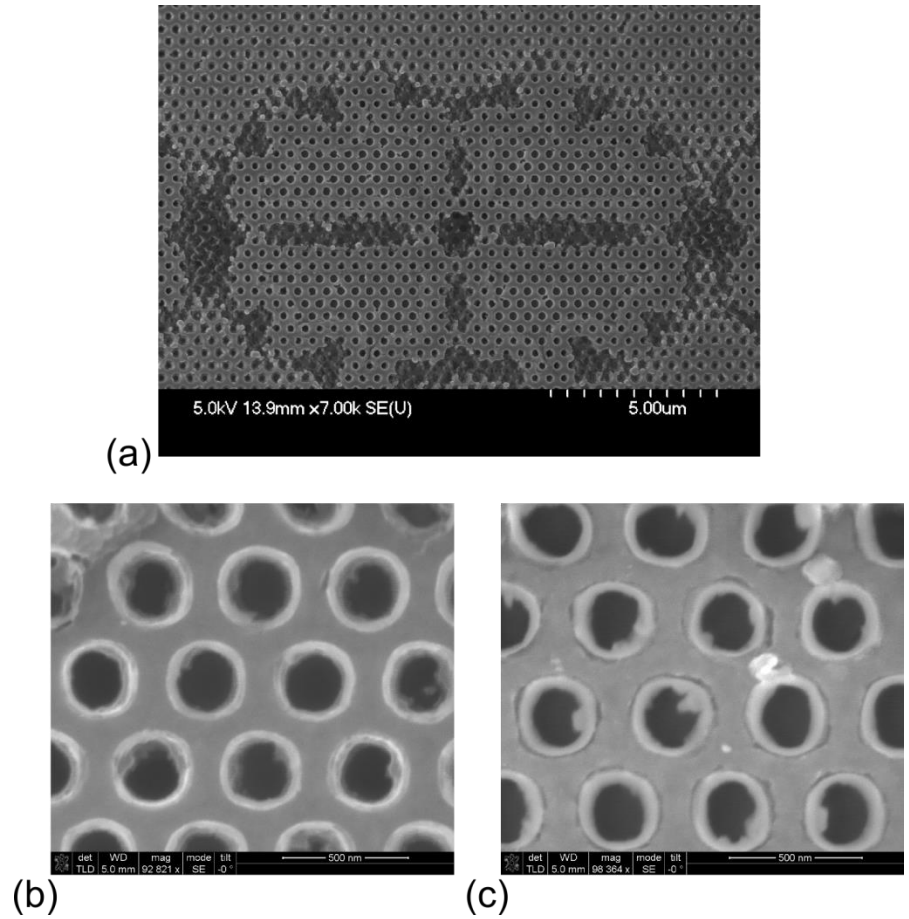

Figure 5.21 Scanning electron micrographs (SEM) of complementary metal-oxide semiconductor (CMOS) chips integrated with plasmonic filters corresponding to varying aluminium etch times. (a) SEM image of a the hole array after a 500 % over-etch time. It can be observed that some of the aluminium regions, which were initially masked around the photodiodes, have been etched. (b) SEM image of a hole array with a period of 430 nm having underwent a 300 % over-etch time and (c) a 500 % over-etch time.

5.3.2 Characterisation and Results

Characterisation of the plasmonic filter dose tests on the CMOS chips was performed using a Bentham TMc300 Monochromator to illuminate the chip surface with incrementally varying wavelengths throughout the visible range. An image was acquired for each wavelength increment such that the spectral properties of the different plasmonic filters

could be determined by normalising the average output of the photodiodes associated with a given colour filter to the average output of photodiodes with an open window above them. This process was performed by analysing the images using a script that had been written in MATLAB.

It was found that in most cases the spectral profile from each of the plasmonic filters on the CMOS chips was poor as a result of the challenges presented in fabricating the hole arrays on a non-planar surface. This is to be expected from the poor quality hole profiles, and incomplete etching of the hole arrays. Nonetheless it is still possible to observe red, green and blue colour bands within the extracted normalised transmission spectra in the case of a CMOS chip with a 500 % aluminium over-etch as shown in Figure 5.22.

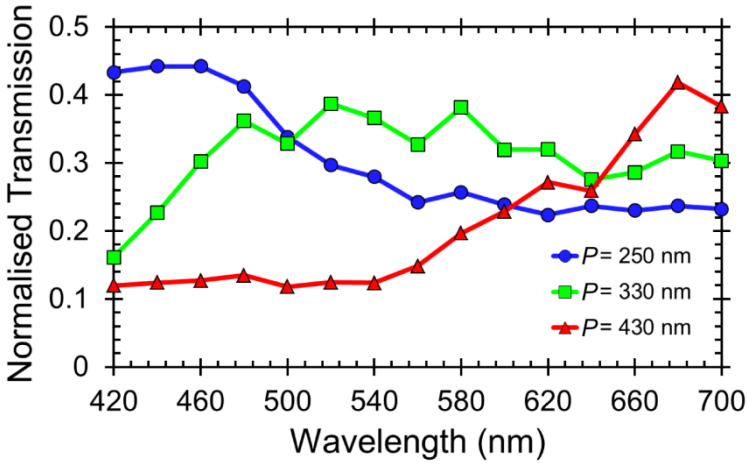

Figure 5.22 Normalised transmission spectra from plasmonic filters fabricated on the surface of a complementary metal-oxide semiconductor (CMOS) chip. The legend denotes the array period, *P*, of the hole arrays.

The blue filter, with a hole array period of 250 nm, exhibits a normalised transmission peak of approximately 44 % at 440 nm, which corresponds to the highest normalised transmission of the three filters. The normalised transmission of the blue filter does not drop below approximately 22 % over the whole visible band and consequently it is likely that the blue filter would be unsuitable for colour imaging. The green filter, with an array period of 330 nm, does not exhibit favourable filtering characteristics over the whole visible band. Despite a significant decrease in normalised transmission at short wavelengths and a slight decrease at long wavelengths, it is unlikely that the green filter could be used to discriminate between the different colour bands. The green filter also appears to exhibit Fabry-Perot oscillations, which have been reported previously for plasmonic filters integrated with CMOS chips [9,10]. The red filter, with a hole period of 430 nm, exhibits the most promising characteristics for colour imaging applications. This is to be expected due to the simpler fabrication of larger holes compared with the smaller

diameter holes used in the green and blue filters. The red filter exhibits a peak normalised transmission of approximately 42 % at 680 nm and this decreases to approximately 12 % at shorter wavelengths. The red filter may exhibit suitable spectral discrimination for colour imaging applications, however without an improvement in the filtering characteristics of the green and blue filters it is unlikely that this plasmonic colour filter set would be suitable for colour imaging.

5.4 Integration of Colour Filters with CMOS Image Sensors – Chip 2

The second chip was designed specifically to allow visible and terahertz (THz) imaging using a single chip by combining CMOS technology with SMMs. The first step in modifying this chip to create a multi-spectral imaging (MSI) system was integration with plasmonic filters and this process will be described in the remainder of this Chapter. In this Chapter the chip is only considered with regards to the photodiode array and no consideration is given to the integration of THz MM structures at this stage. Further details will be outlined in Chapter 7 on how the chip will incorporate both plasmonic and metamaterial (MM) structures.

The chip incorporates solutions to the problems encountered whilst integrating plasmonic filters with the first chip that was presented in Section 5.3. The chip contains alignment markers embedded within the CMOS layers and therefore allows accurate alignment of the plasmonic filter array to the photodiode array without the time consuming requirement to fabricate separate, less accurate, alignment markers. The step height between the region above the plasmonic filters and the surrounding regions has also been reduced to approximately 450 nm, thereby reducing the issues encountered due to surface topography that were encountered with the previous chip. Fabrication of the hole arrays on the chip surface was successful and repeatable with excellent alignment accuracy. Preliminary plasmonic filter characterisation results are presented at the end of this Section.

The chip was manufactured using a 0.18 μm Texas Instruments (TI) process. The photodiode arrays on the chip surface were separated into four sub-arrays, with approximately 384 x 384 pixels in each sub-array. The chip size was approximately 8 mm x 8.1 mm. The alignment accuracy improvement due to the embedded alignment markers meant that it was possibly to align each individual filter to a single photodiode, therefore resulting in increased resolution when compared to the previous chip.

For this chip a periodic checkerboard CFA, as was described for the previous chip, could not be used because certain regions correspond to “dead pixels”, which are not sensitive to visible light as they are used to provide alternative functions that are necessary for the THz detector component of the MSI chip. Therefore an alternative array structure was designed to maximise the resolution of the imager, by ensuring that each “dead pixel” corresponding to an open window in the metal film, thereby ensuring no colour information was lost for any pixel. An illustration of the proposed CFA design is shown in Figure 5.23.

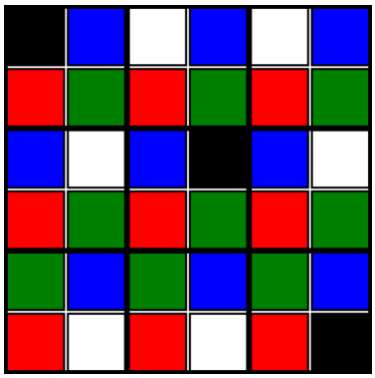

Figure 5.23 Proposed colour filter array (CFA) layout for the integration of plasmonic filters with the multi-spectral imaging (MSI) chip. The black squares correspond to inactive pixels and the white squares correspond to regions where the aluminium is completely removed to allow white light transmission.

5.4.1 Fabrication

The plasmonic filter fabrication procedure undertaken on chip 2 followed the same method as outlined previously for chip 1 in Section 5.3.1. The over-etch times were also influenced by the results of the previous Section. After development of the ZEP520 resist, the optimised etching procedure for the plasmonic filters on the CMOS chip was as follows: the sample was exposed to O_2 plasma using the Barrel Asher at 50 W for 1 minute; the silicon nitride was etched using the RIE80+ with a 100 % over-etch, before the aluminium was etched in the System 100 with a 200 % over-etch; the RIE80+ was used to O_2 clean the sample to remove the resist at 100 W for 500 seconds and the RIE80+ was then used to etch the remaining silicon nitride with a 100 % over-etch. The higher degree of planarisation of the surface of chip 2 when compared with chip 1 ensured that the fabrication process was repeatable and consistently led to the fabrication of high quality plasmonic filter hole arrays. SEM images of the hole arrays acquired prior to silicon dioxide deposition are shown in Figure 5.24.

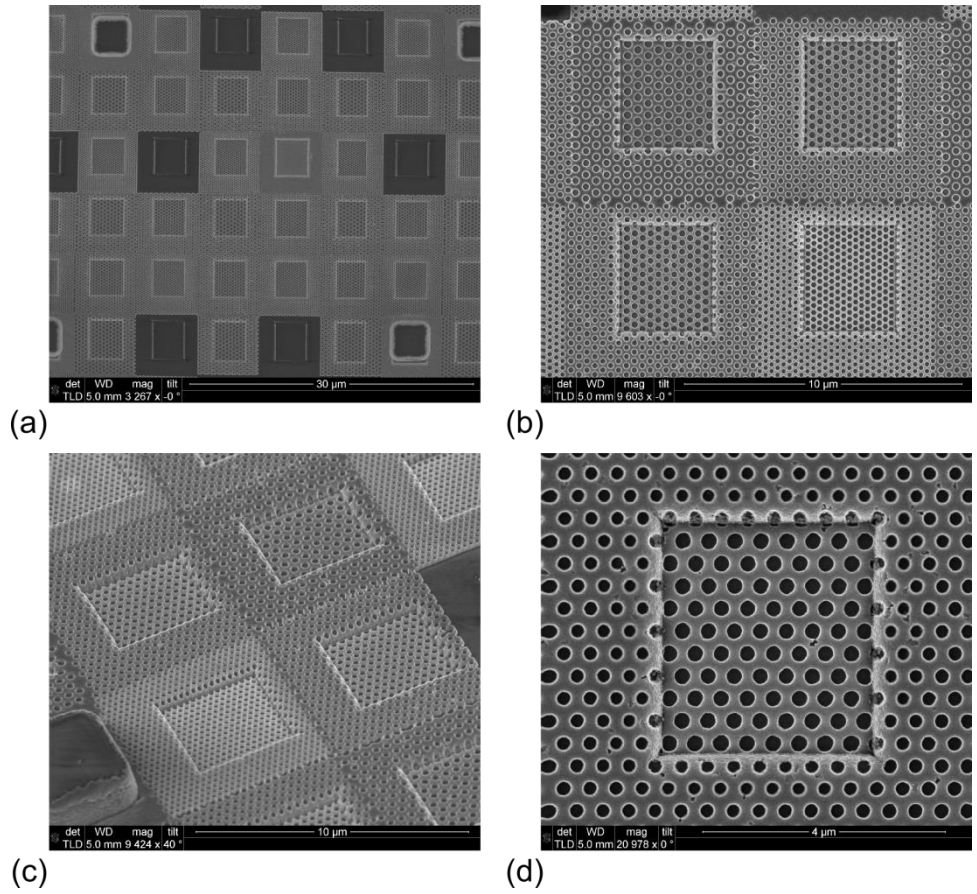

Figure 5.24 Scanning electron microscope (SEM) images of plasmonic filter fabricated on the surface of a complementary metal-oxide semiconductor (CMOS) chip. (a) SEM image of repeated colour filter array (CFA) as is shown in Figure 5.23. (b) SEM image of plasmonic filters with array periods of 250 nm, 330 nm and 430 nm at 0º and at (c) 40º. (d) SEM image of a hole array with an array period of 430 nm. The surface topography is clear in the image and it can be seen that there is little variation of the hole quality over different regions.

5.4.2 Characterisation and Results

Early measurements from a chip integrated with plasmonic filters were acquired using the method outlined in Section 5.3.2. The normalised transmission spectra are shown in Figure 5.25. Once again, it is possible to observe some filtering of light into red, green and blue colour bands. This represents the first step towards acquiring a colour image using plasmonic filters fabricated on to surface of the MSI CMOS chips.

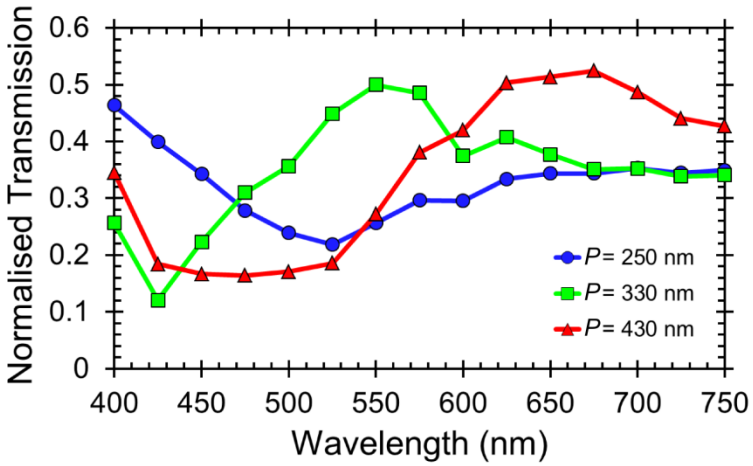

Figure 5.25 Normalised transmission spectra from plasmonic filters fabricated on the surface of the second complementary metal-oxide semiconductor (CMOS) chip. The legend denotes the array period, *P*, of the hole arrays.

5.5 Summary

Plasmonic filters can be engineered to operate throughout the visible band by scaling the array period and hole size. Their operation can also be extended to longer wavelengths, where spoof SPs play a role in the observed EOT. The ability to engineer the band pass characteristics associated with a hole array in an aluminium film, make plasmonic filters particularly attractive for integration with CMOS technology as has been outlined in Chapter 2. In addition to conventional colour imaging, plasmonic filters could also be useful components in MSI systems alongside MMs.

In this Chapter, a 16 colour plasmonic filter set has been designed, simulated, fabricated and characterised. Further scaling of the array period yielded an 8 colour IR plasmonic filter set, where each filter exhibited narrowband transmission at NIR and SWIR wavelengths. The plasmonic filters that have been presented in this Chapter have been designed to be integrated with THz MM components to create SMMs for use in MSI systems. The THz MMs will be presented in Chapter 6 and the hybridisation of plasmonic and MM components will be presented in Chapter 7.

In this Chapter plasmonic filters have been integrated with two different CMOS chips. Chip 1 was not designed for this purpose and therefore issues arose due to alignment problems and surface topography that were resolved on Chip 2. The normalised transmission spectra measured from plasmonic filters on Chip 2 exhibit blue, green and red colour bands, as expected, however, the plasmonic CFA still exhibits unfavourable filtering characteristics. These include high normalised transmission from the blue and green filters at long wavelengths, and large spectral bandwidth from all three filters. Based

on the SEM images of the CFA it can be deduced that these issues are unrelated to poor hole quality, as was observed for the plasmonic filters fabricated on the surface of Chip 1. The unfavourable filtering properties associated with the plasmonic filters on Chip 2 could potentially be attributed to crosstalk. It may be possible to accurately measure the normalised transmission from a single plasmonic filter over a single photodiode by masking the surrounding pixels, however the alignment of the mask to the plasmonic CFA on the chip surface could be challenging. An alternative solution could be to fabricate several plasmonic filters of one colour over multiple photodiodes, or to mask regions over the chip surface by leaving unetched metal during the fabrication process.

Chip 2 also includes features to enable THz imaging through integration with MM structures. Consequently, the integration of plasmonic filters with Chip 2, as described in this Chapter, does not just provide a path to the creation of a plasmonic colour imager; it also represents the first step in integrating SMMs with CMOS technology to create a MSI system.

6. Metamaterials

The history and background theory of metamaterials has been outlined in Chapters 2 and 3, respectively. In this Chapter the design, simulation and characterisation of metamaterial filters and absorbers, optimised for terahertz frequencies are presented. By way of introduction to the metamaterial structures, and as a continuation of the infrared filters presented in the previous Chapter, an infrared metal mesh filter based on a cross slot shape is also shown. In addition to the spectral characteristics of the terahertz metamaterials, the effective electromagnetic parameters have been extracted from the simulations. From these results it can be observed that the metamaterials exhibit the same electromagnetic characteristics as the corresponding devices presented in the literature. The metamaterials are engineered to exhibit resonances close to 2 THz.

The metal mesh filter and metamaterial designs are based on the layer structure and materials of the plasmonic filters presented in Chapter 5. This is to simplify hybridisation of the plasmonic and metamaterial structures for the creation of synthetic multi-spectral materials, as will be presented in Chapter 7. Due to the sensitivity of plasmonic filters to the dielectric properties of the metal, the plasmonic filter design was “fixed” and the metamaterial components were designed around the existing plasmonic structures. As the skin depth of aluminium is less than 60 nm at 2 THz [211,216,240], a 150 nm film is a suitable metal for use in a terahertz metamaterial.

6.1 Metal Mesh Filters

A metal mesh filter (MMF) presents a possible alternative to plasmonic filters for band pass filtering in the infrared (IR) region. In this Section, some early results from investigations into the design of an IR MMF are presented. The MMF consists of a periodic array of etched crosses in an aluminium film that has been evaporated on to a glass slide. It uses the same layer structure as described in Chapter 5 for the plasmonic filters, and therefore simplifies the process of combining both structures into a single film. The MMF exhibits low transmission and wide bandwidth when compared with the IR plasmonic filters presented in the previous Chapter, however this may be attributed to losses in the glass substrate. Consequently, MMFs engineered for shorter wavelengths may exhibit more favourable optical properties, however the dimensions of the cross structure when optimised for shorter wavelengths may prove challenging to fabricate.

6.1.1 Design and Simulation

The MMF was simulated using Lumerical FDTD Solutions. A 150 nm aluminium film, defined by the complex electromagnetic parameters presented by Rakić [216], was positioned between a silicon dioxide substrate and a 200 nm silicon dioxide cap layer defined by Palik [238] electromagnetic parameters. A plane wave source was positioned on one side of the aluminium film and a transmission monitor on the other. Silicon dioxide crosses were positioned in the aluminium film with arm length, l = 1.7 µm, width w = 0.4 µm and period P = 2 µm as illustrated in Figure 6.1(a). A mesh override region around the aluminium film was set with a cell size of 25 nm in the x, y and z directions. Anti-symmetric and symmetric boundary conditions were used in the x and y directions, respectively, and perfectly matched layer (PML) boundary conditions were used in the z direction. A schematic of the simulation layout is shown in Figure 6.1(b). The transmission spectrum of the simulated MMF is shown in Figure 6.2, where transmission is high but with a large bandwidth.

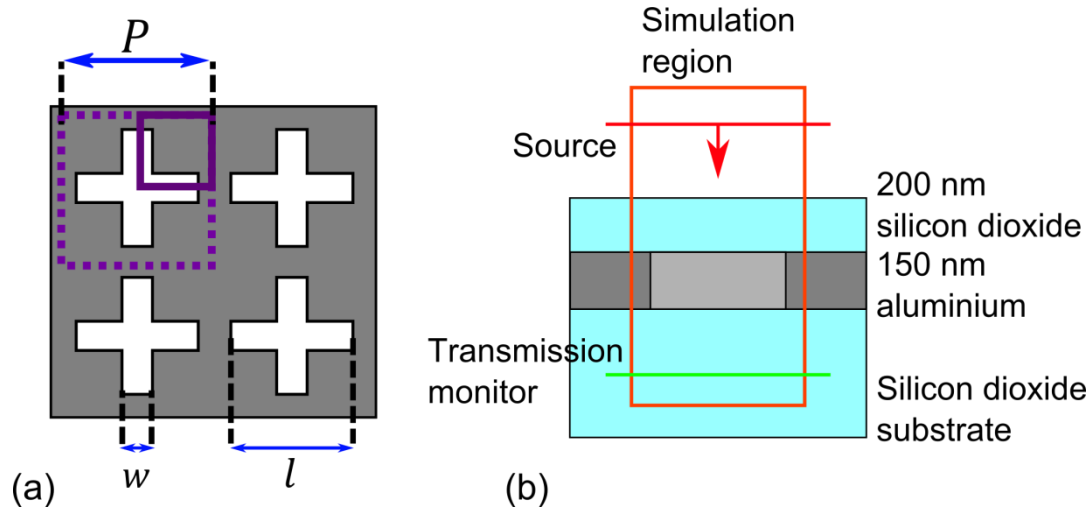

Figure 6.1 Schematic of the simulated metal mesh filter (MMF). (a) Top-down view of the MMF. The simulated region is enclosed by the solid purple box and the broken line encloses the unit cell of the cross array. P denotes the array period, w denotes cross width and l denotes the cross length. (b) Cross section of the MMF. The orange box encloses the simulated unit cell.

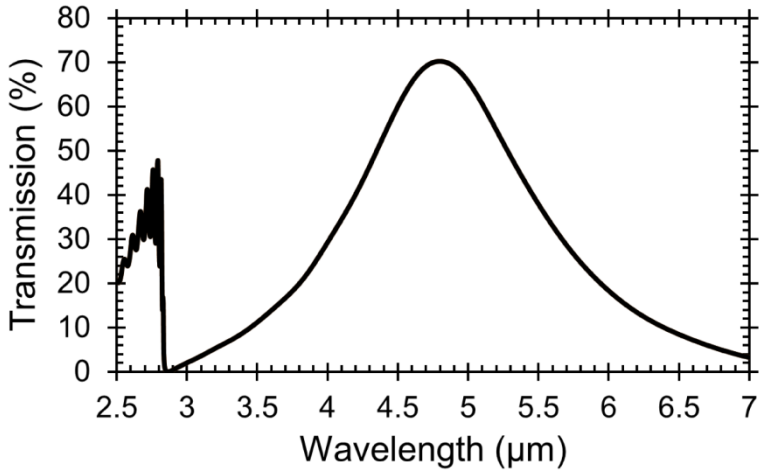

Figure 6.2 Transmission spectrum of the simulated infrared (IR) metal mesh filter (MMF).

6.1.2 Fabrication

The fabrication process for the MMF follows the procedure outlined in Chapter 5, Section 5.1.2 for the plasmonic filters, as a means of retaining consistency of materials and to enable plasmonic filters and MMFs to be fabricated on the same film easily. The electron beam spot size was 50 nm and the variable resolution unit (VRU) was 50. Scanning electron microscope (SEM) images of the IR MMF acquired before deposition of the silicon dioxide cap layer are shown in Figure 6.3.

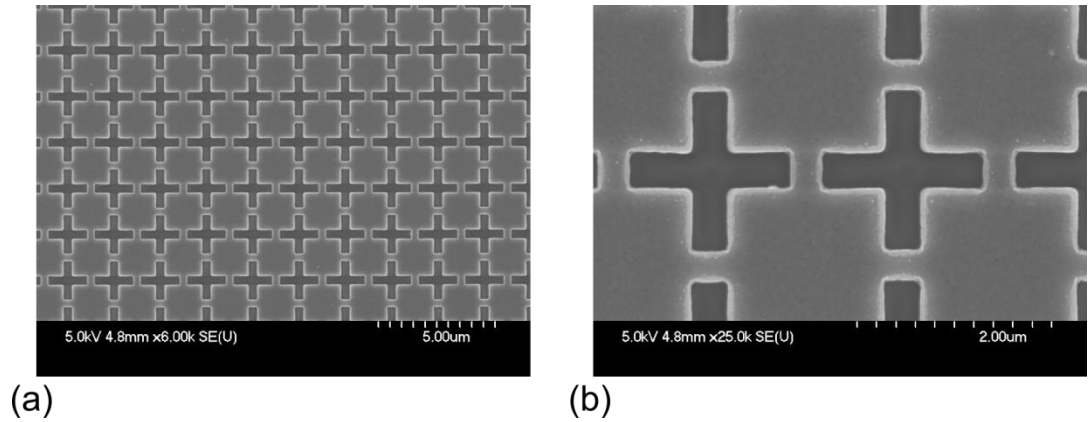

Figure 6.3 Scanning electron micrographs of crosses etched into a 150 nm aluminium film. (a-b) Infrared (IR) metal mesh filter (MMF) composed of etched crosses, at different magnifications.

6.1.3 Characterisation and Results

The transmission spectrum of the MMF was measured using the same procedure that was employed for the IR plasmonic filters using the Bruker Vertex 70 FTIR as described in Chapter 4. The measured transmission spectrum is shown in Figure 6.4. It can be observed that the transmission is lower than observed for the simulated filter, which can be attributed to low transmission through the glass slide, as was present in the longer

wavelength IR plasmonic filters presented in Chapter 5. The bandwidth from both the simulated and fabricated MMF is also wider than observed for the IR plasmonic filters.

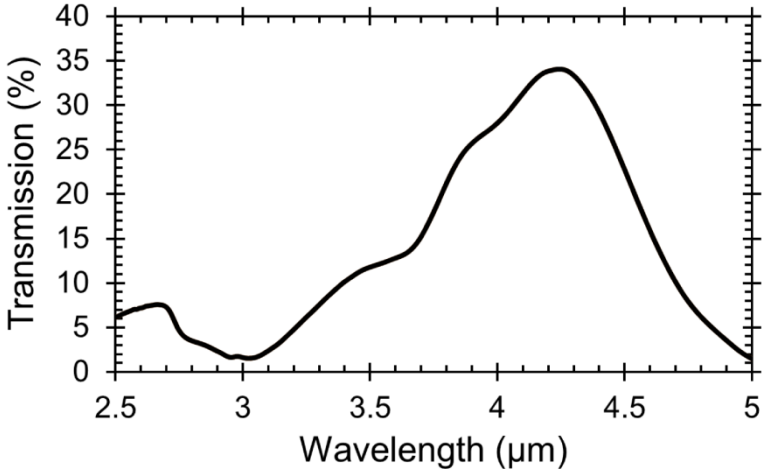

Figure 6.4 Transmission spectrum of the fabricated infrared (IR) metal mesh filter (MMF).

The results presented in this Section illustrate some early work on IR MMFs fabricated on aluminium films. Initial investigations suggest that they exhibit poorer transmission properties than the IR plasmonic filters presented in Chapter 5. With regards to operation at shorter wavelengths, smaller hole structures are simpler to fabricate than well-defined cross structures. As a consequence, IR plasmonic filters have been studied in more detail in the work presented in this Thesis, and have been included in a synthetic multi-spectral material (SMM) which will be presented in Chapter 7. However, MMFs may still prove useful for this project and could warrant further investigation and a more comprehensive study in future work.

6.2 Metamaterial Filters

Two terahertz (THz) metamaterial (MM) filters are presented in this Section. Both filters consist of etched cross style complementary electric ring resonator (cERR) structures etched into a 150 nm aluminium film, to simplify hybridisation with plasmonic filter components. Glass exhibits high loss at THz frequencies, and therefore is not a suitable substrate material for use in a THz filter. As an alternative to a rigid substrate, several different membrane materials were investigated. It was important to ensure that the membrane was thin enough to exhibit low loss at THz frequencies, but also thick enough to maintain mechanical stability. It was also necessary to ensure that the membrane material was lossless at optical wavelengths, to enable hybridisation with plasmonic filters as will be presented in Chapter 7.

The MM filters were simulated using Lumerical FDTD Solutions. Both filters were based on the same cERR design with a fixed unit cell period. The size of the etched region forming the cross shape in the metal film was altered between samples and resulted in variation in the transmission magnitude and bandwidth of the two MM filters. The transmission spectra from the MM filters are presented and there is a slight deviation of the peak frequency when compared with the simulation results. It is likely that this can be associated with a number of factors, including flexing of the membrane and also variations in the refractive index of the deposited and simulated silicon dioxide.

6.2.1 Design and Simulation

Silicon dioxide has been reported as having an absorption coefficient α = 780 m^{-1} at 2 THz [241], which would result in negligible transmission of THz radiation through a glass substrate with a thickness of several hundred microns. Consequently, a glass substrate is unsuitable for supporting a THz MM filter, however a reasonably thin membrane could be sufficiently transparent. Different membrane layers, namely silicon dioxide, silicon nitride and Brewer Science OptiNDEX D1-20 polyimide were investigated. Through fabrication tests it was determined that a 3 µm silicon dioxide layer was the most suitable membrane material; the polyimide membrane frequently broke during fabrication and the silicon nitride was found to exhibit loss at the shorter wavelength end of the visible spectrum.

The 150 nm thick aluminium film of the simulated structure was characterised by the electromagnetic parameters outlined by Rakić [216] and was positioned between a 3 µm silicon dioxide membrane and a 200 nm silicon dioxide cap layer, which had a complex refractive index given by: $n = 2.04 + i\ 0.16$. An S Parameter Analysis tool, as described in Chapter 4 and consisting of a broadband plane wave source, transmission monitor and reflection monitor was used in the simulation. Anti-symmetric and symmetric boundary conditions were used in x and y, respectively and PMLs were used in the z direction. The maximum mesh cell sizes through the cERR were 75 nm in the x and y directions and 25 nm in the z direction. A schematic of the unit cell is shown in Figure 6.5(a) and the corresponding dimensions of the cross are shown in Table 6.1. The simulation layout is shown in Figure 6.5(b). The simulation results, including the extracted effective permittivity, from each of the MM Filter 1 and MM Filter 2 are shown in Figure 6.6, respectively.

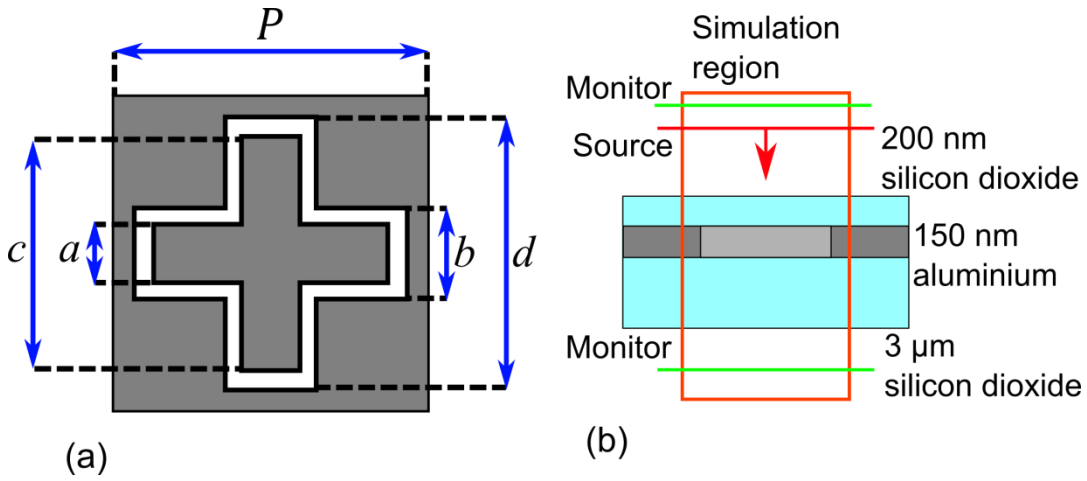

Figure 6.5 Schematic of the terahertz (THz) metamaterial (MM) filter design. (a) Top-down view of the MM filter. *P* denotes the array period; *a*, *b*, *c* and *d* denotes the filter dimensions. (b) Cross section of the simulated MM filter. The orange box encloses the simulated unit cell.

Parameter	MM Filter 1 (µm)	MM Filter 2 (µm)
a	6	5
b	8	10
c	21	20
d	23	26
P	27	27

Table 6.1 Geometric parameters for the two metamaterial (MM) filters.

From Figure 6.6(a) and Figure 6.6(c) it can be observed that MM Filter 2, with larger etch gaps corresponding to a lower metal fill factor, exhibits higher transmission and a wider bandwidth than MM Filter 1. A high metal fill factor is desirable when considering hybridisation with plasmonic filters, as it maximises the area available for patterning with hole arrays. Despite exhibiting lower transmission than MM Filter 2, the narrower bandwidth of MM Filter 1 makes it more desirable for filtering applications due to the greater degree of frequency selectivity.

From the extracted effective permittivity of the MM filters, shown in Figure 6.6(b) and Figure 6.6(d) it can be observed that real component of the permittivity crosses zero at resonant frequency of the MM. This corresponds to an effective plasma frequency. The imaginary component of the permittivity is small at the resonant frequency. These characteristics are typical of this type of MM, as described in Chapter 2, and correspond to an effective Drude response.

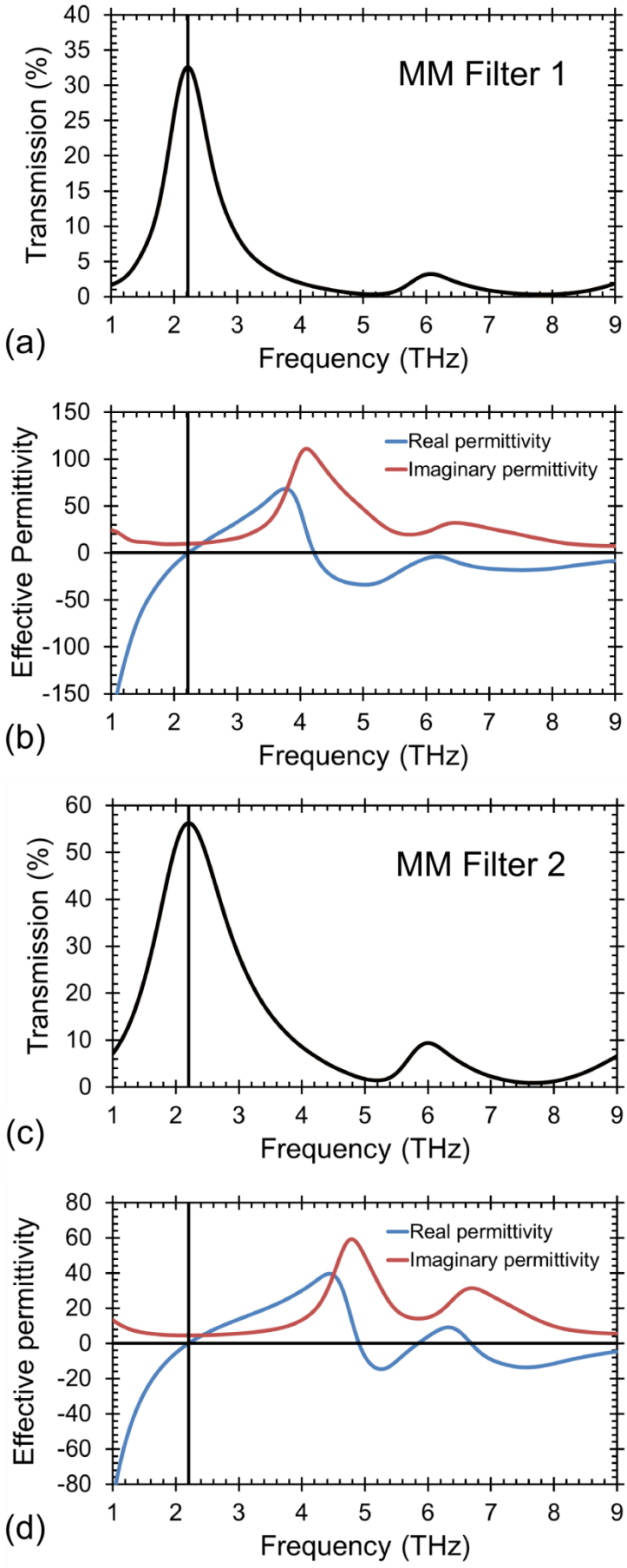

Figure 6.6 Metamaterial (MM) filter simulation results and extracted effective permittivity. MM Filter 1: (a) Simulated transmission spectrum. (b) Complex effective permittivity of the MM filter; MM Filter 2: (c) Simulated transmission spectrum. (d) Complex effective permittivity of the MM filter.

6.2.2 Fabrication

The fabrication process consisted of building up the MM filter layers on a silicon substrate, before back etching the silicon to leave the thin supporting membrane. A 4 inch silicon wafer with a thickness of approximately 300 µm was solvent cleaned using acetone and then isopropyl alcohol (IPA), with 5 minutes of ultrasonic cleaning at each stage. The wafer was then rinsed with reverse osmosis (RO) water. A 3 µm silicon dioxide layer was deposited on to the silicon wafer using plasma enhanced chemical vapour deposition (PECVD) followed by a 150 nm aluminium film using metal evaporation. A 50 nm silicon nitride layer was then deposited on to the aluminium surface using inductively coupled plasma enhanced chemical vapour deposition (ICP-CVD).

The silicon nitride surface was spin coated with Microposit Primer, to improve adhesion of the resist to the substrate, followed by spin coating with a protective layer of S1818 photoresist. The Microposit Primer was spin coated at 4,000 rpm for 5 seconds, then baked on a hot plate at 120 ºC for 1 minute. The S1818 was spin coated on the sample surface at 4,000 rpm for 30 seconds and baked on a hot plate at 105 ºC for 5 minutes. The wafer was then scribed and cleaved into multiple 2 cm x 2 cm squares and the small pieces underwent cleaning steps to remove the S1818 photoresist. This was achieved by solvent cleaning the samples, as described previously, followed by an oxygen (O_2) plasma clean in the Barrel Asher at 200 W for 5 minutes, which was then followed by a repeat of the solvent cleaning steps. The fabrication process then continued as was described in Chapter 5, Section 5.1.2 for the plasmonic filters.

In addition to the cERR structures, which extended over a region of 12 mm x 12 mm, large alignment marker crosses were positioned at each corner of the cERR region. The alignment cross arms were 550 µm long and 60 µm wide and were used to align to corresponding cross structures on the photomask. For the electron beam lithography (EBL) step the resolution was 1 nm, the VRU was 50 and the beam spot size was 50 nm with a dose of 400 µC/cm^2. SEM images of the fabricated cERR array for MM Filter 1 and MM Filter 2 are shown in Figure 6.7.

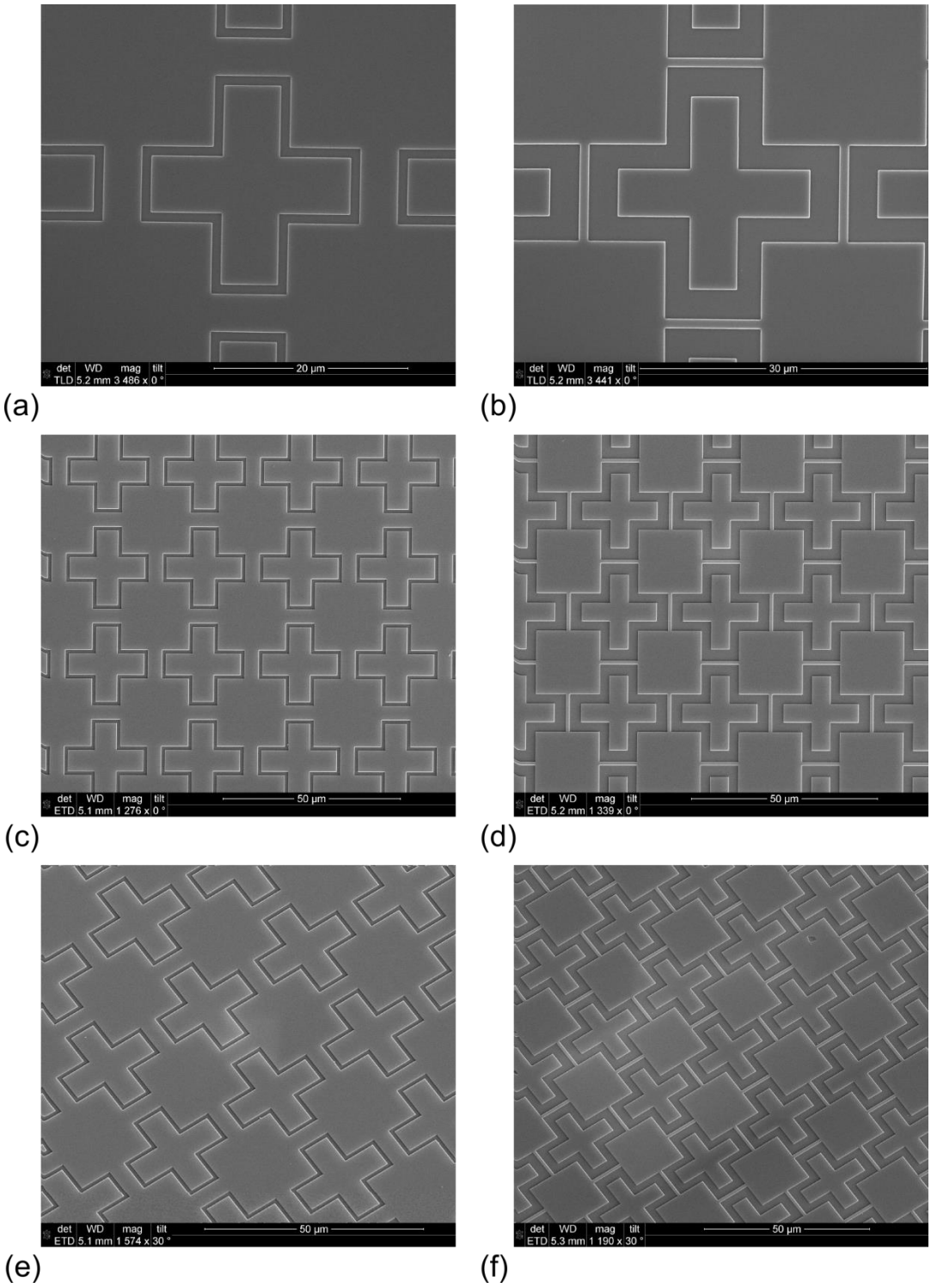

Figure 6.7 Scanning electron micrographs of the complementary electric ring resonator (cERR) arrays etched into a 150 nm aluminium film. MM Filter 1 is shown in (a, c, e) and MM Filter 2 is shown in (b, d, f). The sample is rotated by 30º in (e, f).

After deposition of the 200 nm silicon dioxide cap layer, it was necessary to etch the underside of the silicon substrate, to leave the MM filter membrane. A protective layer of S1818 photoresist was spin coated on to the sample surface, as described previously, prior to processing. The silicon surface was spin coated with AZ4562 photoresist at 3,000 rpm for 30 seconds and then placed in an oven at 90 ºC for 40 minutes. This corresponds to a

resist thickness of 7.4 µm. The Suss Microtec Mask Aligner 6 (MA6) was used to expose a 10 mm diameter circle hole from a photomask into the AZ4562 resist. Back side alignment was used to align crosses on the aluminium layer with crosses in the photomask. This ensured that the 10 mm diameter circular window in the silicon was centred on the 12 mm square cERR array. The sample was exposed for 35 seconds and then developed using a mixture of 4 parts RO water and 1 part AZ400K developer for approximately 4 minutes, before being rinsed in RO water. Following development of the photoresist, the sample was exposed to O_2 plasma in the Barrel Asher at 50 W for 1 minute, before being baked on a hot plate at 120 °C for 5 minutes.

A silicon wafer was then used as a carrier for the MM filter samples during dry etch processing. The wafer was spin coated with AZ4562 using the process described previously and hard baked on a hot plate at 120 °C for 5 minutes. The MM filter samples were placed on the carrier wafer using cool grease and the circular window was etched into the silicon using octafluorocyclobutane/sulphur hexafluoride/oxygen ($C_4F_8/SF_6/O_2$) with a flow rate of 110/130/13 sccm at 900 W with a pressure of 36 mTorr in a STS ICP RIE tool. The sample was then removed from the wafer and cleaned using hot acetone and IPA. The fabrication procedure is illustrated in Figure 6.8.

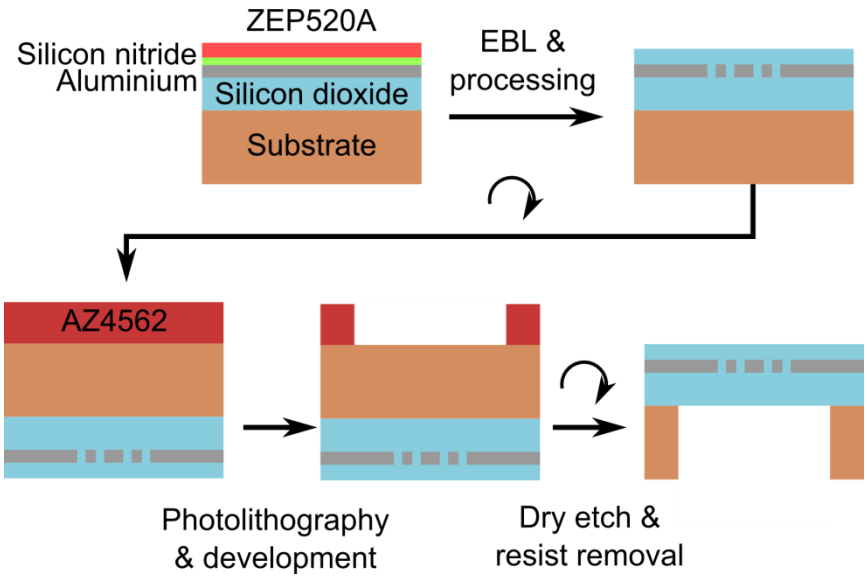

Figure 6.8 Illustration of metamaterial (MM) filter fabrication process flow. After fabrication of the MM structures using electron beam lithography (EBL) and dry etch, the sample is rotated and the silicon surface is spin coated with AZ4562 photoresist. Photolithography is then used to expose a 10 mm diameter circular window into the resist and dry etch processing is used to etch the circular window into the silicon substrate, which leaves the MM filter membrane.

6.2.3 Characterisation and Results

The MM filters were characterised using the Bruker IFS 66v/S FTIR and the experimental procedure outlined in Chapter 4. The measured transmission spectra of MM Filter 1 and MM Filter 2 are shown in Figure 6.9(a) and Figure 6.9(b), respectively. MM Filter 1 and MM Filter 2 exhibit transmission peaks of 34 % at 2.74 THz and 64 % at 2.75 THz, respectively. Simulation results for the MM filters are also shown for comparison. There was a slight spectral shift observed in the transmission spectra of the fabricated filters when compared with the simulated filters presented in Figure 6.6. This may be a result of variation in the deposited silicon dioxide properties between samples and simulations, or due to flexing of the membrane material. This shift can be accounted for by using a dielectric layer with a refractive index given by $n = 1.68 + i\ 0.16$ in the simulation, as shown in Figure 6.9. In this case, the refractive index of the dielectric acts as a fitting parameter to account for variation between the experimental results and the initial simulations.

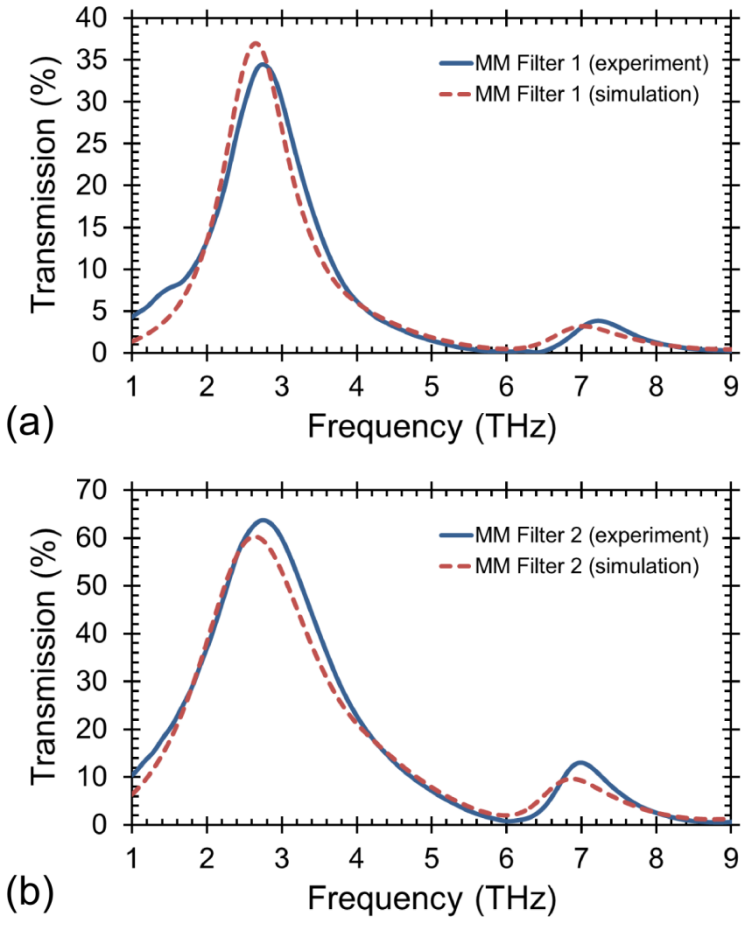

Figure 6.9 Comparison of experimental and simulation results for the metamaterial (MM) filters. (a) MM Filter 1 experimental and simulated transmission spectrum. (b) MM Filter 2 experimental and simulated transmission spectrum.

6.3 Metamaterial Absorbers

Four different MM absorber designs were investigated, each with consideration given to hybridisation with plasmonic filters. The first design used a conventional electric ring resonator (ERR) array, dielectric spacer and ground plane MM absorber structure, which could simplify and improve integration with complementary metal-oxide semiconductor (CMOS) technology, when compared with other absorber structures. The second MM absorber further developed the first absorber design by exploring the impact of a low metal fill factor ERR array to increase the transmitted light to the ground plane, which is beneficial for increasing transmission from the plasmonic filters as will be explored in Chapter 7. The third absorber used two thin concentric ERR crosses within each unit cell, to absorb at two THz frequencies and the fourth design combined a MM filter style top layer, consisting of an array of cERRs, with a metallic ground plane to create an absorber. Simulations and early fabrication of the third and fourth MM absorber designs were performed, however they were not explored in significant detail as it was concluded that the first and second designs were better suited for this project.

Lumerical FDTD Solutions was used to simulate and optimise the MM absorbers. The fabrication process is outlined and from the experimental results, it is shown that the absorption spectra from the fabricated MM absorber structures are in good agreement with the simulation results.

6.3.1 Design and Simulation

MM absorbers are typically 3-layer structures consisting of an ERR array, dielectric spacer and a ground plane, built on a substrate. As a goal of this work was to integrate MMs with plasmonic filters, it was necessary to ensure that the substrate material and dielectric spacer were both transparent, and preferably composed of the same material to satisfy the refractive index matching condition at each interface. The plasmonic filters described in Chapter 5 and composed of a 150 nm aluminium film also had to be part of this structure.

The main MM absorber, which will be referred to as MM Absorber 1, used a glass substrate, 150 nm aluminium ground plane and a 3 µm silicon dioxide spacer with a 150 nm thick aluminium ERR array composed of aluminium. The impact of varying the cross structure, thickness and unit cell period of Absorber 1 was investigated by simulations. MM Absorber 2 used the same layer structure as MM Absorber 1, however a different unit cell period and ERR dimensions were used to try to reduce the metal fill factor and maximise the light being transmitted through to the ground layer. MM Absorber 3 was a

dual band absorber with the same layer structure as described for MM Absorber 1, but with two thin concentric ERR crosses within each absorber unit cell. For these three designs, the intention would be to fabricate plasmonic filters into the ground plane of the absorber, as will be explored in Chapter 7. MM Absorber 4 used an alternative design that consisted of a 150 nm aluminium top layer patterned with cERR-style structures, and a perforated 150 nm aluminium ground plane. In this case the intention would be to fabricate plasmonic filters into the top layer, and consequently a 200 nm silicon dioxide layer was required on the top aluminium surface. As MM Absorber 1 and MM Absorber 2 were the main absorber structures used in this work several designs based on this structure were simulated, fabricated and characterised. Only simulation results and preliminary fabrication work for Absorbers 3 and 4 are presented. The dimensions associated with the different absorber structures are listed in Table 6.2 and the four absorber structures investigated in this work are illustrated in Figure 6.10.

The absorber simulation layout is similar as to what was described previously for the MM filters. For MM Absorber 1, a 150 nm aluminium ground plane was separated by a 150 nm thick ERR structure by a 3 µm silicon dioxide dielectric spacer, as shown in Figure 6.10(a). The electromagnetic parameters described by Rakić [216] were used to define the aluminium layers and the silicon dioxide was modelled using the complex refractive index: $n = 2.04 + i\ 0.16$. A S Parameter Analysis tool was used to provide the source and monitors. The boundary conditions and mesh override were as described for the MM filters simulations in Section 6.2.1. The absorption spectrum and extracted electromagnetic parameters for MM Absorber 1 are shown in Figure 6.11. The absorption spectrum was calculated using equation (3.61), which is dependent on the reflection and transmission spectra from the MM absorber.

Parameter	MM Absorber 1 (µm)	MM Absorber 2 (µm)	MM Absorber 3 (µm)	MM Absorber 4 (µm)
a	5	6	5, 9	6
b	10	9	6, 10	8
c	20	21	20, 25	21
d	26	25	21, 26	23
P	27	30	27	27

Table 6.2 Geometric parameters for the four metamaterial (MM) absorbers.

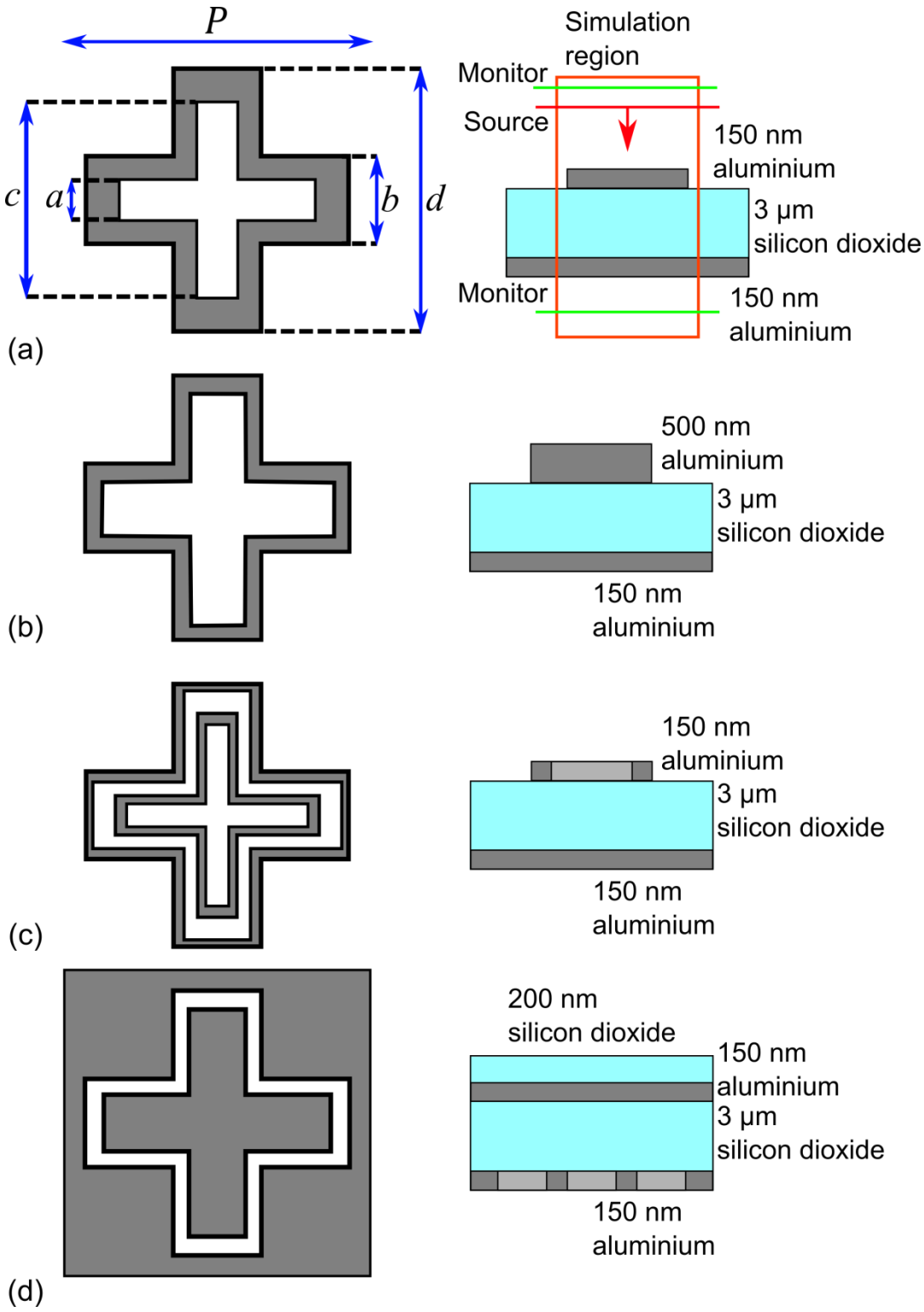

Figure 6.10 Schematic illustrations of the four terahertz (THz) metamaterial (MM) absorbers. Schematic of the top down view and cross section for (a) MM Absorber 1, (b) MM Absorber 2, (c) MM Absorber 3 and (d) MM Absorber 4. *a*, *b*, *c* and *d* in (a) denote the geometry of the ERR structure and *P* is the unit cell period, as is listed in Table 6.2. The dimensions and simulation set up shown in (a) also apply to (b-d).

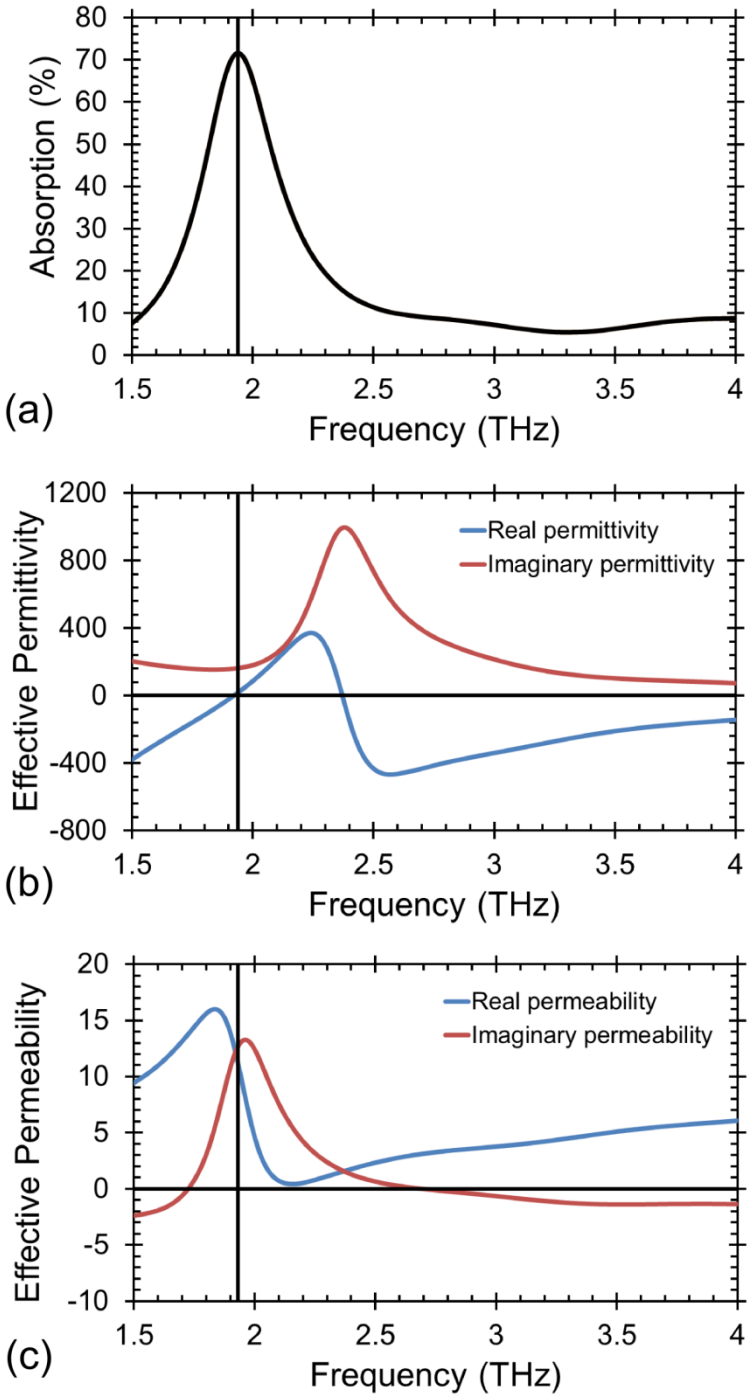

Figure 6.11 Metamaterial (MM) Absorber 1 simulation results and extracted effective permittivity. (a) Simulated absorption spectrum. (b) Extracted complex effective permittivity. (c) Extracted complex effective permeability.

It can be observed in Figure 6.11(a) that MM Absorber 1 exhibits narrowband absorption with a peak of 72 % at 1.94 THz. It can also be seen from Figure 6.11(b) and Figure 6.11(c) that MM Absorber 1 displays effective electromagnetic characteristics that are typical of this type of MM absorber, as was discussed in Chapter 2. At resonance the effective permittivity exhibits a Drude-like response, with a Lorentz-like resonance at a higher frequency. There is also a Lorentz-like response at resonance in the effective permeability.

MM Absorber 2 uses the same layer structure as MM Absorber 1, however with a thinner cross and larger array period, leading to a smaller metal fill factor. The thinner cross structure in x and y led to decreased absorption, however it was found that by using a thicker cross in the z direction the absorption properties could be improved. MM Absorber 2 simulations results for varying ERR array thickness, t, is shown in Figure 6.12. The simulation set up was as described previously for MM Absorber 1.

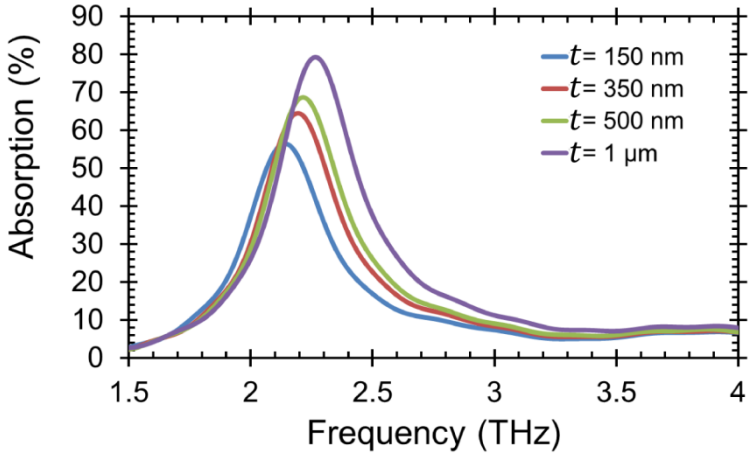

Figure 6.12 Metamaterial (MM) Absorber 2 simulation results for varying electric ring resonator thicknesses, given by t.

It can be observed in the MM Absorber 2 simulation results presented in Figure 6.12 that there is a general trend of increasing absorption for thicker ERR layers. The improvement in absorber performance can possibly be attributed to the relative size of the cross thickness compared to the aluminium skin depth; for thicker crosses there is a larger metal volume that the incident radiation can interact with. The absorption magnitude varies from 57 % when t = 150 nm, to 79 % when t = 1 µm. A slight blue shift can also be observed in the peak position. The main ERR thickness used for MM Absorber 2 was 500 nm, to act as a trade-off to ensure fast metal evaporation compared with thicker ERRs and improved absorption compared with thinner ERRs. In this case, the absorption magnitude is 69 % at 2.22 THz.

MM Absorber 3 was simulated using the same method outlined for MM Absorber 2. The absorption spectrum is shown in Figure 6.13. It can be observed that two absorption peaks are present however absorption is substantially lower than has been shown for MM Absorber 1 and MM Absorber 2. Consequently, MM Absorber 3 is unsuitable for this project when compared with the other two absorbers, however it may be possible to find a method to improve the absorption characteristics by performing a more in depth simulation study on the structure.

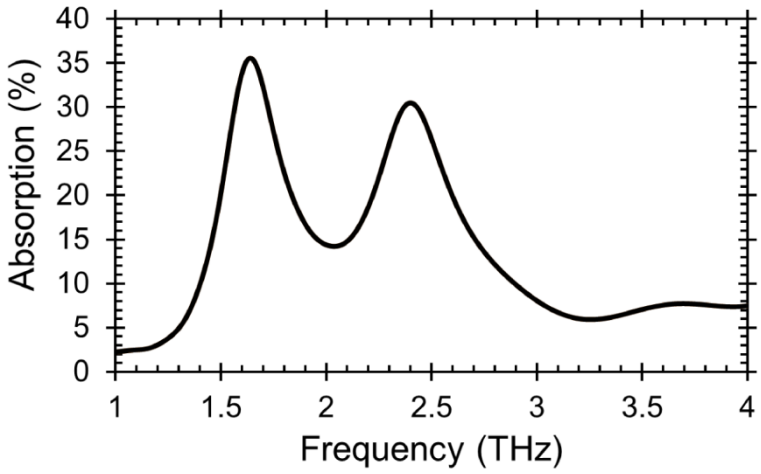

Figure 6.13 Metamaterial (MM) Absorber 3 simulated absorption spectrum.

MM Absorber 4 was simulated using the same method described for the previous three MM absorbers. Additional simulations were performed for large perforations in the ground plane, with the assumption that when integrated with plasmonic filters, the holes in the ground plane would allow transmission of visible light through the material. The perforations simulated correspond to 5 µm silicon dioxide squares in the ground plane, resulting in 9 squares per unit cell, and a single 17 µm silicon dioxide square in the ground plane, corresponding to a single window per unit cell. The simulation results for a solid, unperforated ground plane, and the ground planes with the 5 µm and 17 µm windows are shown in Figure 6.14. The ground planes are also illustrated in Figure 6.14.

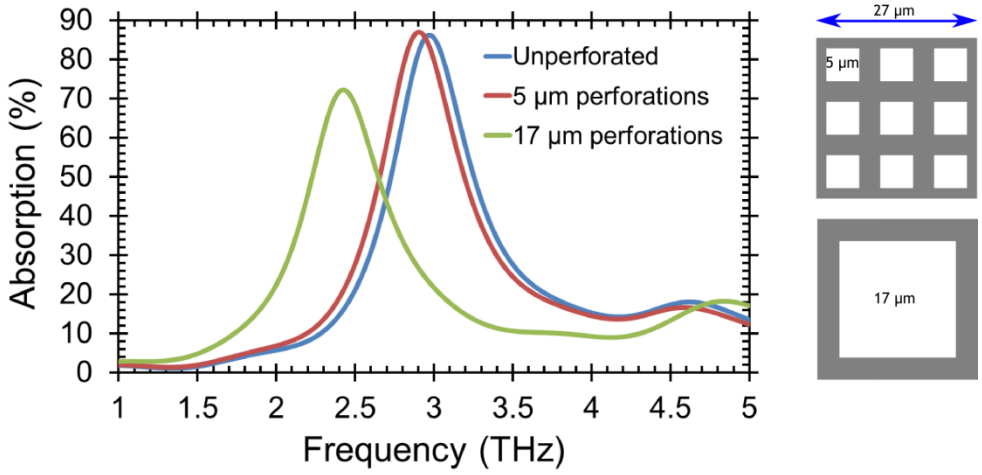

Figure 6.14 Metamaterial (MM) Absorber 4 simulated absorption spectrum for different ground plane perforations, as shown to the right of the graph.

MM Absorber 4 can be seen to exhibit high transmission for all three cases presented. There can also be seen to be little change in the spectral properties of the MM absorber when no perforations are present and when 5 µm perforations are present. The single, larger 17 µm perforation in the ground plane results in a decrease in absorption and a shift in the peak frequency, however absorption still remains high. Consequently, this MM absorber was a good candidate for integration with plasmonic filters and some early fabrication work was performed, as will be described in this Chapter and in Chapter 7. However, due to perceived complications for integration with CMOS technology, MM Absorber 1 and 2 were deemed more suitable for this project.

6.3.2 Fabrication

The fabrication process for MM Absorber 1 and 2 used metallisation and dielectric deposition steps to build up the MM layers on a glass substrate, with a lift off process to define the ERR array. The glass substrate was solvent cleaned using Opticlear, acetone and then IPA, with 5 minutes of ultrasonic agitation at each stage, followed by rinsing in RO water. 150 nm of aluminium was then evaporated on to the glass surface and 3 µm of silicon dioxide was evaporated on to the sample surface using PECVD. The ERR array was then fabricated on the top silicon dioxide layer using a lift off process.

A 1.2 µm thick bilayer of poly-methyl methacrylate (PMMA) was spin coated on to the silicon dioxide, consisting of 15 % 2010 PMMA, followed by 4 % 2041 PMMA. Each layer was spin coated at 5,000 rpm for 1 minute and baked on a hot plate at 154 ºC for 2 minutes. The ERR array pattern was exposed over an area of 12 mm x 12 mm using EBL with 1 nm resolution, a spot size of 50 nm, a VRU of 50 and a dose of 500 µC/cm^2. The patterned PMMA was developed using isopropyl alcohol:methyl isobutyl ketone (IPA:MIBK) with a ratio of 1:1 for 45 seconds at 23 ºC, before being rinsed in IPA and exposed to O_2 plasma at 50 W for 1 minute. Aluminium was then evaporated on the sample surface, and the surplus metal and remaining resist was removed using hot acetone and rinsed in IPA. 150 nm of aluminium was used for MM Absorber 1 and MM Absorber 2 was fabricated using 150 nm and 500 nm thick ERRs. SEM images of the fabricated ERR arrays for MM Absorber 1 and 2 are shown in Figure 6.15. The fabrication procedure is illustrated in Figure 6.16.

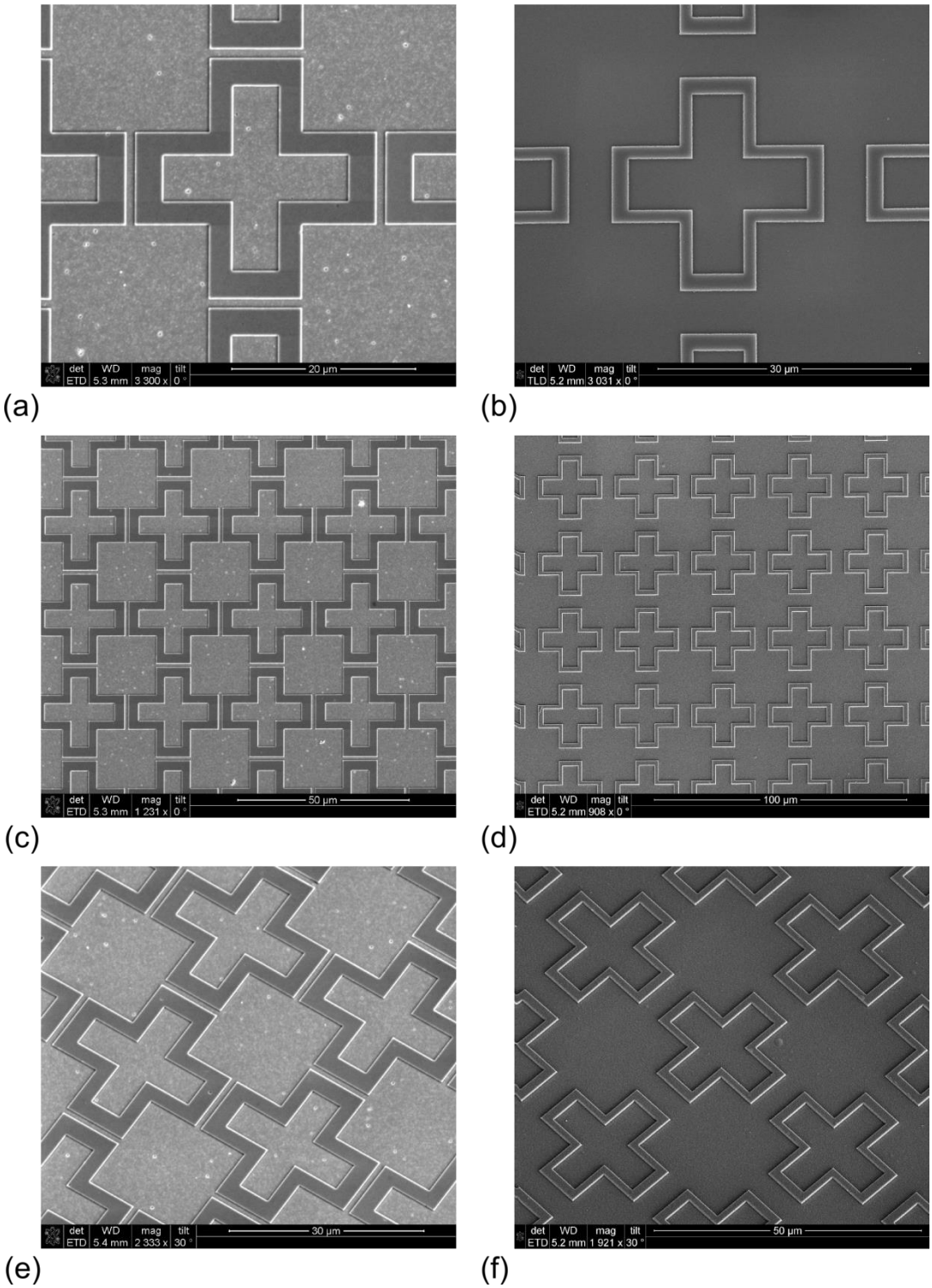

Figure 6.15 Scanning electron micrographs of the electric ring resonator (ERR) arrays of metamaterial (MM) Absorber 1 and MM Absorber 2. MM Absorber 1 is shown in (a, c, e) and MM Absorber 2 is shown in (b, d, f). The sample is rotated by 30º in (e, f).

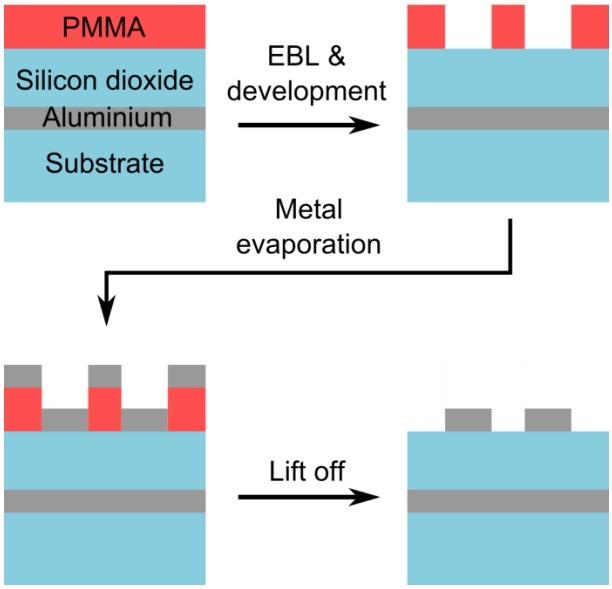

Figure 6.16 Illustration of metamaterial (MM) absorber electric ring resonator (ERR) array fabrication process flow. After evaporation of the aluminium ground plane and deposition of the silicon dioxide spacer, the ERR array is patterned into the electron beam resist. Following development of the resist, metal lift off is performed to create the ERR array on the top surface of the sample.

Early fabrication processing was performed for MM Absorber 3 and MM Absorber 4, the result of which can be seen in the optical microscope images shown in Figure 6.17. The images presented in Figure 6.17 are dose tests of the cross arrays, with no ground plane present. Both cross arrays were fabricated using the plasmonic filter fabrication method comprising EBL and dry etch steps as outlined in Chapter 5, Section 5.1.2.

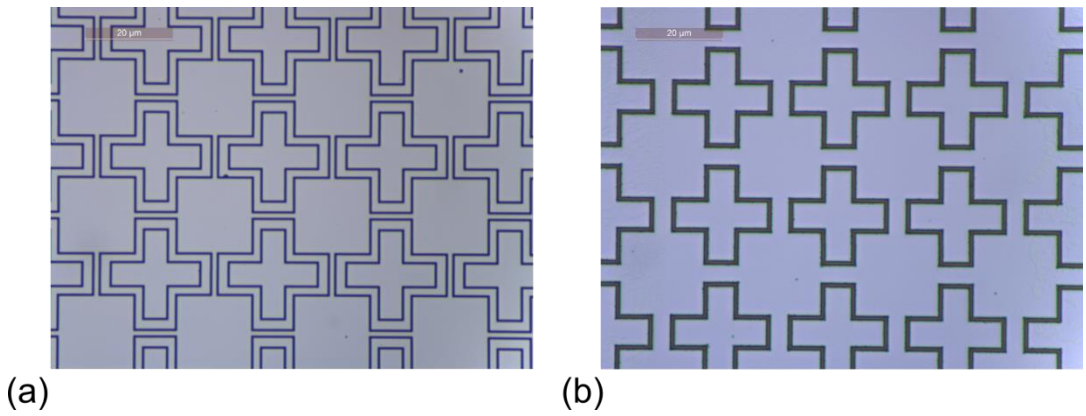

Figure 6.17 Optical microscope images of metamaterial (MM) Absorber 3 and 4 cross arrays from dose tests. (a) Transmission microscope image of MM Absorber 3 electric ring resonator (ERR) array. (b) Reflection microscope image of MM Absorber 4 complementary electric ring resonator (cERR) array.

6.3.3 Characterisation and Results

MM Absorber 1 and MM Absorber 2 were characterised using the Bruker IFS 66v/S FTIR and the measurement method described in Chapter 4. The absorption spectrum can be determined by measuring the reflection and transmission from each absorber, however as transmission was negligible due to the continuous metal ground plane, a transmission measurement was not necessary. The measured absorption spectrum of MM Absorber 1 is shown in Figure 6.18. The results of the simulated absorber are also shown for comparison. It can be observed that there is good agreement between both simulation and experimental results: the fabricated absorber exhibits an absorption peak of 67 % at 1.93 THz and the simulated absorber exhibits an absorption peak of 72 % at 1.94 THz.

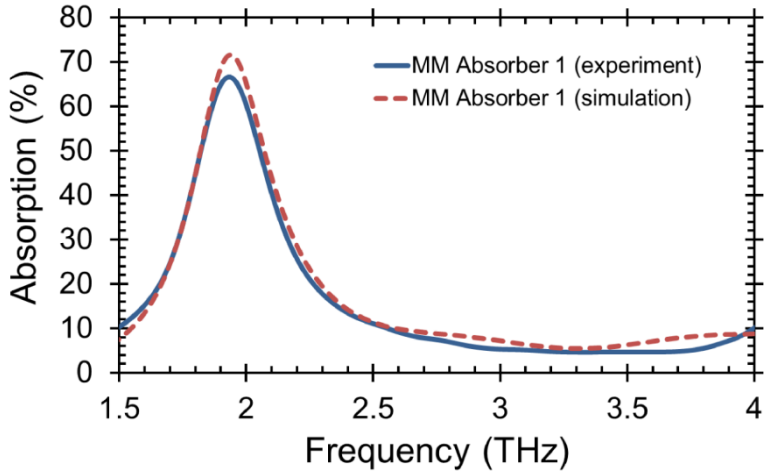

Figure 6.18 Comparison of experimental and simulation results for metamaterial (MM) Absorber 1.

The absorption spectra for MM Absorber 2 with the 150 nm thick ERR array and 500 nm thick ERR array are shown in Figure 6.19. The simulation results for the different MM Absorber 2 ERR array thicknesses are shown for comparison. The experimental results show an absorption peak of 49 % at 2.12 THz when t = 150 nm, and an absorption peak of 64 % at 2.18 THz when t = 500 nm. There is good agreement between the results of the simulated and fabricated MM Absorber 2 structures, and the experimental results can be seen to follow the trend shown in the simulation results, where thicker ERR layers results in higher absorption and a shift in the peak position.

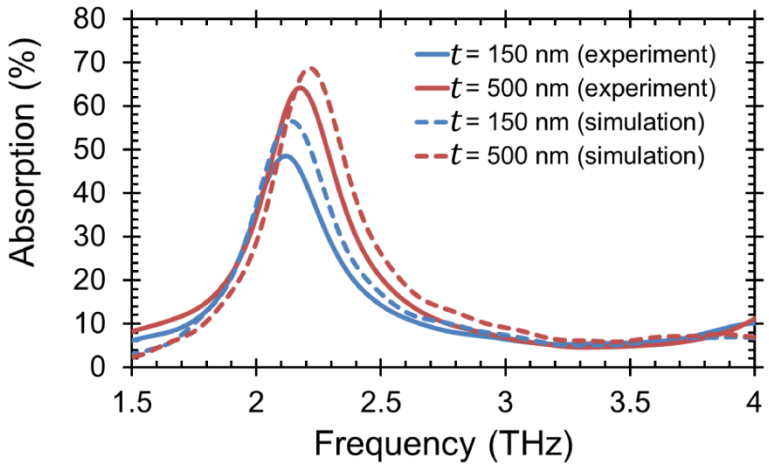

Figure 6.19 Comparison of experimental and simulation results for metamaterial (MM) Absorber 2 for different electric ring resonator thicknesses, given by t in the figure legend.

The simulation results shown in Figure 6.18 and Figure 6.19 correspond to MM absorbers with dielectric layers characterised by the refractive index: $n = 2.04 + i\ 0.16$. This is the same complex refractive index that was used previously for the MM filter simulations presented in Section 6.2.1 and the MM absorber simulations presented in Section 6.3.1. As was the case for the comparison of experimental and simulation results for the MM filters presented in Section 6.2.3, the refractive index of the dielectric layer acts as a fitting parameter. However there is a discrepancy between the real component of the refractive index of the dielectric used in the MM filter simulations (n_1 = 1.68), and the MM absorber simulations (n_1 = 2.04), despite the dielectric film having been deposited using the same method.

The real component of the refractive index of silicon dioxide has been quoted as being equal to 1.965 at 2 THz [241], which is is in good agreement with the real component of the refractive index used in the MM absorber simulations. However, the refractive index that is required to fit the MM filter simulations to the experimental data is significantly smaller than expected. As mentioned previously, this can possibly be attributed to flexing of the MM filter membrane. There could also be variations in deposition between different fabricated samples. The different substrate materials used for the MM absorbers and MM filters may also influence the properties of the deposited film. Nonetheless, the size of the discrepancy between the real refractive index components used in the different models suggests that other factors may be impacting the observed characteristics of the MM filters.

6.4 Summary

The electromagnetic properties of a MM can be engineered by altering its geometric parameters on the subwavelength scale. The lack of natural materials with frequency selective THz properties make MMs well suited for THz imaging applications. This is particularly true of MM absorbers, which could be used to develop a THz imaging system by integrating the absorber with a bolometric sensor, as has been described in Chapter 2. The suitability of MMs for THz imaging applications and the ability to engineer their characteristics makes them a valuable component to be considered alongside plasmonic filters for use in a multi-spectral imaging (MSI) system operating over a large wavelength range.

In this Chapter, a range of different MM filters and MM absorbers, with engineered properties at THz frequencies have been simulated, fabricated and characterised. The MM structures have been designed to be integrated with plasmonic filters, and with MSI applications in mind. The sensitivity of plasmonic filters to the dielectric properties of metals, in addition to the relative length scales of optical plasmonic structures when compared with THz MMs geometries meant that hybridisation required the plasmonic filter design to be “fixed” and the THz MMs designed around the plasmonic filter requirements. This was also necessary to ensure hybridisation was simplified by using common fabrication methods and materials between plasmonic filters, as presented in Chapter 5, and the MMs presented in this Chapter. In the following Chapter, the results from hybridisation of plasmonic filters and MMs to create SMMs will be presented.

7. Multi-Spectral Materials

Multi-spectral imaging systems operating over multiple spectral regions typically require different materials, detectors and detection methods for each spectral band, therefore presenting several challenges in the development of a single camera capable of imaging over a large wavelength range. Many of these issues can potentially be overcome by hybridising different structured photonic materials that can exploit different resonant phenomena, whilst using common materials and fabrication processing. Plasmonic filters and metamaterials, as presented in Chapter 5 and Chapter 6, respectively, can be fabricated using the same processes and materials, therefore it is possible to hybridise plasmonic and metamaterial structures to create multi-spectral materials, with engineered resonances ranging from visible to terahertz wavebands. Hybridisation of these structures could lead to the development of a coaxial multi-spectral imaging system, where each spectrally selective pixel could share a common axis. This would maximise the spectral information density of the optical system which could lead to small, high resolution multi-spectral imagers. It could also eliminate the problems presented by spatial variation between spectrally different regions on the surface of the imager, which could reduce errors, improve image quality and simplify image processing.

In this Chapter, synthetic multi-spectral materials capable of operating from visible to terahertz wavelengths and consisting of hybridised plasmonic and metamaterial components are presented. Due to the relative length scales of the optical and terahertz components, they have negligible impact on the resonant properties of each other, therefore it is reasonable to design and optimise both structures independently as has been presented in Chapters 5 and 6. Some discussion and simulation results are presented to support this statement.

7.1 Nanoholes at Terahertz Frequencies

The wavelength of terahertz (THz) radiation and the metamaterial (MM) unit cell periods are significantly larger than the diameter of the holes that compose the plasmonic filters. Consequently, a sufficiently fine simulation mesh to accurately represent the hole arrays resulted in very high memory requirements, making simulation of the complete synthetic multi-spectral materials (SMM) impractical. To overcome this issue, the impact of nanoholes on the optical characteristics of an aluminium film at THz frequencies was investigated.

The initial simulations consisted of an aluminium film, defined by the complex refractive index parameters presented by Rakić [216], illuminated using a broadband THz source. Transmission and reflection spectra from either side of the film were recorded in the range from 1 THz to 9 THz. A single etch hole was placed in the film with a diameter of 140 nm and an array period of 250 nm, which was defined using anti-symmetric and symmetric boundary conditions in x and y, respectively. Perfectly matched layer (PML) boundary conditions were used in the z direction. A mesh override region was defined in the vicinity of the metal, that limited the maximum cell size to 5 nm in x, y and z. The aluminium thickness was varied from 50 nm to 200 nm and simulations were also performed for metal films without holes; it was discovered that transmission was negligible in all cases. The 50 nm film perforated with holes yielded the highest transmission of approximately $3.3\text{x}10^{-5}$ and transmission through the 150 nm aluminium film patterned with holes was of the order of 10^{-6}. This corresponds to an increase in transmission when compared with the unpatterned metal film, however transmission is still sufficiently low to represent the plasmonic filters as an optically thick unperforated metal film at THz frequencies.

Further simulations were performed using triangular hole arrays in a 150 nm aluminium film to accurately represent the plasmonic filters fabricated in this work. The simulation was prepared as described previously, for hole diameters of 130 nm and 290 nm with array periods of 230 nm and 550 nm, respectively. These array periods and hole sizes correspond to blue and near infrared (NIR) filters used in the first two SMMs, which are presented in Sections 7.2 and 7.3. Once again, the observed transmission was of the order of 10^{-6}. The largest array period and hole size in the third SMM, presented in Section 7.4, correspond to a period and diameter of 2.942 μm and 1.486 μm, respectively. The transmission in this case was of the order of 10^{-4}, demonstrating that the increasing hole size leads to higher transmission through the perforated metal film at THz frequencies, as expected. However, the transmission remains negligible through the perforated film such that it is still reasonable to consider the plasmonic filters as unperforated aluminium films at THz frequencies.

These results demonstrate that it is reasonable to consider the plasmonic and MM components independently when designing and simulating the structures for use in the SMMs, therefore the results presented in Chapters 5 and 6 represent the design process for the individual components that comprise the hybrid structures. However, additional consideration must be given to how the MM components impact the measured optical transmission from the plasmonic filters. The size of electric ring resonator (ERR) and

complementary electric ring resonator (cERR) unit cells ensures that they have minimal impact on the resonant properties of the plasmonic filters, however they can still lead to a decrease or increase in the measured transmission over the whole visible range. As this is a result of the measurement method, the spectra can be scaled to account for the presence of the MMs by considering the geometry of the individual MM structures. This will be discussed further in the subsequent sections with regards to the specific devices.

7.2 Multi-Spectral Filter

The first SMM is a multi-spectral filter that is capable of filtering 15 optical wavelengths and a single NIR wavelength whilst simultaneously filtering a single THz frequency. The SMM is a hybrid structure that combines the optical and NIR plasmonic filters, presented in Chapter 5, and a THz MM filter, presented in Chapter 6. The hybrid plasmonic and MM structures are patterned into a single film using a single lithographic step and therefore this device demonstrates that it is possible to engineer the electromagnetic characteristics of a single metal film over several decades of wavelength by virtue of unique structured photonic material components.

7.2.1 Design and Fabrication

The multi-spectral filter consists of 16 plasmonic filters corresponding to the array periods and hole sizes presented in Chapter 5, Section 5.1; and MM Filter 1 as was presented in Chapter 6, Section 6.2. The plasmonic and MM structures were etched into the same 150 nm thick aluminium film, such that the SMM was fabricated using a single metal film with a single electron beam lithography (EBL) process. Despite exhibiting lower transmission than MM Filter 2, MM Filter 1 had a narrower bandwidth and larger metal fill factor, therefore increasing the surface area which could be patterned with plasmonic filters.

The layer structure of the multi-spectral filter is unchanged from the layer structure of the MM filters presented in Chapter 6, and consequently similar processing steps can be used to fabricate the SMM. The SMM consists of a 3 μm silicon dioxide layer, a 150 nm aluminium film patterned with hole arrays and cERRs, and a 200 nm silicon dioxide cap layer. The structure is fabricated on a silicon substrate into which a 10 mm diameter hole is etched, thereby leaving the membrane structure and allowing optical and THz transmission measurements to be made. The cERR array extends over a square area of side length 12 mm and each plasmonic filter extends over a square area of side length 1 mm. Each plasmonic filter is a distance of 0.33 mm from the adjacent filters. A schematic showing the unit cell of the MM filter component of the SMM is shown in Figure 7.1(a), where the

geometric parameters correspond to those listed in Table 6.1 for MM Filter 1. An illustration of the SMM layout is shown in Figure 7.1(b) and a cross section of the SMM, showing the layer structure, is shown in Figure 7.1(c).

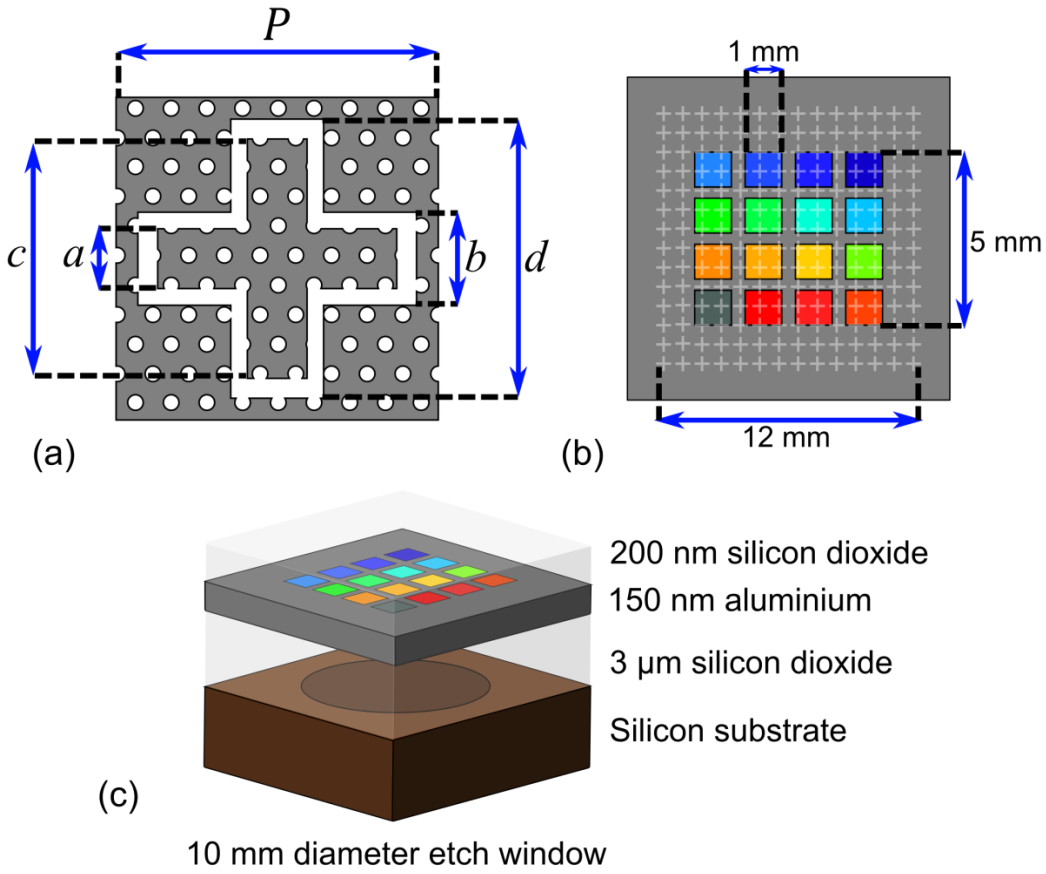

Figure 7.1 Schematic illustrations of the synthetic multi-spectral material (SMM) filter (not to scale). (a) Schematic of the terahertz (THz) metamaterial (MM) filter unit cell which also includes the plasmonic filter hole arrays. (b) Top down schematic of the SMM, illustrating the layout of the plasmonic filters and MM components. (c) 3D cross section of the multi-spectral filter.

As described in Section 7.1, the plasmonic filter and MM components of the SMMs can be simulated independently, and therefore the simulation results presented in Chapters 5 and 6 correspond to the optimised plasmonic filter and MM filter components of the SMM filter. The fabrication process for the multi-spectral filter follows the method outlined for the MM filters presented in Chapter 6, Section 6.2.2, however 16 plasmonic filters are also patterned into the ZEP520A resist during the EBL stage. The plasmonic filters and cERR array were etched into the aluminium film using the plasmonic filter fabrication method outlined in Chapter 5, Section 5.1.2. A scanning electron microscope (SEM) image of a cERR unit cell, and plasmonic filter hole array with a period of 430 nm is shown in Figure 7.2a. A SEM of the etched hole array, corresponding to a hole period of 430 nm is shown in Figure 7.2(b). Transmission microscope images over blue, green, yellow and red

plasmonic filter regions, corresponding to array periods of 250 nm, 340 nm, 380 nm and 430 nm, respectively, are shown in Figure 7.2(c-f).

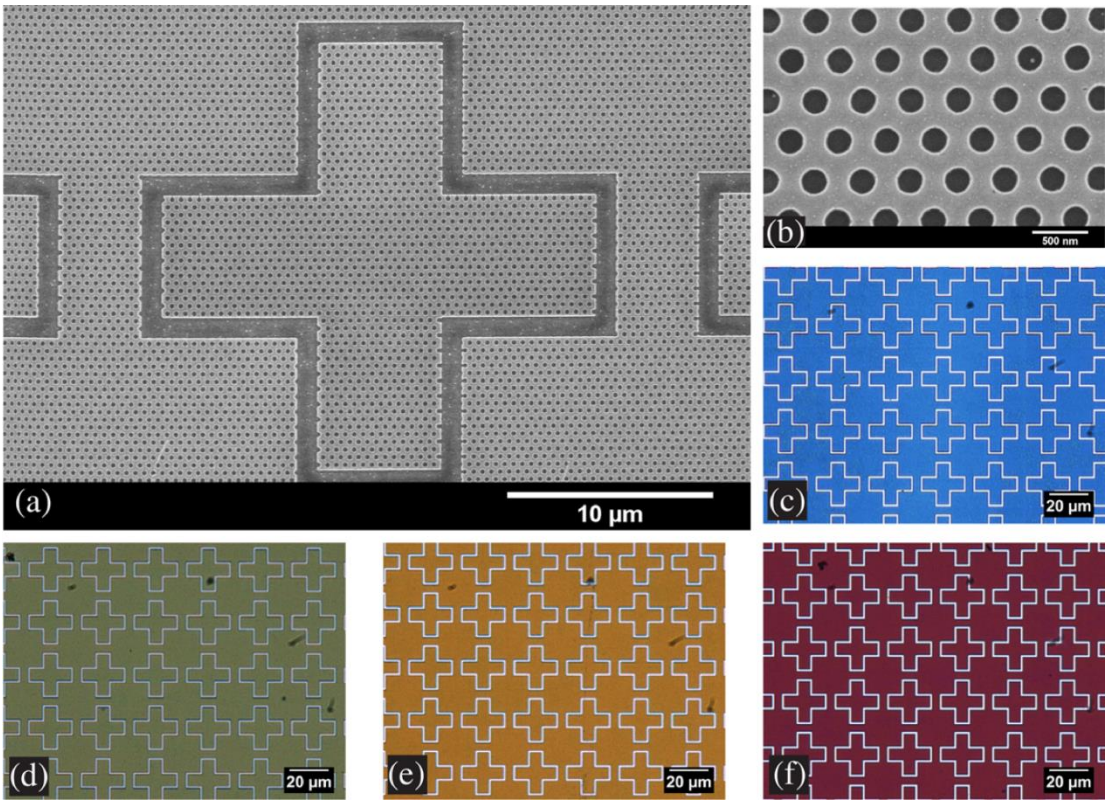

Figure 7.2 Images of the fabricated multi-spectral filter. (a) A scanning electron micrograph of the complementary electric ring resonator (cERR) unit cell and plasmonic filter hole array with an array period of 430 nm. (b) A scanning electron micrograph of a plasmonic filter hole array with an array period of 430 nm, corresponding to a red colour filter. (c) Transmission microscope images of blue (period = 250 nm), (d) green (period = 340 nm), (e) yellow (period = 380 nm) and (f) red (period = 430 nm) plasmonic filter regions of the synthetic multi-spectral material (SMM).

7.2.2 Characterisation and Results

The transmission measurements from the optical and NIR plasmonic filter components of the SMM were measured using the TFProbe MSP300 microspectrophotometer and transmission measurements from the THz MM filter component were measured using the Bruker IFS 66v/S Fourier transform infrared spectrometer (FTIR). The experimental method was as outlined in Chapter 4. The transmission spectra for the plasmonic filter components are shown in Figure 7.3(a-c). The legend denotes the array period, P, of each filter component and the hole diameter, d, that was measured using the SEM prior to deposition of the silicon dioxide cap layer. The transmission spectrum from the MM filter component of the SMM is shown in Figure 7.3(d). A plot showing transmission properties of the SMM over a large spectral range is shown in Figure 7.4. From these results it can be observed that the optical properties of the multi-spectral material have been engineered over several decades of wavelength by virtue of hybrid plasmonic and MM components.

Fabry-Perot oscillations can be observed in the measured transmission spectra of the plasmonic filters, shown in Figure 7.3(a-c), as a result of the silicon dioxide layer acting as a 3 μm cavity [121]. It can be observed that the oscillation peaks are slightly shifted between different filter spectra which can be attributed to slight flexing of the membrane due to stresses in the material.

The peak wavelengths of the 16 plasmonic filter components of the SMM, varying with array period, are compared with the simulated plasmonic filters in Figure 7.5(a). The simulated structure was the same as described previously in Chapter 5, Section 5.1.1, but in this case the measured hole sizes as listed in the legend of Figure 7.3, were used in the simulations. It can be observed that there is a linear relationship between peak wavelength and array period, however in certain regions, such as from 330 nm to 350 nm, the peak wavelength appears to plateau with increasing period. This can be attributed to Fabry-Perot oscillations.

The cERRs do not exhibit a resonant response at visible wavelengths and the plasmonic filter hole dimensions are sufficiently subwavelength to have no influence on the THz MM component of the SMM, as discussed in Section 7.1. However, the etched cERR structures in the aluminium film allow transmission of white light through the structure, as can be observed in Figure 7.2(c-f), and in the measured plasmonic filter spectra, shown in Figure 7.3(a-c). Due to the magnification of the objective lens and spot size used for the optical measurement, the white light due to the cERR has no dependence on measurement position and can be related to the metal fill factor of the aluminium film.

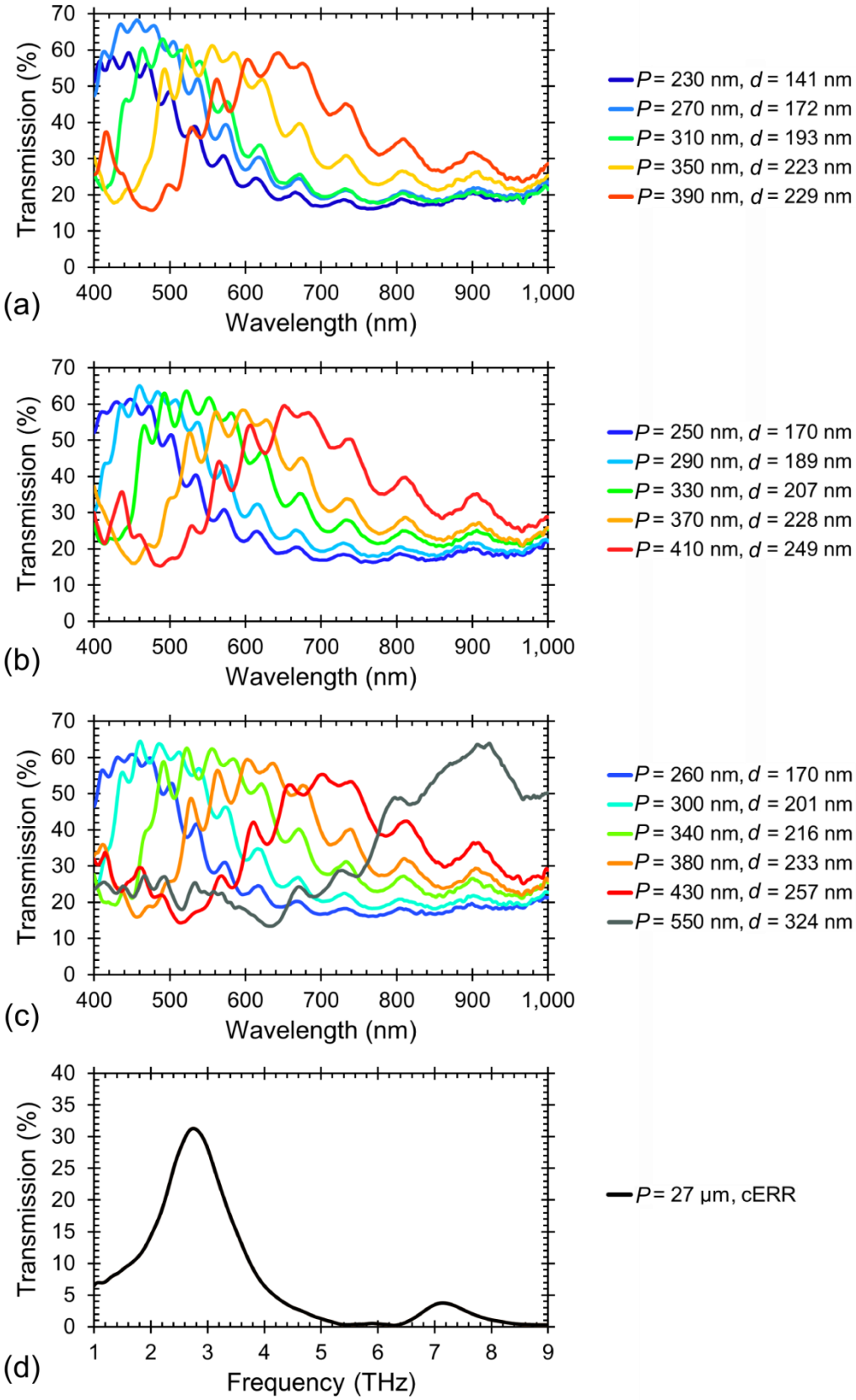

Figure 7.3 Measured transmission spectra for the synthetic multi-spectral material (SMM) filter. (a-c) Plasmonic filter component transmission spectra. (d) Metamaterial (MM) filter component transmission spectrum. The legend denotes the hole period, *P*, and the hole diameter, *d*.

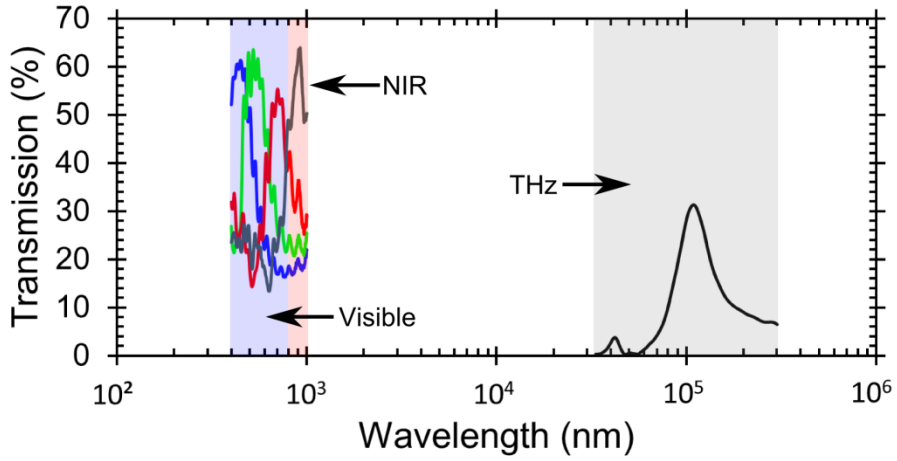

Figure 7.4 Measured transmission spectra from the multi-spectral filter corresponding to the blue (period = 250 nm), green (period = 330 nm), red (period = 430 nm) and near infrared (NIR) (period = 550 nm) plasmonic filter components and the terahertz (THz) metamaterial (MM) filter component.

In the case of MM Filter 1, as is used in the SMM, 88% of the surface area over each plasmonic filter region is metal and therefore patterned with hole arrays. Simulation results for blue, green and red plasmonic filters corresponding to array periods of 250 nm, 330 nm and 430 nm, respectively, and for the measured hole sizes that are listed in the legend of Figure 7.3 are shown in Figure 7.5(b). The simulation results are compared with the blue, green and red plasmonic filter components of the multi-spectral filter, where the transmission has been scaled with respect to the metal fill factor, to account for the presence of the cERR etch gaps. Consequently, the scaled experimental results correspond to an approximation of the plasmonic filter transmission spectra that would be observed if no MM components were present.

No Fabry-Perot oscillations are observed in the simulated plasmonic filter transmission spectra, as the simulated structures did not include a 3 µm silicon dioxide layer. Other than the expected lack of Fabry-Perot modes, there is good agreement between the scaled experimental spectra and the simulation results for the plasmonic filter component of the SMM. It may be possible to alter the cERR geometries such that metal fill factor is increased, thereby further reducing the impact of white light transmission through the etch gaps. By consideration of cERR positioning it may also be possible to further reduce, or even eliminate, the impact of the etched cross structures for a given application, such as complementary metal-oxide semiconductor (CMOS) imaging.

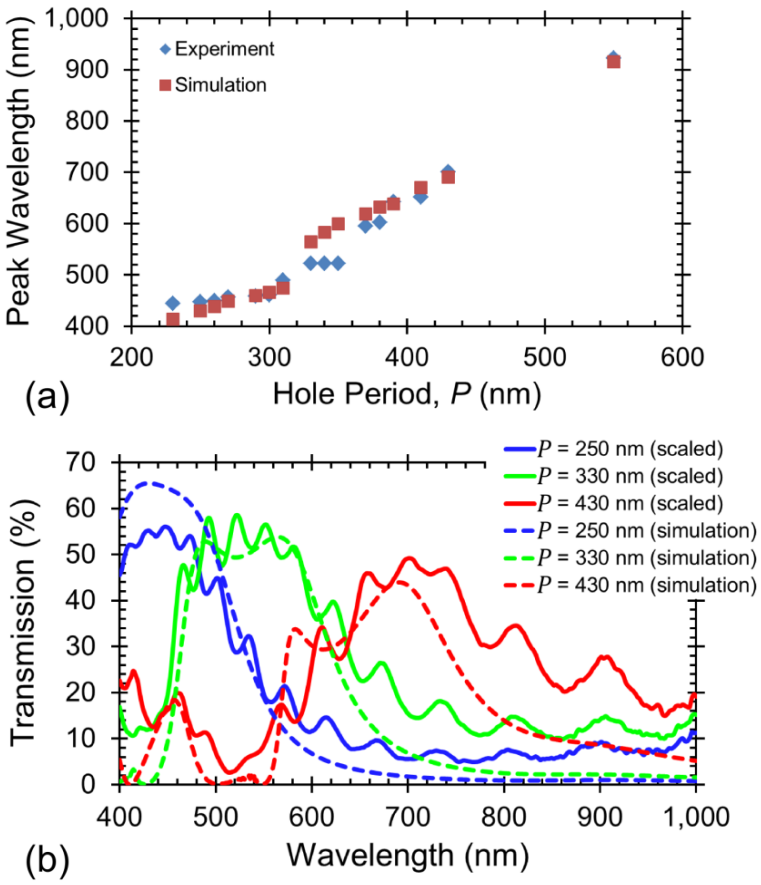

Figure 7.5 Comparison of the experimental results and simulation results from the plasmonic filter components of the multi-spectral filter. (a) Peak wavelength versus array period for the plasmonic filter components of the synthetic multi-spectral material (SMM). (b) Simulation results for blue, green and red plasmonic filters compared with the scaled SMM plasmonic filter component spectra. The experimentally measured spectra are scaled to account for the presence of etch gaps in the aluminium film that compose the metamaterial (MM) filter.

In addition to the optical and NIR filtering properties, the SMM also exhibits filtering characteristics at a single THz frequency due to the MM filter component of the device. In Figure 7.3(d), it can be observed that the SMM acts as a band pass filter with a transmission peak of 31 % at 2.75 THz. The transmission spectrum of the THz MM filter component of the SMM is compared with the experimental results and simulation results of MM Filter 1, as was presented in Chapter 6, Section 6.2.3, in Figure 7.6. The experimental and simulation results for MM filter 1 correspond to transmission peaks of 34 % at 2.74 THz and 37 % at 2.65 THz, respectively, which aligns well with the experimental results from the SMM. These results show that the MM filter component of the SMM is only slightly affected by the presence of plasmonic filter hole arrays, as was expected from the simulation results presented in Section 7.1.

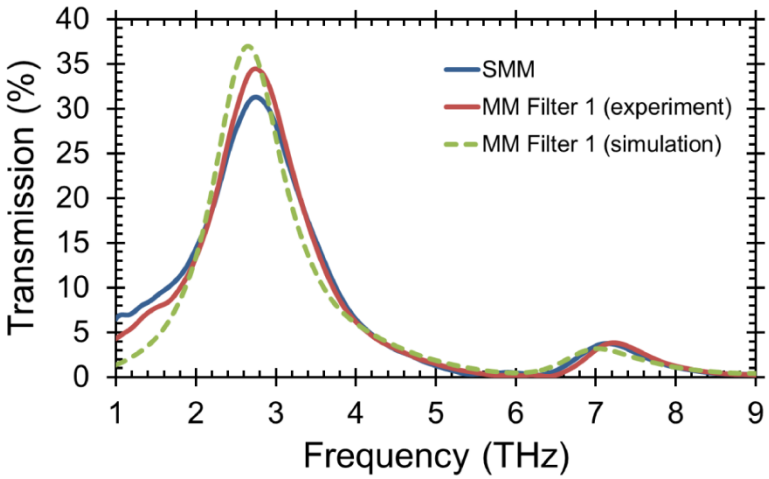

Figure 7.6 Comparison of the experimental results from the metamaterial (MM) filter component of the synthetic multi-spectral material (SMM) compared with the experimental and simulation results of MM Filter 1, as was presented in Chapter 6.

7.3 Multi-Spectral Material – Optical, NIR, THz

The second SMM combines 15 optical plasmonic filters, a single NIR plasmonic filter and a THz MM absorber. As discussed in Chapter 2, optical plasmonic filters can be combined with CMOS image sensors to create a colour imager and THz MM absorbers can be combined with microbolometers to create a THz camera. Therefore, the hybrid plasmonic filter and MM absorber structure represents a substantial step forward in combining these two technologies in a single multi-spectral camera. The optical and NIR plasmonic filters correspond to the designs presented in Chapter 5, and the MM absorber is based on an absorber structure presented in Chapter 6.

7.3.1 Design and Fabrication

The SMM is a hybrid structure consisting of 16 plasmonic filters with the array periods and hole sizes that were presented in Chapter 5, Section 5.1, and a THz MM Absorber that corresponds to MM Absorber 1, as described in Chapter 6, Section 6.3. In the case of the SMM, the optical and NIR plasmonic filters are etched into the ground plane of MM Absorber 1. The layer structure is unchanged from the MM absorber design described in Chapter 6 and consists of a 150 nm aluminium ground plane on a glass substrate, a 3 µm silicon dioxide spacer and a 150 nm ERR layer. The ERR array extends over a region of 12 mm x 12 mm and the plasmonic filters extend over an area of 1 mm x 1 mm, with a gap of 0.33 mm between neighbouring filters. A schematic showing the MM absorber component unit cell, above the plasmonic filter ground plane, is illustrated in Figure 7.7(a). The layout of the SMM is shown in Figure 7.7(b). A 3D cross section of the MM absorber unit cell, illustrating the layer structure of the SMM, is shown in Figure 7.7(c).

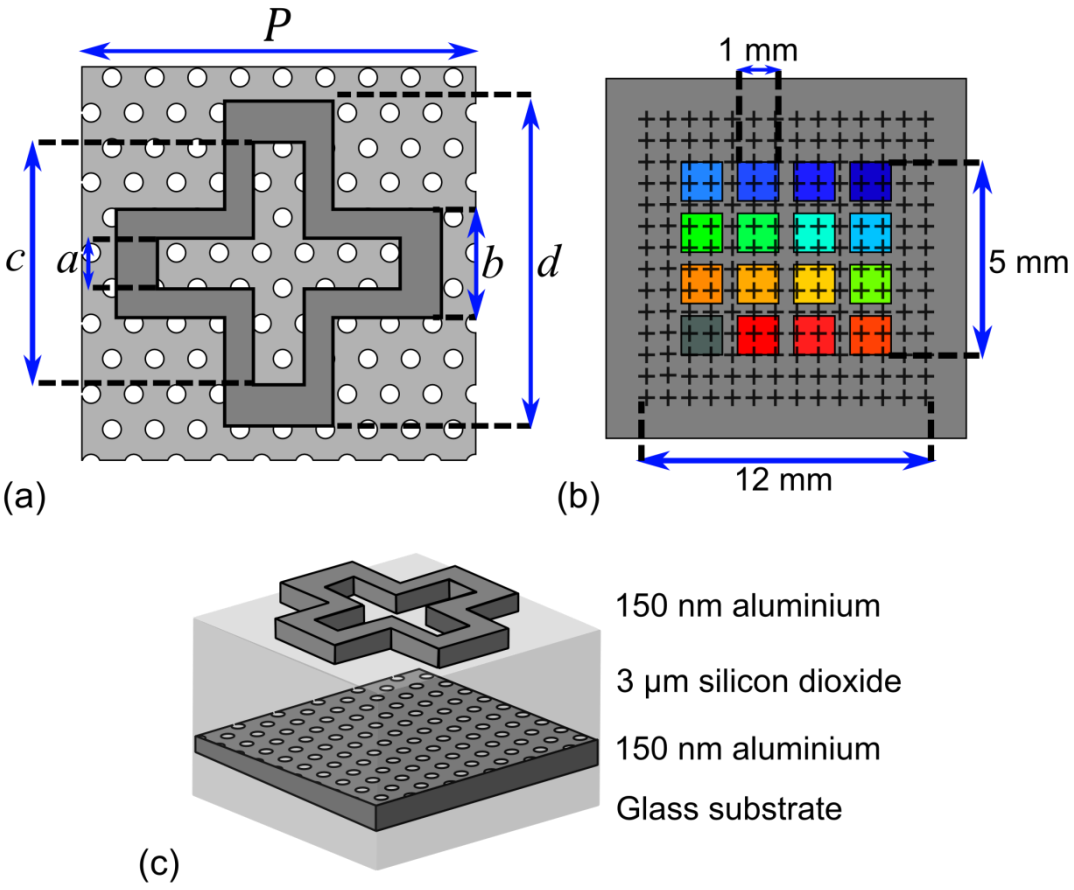

Figure 7.7 Schematic illustrations of the second synthetic multi-spectral material (SMM) that combines plasmonic filters and a metamaterial (MM) absorber (not to scale). (a) Schematic of the terahertz (THz) MM absorber unit cell which also includes the plasmonic filter hole arrays in the lower ground layer. (b) Top down schematic of the SMM, illustrating the layout of the plasmonic filters and MM components. (c) 3D cross section of the MM absorber component unit cell of the SMM.

The fabrication procedure for the SMM combines the plasmonic filter fabrication process described in Chapter 5, Section 5.1.2, with the MM absorber fabrication process, described in Chapter 6, Section 6.3.2. The first step was the fabrication of the 16 colour plasmonic filter set, consisting of etched hole arrays on a 150 nm aluminium layer on a glass substrate, using EBL and dry etch. The plasmonic filter fabrication process was followed up until the stage where the ZEP520A and silicon nitride layers had been removed. At this stage the etched aluminium film is exposed and normally a 200 nm silicon dioxide cap layer is deposited on the surface to complete the plasmonic filters. However for fabrication of the SMM, a 3 µm silicon dioxide cap layer was deposited on to the plasmonic filter ground plane instead, and the fabrication process continued using the MM absorber fabrication procedure to define the ERR array using a combination of EBL and lift off. Transmission microscope images over blue, green and red plasmonic filter regions of the SMM, corresponding to array period of 250 nm, 340 nm and 410 nm, are shown in Figure 7.8(a-c). A tessellated image, composed of multiple transmission microscope images, and

showing the region of the SMM patterned with plasmonic filters is shown in Figure 7.8(d). In Figure 7.8(d), it can be observed that the ERRs are too small to be resolved in the image but they result in a decrease in the observed transmission from each plasmonic filter.

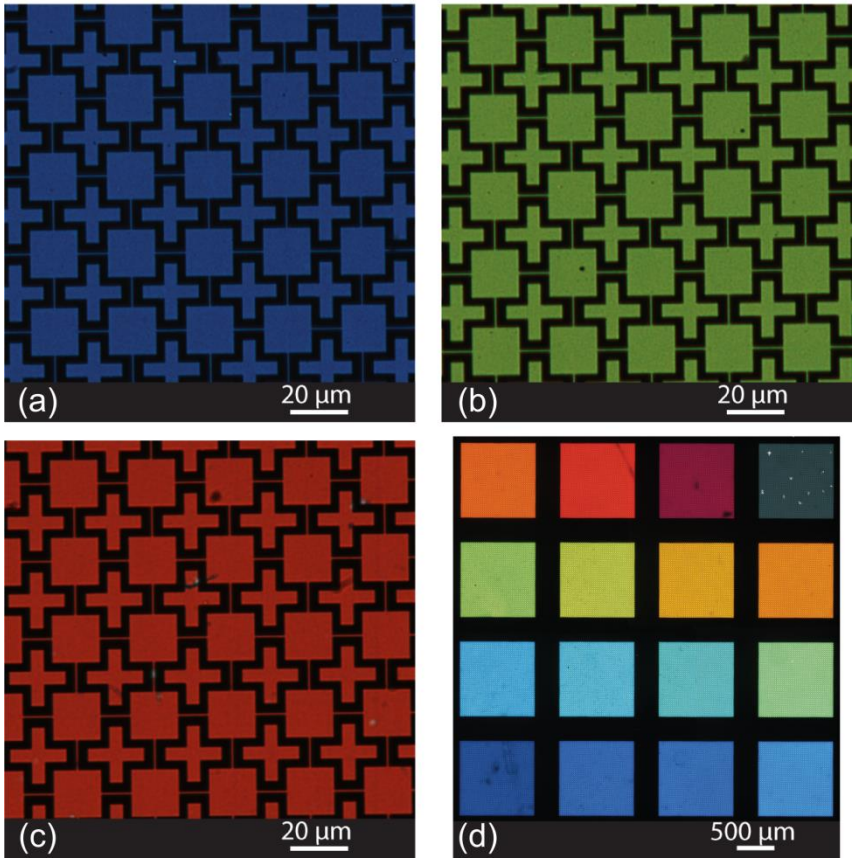

Figure 7.8 Transmission microscope images of the fabricated synthetic multi-spectral material (SMM), corresponding to (a) blue (period = 250 nm), (b) green (period = 340 nm) and (c) red (period = 410 nm) plasmonic filter regions. (d) Tessellated transmission microscope image of the area of the SMM covered with plasmonic filters. The ERRs are not resolved in this image.

7.3.2 Characterisation and Results

The transmission spectra from the plasmonic filter components of the SMM were measured using the TFProbe MSP300 and the absorption spectrum from the MM absorber component was measured using the Bruker IFS 66v/S FTIR using the experimental methods outlined in Chapter 4. The measured transmission from the plasmonic filter components of the SMM are displayed in Figure 7.9(a-c) where the legend denotes the hole period and measured hole size. The absorption spectrum from the THz MM absorber component of the SMM is shown in Figure 7.9(d).

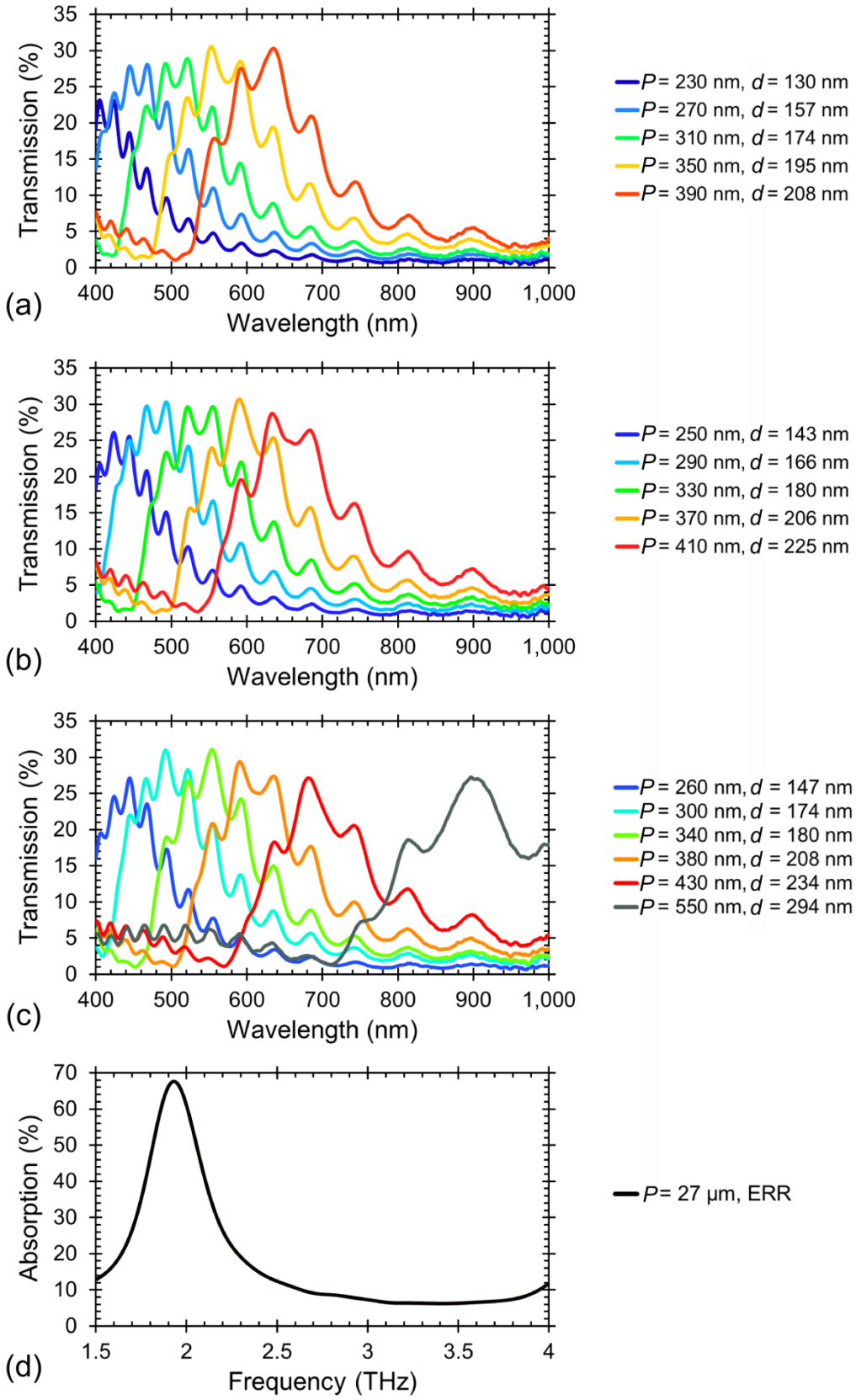

Figure 7.9 Measured transmission spectra and absorption spectrum for the synthetic multi-spectral material (SMM) consisting of hybrid plasmonic filter and metamaterial (MM) absorber structures. (a-c) Plasmonic filter component transmission spectra. (d) MM absorber component absorption spectrum. The legend denotes the hole period, *P*, and the hole diameter, *d*.

Fabry-Perot oscillations can be observed in the transmission spectra of the plasmonic filters, as was observed for the multi-spectral filter. In this case, the rigid structure means that the peaks are consistent over all filters, and by consideration of the peak positions, the 3 μm silicon dioxide layer was found to correspond to a resonator cavity with a refractive index of 1.48 [121].

The ERR array leads to a drop in the measured transmission from the plasmonic filter components due to the measurement method, which effectively averages the contribution of the ERR components, such that there is no spatial variation in the measured transmission. This can be observed in Figure 7.8(d) where the ERR array cannot be resolved in the low magnification image and the plasmonic filter colours appear slightly duller than the colour swatch shown in Figure 5.9 in Chapter 5. The plasmonic filter spectra can, again, be scaled to account for the impact of the MM structures by consideration of the relevant metal fill factor. In this case, the ERR array covers 33.6 % of the SMM surface.

The transmission spectra from blue, green and red plasmonic filter components of the SMM, with array periods of 250 nm, 340 nm and 410 nm, respectively, were scaled to account for the presence of the ERR array and the resultant spectra are shown in Figure 7.10. Simulation results for the blue, green and red plasmonic filters are also shown for comparison. The plasmonic filters were simulated using the procedure described in Chapter 5, Section 5.1.1 and with the measured hole sizes that are listed in the legend of Figure 7.9. It can be observed that the simulated filters align well with the scaled transmission from the plasmonic filter components of the SMM. Once again, the scaled results represent an approximation of the transmission spectra that would be observed from standalone plasmonic filters or if the transmission measurement was made over a sufficiently small region between ERRs. Careful positioning, scaling or altering the geometries of the ERRs could potentially reduce or even eliminate their influence on the plasmonic colour filters for CMOS imaging applications. The SMM presented in Section 7.4 uses MM Absorber 2, which has a smaller metal fill factor ERR array and therefore reduces the impact of the MM components on the measured plasmonic filter transmission spectra.

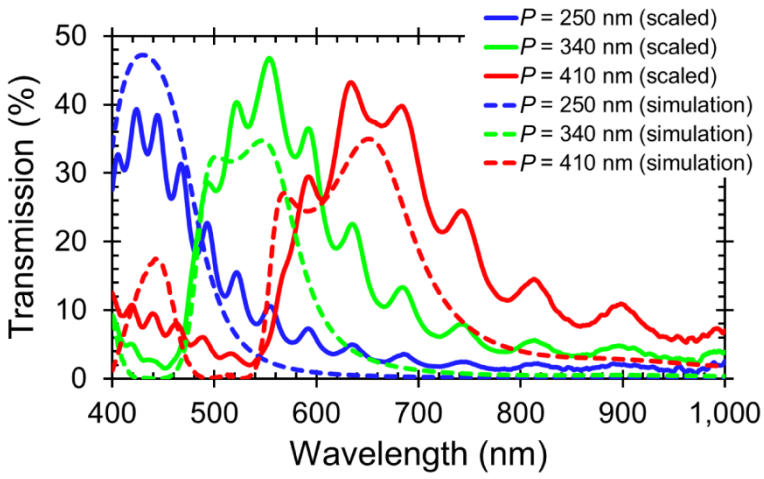

Figure 7.10 Simulation results for blue, green and red plasmonic filters with array period, *P*, compared with the scaled synthetic multi-spectral material (SMM) plasmonic filter component spectra. The experimentally measured spectra are scaled to account for the reduction in plasmonic filter transmission due to the electric ring resonator (ERR) array on the SMM surface.

The SMM also absorbs at a single THz frequency, with an absorption peak of 67 % at 1.93 THz as can be observed in Figure 7.9(d). The absorption due to the MM absorber component of the SMM is compared with the absorption spectrum of MM Absorber 1, as was presented in Chapter 6, Section 6.3.3, in Figure 7.11. The simulation results for MM Absorber 1 are also shown. It can be seen that both the fabricated SMM and the fabricated MM absorber exhibit similar absorption profiles and the simulated absorber exhibits an absorption peak of 72 % at 1.94 THz. This demonstrates that the plasmonic filters have a negligible impact on the optical properties of the MM absorber component of the SMM, which is in agreement with the results presented in Section 7.1.

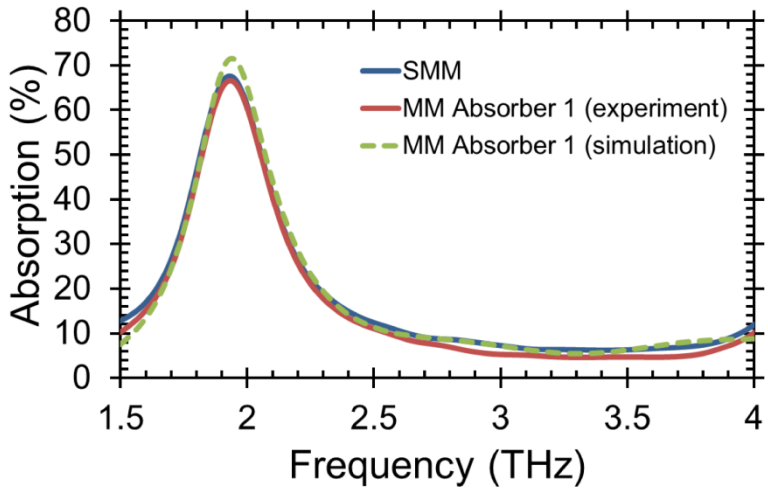

Figure 7.11 Comparison of the experimental results from the metamaterial (MM) absorber component of the synthetic multi-spectral material (SMM) compared with the experimental and simulation results of MM Absorber 1, as was presented in Chapter 6.

7.3.3 Alternative Design

An alternative SMM that combined MM Absorber 4 with plasmonic filters was designed and early fabrication steps were carried out, however it was abandoned in favour of the previously presented SMM. The structure of the original SMM made it more favourable for integration with CMOS technology, as will be explored in Section 7.5. Preliminary fabrication results for the alternative SMM are presented here as it may be a valuable design to revisit in the future. The MM absorber component is as was described for MM Absorber 4 in Chapter 6. The perforated ground plane was fabricated using EBL, metal evaporation and lift off. The fabrication procedure for the SMM followed the method described in Chapter 6 for the MM absorbers, however in this case plasmonic filter hole arrays were etched into the top metal layer at the same time as the cross array, using similar processing as was outlined for the multi-spectral filter. As a dielectric substrate was used, a charge conduction layer was necessary to prevent accumulation of charge during the EBL step. The charge conduction layer consisted of a 30 nm aluminium film evaporated on to the poly-methyl methacrylate (PMMA) surface prior to EBL. MFCD 26 was used to remove the aluminium layer prior to development and lift off. A 3D cross section schematic of the SMM is shown in Figure 7.12(a). Transmission microscope images of fabricated SMMs with 17 µm square ground plane perforations and 5 µm square ground plane perforations are shown in Figure 7.12(b) and Figure 7.12(c), respectively.

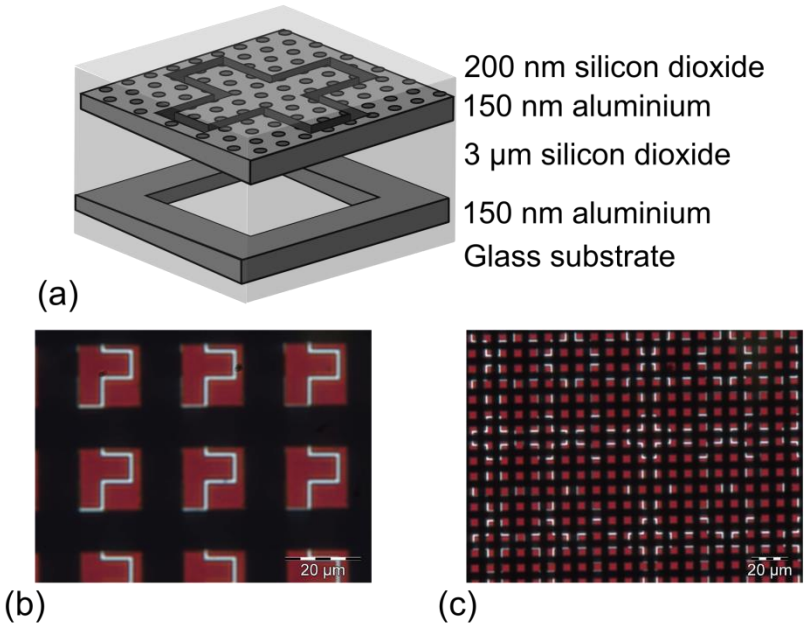

Figure 7.12 Schematic illustration and transmission microscope images of an alternative synthetic multi-spectral material (SMM) that combines plasmonic filters and a metamaterial (MM) absorber (not to scale). (a) Schematic of the terahertz (THz) MM absorber unit cell which also includes the plasmonic filters in the top layer and a perforation in the ground plane. (b) Transmission microscope image of a SMM with 17 µm square ground plane perforations over a red plasmonic filter region. (c) Transmission microscope image of a SMM with 5 µm square ground plane perforations over a red plasmonic filter region.

7.4 Multi-Spectral Material – Optical, NIR, SWIR, MIR, THz

The third SMM consists of three optical plasmonic filters, one NIR plasmonic filter, one short wave infrared (SWIR) plasmonic filter and two mid infrared (MIR) plasmonic filters integrated with a THz MM Absorber. The structure and layout of the SMM are similar to the second SMM presented in section 7.3, however the IR filters are extended up to MIR wavelengths, and the MM absorber unit cell is altered to decrease the fill factor, thereby increasing the measured plasmonic filter transmission. The plasmonic filter components are based on designs presented in Chapter 5, and the MM absorber component corresponds to a MM presented in Chapter 6. Such a material could be combined with CMOS technology incorporating suitable sensors to create a multi-spectral imaging (MSI) system capable of trichromatic visible imaging, tetrachromatic IR imaging and monochromatic THz imaging.

7.4.1 Design and Fabrication

The SMM consists of 7 plasmonic filters fabricated into the ground plane of a MM absorber. The MM absorber component of the SMM is as was described in Chapter 6, Section 6.3 for MM Absorber 2. The layer structure is also as described previously: a 150 nm aluminium film on a glass slide, a 3 µm silicon dioxide spacer layer and a 500 nm aluminium ERR. Four of the plasmonic filter components correspond to the blue, green, red and NIR plasmonic filters, with array periods of 250 nm, 330 nm, 430 nm and 500 nm, respectively, as presented in Chapter 5 Section 5.1. The remaining three plasmonic filters are based on the IR filters presented in Chapter 5, Section 5.2. The SWIR plasmonic filter operates within the wavelength range presented previously, and the two MIR filters operate at longer wavelengths through scaling of the array periods and hole sizes. The SWIR and two MIR plasmonic filters use array periods of 1765 nm, 2353 nm and 2942 nm, respectively. Due to the different measurement methods required to characterise the optical and IR filters, the plasmonic filter surface area varies depending on the filtered wavelength. The optical and NIR filters cover an area of 1 mm x 1mm and the SWIR and MIR filters cover an area of 3 mm x 3mm. The ERR array covers an area of 12 mm x 12 mm and has a metal fill factor of 17 %. A schematic of the MM Absorber unit cell is shown in Figure 7.13(a). The layout of the plasmonic filters below the ERR array is shown in Figure 7.13(b) and a cross section of the SMM is shown in Figure 7.13(c). The labelled regions, MIR1 and MIR2, correspond to plasmonic filters with array periods of 2353 nm and 2942 nm, respectively. The fabrication process was as described for the second SMM in Section 7.3.1. The first step was the fabrication of the 7 plasmonic filters into the ground

plane of the MM absorber, followed by deposition of the 3 µm dielectric spacer. The ERR array was then defined using lift off processing after an EBL step. A transmission microscope image of the ERR array over the MIR1 filter region, corresponding to an array period of 2353 nm is shown in Figure 7.14(a). A transmission microscope image taken over the plasmonic filter regions of the SMM surface is shown in Figure 7.14(b).

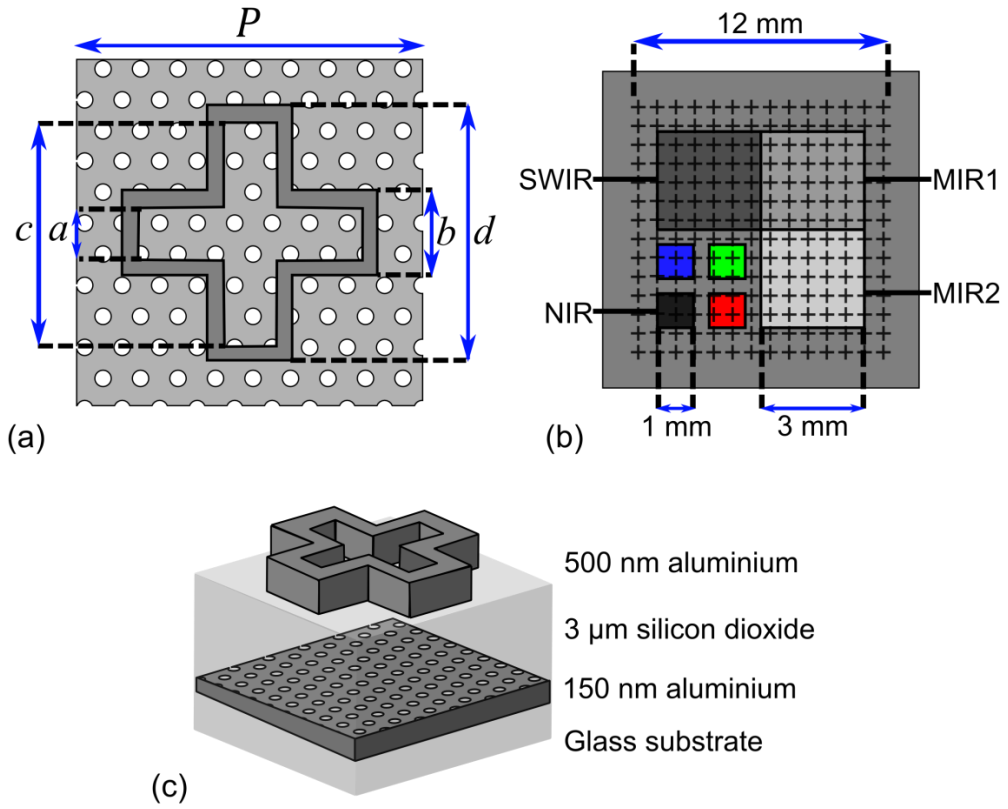

Figure 7.13 Schematic illustrations of the third synthetic multi-spectral material (SMM) that combines optical and infrared (IR) plasmonic filters and a terahertz (THz) metamaterial (MM) absorber (not to scale). (a) Schematic of the THz MM absorber unit cell which also includes the plasmonic filter hole arrays in the lower ground layer. (b) Top down schematic of the SMM, illustrating the layout of the plasmonic filters and MM components. (c) 3D cross section of the MM absorber component unit cell of the SMM.

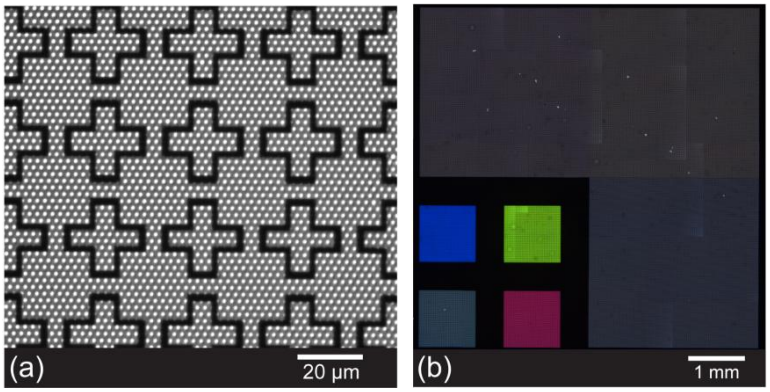

Figure 7.14 Transmission microscope images of the third synthetic multi-spectral material (SMM). (a) Transmission microscope image of the electric ring resonator (ERR) array over a plasmonic filter region with an array period of 2353 nm. (b) Transmission microscope image over the different plasmonic filter regions of the SMM. The image consists of multiple microscope images that have been stitched together and therefore variations in intensity within individual filter regions are due to variations in exposure for different images.

7.4.2 Characterisation and Results

The optical and NIR plasmonic filter components of the SMM were characterised using the TFProbe MSP300, the SWIR and MIR plasmonic filters were characterised using the Bruker Vertex 70 FTIR and the THz MM absorber component was characterised using the Bruker IFS 66v/S FTIR, with the experimental procedures outlined in Chapter 4. The transmission spectra from the optical and NIR plasmonic filter components are shown in Figure 7.15(a) and the transmission spectra from the SWIR and MIR plasmonic filter components are shown in Figure 7.15(b). The absorption spectrum of the MM absorber component of the SMM is shown in Figure 7.15(c).

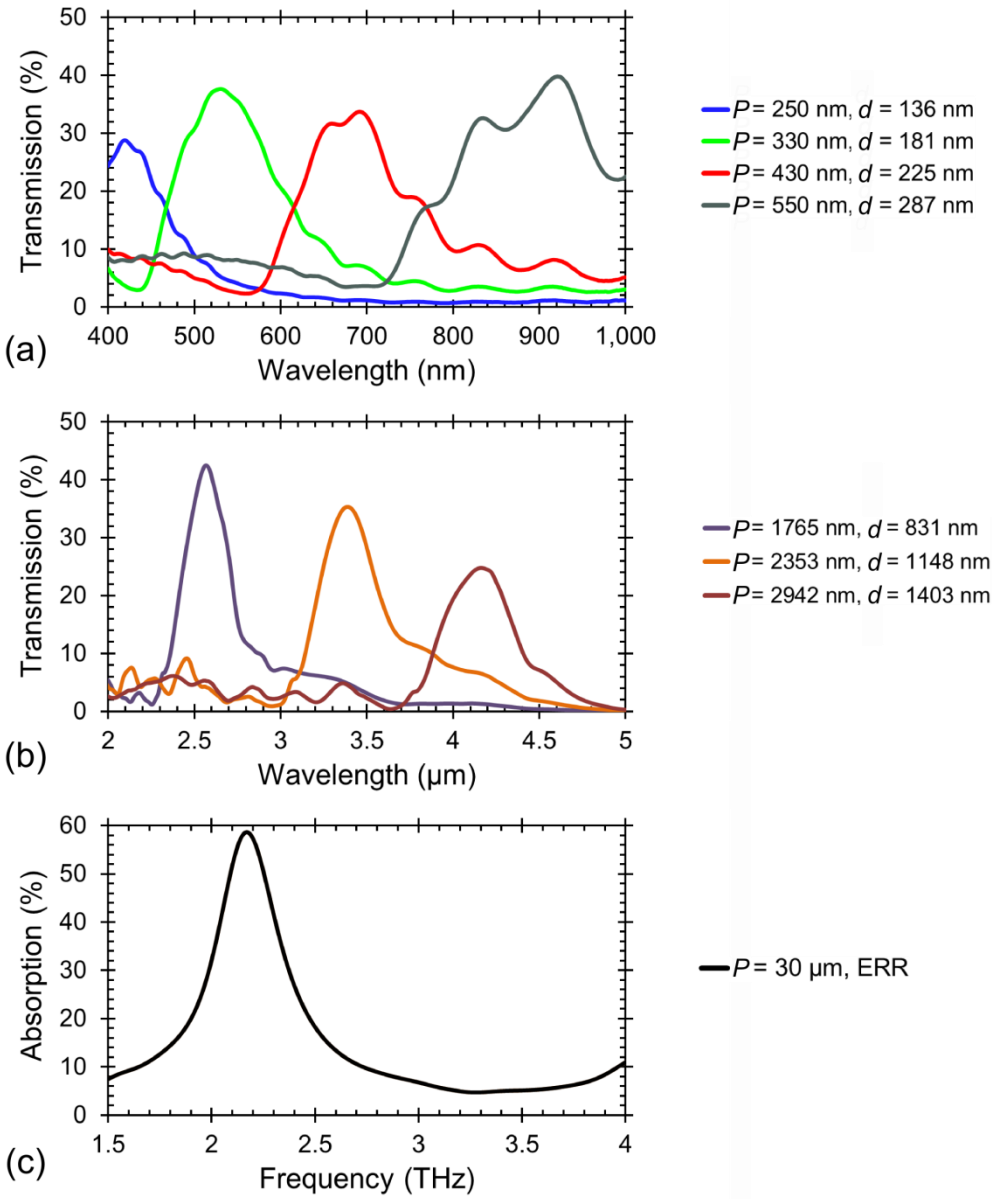

Figure 7.15 Measured transmission spectra and absorption spectrum for the synthetic multi-spectral material (SMM) consisting of optical and infrared (IR) plasmonic filters and a metamaterial (MM) absorber. (a) Optical and near infrared (NIR) plasmonic filter components transmission spectra. (b) Short wave infrared (SWIR) and mid infrared (MIR) plasmonic filter components transmission spectra. (c) MM absorber component absorption spectrum. The legend denotes the hole period, *P*, and the measured hole diameter, *d*.

The variation of peak wavelength with hole period for the plasmonic filter components of the SMM are shown in Figure 7.16. Also shown for comparison are the simulation results using the simulation procedure outlined in Chapter 5 for the optical and IR plasmonic filters, respectively, and the measured hole sizes as listed in the legend of Figure 7.15. It can be observed that there is good agreement between experimental and simulation results for the plasmonic filters and the slight variations that occur, mainly at longer wavelengths, are most likely a result of minor variation in the refractive index value of the fabricated and simulated silicon dioxide layers. In addition to the inclusion of SWIR and MIR plasmonic filters, the third SMM exhibits slightly higher optical and NIR transmission than observed in Section 7.3.2 for the second SMM. This can be attributed to the decreased metal fill factor of the ERR array.

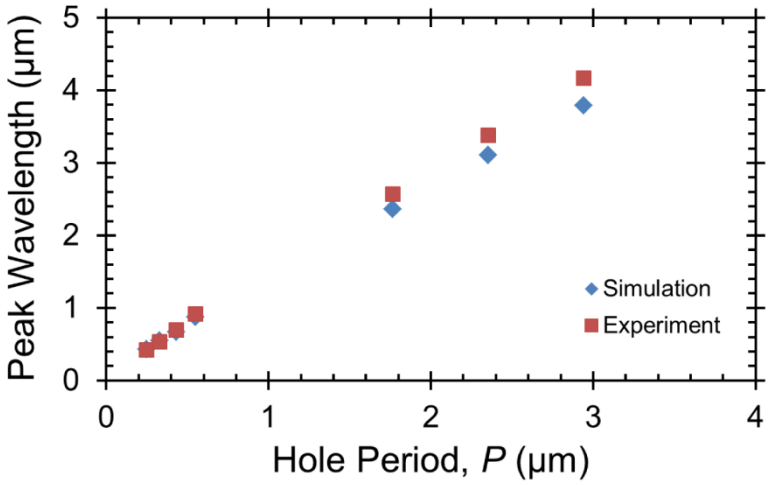

Figure 7.16 Variation of peak wavelength with hole period from the synthetic multi-spectral material (SMM) compared with plasmonic filter simulation results.

The MM absorber component of the SMM exhibits an absorption peak of 59 % at 2.17 THz. The THz absorption spectrum of the SMM is compared with the absorption spectrum and simulation results from MM Absorber 2, as described in Chapter 6, Section 6.3.3, in Figure 7.17. MM Absorber 2 exhibits an absorption peak of 64 % at 2.18 THz and the simulated MM absorber exhibits an absorption peak of 69 % at 2.22 THz. It can therefore be seen that the plasmonic filters only have a minor impact on absorption spectrum of the SMM when compared to a standalone MM absorber, as expected from the simulations performed in Section 7.1, and the experimental result presented in Sections 7.2 and 7.3.

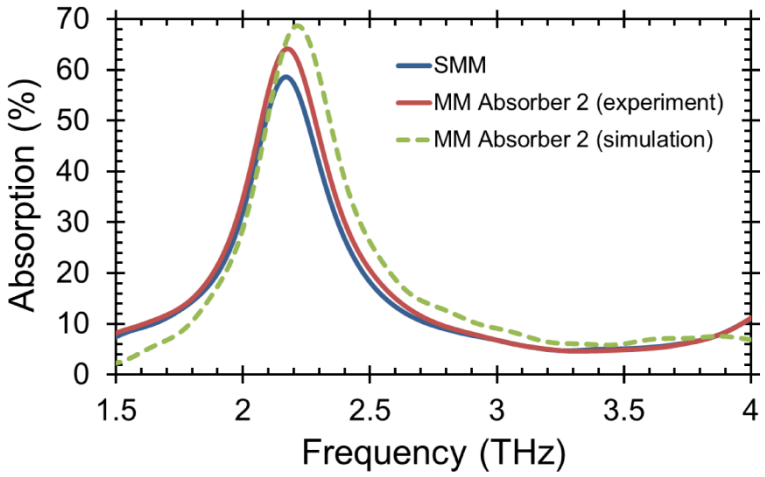

Figure 7.17 Comparison of the experimental results from the metamaterial (MM) absorber component of the synthetic multi-spectral material (SMM) compared with the experimental and simulation results of MM Absorber 2, as was presented in Chapter 6.

7.5 Multi-Spectral Imager

The SMMs that have been presented in this Chapter represent the first step in the creation of a MSI system capable of imaging over several decades of wavelength and consisting of a single camera. The initial iteration of the MSI system was designed to incorporate colour and THz imaging systems into a single CMOS chip; later iterations will look to implement IR detection.

The completed MSI system will consist of plasmonic filters and photodiodes for colour imaging, and MM absorbers and microbolometers for THz imaging. The CMOS chip design offers a high degree of flexibility with regards to post-processing the chip and therefore several designs can be tested without the requirement to frequently redesign the entire chip. The first step of integrating SMMs with the chip has already been presented in Chapter 5, Section 5.4. The MSI chip was designed with EBL alignment makers embedded in the CMOS layers and with minimal surface topography to overcome the problems that were encountered when fabricating on the surface of the chip presented in Chapter 5, Section 5.3.

Due to the feature sizes of the plasmonic filter component of the SMMs, they cannot be fabricated cheaply as part of the CMOS process and therefore it was desirable to fabricate the plasmonic structures in the post-processing stage. This also allowed greater flexibility in altering the properties of the plasmonic filter components. Plasmonic filters fabricated on the chip surface, as opposed to within one of the low metal layers, could potentially lead to increased colour cross talk due to the distance between the filters and the photodiodes, but this was considered a worthwhile compromise. It would be possible to integrate the

MM absorber component of the SMM in the CMOS layers however this could be restrictive when considering alternative MM absorber designs. It may also result in the THz imaging component of the chip being reliant on a single untested MM absorber design. Consequently, it was decided that the MM absorber component should also be fabricated during post-processing. It should also be noted that the MM absorber unit cells are required to be thermally isolated from neighbouring unit cells, to enable multi-pixel imaging.

The plasmonic filters were to be used with photodiodes for colour imaging and the MM absorbers were to be combined with vanadium oxide (VOx) sensors for THz imaging. The chip was designed to consist of a photodiode array and a periodic arrangement of raised studs to read out from the VOx sensor. As no plasmonic or MM structures were embedded in the CMOS layers, the chip could be post-processed to act as a plasmonic colour imager, a THz MM absorber imager, or the combined MSI camera. The chip was designed to use SMMs similar to those presented in Sections 7.3 and 7.4. It would also be possible to use the alternative SMM design, presented in Section 7.3.3, however this would result in the plasmonic filters being further away from the photodiodes than with the other SMM designs.

The layout of two proposed MSI camera designs through integration of SMM structures with the CMOS chip are shown in Figure 7.18. Figure 7.18(a) shows a SMM design similar to those presented in Sections 7.3 and 7.4. Figure 7.18(b) shows a different design, where the MM absorber ground plane consists of perforations to allow transmission of light to the lower plasmonic filter layer that is fabricated directly on to the chip surface. This design could be altered to eliminate the requirement for ground plane perforations by using sufficiently small MM structures to allow light to be transmitted through the gap between adjacent unit cells. Both designs use a thermally isolated MM absorber, consisting of a disconnected ground plane between free standing unit cells with a VOx sensor, for THz imaging, and a plasmonic filter layer above the photodiode array for colour imaging. The MSI system design presented in Figure 7.18(a) allows light transmission from the plasmonic filter ground plane to the photodiode array, however as the plasmonic filter layer is part of the thermally isolated MM absorber it may undergo some deformation due to the thin, unsupported MM structure. It also positions the colour filter array a larger distance from the photodiode array when compared with the MSI system design shown in Figure 7.18(b) and therefore may lead to increased colour crosstalk. The MSI system design presented in Figure 7.18(b) separates the MM absorber and filter component to

ensure that the plasmonic filter array is fabricated on the rigid chip surface. Perforations in the MM absorber ground plane allow light to be transmitted through the MM absorber component to the CFA and the photodiodes. The requirement for a perforated ground plane could lead to decreased light passing to the plasmonic filters and a decrease in absorption.

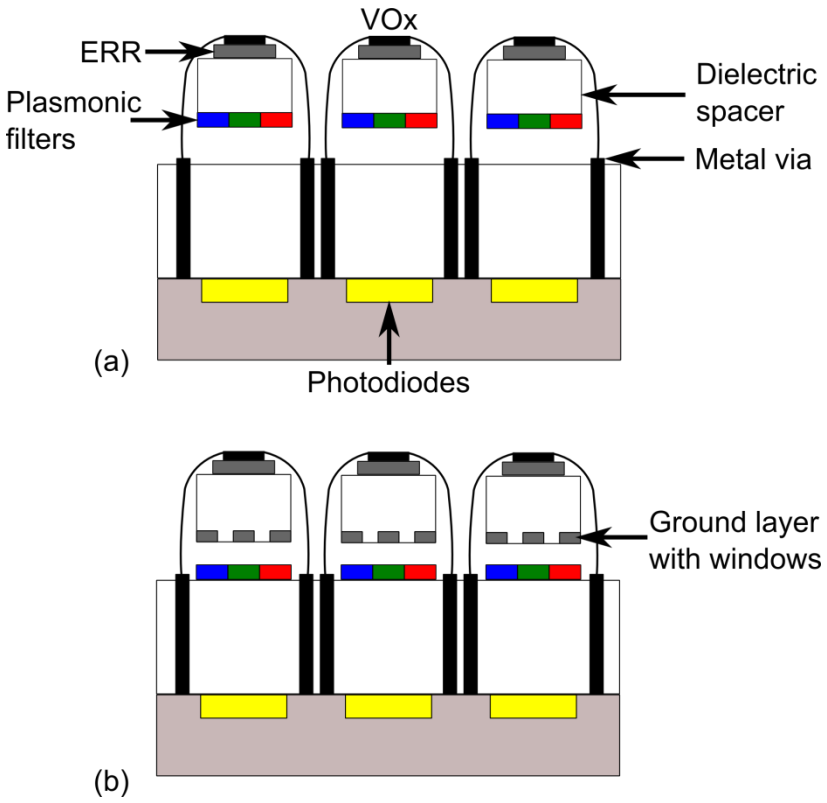

Figure 7.18 Schematic illustrations of potential methods to integrate synthetic multi-spectral materials (SMM) with complementary metal-oxide semiconductor (CMOS) chips to create a multi-spectral imager operating at optical and terahertz (THz) wavebands. Both layouts use thermally isolated metamaterial (MM) absorber unit cells combined with vanadium oxide (VOx). The MM absorber component is connected to the chip using metal vias. Plasmonic filters are used with photodiodes for colour imaging. (a) Illustration of a SMM integrated with CMOS technology where plasmonic filters are fabricated into the MM absorber ground layer. (b) Illustration of a SMM integrated with CMOS technology where plasmonic filters are fabricated directly on to the surface of the chip and the MM absorber ground layer is perforated to allow transmission of light to the plasmonic filters and photodiodes.

The chip layout was designed to incorporate a MM absorber with an array period of 40 µm and a colour pixel of 6.7 µm. Illustrations of potential layouts of the plasmonic filters and MM absorbers on the MSI chip is shown in Figure 7.19. As the ERR structure and VOx would block the transmission of light to the plasmonic filters it is necessary to position the plasmonic filters and ERRs in such a way that ensures that light can reach the plasmonic filters and the photodiodes to form a colour image whilst still maintaining sufficiently high absorption in the MM absorber component to image at THz frequencies. These layouts correspond to the design presented in Figure 7.18(b) and consider a sufficiently small MM absorber, instead of a perforated ground layer, to allow transmission of light to the photodiodes positioned in the regions between MM absorbers. The simplest design, shown

in Figure 7.19(a), uses each THz pixel to image a single colour. This layout simplifies fabrication and could improve performance at the expense of decreased resolution. Figure 7.19(b) shows a layout for a MSI system where each area enclosed by a THz pixel contains both colour and THz information. A CFA layout based on the Bayer pattern [87] described in Chapter 2 is shown in Figure 7.19(c). All layouts would require substantial image processing involving interpolation to ensure high quality reconstruction of a colour image.

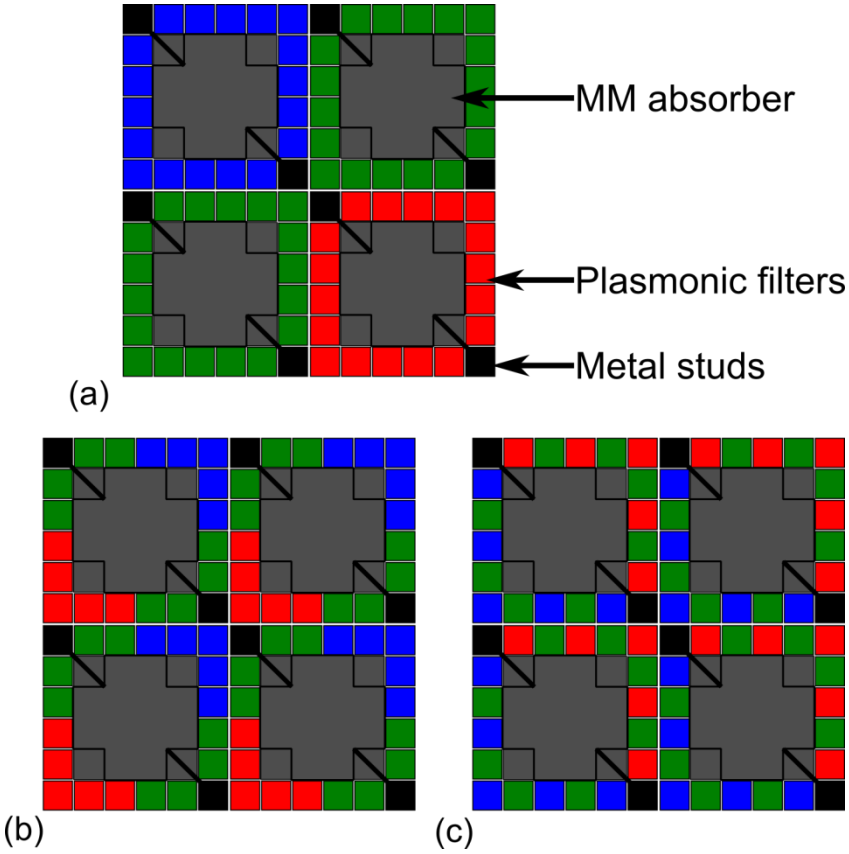

Figure 7.19 Illustrations of potential plasmonic filter colour filter array (CFA) layouts to allow colour imaging using the multi-spectral imaging (MSI) system. (a) Illustration of CFA layout where each terahertz (THz) pixel corresponds to a single colour. (b) Illustration of a CFA layout where each THz pixel corresponds to a single visible pixel with all colour information. (c) Illustration of a CFA layout based on the Bayer pattern, but with certain pixels obscured by the MM absorber.

7.6 Summary

Structured photonic materials such as plasmonic filters and MMs are of particular interest for imaging applications as it is possible to engineer their optical characteristics over a large spectral range. As both plasmonic filters and MMs can be designed to share common materials and fabrication processing it is possible to hybridise these two unique structures, as demonstrated in this Chapter. Such hybrid structures combine the beneficial characteristics of both individual structures, which are often used in distant wavebands, to create new SMMs that operate over several decades of wavelength and have potential applications in the development of coaxial, high resolution MSI systems.

In this Chapter, 15 optical plasmonic filters and a NIR plasmonic filter have been integrated with a THz MM filter to create a new SMM. This hybrid material represented the first step in co-integration of these structures to aid in the development of a MSI system. Using a single lithographic step, a single metal film was engineered to filter at both optical wavelengths and THz frequencies simultaneously. Due to the relative length scales of the components it was observed that the plasmonic and MM resonances could be engineered independently without significantly impacting the resonant characteristics of each other. The second SMM combined a THz MM absorber with 15 optical plasmonic filters and a single NIR plasmonic filter. In this case the plasmonic filter components were patterned into the ground plane of the MM absorber component. MM absorbers are well suited for THz imaging when combined with a suitable sensor and plasmonic filters can be combined with photodiodes to create a colour imager. Therefore the second SMM represents a significant milestone in combining these two technologies into a single MSI camera. The third SMM builds on the ideas developed in the second SMM by using a low metal fill factor ERR array, to increase transmission of light to the plasmonic filter ground plane, and also extends the filtering characteristics of the SMM up to MIR wavelengths. Combining such a SMM with suitable sensors could lead to the development of a MSI system capable of colour imaging, IR imaging and THz imaging.

The Chapter concludes with a discussion on the MSI chip and how it could incorporate SMMs to create a MSI system capable of operating at optical and THz wavelengths simultaneously. The initial integration of structured photonic materials with the CMOS chip was presented in Chapter 5, Section 5.4 where plasmonic filters were fabricated on to the chip surface. The Microsystem Technology Group is currently undertaking the necessary work to integrate THz MM absorbers with the chip to enable THz imaging. Upon completion of the individual colour and THz imagers, the fabrication processes will

be combined to integrate the SMMs with CMOS technology, which could lead to the creation of an MSI system that can operate at optical and THz wavelengths simultaneously.

8. Conclusions and Future Work

In the work presented in this Thesis I have designed, simulated, fabricated and characterised plasmonic filters and terahertz (THz) metamaterials (MM), which have been used to develop new hybrid structured photonic materials, known as synthetic multi-spectral materials (SMM). SMMs have been developed to be integrated with complementary metal-oxide semiconductor (CMOS) technology to create a wide-band multi-spectral imaging (MSI) system in a single camera. The conclusions from the development of the two individual structured photonic materials and the hybrid structures, in addition to some discussion on future work, are presented below.

8.1 Optical and Infrared Plasmonic Filters

Optical plasmonic filters, consisting of triangular hole arrays etched into a 150 nm thick aluminium film, were simulated and optimised using Lumerical FDTD Solutions. The array periods and hole sizes were scaled to create 15 plasmonic colour filters and a single near infrared (NIR) plasmonic filter in the range from 400 nm to 1 μm. Simulations were also performed to monitor the angular dependence and the impact of hole size on the transmission spectra of blue, green and red plasmonic filters. The hole arrays were etched into the aluminium film using electron beam lithography (EBL) and dry etch. The fabricated plasmonic filters exhibited spectral characteristics similar to those observed in the simulated filters. The peak transmission of the fabricated filters ranged from 34 % to 54 % and the full width at half maximum (FWHM) ranged from approximately 100 nm to approximately 150 nm for the colour filters and was significantly wider, at approximately 200 nm, for the NIR plasmonic filter.

The array periods and hole sizes of the optical plasmonic filters were then scaled to create 8 plasmonic filters engineered for short wave infrared (SWIR) wavelengths. The optical and SWIR plasmonic filters consisted of the same layer structure, and consequently could both be fabricated on to the same metal film. The poor confinement of surface plasmon polaritons (SPP) to the aluminium surface at longer wavelengths suggests that spoof surface plasmons (SP), arising from the etched metal surface acting as a MM, are necessary to explain the observed extraordinary optical transmission (EOT). The SWIR plasmonic filters exhibited narrowband transmission over 60 % up until the longest wavelength filter which exhibited a decrease in transmission as a result of the optical properties of the glass substrate. Preliminary results from a metal mesh filter (MMF) for IR wavelengths were also presented however the MMF exhibited a wider bandwidth than the IR plasmonic filters.

Optical plasmonic filters have been fabricated on the surface of two CMOS image sensors. For the first chip it was first necessary to fabricate reference markers to enable alignment of plasmonic filters to the photodiode array on the chip. The alignment markers were fabricated using EBL processing, evaporation of gold, and lift off. The position of the fabricated markers were then measured with reference to features on the chip surface and used in subsequent EBL alignment steps. It was estimated that alignment accuracy between 1 µm and 2 µm was achievable using this method. The first chip has a step height of approximately 1 µm between the region on the surface above the photodiodes and the surrounding area. This led to poor quality hole profiles after etching which is most likely due to variation of the spin coated resist thickness due to surface topography. The necessary dry etch processing time to fully etch the hole arrays was also found to be significantly longer than observed for optical filters fabricated on flat glass slides. The transmission spectra from blue, green and red plasmonic filter regions were evaluated by using a monochromator and normalising the average photodiode output over a plasmonic filter region to the average output from unobstructed photodiodes. As expected from the observed hole array quality, the normalised transmission spectra did not exhibit the necessary narrowband characteristics for imaging applications, however it was still possible to distinguish blue, green and red colour bands from the filter spectra. The second chip had alignment markers embedded within the CMOS layers and also had reduced surface topography. This allowed repeatable and high quality fabrication of the hole arrays with good alignment accuracy. The second chip also included features necessary to incorporate THz imaging functionality and consequently the fabrication of the plasmonic filters on the CMOS chip surface represents a significant step in the development of a combined colour and THz MSI camera.

8.2 Terahertz Metamaterial Filters and Absorbers

Two THz MM filters, consisting of complementary electric ring resonator (cERR) arrays etched into a 150 nm aluminium film were simulated, fabricated and characterised. Both filters were based on the same etched cross design, but with different etched cross surface areas. The MM filters were fabricated on a silicon substrate which was back etched to leave a thin membrane material. This was to allow transmission of both optical and THz radiation, which enabled the MM filter design to incorporate optical plasmonic filters at a later stage. The MM filter with the smallest etched surface area, and therefore largest metal fill factor, had a transmission peak of 34 % at 2.74 THz and the low metal fill factor MM filter had a wider transmission peak of 64 % at 2.75 THz. The extracted effective

permittivity from the simulated MM filters displayed a Drude-like response and effective plasma frequency at resonance.

Four MM absorbers were designed and simulated, and the two MM absorbers that were considered most suitable for integration with plasmonic filters were also fabricated and characterised. The first MM absorber consisted of an aluminium electric ring resonator (ERR) separated from an aluminium ground layer by a silicon dioxide dielectric spacer and was seen to exhibit an absorption peak of 67 % at 1.93 THz. The extracted effective electromagnetic parameters from the simulated MM absorber exhibited features that are characteristic of this type of absorber structure. This included a Drude-like response in the effective permittivity and a Lorentz-like response in the effective permeability at resonance. The second MM absorber was based on the first MM absorber, but with a lower metal fill factor ERR array by using a narrower cross structure and a larger array period. This resulted in a decrease in the absorption magnitude of the MM absorber, however it was found that by using a thicker ERR layer the absorption characteristics could be improved. For a 500 nm thick ERR layer, the absorption magnitude was measured as 64 % at 2.18 THz. The third MM absorber consisted of the same layer structure as described previously, but with two narrow concentric ERRs within each unit cell. The simulation results showed that this MM exhibited two resonances and consequently acted as a dual band MM absorber. The fourth MM absorber consisted of a cERR-style top layer separated from a ground plane by a dielectric spacer. The first three MM absorbers were designed to have plasmonic filters fabricated into the ground plane layer, however in the case of the fourth MM absorber, the plasmonic filters were intended to be patterned into the top layer. It was therefore necessary to perforate the ground plane to allow transmission of visible light through the MM structure. Simulations of the fourth MM absorber for different ground plane perforations demonstrated that nine 5 μm perforations per unit cell had little impact on the absorption characteristics of the MM absorber, but a single 17 μm perforation per unit cell led to a decrease in the absorption magnitude.

8.3 Synthetic Multi-Spectral Materials

The range of different materials and detection methods required to image over different spectral regions means that wide-band MSI systems usually require several spectrally specific cameras to constitute a complete MSI imaging system. In this work I have presented an alternative approach by hybridising two structured photonic materials, namely plasmonic filters and MMs, to create SMMs, which can exhibit spectrally distant resonant characteristics that can be engineered by altering the structures of the individual plasmonic

and MM components. SMMs could be integrated with suitable sensors to create a MSI system consisting of a single camera that is capable of imaging visible, IR and THz wavebands simultaneously.

It was found through simulation studies that nanoholes had a negligible impact on the optical properties of a 150 nm aluminium film at THz frequencies. It was therefore determined that plasmonic filters could be approximated as an unperforated metal film in the THz frequency range and that the plasmonic and MM components of SMM could be designed independently. Therefore the plasmonic filters and MMs presented in previous sections represented the design process of the structured photonic material components used to construct the SMMs.

The first SMM combined 15 optical plasmonic filters, a single NIR plasmonic filter and a THz MM filter to create a multi-spectral filter. All structures were etched into a single 150 nm aluminium film on a silicon substrate, which was back etched to leave a thin supporting membrane to allow transmission at both optical and THz frequencies. The plasmonic filter components of the SMM exhibited distinct colour bands in the transmission spectra, which were a result of the different hole array periods. White light transmission was also measured from all plasmonic filters, which was a result of the cERR etch gaps and the measurement method. Consideration of the metal fill factor allowed the measured transmission to be scaled, which led to an approximation of the transmission spectra that would be observed from standalone filters. For a given application, the MM components could be scaled and positioned to ensure that their influence in the plasmonic filter transmission spectra could be minimised or possibly eliminated. The SMM also exhibited a transmission peak of 31 % at 2.75 THz, which is in good agreement with the transmission properties of the a standalone MM filter, without plasmonic filter hole arrays etched into the metal surface.

The second SMM combined 15 optical plasmonic filters, a single NIR plasmonic filter and a THz MM absorber. In this case, plasmonic filters were etched into the ground plane of the MM absorber structure. The plasmonic filter components displayed band pass filtering throughout the optical and NIR wavelength range and it was observed that the ERR array led to a decrease is the measured transmission. The transmission spectra of blue, green and red plasmonic filter components were scaled to account for the presence of the ERR array and the resultant spectra was found to be in good agreement with simulated plasmonic filters. The SMM also exhibited an absorption peak of 67 % at 1.93 THz, which agrees with what was observed for a standalone MM absorber, with an unperforated ground plane.

The third SMM combined three optical plasmonic filters, a single NIR plasmonic filter, a single SWIR plasmonic filter and two MIR plasmonic filters with a THz MM absorber. Compared with the previous SMM, the MM absorber component used a low metal fill factor ERR array to reduce the impact of the ERRs on the measured plasmonic filter component transmission. The MM absorber component of the SMM exhibited an absorption peak of 59 % at 2.17 THz, which is in good agreement with the absorption observed from the same MM absorber structure without ground plane perforations.

8.4 Future Work

The focus of the work presented in this Thesis has been the development of SMMs through hybridisation of plasmonic filters and THz MMs. The next step would be the integration of SMMs with suitable sensor materials to create a MSI system capable of operating at visible and THz wavelengths. In future this could be extended to also incorporate IR wavelengths. The best way to approach this challenge would be to complete the individual visible and THz detector technologies first, before combining them to create the MSI camera.

Substantial work has already been carried out in combining plasmonic filters with CMOS image sensors [9,10,103], as has been outlined in Chapter 2. Colour imaging has previously been reported using plasmonic filters and CMOS sensors [11], however in this case the hole arrays were not fabricated directly on to the chip surface or within the CMOS layer stack, as would be required for a MSI camera which would incorporate the more complex SMM structures. In Chapter 5, the fabrication process development for integration of plasmonic filters on the surface of a chip designed for MSI applications was presented, in addition to some preliminary results. The next step should be the continued fabrication of plasmonic filters on the surface of the MSI chip, with the intention of acquiring a colour image. At that stage it would be necessary to develop image processing algorithms to extract the individual colour bands, perform interpolation and reconstruct the complete colour image. Additional image processing would also be required to ensure each colour was reproduced accurately, and it may even be beneficial to use CIE 1931 CMF plasmonic colour filters to form the colour filter array (CFA) [104]. After acquisition of the first colour image using a CFA consisting of the standard blue, green and red channels, colour reproduction could be improved by using a larger number of colour filters. The simplicity of engineering a desired spectral response from plasmonic filters, as demonstrated by the 16 colour plasmonic filter set presented in Chapter 5, means that it should be a simple step to proceed towards higher spectral resolution.

As has been described previously, THz MM absorbers are well-suited for THz imaging applications and recently a MM absorber fabricated as part of a CMOS chip has been combined with a vanadium oxide (VOx) microbolometer and used with a Nipkow disk to create a THz imager [242]. The next natural step would be scaling the THz detector to a focal plane array (FPA) format and this work is currently being undertaken by the Microsystem Technology Group. As the MSI chip contains photodiodes and the relevant readout electronics for the THz detector component, it should be possible to integrate MM absorbers with VOx microbolometers on the CMOS chip to acquire a multi-spectral monochrome visible and THz image, prior to considering the more complex implementation of both plasmonic filters and MM absorbers to yield colour and THz imaging.

Discussion on how the SMMs could be implemented with the CMOS chip has already been presented in Chapter 7. By ensuring the MM absorbers are thermally isolated and the plasmonic filters are positioned carefully it should be possible to acquire both multi-pixel THz and colour images. Due to the visible regions blocked by MM absorber components it would be essential to incorporate image processing algorithms that use interpolation to estimate the missing colour information whilst still maintaining high resolution. However this may lead to errors in the colour images such that alternative MM absorber geometries and sizes may have to be considered to find a compromise between the quality of each of the spectrally different images. Assuming the resolution of the visible image is high it would be possible to use image fusion algorithms to combine both the visible and the THz images and compensate for the lower resolution THz image [187–189,208,209]. Future work could incorporate IR detection methods, such as indium antimonide photodiodes [3,77] or IR MM absorbers [138] coupled with microbolometers. The simplicity of scaling structured photonic materials also means that the operational wavelengths of the MSI system could easily be engineered for a number of applications.

References

1. S. Chaudhuri and K. Kotwal, *Hyperspectral Image Fusion* (Springer, 2013).

2. D. L. Hall and J. Llinas, "An Introduction to Multisensor Data Fusion," Proc. IEEE **85**(1), 6–23 (1997).

3. S. M. Sze, *Semiconductor Devices: Physics and Technology*, 2nd ed. (Wiley, 2002).

4. F. Niklaus, C. Vieider, and H. Jakobsen, "MEMS-Based Uncooled Infrared Bolometer Arrays - A Review," Proc. SPIE **6836**, 68360D (2007).

5. J. L. Tissot, C. Trouilleau, B. Fieque, A. Crastes, and O. Legras, "Uncooled microbolometer detector: recent developments at ULIS," Opto-Electron. Rev. **14**(1), 25–32 (2006).

6. A. W. M. Lee, B. S. Williams, S. Kumar, Q. Hu, and J. L. Reno, "Real-Time Imaging Using a 4.3-THz Quantum Cascade Laser and a 320x240 Microbolometer Focal-Plane Array," IEEE Photon. Technol. Lett. **18**(13), 1415–1417 (2006).

7. M. Perenzoni, N. Massari, S. Pocas, J. Meilhan, and F. Simoens, "A Monolithic Visible, Infrared and Terahertz 2D Detector," in *2010 35th International Conference on Infrared Millimeter and Terahertz Waves (IRMMW-THz)* (IEEE, 2010), pp. 1–2.

8. M. Perenzoni, N. Massari, D. Stoppa, S. Pocas, B. Delplanque, J. Meilhan, F. Simoens, and W. Rabaud, "A 160x160-pixel Image Sensor for Multispectral Visible, Infrared and Terahertz Detection," in *2012 Proceedings of the European Solid State Circuits Conference (ESSCIRC)* (IEEE, 2012), pp. 93–96.

9. Q. Chen, D. Chitnis, K. Walls, T. D. Drysdale, S. Collins, and D. R. S. Cumming, "CMOS Photodetectors Integrated With Plasmonic Color Filters," IEEE Photon. Technol. Lett. **24**(3), 197–199 (2012).

10. Q. Chen, D. Das, D. Chitnis, K. Walls, T. D. Drysdale, S. Collins, and D. R. S. Cumming, "A CMOS Image Sensor Integrated with Plasmonic Colour Filters," Plasmonics **7**(4), 695–699 (2012).

11. S. P. Burgos, S. Yokogawa, and H. A. Atwater, "Color Imaging via Nearest Neighbor Hole Coupling in Plasmonic Color Filters Integrated onto a Complementary Metal-Oxide Semiconductor Image Sensor," ACS Nano **7**(11), 10038–10047 (2013).

12. N. I. Landy, C. M. Bingham, T. Tyler, N. Jokerst, D. R. Smith, and W. J. Padilla, "Design, theory, and measurement of a polarization insensitive absorber for terahertz imaging," Phys. Rev. B **79**, 125104 (2009).

13. H. Tao, N. I. Landy, C. M. Bingham, X. Zhang, R. D. Averitt, and W. J. Padilla, "A metamaterial absorber for the terahertz regime: Design, fabrication and characterization," Opt. Express **16**(10), 7181–7188 (2008).

14. J. Grant, Y. Ma, S. Saha, L. B. Lok, A. Khalid, and D. R. S. Cumming, "Polarization insensitive terahertz metamaterial absorber," Opt. Lett. **36**(8), 1524–1526 (2011).

15. H. P. Myers, *Introductory Solid State Physics*, 2nd ed. (CRC Press, 1997).

16. S. A. Maier, *Plasmonics: Fundamentals and Applications* (Springer, 2007).

17. H. Raether, *Surface Plasmons on Smooth and Rough Surfaces and on Gratings* (Springer, 1988).

18. P. G. Kik and M. L. Brongersma, "Chapter 1: Surface Plasmon Nanophotonics" in *Surface Plasmon Nanophotonics*, M. L. Brongersma and P. G. Kik eds. (Springer, 2007).

19. W. L. Barnes, A. Dereux, and T. W. Ebbesen, "Surface plasmon subwavelength optics," Nature **424**, 824–830 (2003).

20. W. A. Murray and W. L. Barnes, "Plasmonic Materials," Adv. Mater. **19**, 3771–3782 (2007).

21. S. A. Maier and H. A. Atwater, "Plasmonics: Localization and guiding of electromagnetic energy in metal/dielectric structures," J. Appl. Phys. **98**, 011101 (2005).

22. M. I. Stockman, "Nanoplasmonics: The physics behind the applications," Physics Today, 39–44 (February 2011).

23. W. L. Barnes, "Surface plasmon–polariton length scales: a route to sub-wavelength optics," J. Opt. A: Pure Appl. Opt. **8**, S87–S93 (2006).

24. I. Newton, *Opticks: Or, A Treatise of the Reflexions, Refractions, Inflexions and Colours of Light. Also Two Treatises of the Species and Magnitude of Curvilinear Figures.* London, Printed for Sam. Smith, and Benj. Walford. Printers to the Royal Society, at the Prince's Arms in St. Paul's Church-yard (1704).

25. U. Leonhardt, "Invisibility cup," Nature Photon. **1**, 207–208 (2007).

26. I. Freestone, N. Meeks, M. Sax, and C. Higgitt, "The Lycurgus Cup – A Roman Nanotechnology," Gold Bull. **40**(4), 270–277 (2007).

27. J. C. Maxwell Garnett, "Colours in Metal Glasses and in Metallic Films," Phil. Trans. R. Soc. Lond. A **203**, 385–420 (1904).

28. G. Mie, "Contributions on the optics of turbid media, particularly colloidal metal solutions," Annalen der Physik, Series IV **25**(3), 337–445 (1908).

29. U. Kreibig and P. Zacharias, "Surface Plasma Resonances in Small Spherical Silver and Gold Particles," Z. Physik **231**, 128–143 (1970).

30. M. I. Stockman, "Nanoplasmonics: past, present, and gilmpse into future," Opt. Express **19**(22), 22029–22106 (2011).

31. J. A. Ruemmele, W. P. Hall, L. K. Ruvuna, and R. P. Van Duyne, “A Localized Surface Plasmon Resonance Imaging Instrument for Multiplexed Biosensing,” Anal. Chem. **85**, 4560–4566 (2013).

32. S. Nie and S. R. Emory, “Probing Single Molecules and Single Nanoparticles by Surface-Enhanced Raman Scattering,” Science **275**, 1102–1106 (1997).

33. R. W. Wood, “On a Remarkable Case of Uneven Distribution of Light in a Diffraction Grating Spectrum,” Proc. Phys. Soc. London **18**, 396–402 (1902).

34. D. Maystre, “Chapter 2: Theory of Wood’s Anomalies” in *Plasmonics: From Basics to Advanced Topics*, S. Enoch and N. Bonod, eds. (Springer, 2012).

35. D. Sarid and W. Challener, *Modern Introduction to Surface Plasmons: Theory Mathematica Modeling, and Applications* (Cambridge University Press, 2010).

36. U. Fano, “The Theory of Anomalous Diffraction Gratings and of Quasi-Stationary Waves on Metallic Surfaces (Sommerfeld’s Waves),” J. Opt. Soc. Am. **31**(3), 213–222 (1941).

37. R. H. Ritchie, E. T. Arakawa, J. J. Cowan, and R. N. Hamm, “Surface-Plasmon Resonance Effect in Grating Diffraction,” Phys. Rev. Lett. **21**(22), 1530–1533 (1968).

38. E. Kretschmann and H. Raether, “Radiative Decay of Non Radiative Surface Plasmons Excited by Light,” Z. Naturforsch. **23a**, 2135–2136 (1968).

39. A. Otto, “Excitation of Nonradiative Surface Plasma Waves in Silver by the Method of Frustrated Total Reflection,” Zeitschrift für Physik **216**, 398–410 (1968).

40. A. G. Brolo, “Plasmonics for future biosensors,” Nature Photon. **6**, 709–713 (2012).

41. L. Verslegers, P. B. Catrysse, Z. Yu, J. S. White, E. S. Barnard, M. L. Brongersma, and S. Fan, “Planar Lenses Based on Nanoscale Slit Arrays in a Metallic Film,” Nano Lett. **9**(1), 235–238 (2009).

42. Q. Chen and D. R. S. Cumming, “Visible light focusing demonstrated by plasmonic lenses based on nano-slits in an aluminum film,” Opt. Express **18**(14), 14788–14793 (2010).

43. W. Srituravanich, N. Fang, C. Sun, Q. Luo, and X. Zhang, “Plasmonic Nanolithography,” Nano Lett. **4**(6), 1085–1088 (2004).

44. S. Seo, H. C. Kim, H. Ko, and M. Cheng, “Subwavelength proximity nanolithography using a plasmonic lens,” J. Vac. Sci. Technol. B **25**(6), 2271–2276 (2007).

45. T. W. Ebbesen, H. J. Lezec, H. F. Ghaemi, T. Thio, and P. A. Wolff, “Extraordinary optical transmission through sub-wavelength hole arrays,” Nature **391**, 667–669 (1998).

46. H. F. Ghaemi, T. Thio, D. E. Grupp, T. W. Ebbesen, and H. J. Lezec, “Surface plasmons enhance optical transmission through subwavelength holes,” Phys. Rev. B **58**(11), 6779–6782 (1998).

47. H. A. Bethe, “Theory of Diffraction by Small Holes,” Phys. Rev. **66**(7,8), 163–182 (1944).

48. C. Genet and T. W. Ebbesen, “Light in tiny holes,” Nature **445**, 39–46 (2007).

49. H. J. Lezec and T. Thio, “Diffracted evanescent wave model for enhanced and suppressed optical transmission through subwavelength hole arrays,” Opt. Express **12**(16), 3629–3651 (2004).

50. J. Weiner, “The physics of light transmission through subwavelength apertures and aperture arrays,” Rep. Prog. Phys. **72**, 064401 (2009).

51. L. Martín-Moreno, F. J. García-Vidal, H. J. Lezec, K. M. Pellerin, T. Thio, J. B. Pendry, and T. W. Ebbesen, “Theory of Extraordinary Optical Transmission through Subwavelength Hole Arrays,” Phys. Rev. Lett. **86**(6), 1114–1117 (2001).

52. W. L. Barnes, W. A. Murray, J. Dintinger, E. Devaux, and T. W. Ebbesen, “Surface Plasmon Polaritons and Their Role in the Enhanced Transmission of Light through Periodic Arrays of Subwavelength Holes in a Metal Film,” Phys. Rev. Lett. **92**(10), 107401 (2004).

53. A. Degiron, H. J. Lezec, W. L. Barnes, and T. W. Ebbesen, “Effects of hole depth on enhanced light transmission through subwavelength hole arrays,” Appl. Phys. Lett. **81**(23), 4327–4329 (2002).

54. T. Thio, H. F. Ghaemi, H. J. Lezec, P. A. Wolff, and T. W. Ebbesen, “Surface-plasmon-enhanced transmission through hole arrays in Cr films,” J. Opt. Soc. Am. B **16**(10), 1743–1748 (1999).

55. D. E. Grupp, H. J. Lezec, T. W. Ebbesen, K. M. Pellerin, and T. Thio, “Crucial role of metal surface in enhanced transmission through subwavelength apertures,” Appl. Phys. Lett. **77**(11), 1569–1571 (2000).

56. F. Przybilla, A. Degiron, J.-Y. Laluet, C. Genet, and T. W. Ebbesen, "Optical transmission in perforated noble and transition metal films," J. Opt. A: Pure Appl. Opt. **8**, 458–463 (2006).

57. A. Krishnan, T. Thio, T. J. Kim, H. J. Lezec, T. W. Ebbesen, P. A. Wolff, J. Pendry, L. Martin-Moreno, and F. J. Garcia-Vidal, "Evanescently coupled resonance in surface plasmon enhanced transmission," Opt. Commun. **200**, 1–7 (2001).

58. S. Xiao, N. A. Mortensen, and M. Qiu, “Enhanced transmission through arrays of subwavelength holes in gold films coated by a finite dielectric layer,” J. Eur. Opt. Soc, Rapid Publ. **2**, 07009 (2007).

59. Q. Chen and D. R. S. Cumming, “High transmission and low color cross-talk plasmonic color filters using triangular-lattice hole arrays in aluminum films,” Opt. Express **18**(13), 14056–14062 (2010).

60. Z. Fan, L. Zhan, X. Hu, and Y. Xia, “Critical process of extraordinary optical transmission through periodic subwavelength hole array : Hole-assisted evanescent-field coupling,” Opt. Commun. **281**, 5467–5471 (2008).

61. H. Gao, J. Henzie, and T. W. Odom, “Direct Evidence for Surface Plasmon-Mediated Enhanced Light Transmission through Metallic Nanohole Arrays,” Nano Lett. **6**(9), 2104–2108 (2006).

62. J. B. Pendry, L. Martín-Moreno, and F. J. Garcia-Vidal, “Mimicking Surface Plasmons with Structured Surfaces,” Science **305**, 847–848 (2004).

63. F. J. Garcia-Vidal, L. Martín-Moreno, and J. B. Pendry, “Surfaces with holes in them: new plasmonic metamaterials,” J. Opt. A: Pure Appl. Opt. **7**, S97–S101 (2005).

64. A. K. Azad, Y. Zhao, W. Zhang, and M. He, “Effect of dielectric properties of metals on terahertz transmission in subwavelength hole arrays,” Opt. Lett. **31**(17), 2637–2639 (2006).

65. H. Cao and A. Nahata, “Resonantly enhanced transmission of terahertz radiation through a periodic array of subwavelength apertures,” Opt. Express **12**(6), 1004–1010 (2004).

66. Y. Yang and D. R. Grischkowsky, “High-Resolution THz Transmission and Reflection Measurements and Consequent Understanding of Resonant Hole-Arrays,” IEEE Trans. Terahertz Sci. Technol. **3**(2), 151–157 (2013).

67. Y.-H. Ye and J.-Y. Zhang, “Middle-infrared transmission enhancement through periodically perforated metal films,” Appl. Phys. Lett. **84**(16), 2977–2979 (2004).

68. R. Ortuño, C. García-Meca, F. J. Rodríguez-Fortuño, A. Håkansson, A. Griol, J. Hurtado, J. A. Ayucar, L. Bellieres, P. J. Rodríguez, F. López-Royo, J. Martí, and A. Martínez, “Midinfrared filters based on extraordinary optical transmission through subwavelength structured gold films,” J. Appl. Phys. **106**, 124313 (2009).

69. P. R. West, S. Ishii, G. V. Naik, N. K. Emani, V. M. Shalaev, and A. Boltasseva, “Searching for better plasmonic materials,” Laser Photon. Rev. **4**(6), 795–808 (2010).

70. H.-S. Lee, Y.-T. Yoon, S.-S. Lee, S.-H. Kim, and K.-D. Lee, “Color filter based on a subwavelength patterned metal grating,” Opt. Express **15**(23), 15457–15463 (2007).

71. D. Inoue, A. Miura, T. Nomura, H. Fujikawa, K. Sato, N. Ikeda, D. Tsuya, Y. Sugimoto, and Y. Koide, “Polarization independent visible color filter comprising an aluminum film with surface-plasmon enhanced transmission through a subwavelength array of holes,” Appl. Phys. Lett. **98**, 093113 (2011).

72. S. Yokogawa, S. P. Burgos, and H. A. Atwater, “Plasmonic Color Filters for CMOS Image Sensor Applications.," Nano Lett. **12**, 4349–4354 (2012).

73. D. Pacifici, H. J. Lezec, L. A. Sweatlock, R. J. Walters, and H. A. Atwater, “Universal optical transmission features in periodic and quasiperiodic hole arrays,” Opt. Express **16**(12), 9222–9238 (2008).

74. E. Reinhard, E. A. Khan, A. O. Akyüz, and G. M. Johnson, *Color Imaging: Fundamentals and Applications* (A K Peters, Ltd., 2008).

75. J. Adams, K. Parulski, and K. Spaulding, "Color Processing in Digital Cameras," IEEE Micro **18**(6), 20–30 (1998).

76. A. El Gamal and H. Eltoukhy, "CMOS Image Sensors," IEEE Circuits & Devices Magazine **21**(3), 6–20 (2005).

77. C. Posch, "Chapter 4: Detectors, Pixels and Signal Processing" in *Smart Cameras*, A. N. Belbachir, ed. (Springer, 2010).

78. J. Nakamura, "Chapter 3: Basics of Image Sensors" in *Image Sensors and Signal Processing for Digital Still Cameras*, J. Nakamura, ed. (CRC Press, Taylor & Francis Group, 2006).

79. R. Fontaine, "Recent Innovations in CMOS Image Sensors," in *2011 22nd Annual IEEE/SEMI Advanced Semiconductor Manufacturing Conference (ASMC)* (IEEE, 2011), pp. 1–5.

80. E. R. Fossum, "CMOS Image Sensors : Electronic Camera-On-A-Chip," IEEE Trans. Electron Devices **44**(10), 1689–1698 (1997).

81. M. Bigas, E. Cabruja, J. Forest, and J. Salvi, "Review of CMOS image sensors," Microelectron. J. **37**, 433–451 (2006).

82. G. Wyszecki and W. S. Stiles, *Color Science: Concepts and Methods, Quantitative Data and Formulae*, 2nd ed., Wiley Classics Library Edition (Wiley, 2000).

83. G. Sharma and H. J. Trussell, "Digital Color Imaging," IEEE Trans. Image Process. **6**(7), 901–932 (1997).

84. M. James Shyu and J. Parkkinen, "Chapter 1: Fundamentals of Color" in *Advanced Color Image Processing and Analysis*, C. Fernandez-Maloigne, ed. (Springer, 2013).

85. P.-C. Hung, "Chapter 7: Color Theory and Its Application to Digital Still Cameras" in *Image Sensors and Signal Processing for Digital Still Cameras*, J. Nakamura, ed. (CRC Press, Taylor & Francis Group, 2006).

86. "Selected Colrimetric Tables, International Commission on Illumination," Accessed: 09/01/2015. http://www.cie.co.at/index.php/LEFTMENUE/index.php?i_ca_id=298

87. B. E. Bayer, "Color imaging array," Patent, US3971065 A, (1976).

88. H. Honda, Y. Iida, and Y. Egawa, "High Sensitivity Color CMOS Image Sensor with WRGB Color Filter Array and Color Separation Process Using Edge Detection," in *Proc. of 2007 International Image Sensor Workshop* (2007), pp. 263–266.

89. C.-H. Koo, H.-K. Kim, K.-H. Paik, D.-C. Park, K.-H. Lee, Y.-K. Park, C.-R. Moon, S.-H. Lee, S.-H. Hwang, D.-H. Lee, and J.-T. Kong, "Improvement of Crosstalk on 5M CMOS Image Sensor with 1.7x1.7μm^2 pixels," Proc. SPIE **6471**, 647115 (2007).

90. Y. Huo, C. C. Fesenmaier, and P. B. Catrysse, "Microlens performance limits in sub-2μm pixel CMOS image sensors," Opt. Express **18**(6), 5861–5872 (2010).

91. T. Joy, S. Pyo, S. Park, C. Choi, C. Palsule, H. Han, C. Feng, S. Lee, J. McKee, P. Altice, C. Hong, C. Boemler, J. Hynecek, M. Louie, J. Lee, D. Kim, H. Haddad, and B. Pain, "Development of a Production-Ready, Back-Illuminated CMOS Image Sensor with Small Pixels," in *IEEE International Electron Devices Meeting, 2007. IEDM 2007.* (IEEE, 2007), pp. 1007–1010.

92. A. Theuwissen, "CMOS Image Sensors: State-Of-The-Art and Future Perspectives," in *33rd European Solid State Circuites Conference, 2007. ESSCIRC 2007,* (IEEE, 2007), pp. 21–27.

93. "International Technology Roadmap for Semiconductors, 2011 Edition, Executive Summary," Accessed: 19/03/2015. http://www.itrs.net/ITRS%201999-2014%20Mtgs,%20Presentations%20&%20Links/2012ITRS/Home2012.htm

94. C.-R. Moon, J.-C. Shin, J. Kim, Y. K. Lee, Y.-J. Cho, Y.-Y. Yu, S.-H. Hwang, D.-C. Park, B. J. Park, H.-Y. Kim, S.-H. Lee, J. Jung, S.-H. Cho, K. Lee, K. Koh, D. Lee, and K. Kim, "Dedicated Process Architecture and the Characteristics of 1.4μm Pixel CMOS Image Sensor with 8M Density," in *2007 IEEE Symposium on VLSI Technology* (IEEE, 2007), pp. 62–63.

95. K.-B. Cho, C. Lee, S. Eikedall, A. Baum, J. Jiang, C. Xu, X. Fan, and R. Kauffman, "A 1/2.5 inch 8.1Mpixel CMOS Image Sensor for Digital Cameras," in *IEEE International Solid-State Circuits Conference, 2007. ISSCC 2007.* (2007).

96. P. B. Catrysse, "Monolithic Integration of Electronics and Sub-wavelength Metal Optics in Deep Submicron CMOS Technology," Mater. Res. Soc. Symp. Proc. **869**, (2005).

97. L. Frey, P. Parrein, J. Raby, C. Pellé, D. Hérault, M. Marty, and J. Michailos, "Color filters including infrared cut-off integrated on CMOS image sensor," Opt. Express **19**(14), 13073–13080 (2011).

98. P. L. P. Dillon, A. T. Brault, J. R. Horak, E. Garcia, T. W. Martin, and W. A. Light, "Fabrication and Performance of Color Filter Arrays for Solid-State Imagers," IEEE Journal of Solid-State Circuits **13**(1), 23–27 (1978).

99. P. B. Catrysse and B. A. Wandell, "Integrated color pixels in 0.18-μm complementary metal oxide semiconductor technology," J. Opt. Soc. Am. A **20**(12), 2293–2306 (2003).

100. P. B. Catrysse, W. Suh, S. Fan, and M. Peeters, "One-mode model for patterned metal layers inside integrated color pixels," Opt. Lett. **29**(9), 974–976 (2004).

101. H. Park and K. B. Crozier, "Multispectral imaging with vertical silicon nanowires," Scientific Reports **3**(2460), 1–6 (2013).

102. K. Walls, Q. Chen, D. R. S. Cumming, and T. D. Drysdale, “Fabry-Pérot Resonator with Nanostructures for Multispectral Visible Filtering,” in *2012 12th IEEE Conference on Nanotechnology (IEEE-Nano)* (IEEE, 2012).

103. S. Junger, W. Tschekalinskij, N. Verwaal, and N. Weber, “On-chip nanostructures for polarization imaging and multispectral sensing using dedicated layers of modified CMOS processes,” Proc. SPIE **7946**, 7461D (2011).

104. K. Walls, Q. Chen, S. Collins, D. R. S. Cumming, and T. D. Drysdale, “Automated Design, Fabrication, and Characterization of Color Matching Plasmonic Filters,” IEEE Photon. Technol. Lett. **24**(7), 602–604 (2012).

105. J. B. Pendry, A. J. Holden, W. J. Stewart, and I. Youngs, “Extremely Low Frequency Plasmons in Metallic Mesostructures,” Phys. Rev. Lett. **76**(25), 4773–4776 (1996).

106. D. R. Smith, W. J. Padilla, D. C. Vier, S. C. Nemat-Nasser, and S. Schultz, “Composite Medium with Simultaneously Negative Permeability and Permittivity,” Phys. Rev. Lett. **84**(18), 4184–4187 (2000).

107. D. Schurig, J. J. Mock, and D. R. Smith, “Electric-field-coupled resonators for negative permittivity metamaterials,” Appl. Phys. Lett. **88**, 041109 (2006).

108. W. J. Padilla, M. T. Aronsson, C. Highstrete, M. Lee, A. J. Taylor, and R. D. Averitt, “Electrically resonant terahertz metamaterials: Theoretical and experimental investigations,” Phys. Rev. B **75**, 041102 (2007).

109. J. B. Pendry, A. J. Holden, D. J. Robbins, and W. J. Stewart, “Magnetism from Conductors and Enhanced Nonlinear Phenomena,” IEEE Trans. Microw. Theory Techn. **47**(11), 2075–2084 (1999).

110. D. R. Smith, J. B. Pendry, and M. C. K. Wiltshire, “Metamaterials and Negative Refractive Index,” Science **305**, 788–792 (2004).

111. D. R. Smith, S. Schultz, P. Markos, and C. M. Soukoulis, “Determination of effective permittivity and permeability of metamaterials from reflection and transmission coefficients,” Phys. Rev. B **65**, 195104 (2002).

112. D. R. Smith, D. C. Vier, T. Koschny, and C. M. Soukoulis, “Electromagnetic parameter retrieval from inhomogeneous metamaterials,” Phys. Rev. E **71**, 036617 (2005).

113. R. A. Shelby, D. R. Smith, and S. Schultz, “Experimental verification of a negative index of refraction,” Science **292**, 77–79 (2001).

114. J. B. Pendry, “Negative Refraction Makes a Perfect Lens,” Phys. Rev. Lett. **85**(18), 3966–3969 (2000).

115. D. Schurig, J. J. Mock, B. J. Justice, S. A. Cummer, J. B. Pendry, A. F. Starr, and D. R. Smith, “Metamaterial Electromagnetic Cloak at Microwave Frequencies,” Science **314**, 977–980 (2006).

116. N. I. Landy, S. Sajuyigbe, J. J. Mock, D. R. Smith, and W. J. Padilla, “Perfect Metamaterial Absorber,” Phys. Rev. Lett. **100**, 207402 (2008).

117. B. Reinhard, O. Paul, and M. Rahm, “Metamaterial-Based Photonic Devices for Terahertz Technology,” IEEE J. Sel. Topics Quantum Electron. **19**(1), 8500912 (2013).

118. V. G. Veselago, "The Electrodynamics of Substances with Simultaneously Negative Values of ε and μ," Sov. Phys. Usp. **10**(4), 509–514 (1968).

119. T. J. Cui, R. Liu, and D. R. Smith, “Chapter 1: Introduction to Metamaterials” in *Metamaterials: Theory, Design and Applications*, T. J. Cui, D. R. Smith, and R. Liu, eds. (Springer, 2010).

120. R. W. Ziolkowski and N. Engheta, “Chapter 1: Introduction, History, and Selected Topics in Fundamental Theories of Metamaterials” in *Metamaterials: Physics and Engineering Explorations*, N. Engheta and R. W. Ziolkowski, eds. (Wiley, 2006).

121. F. A. Jenkins and H. E. White, *Fundamentals of Optics*, 4th ed. (McGraw-Hill, 1981).

122. J. Wilson and J. Hawkes, *Optoelectronics: An Introduction*, 3rd ed. (Prentice Hall Europe, 1998).

123. H.-T. Chen, J. F. O’Hara, A. J. Taylor, R. D. Averitt, C. Highstrete, M. Lee, and W. J. Padilla, “Complementary planar terahertz metamaterials,” Opt. Express **15**(3), 1084–1095 (2007).

124. R. Ulrich, “Far-Infrared Properties of Metallic Mesh and its Complementary Structure,” Infrared Physics **7**, 37–55 (1967).

125. A. M. Melo, A. L. Gobbi, M. H. O. Piazzetta, and A. M. P. A. da Silva, “Cross-Shaped Terahertz Metal Mesh Filters: Historical Review and Results,” Advances in Optical Technologies **2012**, 1–12 (2012).

126. K. D. Möller, K. R. Farmer, D. V. P. Ivanov, O. Sternberg, K. P. Stewart, and P. Lalanne, “Thin and thick cross shaped metal grids,” Infrared Phys. Techn. **40**, 475–485 (1999).

127. D. W. Porterfield, J. L. Hesler, R. Densing, E. R. Mueller, T. W. Crowe, and R. M. Weikle II, “Resonant metal-mesh bandpass filters for the far infrared,” Appl. Opt. **33**(25), 6046–6052 (1994).

128. A. M. Melo, M. A. Kornberg, P. Kaufmann, M. H. Piazzetta, E. C. Bortolucci, M. B. Zakia, O. H. Bauer, A. Poglitsch, and A. M. P. Alves da Silva, “Metal mesh resonant filters for terahertz frequencies,” Appl. Opt. **47**(32), 6064–6069 (2008).

129. Y. Ma, A. Khalid, T. D. Drysdale, and D. R. S. Cumming, “Direct fabrication of terahertz optical devices on low-absorption polymer substrates,” Opt. Lett. **34**(10), 1555–1557 (2009).

130. C. M. Rhoads, E. K. Damon, and B. A. Munk, “Mid-infrared filters using conducting elements,” Appl. Opt. **21**(15), 2814–2816 (1982).

131. K. D. Möller, J. B. Warren, J. B. Heaney, and C. Kotecki, "Cross-shaped bandpass filters for the near- and mid-infrared wavelength regions," Appl. Opt. **35**(31), 6210–6215 (1996).

132. W. J. Padilla, A. J. Taylor, C. Highstrete, M. Lee, and R. D. Averitt, "Dynamical Electric and Magnetic Metamaterial Response at Terahertz Frequencies," Phys. Rev. Lett. **96**, 107401 (2006).

133. O. Paul, R. Beigang, and M. Rahm, "Highly Selective Terahertz Bandpass Filters Based on Trapped Mode Excitation," Opt. Express **17**(21), 18590–18595 (2009).

134. Y.-J. Chiang, C.-S. Yang, Y.-H. Yang, C.-L. Pan, and T.-J. Yen, "An ultrabroad terahertz bandpass filter based on multiple-resonance excitation of a composite metamaterial," Appl. Phys. Lett. **99**, 191909 (2011).

135. A. C. Strikwerda, M. Zalkovskij, A. Krabbe, D. L. Lorenzen, A. V. Lavrinenko, and P. U. Jepsen, "Metamaterial Composite with an Ultra-Broadband Usable Range of over 25 Terahertz," in *CLEO: Science and Innovations* (2014).

136. C. M. Watts, X. Liu, and W. J. Padilla, "Metamaterial Electromagnetic Wave Absorbers," Adv. Optical Mater. **24**, OP98–OP120 (2012).

137. J. Hao, J. Wang, X. Liu, W. J. Padilla, L. Zhou, and M. Qiu, "High performance optical absorber based on a plasmonic metamaterial," Appl. Phys. Lett. **96**, 251104 (2010).

138. X. Liu, T. Starr, A. F. Starr, and W. J. Padilla, "Infrared Spatial and Frequency Selective Metamaterial with Near-Unity Absorbance," Phys. Rev. Lett. **104**, 207403 (2010).

139. J. Grant, Y. Ma, S. Saha, A. Khalid, and D. R. S. Cumming, "Polarization insensitive, broadband THz metamaterial absorber," Opt. Lett. **36**(17), 3476–3478 (2011).

140. Y. Ma, Q. Chen, J. Grant, S. C. Saha, A. Khalid, and D. R. S. Cumming, "A terahertz polarization insensitive dual band metamaterial absorber," Opt. Lett. **36**(6), 945–947 (2011).

141. H. Tao, C. M. Bingham, D. Pilon, K. Fan, A. C. Strikwerda, D. Shrekenhamer, W. J. Padilla, X. Zhang, and R. D. Averitt, "A dual band terahertz metamaterial absorber," J. Phys. D: Appl. Phys. **43**, 225102 (2010).

142. X. Shen, T. J. Cui, J. Zhao, H. F. Ma, W. X. Jiang, and H. Li, "Polarization-independent wide-angle triple-band metamaterial absorber," Opt. Express **19**(10), 9401–9407 (2011).

143. G. P. Williams, "Filling the THz gap-high power sources and applications," Rep. Prog. Phys. **69**, 301–326 (2006).

144. B. Ferguson and X.-C. Zhang, "Materials for terahertz science and technology," Nature Mater. **1**, 26–33 (2002).

145. M. Tonouchi, “Cutting-edge terahertz technology,” Nature Photon. **1**, 97–105 (2007).

146. D. A. Crawley, C. Longbottom, B. E. Cole, C. M. Ciesla, D. Arnone, V. P. Wallace, and M. Pepper, “Terahertz Pulse Imaging: A Pilot Study of Potential Applications in Dentistry,” Caries Res **37**, 352–359 (2003).

147. R. M. Woodward, V. P. Wallace, R. J. Pye, B. E. Cole, D. D. Arnone, E. H. Linfield, and M. Pepper, “Terahertz Pulse Imaging of ex vivo Basal Cell Carcinoma,” J. Invest. Dermatol. **120**(1), 72–78 (2003).

148. C. Yu, S. Fan, Y. Sun, and E. Pickwell-Macpherson, “The potential of terahertz imaging for cancer diagnosis: A review of investigations to date,” Quant Imaging Med Surg **2**, 33–45 (2012).

149. R. Appleby and H. B. Wallace, “Standoff Detection of Weapons and Contraband in the 100 GHz to 1 THz Region,” IEEE Trans. Antennas Propag. **55**(11), 2944–2956 (2007).

150. J. F. Federici, B. Schulkin, F. Huang, D. Gary, R. Barat, F. Oliveira, and D. Zimdars, “THz imaging and sensing for security applications-explosives, weapons and drugs,” Semicond. Sci. Technol. **20**, S266–S280 (2005).

151. E. L. Jacobs, S. Moyer, C. C. Franck, F. C. DeLucia, C. Casto, D. T. Petkie, S. R. Murrill, and C. E. Halford, “Concealed weapon identification using terahertz imaging sensors,” Proc. SPIE **6212**, 62120J (2006).

152. D. Zimdars and J. S. White, "Terahertz reflection imaging for package and personnel inspection," Proc. SPIE **5411**, 78–83 (2004).

153. K. Kawase, Y. Ogawa, Y. Watanabe, and H. Inoue, “Non-destructive terahertz imaging of illicit drugs using spectral fingerprints,” Opt. Express **11**(20), 2549–2554 (2003).

154. M. C. Kemp, P. F. Taday, B. E. Cole, J. A. Cluff, A. J. Fitzgerald, and W. R. Tribe, “Security applications of terahertz technology,” Proc. SPIE **5070**, 44–52 (2003).

155. A. J. Fitzgerald, V. P. Wallace, M. Jimenez-Linan, L. Bobrow, R. J. Pye, A. D. Purushotham, and D. D. Arnone, “Terahertz Pulsed Imaging of Human Breast Tumors,” Radiology **239**(2), 533–540 (2006).

156. D. Crawley, C. Longbottom, V. P. Wallace, B. Cole, D. Arnone, and M. Pepper, “Three-dimensional terahertz pulse imaging of dental tissue,” J. Biomed. Opt. **8**(2), 303–307 (2003).

157. C. Baker, T. Lo, W. R. Tribe, B. E. Cole, M. R. Hogbin, and M. C. Kemp, “Detection of Concealed Explosives at a Distance Using Terahertz Technology,” Proc. IEEE **95**(8), 1559–1565 (2007).

158. D. T. Petkie, C. Casto, F. C. De Lucia, S. R. Murrill, B. Redman, R. L. Espinola, C. C. Franck, E. L. Jacobs, S. T. Griffin, C. E. Halford, J. Reynolds, S. O'Brien, and D. Tofsted, "Active and passive imaging in the THz spectral region: phenomenology, dynamic range, modes, and illumination," J. Opt. Soc. Am. B **25**(9), 1523–1531 (2008).

159. B. S. Williams, "Terahertz quantum-cascade lasers," Nature Photon. **1**, 517–525 (2007).

160. W. Schatz, "Generation of Tunable Far-Infrared Radiation by Optical Pumping Molecular Gas Lasers," Infrared Phys. Technol. **36**(1), 387–393 (1995).

161. G. P. Williams, "FAR-IR/THz radiation from the Jefferson Laboratory, energy recovered linac, free electron laser," Rev. Sci. Instrum. **73**(3), 1461–1463 (2002).

162. A. Dobroiu, M. Yamashita, Y. N. Ohshima, Y. Morita, C. Otani, and K. Kawase, "Terahertz imaging system based on a backward-wave oscillator," Appl. Opt. **43**(30), 5637–5646 (2004).

163. N. Orihashi, S. Suzuki, and M. Asada, "One THz harmonic oscillation of resonant tunneling diodes," Appl. Phys. Lett. **87**, 233501 (2005).

164. S. Sankaran and K. K. O, "Schottky Barrier Diodes for Millimeter Wave Detection in a Foundry CMOS Process," IEEE Electron Device Lett. **26**(7), 492–494 (2005).

165. L. Minkevičius, V. Tamošiūnas, I. Kašalynas, D. Seliuta, G. Valušis, A. Lisauskas, S. Boppel, H. G. Roskos, and K. Köhler, "Terahertz heterodyne imaging with InGaAs-based bow-tie diodes," Appl. Phys. Lett. **99**, 131101 (2011).

166. U. R. Pfeiffer and E. Öjefors, "A 600-GHz CMOS Focal-Plane Array for Terahertz Imaging Applications," in *34th European Solid-State Circuits Conference, 2008. ESSCIRC 2008.* (IEEE, 2008), pp. 110–113.

167. J. E. Bjarnason, T. L. J. Chan, A. W. M. Lee, M. A. Celis, and E. R. Brown, "Millimeter-wave, terahertz, and mid-infrared transmission through common clothing," Appl. Phys. Lett. **85**(4), 519–521 (2004).

168. P. Helistö, A. Luukanen, L. Grönberg, J. S. Penttilä, H. Seppä, H. Sipola, C. R. Dietlein, and E. N. Grossman, "Antenna-coupled microbolometers for passive THz direct detection imaging arrays," in *Proceedings of the 1st European Microwave Integrated Circuits Conference, 2006*. (IEEE, 2006), pp. 35–38.

169. S. Cibella, M. Ortolani, R. Leoni, G. Torrioli, L. Mahler, J.-H. Xu, A. Tredicucci, H. E. Beere, and D. A. Ritchie, "Wide dynamic range terahertz detector pixel for active spectroscopic imaging with quantum cascade lasers," Appl. Phys. Lett. **95**, 213501 (2009).

170. D.-T. Nguyen, F. Simoens, J.-L. Ouvrier-Buffet, J. Meilhan, and J.-L. Coutaz, "Broadband THz Uncooled Antenna-Coupled Microbolometer Array—Electromagnetic Design, Simulations and Measurements," IEEE Trans. THz Sci. Technol. **2**(3), 299–305 (2012).

171. F. Simoens, J. Meilhan, S. Gidon, G. Lasfargues, J. Lalanne Dera, J. L. Ouvrier-Buffet, S. Pocas, W. Rabaud, F. Guellec, B. Dupont, S. Martin, and A. C. Simon, "Antenna-coupled microbolometer based uncooled 2D array and camera for 2D real-time terahertz imaging," in Proc. SPIE **8846**, 8460O (2013).

172. J. Oden, J. Meilhan, J. Lalanne-Dera, J.-F. Roux, F. Garet, J.-L. Coutaz, and F. Simoens, "Imaging of broadband terahertz beams using an array of antenna-coupled microbolometers operating at room temperature," Opt. Express **21**(4), 4817–4825 (2013).

173. F. Simoens and J. Meilhan, "Terahertz real-time imaging uncooled array based on antenna- cavity and cavity-coupled bolometers," Phil. Trans. R. Soc. A **372**, 20130111 (2014).

174. M. Almasri, D. P. Butler, and Z. Çelik-Butler, "Self-Supporting Uncooled Infrared Microbolometers With Low-Thermal Mass," J. Microelectromech. Syst. **10**(3), 469–476 (2001).

175. A. Ribés, "Chapter 14: Image Spectrometers, Color High Fidelity, and Fine-Art Paintings," in *Advanced Color Image Processing and Analysis*, C. Fernandez-Maloigne, ed. (Springer, 2013).

176. A. Robles-Kelly and C. P. Huynh, *Imaging Spectroscopy for Scene Analysis* (Springer, 2013).

177. V. C. Coffey, "Multispectral Imaging Moves into the Mainstream," Optics & Photonics News, 18–24 (April 2012).

178. J. M. Eichenholz and J. Dougherty, "Ultracompact Fully Integrated MegaPixel MultiSpectral Imager," Proc. SPIE **7218**, 721814 (2009).

179. J. M. Eichenholz, N. Barnett, Y. Juang, D. Fish, S. Spano, E. Lindsley, and D. L. Farkas, "Real time Megapixel Multispectral Bioimaging," Proc. SPIE **7568**, 75681L (2010).

180. D. Yi and L. Kong, "A real-time multispectral imaging system for low- or mid-altitude remote sensing," Proc. SPIE **8516**, 85160E (2012).

181. D. Yi, C. Wang, H. Qi, L. Kong, F. Wang, and A. Adibi, "Real-Time Multispectral Imager for Home-Based Health Care," IEEE Trans. Biomed. Eng. **58**(3), 736–740 (2011).

182. H. Liang, "Advances in multispectral and hyperspectral imaging for archaeology and art conservation," Appl. Phys. A **106**, 309–323 (2012).

183. G. Bianco, F. Bruno, and M. Muzzupappa, "Multispectral data cube acquisition of aligned images for document analysis by means of a filter-wheel camera provided with focus control," J. Cult. Herit. **14**, 190–200 (2013).

184. J. Brauers, N. Schulte, and T. Aach, "Multispectral Filter-Wheel Cameras: Geometric Distortion Model and Compensation Algorithms," IEEE Trans. Image Process. **17**(12), 2368–2380 (2008).

185. J. Qin, K. Chao, M. S. Kim, R. Lu, and T. F. Burks, “Hyperspectral and multispectral imaging for evaluating food safety and quality,” J. Food Eng. **118**, 157–171 (2013).

186. F. Rutz, R. Rehm, A. Wörl, J. Schmitz, M. Wauro, J. Niemasz, M. Masur, M. Walther, R. Scheibner, and J. Ziegler, “Imaging detection of CO_2 using a bispectral type-II superlattice infrared camera,” in *11th International Conference on Quantitative InfraRed Thermography* (2012).

187. M. Kowalski, M. Kastek, H. Polakowski, N. Palka, M. Piszczek, and M. Szustakowski, "Multispectral concealed weapon detection in visible, infrared, and terahertz," Proc. SPIE **9102**, 91020T (2014).

188. M. Kowalski, M. Kastek, N. Palka, H. Polakowski, M. Szustakowski, and M. Piszczek, “Investigations of concealed objects detection in visible, infrared and terahertz ranges,” Photonics Lett. Pol. **5**(4), 167–169 (2013).

189. T. May, G. Zieger, S. Anders, V. Zakosarenko, H.-G. Meyer, M. Schubert, M. Starkloff, M. Rößler, G. Thorwirth, and U. Krause, “Safe VISITOR: VISible, Infrared and Terahertz Object Recognition for security screening application,” Proc. SPIE **7309**, 73090E (2009).

190. T. Xu, Y.-K. Wu, X. Luo, and L. J. Guo, “Plasmonic nanoresonators for high-resolution colour filtering and spectral imaging,” Nat. Commun. **1**(59), 1–5 (2010).

191. A. Cosentino, “Identification of pigments by multispectral imaging; a flowchart method,” Heritage Science **2**(8), 1–12 (2014).

192. K. Martinez, J. Cupitt, D. Saunders, and R. Pillay, “Ten Years of Art Imaging Research,” Proc. IEEE **90**(1), 28–41 (2002).

193. G. Polder, G. W. A. M. van der Heijden, H. van der Voet, and I. T. Young, “Measuring surface distribution of carotenes and chlorophyll in ripening tomatoes using imaging spectrometry,” Postharvest Biol. Tec. **34**, 117–129 (2004).

194. M. Yamaguchi, M. Mitsui, Y. Murakami, H. Fukuda, N. Ohyama, and Y. Kubota, “Multispectral color imaging for dermatology: application in inflammatory and immunologic diseases,” in *13th Color Imaging Conference* (2005).

195. D. Manolakis, D. Marden, and G. A. Shaw, “Hyperspectral Image Processing for Automatic Target Detection Applications,” Lincoln Laboratory Journal **14**(1), 79–116 (2003).

196. A. L. Chan and S. R. Schnelle, “Fusing concurrent visible and infrared videos for improved tracking performance,” Opt. Eng. **52**(1), 017004 (2013).

197. S. G. Kong, J. Heo, F. Boughorbel, Y. Zheng, B. R. Abidi, A. Koschan, M. Yi, and M. A. Abidi, “Multiscale Fusion of Visible and Thermal IR Images for Illumination-Invariant Face Recognition,” Int. J. Comput. Vision **71**(2), 215–233 (2007).

198. S. Khorram, F. H. Koch, C. F. van der Wiele, and S. A. C. Nelson, *Remote Sensing* (Springer, 2012).

199. E. R. Hunt, Jr., W. D. Hively, S. J. Fujikawa, D. S. Linden, C. S. T. Daughtry, and G. W. McCarty, "Acquisition of NIR-Green-Blue Digital Photographs from Unmanned Aircraft for Crop Monitoring," Remote Sens. **2**, 290–305 (2010).

200. A. K. Tilling, G. J. O'Leary, J. G. Ferwerda, S. D. Jones, G. J. Fitzgerald, D. Rodriguez, and R. Belford, "Remote sensing of nitrogen and water stress in wheat," Field Crop. Res. **104**, 77–85 (2007).

201. G. A. Shaw and H. K. Burke, "Spectral Imaging for Remote Sensing," Lincoln Laboratory Journal **14**(1), 3–28 (2003).

202. M. Yamaguchi, T. Teraji, K. Ohsawa, T. Uchiyama, H. Motomura, Y. Murakami, and N. Ohyama, "Color image reproduction based on the multispectral and multiprimary imaging : Experimental evaluation," Proc. SPIE **4663**, 15–26 (2002).

203. B. Hill, "Color capture, color management and the problem of metamerism: does multispectral imaging offer the solution?," Proc. SPIE **3963**, 2–14 (2000).

204. C. M. U. Neale and B. G. Crowther, "An Airborne Multispectral Video/Radiometer Remote Sensing System: Development and Calibration," Remote Sens. Environ. **49**, 187–194 (1994).

205. C. Pohl and J. L. Van Genderen, "Review article - Multisensor image fusion in remote sensing: concepts, methods and applications," Int. J. Remote Sensing **19**(5), 823–854 (1998).

206. H. I. Cakir and S. Khorram, "Pixel Level Fusion of Panchromatic and Multispectral Images Based on Correspondence Analysis," Photogramm. Eng. Remote Sens. **74**(2), 183–192 (2008).

207. Z. Xue and R. S. Blum, "Concealed Weapon Detection Using Color Image Fusion," in *Proceedings of the Sixth International Conference of Information Fusion, 2003* (IEEE, 2003), pp. 622–627.

208. M. Kowalski, N. Palka, M. Piszczek, and M. Szustakowski, "Processing of THz images acquired by passive camera," Photonics Lett. Pol. **4**(3), 97–99 (2012).

209. M. Kowalski, M. Piszczek, N. Palka, and M. Szustakowski, "Improvement of passive THz camera images," Proc. SPIE **8544**, 85440N (2012).

210. D. J. Griffiths, *Introduction to Electrodynamics*, 3rd ed. (Pearson Benjamin Cummings, 2008).

211. R. P. Feynman, R. B. Leighton, and M. Sands, *The Feynman Lectures on Physics: Volume II* (Addison-Wesley, 1977).

212. H. Gao, W. Zhou, and T. W. Odom, "Plasmonic Crystals: A Platform to Catalog Resonances from Ultraviolet to Near-Infrared Wavelengths in a Plasmonic Library," Adv. Funct. Mater. **20**, 529–539 (2010).

213. W. Zhou, H. Gao, and T. W. Odom, "Toward Broadband Plasmonics: Tuning Dispersion in Rhombic Plasmonic Crystals," ACS Nano **4**(2), 1241–1247 (2010).

214. S. Mei, T. Jie, L. Zhi-Yuan, C. Bing-Ying, Z. Dao-Zhong, J. Ai-Zi, and Y. Hai-Fang, "The Role of Periodicity in Enhanced Transmission through Subwavelength Hole Arrays," Chin. Phys. Lett. **23**(2), 486–488 (2006).

215. J. Bravo-Abad, A. I. Fernández-Domínguez, F. J. García-Vidal, and L. Martín-Moreno, "Theory of Extraordinary Transmission of Light through Quasiperiodic Arrays of Subwavelength Holes," Phys. Rev. Lett. **99**, 203905 (2007).

216. A. D. Rakić, "Algorithm for the determination of intrinsic optical constants of metal films: application to aluminum," Appl. Opt. **34**(22), 4755–4767 (1995).

217. A. P. Hibbins, B. R. Evans, and J. R. Sambles, "Experimental Verification of Designer Surface Plasmons," Science **308**, 670–672 (2005).

218. C. A. Balanis, "Circular Waveguides," in *Encyclopedia of RF and Microwave Engineering Volume 1-6*, E. Holzman (article ed.) and K. Chang (book ed.) (Wiley, 2005).

219. F. J. García de Abajo, "Light transmission through a single cylindrical hole in a metallic film," Opt. Express **10**(25), 1475–1484 (2002).

220. X. Chen, T. M. Grzegorczyk, B.-I. Wu, J. Pacheco Jr., and J. A. Kong, "Robust method to retrieve the constitutive effective parameters of metamaterials," Phys. Rev. E **70**, 016608 (2004).

221. J. Woodley and M. Mojahedi, "On the signs of the imaginary parts of the effective permittivity and permeability in metamaterials," J. Opt. Soc. Am. B **27**(5), 1016–1021 (2010).

222. R. L. Musselman, "Electromagnetic Wave Scattering," in *Encyclopedia of RF and Microwave Engineering Volume 1-6*, K. Chang, ed. (Wiley, 2005).

223. K. S. Yee, "Numerical Solution of Initial Boundary Value Problems Involving Maxwell's Equations in Isotropic Media," IEEE Trans. Antennas Propag. **14**(3), 302–307 (1966).

224. A. Taflove, *Computational Electrodynamics: The Finite-Difference Time-Domain Method* (Artech House, 1995).

225. S. G. Rodrigo, *Optical Properties of Nanostructured Metallic Systems: Studied with the Finite-Difference Time-Domain Method* (Springer, 2012).

226. "Lumerical FDTD Solutions," Accessed: 19/03/2015. https://www.lumerical.com/tcad-products/fdtd/

227. "Lumerical Knowledge Base," Accessed: 19/03/2015. http://docs.lumerical.com/en/index.html

228. "James Watt Nanofabrication Centre, Equipment Web Page," Accessed: 19/03/2015. http://www.jwnc.gla.ac.uk/equipment.html

229. J. Hopwood, "Review of inductively coupled plasmas for plasma processing," Plasma Sources Sci. Technol. **1**, 109–116 (1992).

230. J. W. Lee, K. D. Mackenzie, D. Johnson, J. N. Sasserath, S. J. Pearton, and F. Ren, "Low Temperature Silicon Nitride and Silicon Dioxide Film Processing by Inductively Coupled Plasma Chemical Vapor Deposition," J. Electrochem. Soc. **147**(4), 1481–1486 (2000).

231. *Leica Vectorbeam Series, Vectorbeam Operator Manual* (Leica Microsystems Lithography Ltd, 2005).

232. *Electron Beam Lithography Course Notes - University of Glasgow* (2014).

233. S. Thoms, "Belle 6.13," (2007).

234. G. S. Oehrlein, "Reactive-ion etching," Phys. Today **39**(10), 26–33 (1986).

235. "Angstrom Sun Technologies - Microspectrophotometer MSP300," Accessed: 03/03/2015. http://www.angstec.com/products/Microspectrophotometer MSP300

236. W. Herres and J. Gronholz, "Understanding FT-IR Data Processing - Part 1: Data Acquisition and Fourier Transformation," Comp. Appl. Lab. **2**, 216 (1984).

237. V. Saptari, *Fourier-Transform Spectroscopy Instrumentation Engineering* (SPIE - The International Society for Optical Engineering, 2004).

238. E. D. Palik, *Handbook of Optical Constants of Solids, Volumes I, II and III* (Academic Press, 1985).

239. "ImageJ," Accessed: 19/03/2015. http://imagej.nih.gov/ij/

240. N. Laman and D. Grischkowsky, "Terahertz conductivity of thin metal films," Appl. Phys. Lett. **93**, 051105 (2008).

241. M. Naftaly and R. E. Miles, "Terahertz time-domain spectroscopy of silicate glasses and the relationship to material properties," J. Appl. Phys. **102**, 043517 (2007).

242. J. Grant, I. Escorcia-Carranza, C. Li, I. J. H. McCrindle, J. Gough, and D. R. S. Cumming, "A monolithic resonant terahertz sensor element comprising a metamaterial absorber and micro-bolometer," Laser Photon. Rev. **7**, 1043–1048 (2013).